Molecular Carbon Allotropes: Cyclo[*n*]carbons

Lorel M. Scriven

Wolfson College

University of Oxford

A thesis submitted for the degree of

Doctor of Philosophy

Michaelmas 2020

Acknowledgements

I must start by thanking my supervisor, Professor Harry L. Anderson for his constant encouragement and support over the course of my DPhil. The time and effort he has dedicated to helping me achieve my goals is significant, and I am very grateful. My next set of acknowledgements goes to our highly talented collaboration partners Dr Leo Gross, Katharina Kaiser and Dr Fabian Schulz, with whom we formed a formidable team; special thanks must go to Katharina Kaiser for hosting me during my two visits to IBM Research–Zurich and making me feel so welcome. I would also like to thank all the talented postdocs who have taught me so much during my DPhil. To Dr Przemyslaw Gawel and Dr Steffen Woltering for teaching me the ropes of synthetic chemistry and for providing me with much encouragement and support during many failed reactions and to Dr Keith Andrews and Dr Andrew Frawley for their unending source of synthetic chemistry knowledge. Another special thanks must go to Steffen and Andrew for proofreading this thesis.

Synthetic lab work is only feasible when you are surrounded by a fun and supportive team and for this I must thank all members of the group, past and present: Andreas, Yaoyao, Michel, Tom, Wenjun, Steffen, Bart, James, Renee, Sabine, Will, Martin, Hua-Wei, Lara, Pernille, Przemek, Isa, Anjul, Dan, Jonathan, Andrew, Keith, Connor, Boom, Joe, Kristina, Virginia, Henrik, Isaac, Tom, Jeff, Jibin, Kate, Kenny, Sebastian, Sili. Special thanks go to Connor, Steffen, Isa, James and Bart for their endless support, coffee breaks and pub trips throughout my years in Oxford.

Final thanks must go to my family, for their love and support and always encouraging me to achieve my dreams; none of this would have been possible without you. Also to my amazing friends both in and out of Oxford, I could not have got through these years without you.

Abstract

This thesis details the first structural characterisation of a cyclo[*n*]carbon. Carbon allotropes built from rings of two-coordinate atoms, known as cyclo[*n*]carbons, have fascinated chemists for many years, but until now they could not be isolated or structurally characterised, due to their high reactivity. This thesis describes two different routes to cyclo[18]carbon by atomic manipulation of a cyclocarbon oxide $C_{24}O_6$ and a bromocyclocarbon $C_{18}Br_6$ precursor on bilayer NaCl on Cu(111) at 5 K. It then discusses initial attempts towards the on-surface synthesis of antiaromatic cyclo[*n*]carbons.

Chapter 1 reviews the history of synthetic carbon allotropes, in particular the cyclo[*n*]carbons, including all theoretical and experimental investigations into these molecular carbon allotropes. An introduction to the field of scanning probe microscopy is then detailed.

Chapter 2 discusses the on-surface generation of cyclo[18]carbon by elimination of carbon monoxide from a cyclocarbon oxide molecule, $C_{24}O_6$. Characterisation of cyclo[18]carbon by high-resolution atomic force microscopy reveals a polyynic structure with defined positions of alternating triple and single bonds. The high reactivity of cyclocarbon and the cyclocarbon oxides allows covalent coupling by atom manipulation, which has significant promise for the synthesis of other carbon allotropes and carbon-rich materials from the coalescence of cyclocarbon molecules.

Chapter 3 details the synthesis of cyclo[18]carbon by dehalogenation of a bromocyclocarbon precursor, $C_{18}Br_6$, in 64% yield. This method generates cyclo[18]carbon in a higher yield than from the cyclocarbon oxide, $C_{24}O_6$. The experimental images of C_{18} are compared with simulated images for four theoretical model geometries, including possible bond-angle alternation: D_{18h} cumulene, D_{9h} polyyne, D_{9h} cumulene and C_{9h}

polyyne. Cumulenic structures with (D_{9h}) and without (D_{18h}) bond-angle alternation can be excluded. Polyynic structures with (C_{9h}) and without (D_{9h}) bond-angle alternation both show a good agreement with the experiment and are challenging to differentiate.

Chapter 4 explores the synthesis and properties of a series of cyclocarbon oxides as precursors to antiaromatic cyclo[*n*]carbons. The synthesis of cyclocarbon oxide precursors to cyclo[24]carbon ($C_{32}O_8$) and cyclo[20]carbon ($C_{28}O_8$) is discussed however the on-surface sublimation of both molecules proves unsuccessful. Initial investigations into the synthesis of a cyclo[16]carbon precursor, $C_{22}O_6$, are also detailed. Finally, a number of possible future avenues for this project are described.

Supplement to Statement of Authorship

My DPhil has been a part of a fruitful collaboration with IBM Research–Zurich. All atomic force microscopy measurements described in this thesis were carried out in collaboration with the group of Dr Leo Gross at IBM Research–Zurich.

Chapter 2 details the first structural characterisation of a cyclo[*n*]carbon. The author carried out all the synthesis and characterisation of compounds listed in this chapter. All AFM experiments were performed by Katharina Kaiser, Dr Fabian Schulz, Dr Leo Gross and, in part, by the author upon visiting IBM Research-Zurich. Interpretation and analysis of images was carried out by the author, Katharina Kaiser, Dr Fabian Schulz, Dr Przemyslaw Gawel, Dr Leo Gross and Professor Harry Anderson. Dr Fabian Schulz, Dr Przemyslaw Gawel and Katharina Kaiser carried out the DFT calculations. Dr Fabian Schulz performed the AFM simulations.

Chapter 3 details the synthesis of the molecular carbon allotrope cyclo[18]carbon by dehalogenation of a bromocyclocarbon precursor, $C_{18}Br_6$. The author carried out all the synthesis and characterisation of the compounds discussed in this chapter. All AFM images in this chapter were performed by Katharina Kaiser, Dr Fabian Schulz, Dr Leo Gross and, in small part, by the author upon visiting IBM Research-Zurich. Interpretation and analysis of images was carried out by the author, Katharina Kaiser, Dr Fabian Schulz, Dr Leo Gross and Professor Harry Anderson. DFT calculations were carried out by Alistair Sterling and Katharina Kaiser. AFM simulations were performed by Katharina Kaiser.

Chapter 4 details the synthesis and properties of a series of cyclocarbon oxides and their corresponding acetal precursors. The author planned all synthetic routes detailed in this chapter and carried out the synthesis of all compounds except from investigations into the cyclo[16]carbon precursor $C_{22}O_6$ which were carried out by a Part II student Isaac Ettedgui under the supervision of the author. All AFM investigations in this chapter were performed by Katharina Kaiser, Felix Hermann and Dr Leo Gross. NICS and molecular orbital calculations were performed by Dr Michael Jirásek.

Contents

List of publications and awards

Publications

1. Katharina Kaiser,[†] Lorel M. Scriven,[†] Fabian Schulz, Przemyslaw Gawel,* Leo Gross,* Harry L. Anderson* *Science*, **2019**, *365*, 1299–1301.

   [†] These authors contributed equally.
2. Lorel M. Scriven,[†] Katharina Kaiser,[†] Fabian Schulz, Alistair J. Sterling, Steffen L. Woltering, Przemyslaw Gawel, Kirsten E. Christensen, Harry L. Anderson,* Leo Gross* *J. Am. Chem. Soc.* **2020**, *142*, 12921–12924.

   [†] These authors contributed equally
3. Harry L. Anderson, Connor W. Patrick, Lorel M. Scriven, Steffen L. Woltering "A short history of cyclocarbons", *manuscript submitted.*

Awards

- Chemical Science poster prize at CURO-π^3, The Chemistry, Physics and Materials Science of Non-planar Aromatics and Curved π Systems. 5–7th September 2018, University of Oxford.
- Bulletin of the Chemical Society of Japan poster prize at ISNA-18, the 18th International Symposium on Novel Aromatic Compounds. 21–26th July 2019, Sapporo, Japan.
- Pfizer poster prize at the Pfizer Organic Chemistry and Chemical Biology Symposium. 31st October 2019, University of Oxford.

Abbreviations

AFM	Atomic Force Microscopy
AM-AFM	Amplitude Modulation AFM
APCI	Atmospheric-Pressure Chemical Ionisation
B_2pin_2	Bis(pinacolato)diboron
BAA	Bond Angle Alternation
BLA	Bond Length Alternation
CASSCF	Complete Active Space SCF method
CCSD	Coupled-Cluster Singles and Doubles excitation theory
CISD	Configuration Interaction with Single and Double excitations
DBA	9,10-Dibromoanthracene
DFT	Density Functional Theory
DMF	*N,N*-Dimethylformamide
DSC	Differential Scanning Calorimetry
DZP	*d* polarization functions
ESI	Electrospray Ionisation
FM-AFM	Frequency Modulation AFM
FMO	Frontier Molecular Orbitals
FT-IR	Fourier Transform Infra-Red
GGA	Generalised Gradient Approximation
GIMIC	Gauge-Including Magnetically Induced Currents
GPC	Gel Permeation Chromatography
HBC	Hexabenzocoronene
HF	Hartree-Fock
HMPA	Hexamethylphosphoramide
HOMA	Harmonic Oscillator Model of Aromaticity
HOMO	Highest Occupied Molecular Orbital
HPLC	High Performance Liquid Chromatography
HR-MS	High-Resolution Mass-Spectrometry
HSE	Heyd-Scuseria-Ernzerhof
IET	Inelastic Energy Tunneling
LDA	Lithium diisopropylamide
LiHMDS	Lithium bis(trimethylsilyl)amide
LUMO	Lowest Unoccupied Molecular Orbital
MAE	Masked Alkyne Equivalent
MALDI	Matrix-Assisted Laser Desorption Ionisation
MP2	Second-order Møller-Plesset perturbation theory
NBS	*N*-Bromosuccinimide
nc-AFM	non-contact AFM
NICS	Nucleus Independent Chemical Shift
NIR	Negative Ion Resonance
NMR	Nuclear Magnetic Resonance
PBE	Perdew–Burke-Ernzerhof
PIR	Positive Ion Resonance
PPM	Probe-Particle Model
PTFE	Polytetrafluoroethylene
QMC	Quantum Monte Carlo

SCF	Self-Consistent Field
SOJT	Second-Order Jahn-Teller
SPM	Scanning Probe Microscopy
SS-FVP	Solution Spray Flash Vacuum Pyrolysis
STS	Scanning Tunneling Spectroscopy
TBAF	Tetrabutylammonium fluoride
TBATB	Tetrabutylammonium tribromide
Tf	Trifluoromethylsulfonyl
THF	Tetrahydrofuran
TIPS	Tri*iso*propylsilyl
TLC	Thin Layer Chromatography
TMEDA	Tetramethylethylenediamine
TMS	Trimethylsilyl
TMSOTf	Trimethylsilyl trifluoromethanesulfonate
UHV	Ultra-High Vacuum
UV	Ultraviolet

Introduction

Carbon is the fourth most abundant element in the universe[1]. It is also one of the most intriguing elements due to its diverse bonding characteristics that allow carbon to exist in many different forms, named allotropes. The word allotrope is derived from the Ancient Greek with *allos* meaning ‘other’ and *tropos* meaning ‘turn’ (or more literally behaviour) thus the literal translation being ‘other behaviours’ of carbon. The concept of allotropes was introduced in 1841 by the Swedish scientist Baron Jöns Jakob Berzelius[2] upon consideration of the monoclinic and rhombic forms of sulfur. This led him to realise there was no term for differing forms of the same element and thus the term *allotrope* came into being. However, no explanation was given as to the cause of the phenomenon of allotropy. As a result the term became somewhat vague, so much so that it was the focus of a famous quip by Stanley Jevons’ (an economist and logician) in the 1870s who said allotropes were those “curious states, which chemists conveniently dispose of by calling them allotropic, a term freely used when they are puzzled to know what has happened[3]”.

Fortunately, our understanding of allotropes has progressed since and the allotropes of carbon are becoming increasingly well understood. This introduction will detail the field of carbon allotropes, in particular the subject of cyclo[*n*]carbons, the focus of this thesis. The field of scanning probe microscopy will then be introduced as this was the main analytical technique employed in this thesis for the study of the cyclo[*n*]carbons.

1 Introduction

1.1 Carbon allotropes synthesised to date

The two naturally occurring allotropes of carbon, graphite and diamond, have had many uses in society over the centuries[1]. At ambient conditions graphite is the most thermodynamically stable carbon allotrope and has a high natural abundance[4,5]. Diamond is kinetically inert at ambient conditions and is only naturally formed in high pressure and temperature environments hence its much lower natural abundance[6]. The properties of diamond and graphite have been explored over the centuries; for a long time diamond was the hardest known material[7] whereas graphite is highly conductive and self-lubricating[1]. These varied properties drew the attention of scientists to carbon and sparked interest in the possibility of discovering further allotropes.

1.1.1 Discovery of the sp^2 hybridised carbon allotropes

Carbon allotropes can be divided into three categories based on their hybridisation state. Each carbon atom can be connected to four others in a tetrahedral sp^3 hybridised geometry, as in diamond. This infinite covalent network endows diamond with its high strength. In graphite each carbon is connected to three others in a trigonal sp^2 hybridised geometry. Graphite consists of hexagonal carbon arrays with strong covalent bonding in the plane of the sheet and weak van der Waals interactions between them[8]. The sheets can slide over one another, leading to graphite's self-lubricating properties[8]. Carbon can also exist in a linear *sp* hybridised geometry, where each carbon is bonded to two others, but the thermodynamic instability of these species means no naturally occurring allotropes exist with this bonding configuration.

The diverse properties of the naturally occurring carbon allotropes initiated interest in the field of synthetic carbon allotropes[9] (Figure 1.1). *sp^2* Hybridised allotropes have been the main focus of synthetic efforts for the last half century; *sp* hybridised allotropes have also been investigated and will be discussed in Section 1.1.2.

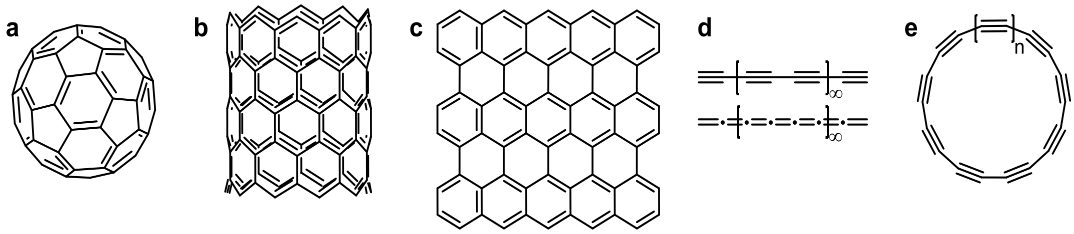

Figure 1.1 Synthetic carbon allotropes **a**) fullerene **b**) carbon nanotube **c**) graphene **d**) carbyne **e**) cyclo[*n*]carbon.

The first entry into the field of synthetic carbon allotropes was the discovery of *sp^2* hybridised buckminsterfullerene C_{60} (Figure 1.1a) by Kroto, Curl and Smalley in 1985[10]. Kroto and co-workers were investigating carbon chains produced upon laser vaporisation of graphite[11]. By mass spectrometry they observed a very intense peak for C_{60}, suggesting a highly stabilised carbon cluster was being formed. The structure of C_{60} was first predicted by Osawa in 1970[11]. A combination of Euler's 12-pentagon closure principle (if 12 pentagons are introduced into a hexagonal sheet it will close) and the fact that two adjacent pentagons are unstable gives the elegant solution of a truncated icosahedron with 32 faces, 20 of which are hexagonal and 12 pentagonal where no two pentagons are adjacent. This seminal work was awarded the 1996 Nobel Prize in Chemistry[11] for "the discovery of carbon atoms bound in the form of a ball".

The field received a further impetus upon the synthesis of bulk quantities of C_{60} by Huffman and co-workers[12] (Figure 1.2). Previous work by Huffman[13] showed that carbon soot produced by vaporisation of graphite was enriched with C_{60} molecules. The seemingly simple preparation of suspending the soot in benzene and then filtering yielded a deep red solution of pure C_{60} which was characterised by mass spectrometry and powder X-ray diffraction analysis. By this method C_{60} could be isolated in 100 mg batches[12]. Huffman beat Kroto to this discovery by a matter of weeks[11]. The field of fullerene chemistry has been growing ever since with an increasing number of applications being found. To name but a few fullerenes have been used in solar cells[14], as HIV drugs[15] or as superconductors[16].

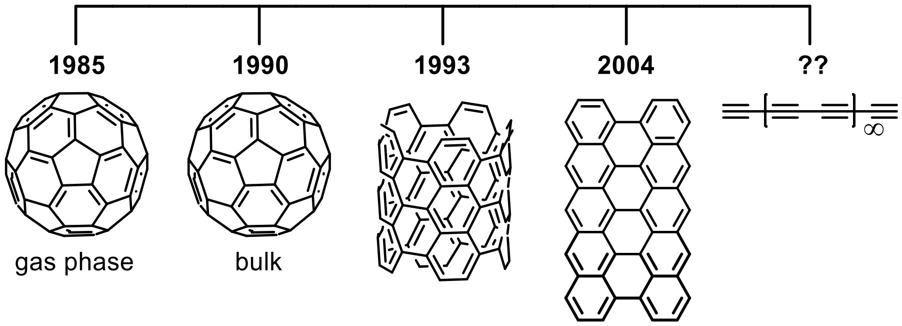

Figure 1.2 Timeline of synthetic carbon allotrope discovery.

Around the time (Figure 1.2) of all the excitement surrounding fullerenes, Iijima started work on the field of carbon nanotubes[17]. Using a similar setup to that used for the preparation of C_{60} he first observed helical graphitic carbon needle-like structures. Using electron microscopy, he found each needle contained multiple carbon nanotubes contained within each other in a Russian doll type morphology. However his crucial work came two years later[18] when he reported the synthesis of single-shell carbon nanotubes with a diameter of 1 nm. He modified his experimental setup to generate carbon nanotubes from the gas phase which allowed single shell carbon nanotubes to be obtained. The field of carbon nanotubes continues to develop with the ultimate aim being their synthesis with controlled length, chirality and diameter[19,20]. The properties of carbon nanotubes found thus far include high tensile strength[21], impressive field emission characteristics[22] and high thermal and electrical conductivity[23].

Up to 2004, cage and tube structures based on a graphene sheet had been isolated but isolation of the graphene sheet itself still eluded scientists until Geim and Novoselov isolated single layer graphene for the first time[24]. Upon experimenting with transferring graphite between pieces of scotch tape they noticed the layers becoming sequentially thinner until they created a single layer graphene fragment[24]. The many properties of graphene have since been investigated and their breadth of character has led to the nickname of the 'miracle material[25]' due to properties like extremely high electron mobility of 2.5×10^5 cm^2 V^{-1} s^{-1}[26], a Young's modulus of 1 TPa[27], complete impermeability to gases[28] and zero band gap[29]. The 2010 Nobel Prize in Physics was awarded to Novoselov and Geim[29] for "groundbreaking experiments regarding the two-dimensional material graphene".

Over the period of discovery of the *sp*^{2} hybridised carbon allotropes scientists had already begun investigating the *sp*-hybridised carbon allotropes[30–32]. This will be the focus of the next sections.

1.1.2 Carbyne

There are two possible allotropes based on *sp* hybridised carbon, cyclo[*n*]carbons and carbyne (Figure 1.1). Cyclo[*n*]carbons were first discussed by Pitzer and Clementi in 1959[33] and will be discussed in Section 1.2. There have been spurious claims that carbyne has been detected in meteorites[34] and prepared by shock fusion of graphite[35] however these claims have been widely discredited[36,37]. Carbyne is predicted to have impressive properties if it can be stabilised such as possessing twice the stiffness of any known material under tension[38] or acting as the optimal molecular wire[38]. However despite a few disputed examples[39,40] there have been no reports of its isolation in the bulk phase and this is not surprising considering the instability of long polyynes; the alkyne units have a high tendency to cross link. Polyynes are the short chain analogues of carbyne, their stability decreases as the length of the carbon chain increases[41]. In order to reach polyynes of sufficient length that their properties start to resemble those of carbyne the chains must be stabilised. Three methods of chemical stabilisation of long polyynes have been reported (Figure 1.3). The first tactic is the use of bulky endcapping groups that sterically protect the polyyne chain thereby preventing intermolecular reactions[42,43]. Tykwinski and co-workers used this technique to prepare the longest bulk carbyne analogue synthesised to date[41,44]. They initially used bulky supertrityl stoppers[41] to sterically protect the polyyne chain and were able to synthesise a chain of 44 acetylenic carbons (Figure 1.3a). They recently improved on this to synthesise pyridyl-endcapped oligoynes with 48 acetylenic carbons[44]. The second technique is to use supramolecular encapsulation[45]. This technique was first proposed by Diederich and co-workers[9], a macrocycle sterically shields the polyyne chain increasing the thermal stability of the system[46] and was extended to longer polyynes by Anderson and coworkers[47,48] (Figure 1.3b). The most recent stabilisation method reported is the synthesis of carbyne inside double walled carbon nanotubes[49]. The nanotube shields the carbyne chain thereby preventing decomposition by cross linking and allowed carbyne chains of up to 6000 carbon atoms to be studied by transmission electron microscopy (Figure 1.3c).

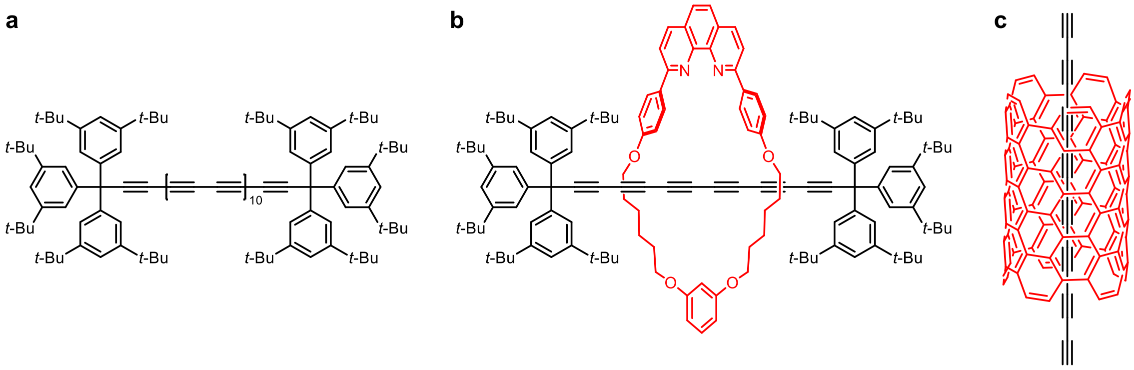

Figure 1.3 Methods of stabilising carbyne derivatives **a**) bulky stopper groups **b**) supramolecular encapsulation **c**) carbon nanotube encapsulation.

There are two possible resonance forms of carbyne, cumulenic or acetylenic (Figure 1.4a). For short chain systems whether a carbon chain adopts a cumulenic or acetylenic geometry is determined by the nature of the end groups[41,47,50]. The difference between polyynic and cumulenic systems lies in the orbital overlap of the two orthogonal π systems (displayed by the red and blue *p* orbitals in this section) and the bond length alternation (BLA) in the carbon chain. A polyynic carbon chain has alternating single and triple bonds and significant BLA. The triple bond can be drawn by orbital overlap as shown in Figure 1.4b. Overlap of the red orbitals produces one of the π bonds and overlap of the blue orbitals produces the second. Cumulenic carbon chains are drawn with one π bond between adjacent carbons (Figure 1.4c) although experimental studies have found there is still some degree of BLA within the chain[51,52]. Odd and even cumulenes have different geometries. Even cumulenes (carbon chain consists of an even number of double bonds and odd number of carbon atoms) possess a perpendicular arrangement of the end groups to ensure uniform overlap across the whole chain (Figure 1.4c) which creates double bonds along the chain. Correspondingly orbital overlap in odd cumulenes (odd number of double bonds but even number of carbon atoms in the carbon chain) results in end groups in the same plane.

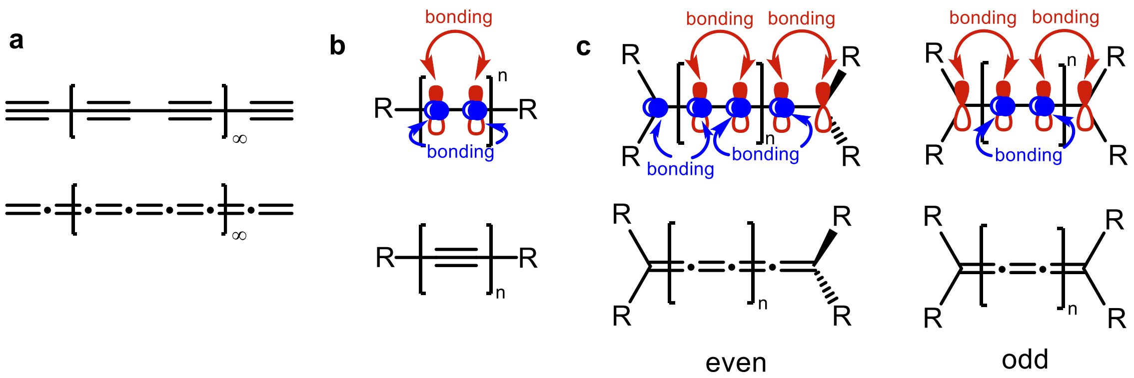

Figure 1.4 Possible bonding configurations in *sp* hybridised carbon allotropes **a**) two resonance forms of carbyne **b**) acetylene orbitals **c**) even and odd cumulene orbitals.

In the case of carbyne, the structure is in the infinite limit as the effect of the end groups no longer applies and effects such as Peierls distortion[53] must be considered. The following discussion is modified from a review by Hoffman[53]. Peierls distortion can be considered as the infinite chain analogue of the Jahn-Teller effect[54] that uses the periodicity of the system to enable the case of an infinitely long carbyne chain to be studied. Cyclobutadiene is a convenient model system to examine the Jahn-Teller effect, even though there is some debate as to whether it is a “true” first-order Jahn-Teller distortion[55]. The Hückel molecular orbitals of cyclobutadiene are shown below (Figure 1.5a). For a first order Jahn-Teller distortion there must be two electrons in two degenerate orbitals and a vibrational mode that can break the degeneracy of the system resulting in a lower energy electron configuration. The symmetry lowering vibration of cyclobutadiene from D_{4h} to D_{2h} results in a decrease in energy of one of the degenerate orbitals (which is filled) and the raising in energy of the other (which is empty) and therefore the net energy of the system is lowered. Second order Jahn-Teller distortions are also possible in some systems. A second order Jahn-Teller distortion involves a non-degenerate system, with two levels of different symmetry. If a symmetry lowering vibration is applied then the levels can interact and repel each other resulting in a net lowering of energy of the system (Figure 1.5b).

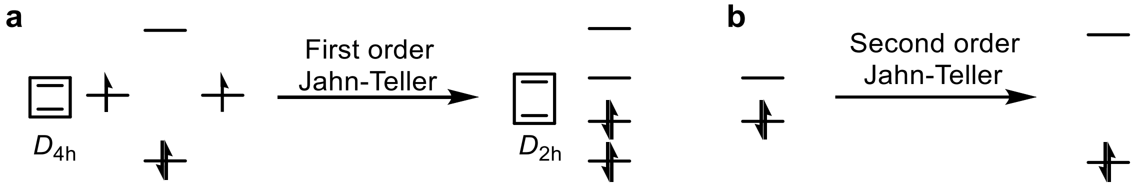

Figure 1.5 Origin of first and second order Jahn-Teller effects. **a**) first order Jahn-Teller distortion of cyclobutadiene, **b**) second order Jahn-Teller distortion of a hypothetical system.

To examine the effect of a Peierls distortion on carbyne its orbitals must be considered as a band structure. For a lattice with equally spaced points, each labelled by an index $n = 0, 1, 2, 3, 4$, etc. with a basis function χ_n symmetry-adapted linear combinations are given by Bloch functions, Equation (1).

$$\varphi_k = \sum_n e^{ikna} x_n \tag{1}$$

Where a is the lattice spacing and k is an index that labels how the wavevector transforms. From the perspective of a chemist the generation of a Bloch function (φ_k) from combinations of basis functions (χ_n) can be thought of analogous to forming a molecular orbital from linear combinations of atomic orbitals, extended to a periodic system. Each value of k has an associated energy level, $E(k)$ and this can be represented as a band diagram, i.e. a plot of

$E(k)$ *vs.* k (Figure 1.6). Different values of k from $k = 0$ (the most bonding contribution) to $k = \pi/2a$ (corresponds to E_F, the Fermi energy of the band) to $k = \pi/a$ (the most antibonding contribution) describe the band features of the solid. The number of values of k between $0 < k < \pi/a$ is quantised but very large so can be considered infinite.

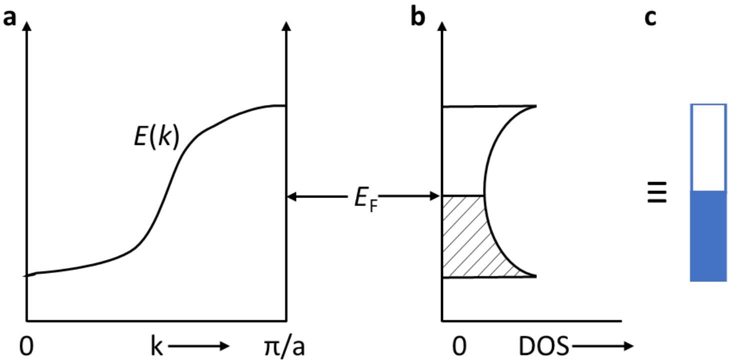

Figure 1.6 a) $E(k)$ *vs.* k diagram **b**) density of states diagram **c**) corresponding band structure representation.

If the orbitals of carbyne are considered as a band structure, as shown in Figure 1.7, then the effect of Peierls distortion on the system can be examined. For any partially filled band there is near degeneracy of k values just above or below the Fermi level. A Peierls distortion occurs when partial filling of a band leads to a non-zero density of states at the Fermi level. Electron-phonon coupling, i.e. a lattice vibration that introduces BLA (Figure 1.7) can open an energy gap at the Fermi level. The effects at the top and bottom of the band are negligible however the effect around the Fermi level E_F is larger, some of the degenerate levels are stabilised and some are destabilised. These effects mean that upon a Peierls distortion (for example introduction of BLA to a carbyne chain) a band gap is introduced around the Fermi level and there is net stabilisation of the system. From this analysis it is likely that carbyne will be a polyyne in the infinite limit as the carbon chain will minimise its energy by undergoing a Peierls distortion[41,56] and therefore carbyne will possess a band gap and act as a semiconductor[57,58]. If carbyne were to exist in a cumulenic state with no Peierls distortion, there would be no band-gap and thus the material would be metallic in character[59–62].

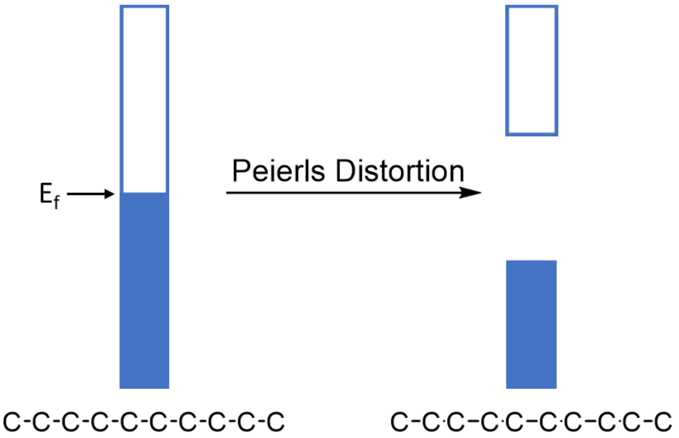

Figure 1.7 The effect of a Peierls distortion on the band structure of carbyne.

As the length of a polyyne chain increases its characteristics are expected to start to resemble that of carbyne. Therefore, the HOMO-LUMO gap (E_g) is predicted to decrease until the value tends towards the band gap of carbyne in the infinite limit. UV spectroscopy can be used as a method to extrapolate the band-gap energy of a system. As the polyyne length increases λ_{max} shifts to longer wavelengths. Meier and co-workers[63] developed a methodology to extrapolate to λ_{sat} which is wavelength in the infinite carbyne limit, Equation (2).

$$\lambda_{(n)} = \lambda_{\infty} - (\lambda_{\infty} - \lambda_1)e^{-a(n-1)} \qquad \textbf{(2)}$$

Where n is the number of acetylene units, $\lambda_{(n)}$ is λ_{max} for a polyyne of length n and λ_{∞} is the value when $n \rightarrow \infty$, a is factor describing how fast convergence is approached. By this analysis Tykwinski and co-workers[41] used UV-vis analysis of their supertrityl capped polyyne chains up to 44 acetylenic carbons to calculate a value of $\lambda_{sat} \approx 485$ nm (2.56 eV) which is reached at approximately $n = 48$. This analysis supported the prediction of carbyne as a polyynic material.

The fact that such extensive structural debate stems from such a seemingly simple molecule is what makes *sp* hybridised carbon allotropes such a focus for chemists. This debate is continued for the cyclo[*n*]carbons and will be detailed in the next section.

1.2 The Cyclo[*n*]carbons

The concept of cyclo[*n*]carbons was first proposed by Pitzer and Clementi in 1959[33] who predicted that cyclic C_n molecules with $n = 4k + 2$ would be stable. This concept was extended by Hoffmann in 1966[30] when he reported Hückel calculations on linear and cyclic C_n for $n = 4–18$ and found that rings are more stable than linear chains for C_{10}, C_{14} and C_{18}. Since then the cyclo[*n*]carbons have been the focus of many synthetic and theoretical chemists over the past half century.

1.2.1 Historical introduction to cyclo[*n*]carbons

Rings of 2-coordinate carbon atoms (cyclo[*n*]carbons, C_n) have been suggested as an alternative family of molecular carbon allotropes. The question of whether cyclocarbons are polyynic, with alternating single and triple bonds, or cumulenic with consecutive double bonds is fundamental and controversial[64–67] (Figure 1.8). Much like the debate surrounding carbyne, the debate regarding the structure of cyclo[*n*]carbon has been fierce and prompted many attempts towards their total synthesis.

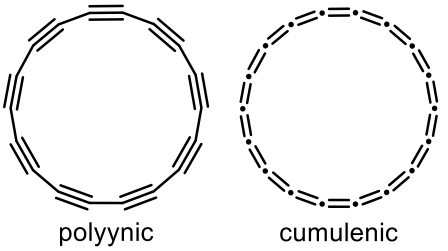

Figure 1.8 Two possible bonding configurations of cyclo[18]carbon, polyynic and cumulenic.

Most attempts at synthesising cyclo[*n*]carbons have used a masked acetylene equivalent incorporated into a cyclic precursor designed to generate cyclo[*n*]carbon when activated by heat or light. Multiple different cyclo[*n*]carbon precursors have been synthesised (Figure 1.9). The first chemist to embark on the total synthesis of a cyclo[*n*]carbon was François Diederich. In his seminal paper in 1989[31] he synthesised a cyclic precursor based on an anthracene masked alkyne equivalent **1** that was designed to lose three anthracene moieties *via* a retro-Diels-Alder reaction[68] under flash vacuum pyrolysis conditions[69]. Upon laser flash heating of a thin film of **1** and monitoring by time-of-flight mass spectrometry cyclo[18]carbon was detected for the first time. The paper ended with the statement "it should be possible to isolate preparative quantities of cyclo[18]carbon[31]" however it was soon realised that any attempts to isolate cyclo[18]carbon in the bulk phase would not be successful due to the inherent instability of this compound.

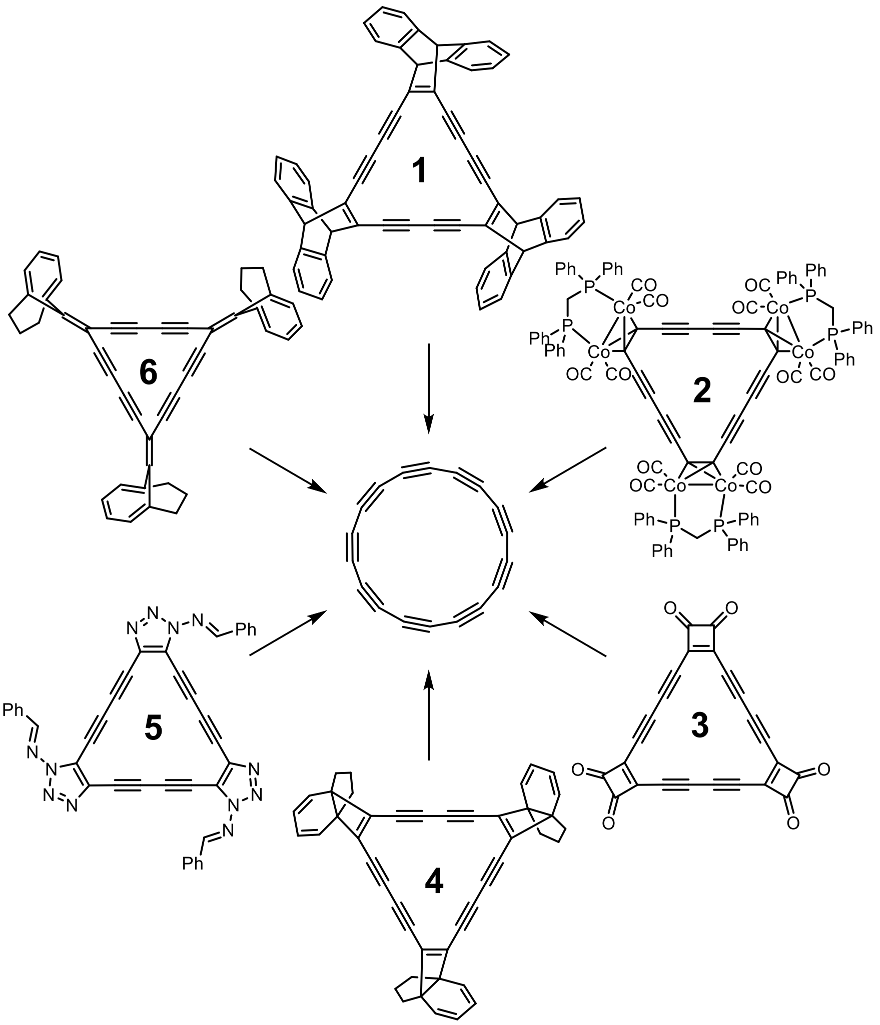

Figure 1.9 Previous synthetic attempts to the cyclo[*n*]carbons.

The Diederich group soon followed up this publication with a rapid succession (Figure 1.10) of papers on two further cyclo[18]carbon precursors. The first was a cyclocarbon oxide precursor **3**[70–73] which generated cyclo[18]carbon upon negative ion laser desorption spectroscopy. The second was a hexacobalt complex of cyclo[18]carbon **2**[74,75] which was designed to generate cyclo[18]carbon upon decomplexation of the cobalt masking groups. Decomplexation of masking cobalt units was first reported by Raithby and co-workers[76] and was extended to longer polyynes by Anderson and co-workers[77] however all attempts to remove cobalt from complex **2** were unsuccessful.

In 1994 Yoshito Tobe entered the field of cyclo[*n*]carbon precursors with a propellane-annulated dehydroannulene cyclo[18]carbon precursor[78,79] **4** designed to generate cyclo[18]carbon upon photochemically activated [2+2] cycloreversion and extrusion of indane. He then went on to synthesise multiple cyclo[*n*]carbon precursors of different sizes[32,80–82] which unmasked to their corresponding cyclo[*n*]carbons upon laser desorption mass spectrometry. Around this time Charles Rees and co-workers[83] developed a cyclocarbon precursor with a 1-amino-1,2,3-triazole masking group **5**. They planned to hydrolyse the benzylidene protecting groups to reveal the free NH cyclocarbon precursor which would undergo oxidation with $Pb(OAc)_4$ to yield cyclo[18]carbon. However they encountered problems with the benzylidene hydrolysis and hence deprotection to cyclo[18]carbon could not be attempted. The last entry to the cyclo[*n*]carbon precursors came in 2003 with Tobe's modified expanded radialene derivative **6**[84] which undergoes a [2+1] cheletropic fragmentation to generate cyclo[*n*]carbon upon photochemical activation.

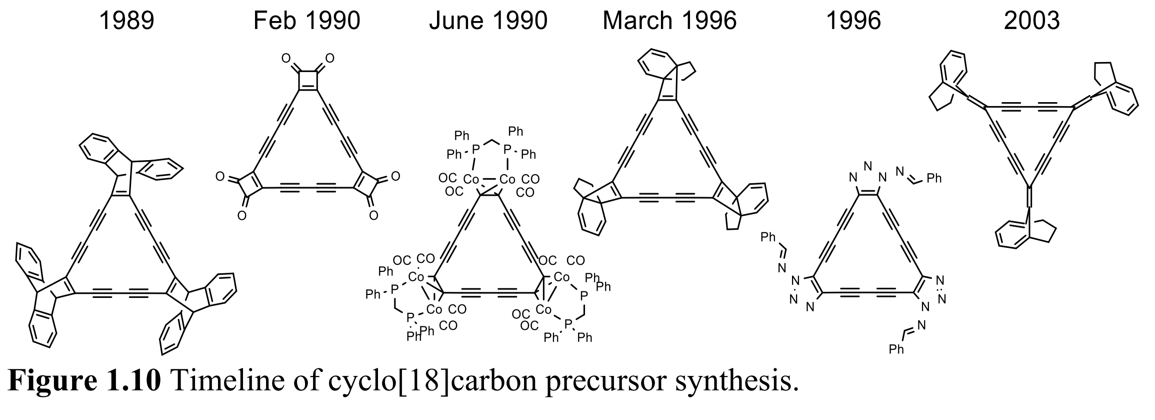

Figure 1.10 Timeline of cyclo[18]carbon precursor synthesis.

An interesting result of the cyclocarbon oxide precursors **3** were the insights they provided into the mechanism of fullerene formation[85–89]. Cyclocarbon oxide precursors to cyclo[18]carbon, cyclo[24]carbon and cyclo[30]carbon were prepared and their positive ion laser desorption mass spectra were analysed. The major product observed in these spectra for cyclo[18]carbon and cyclo[24]carbon appeared at $m/z = 840$ which corresponds to C_{70}^+. Whereas for cyclo[30]carbon the major product was at $m/z = 720$ which corresponds to C_{60}^+. Ionisation energies of the C_{70}^+ and C_{60}^+ signals were used to confirm that they were indeed fullerene structures. Prior to this it was thought fullerenes formed from small carbon fragments (C_1, C_2 and C_3) produced by vaporisation of graphite[89] and thus it is likely that these small fragments coalesce to form cyclo[*n*]carbons which then fuse to form fullerenes. These synthetic attempts gave tantalising glimpses of cyclo[*n*]carbons in the gas phase but they did not give any information regarding their structure which created fierce theoretical debate as detailed in Section 1.2.2.

1.2.2 Structure and properties of cyclo[18]carbon

This section will focus exclusively on the structure and properties of cyclo[18]carbon as a representative aromatic member of the cyclo[*n*]carbon family and the main focus of this thesis. For discussion of the structure and properties of different sizes of cyclo[*n*]carbons please see Section 4.2. Cyclo[18]carbon is an aromatic 18π electron system; Hückel's rules predict for planar, cyclic conjugated systems with $(4n + 2)$ π electrons an aromatic structure with no BLA. Thus a structure with 18 C=C bonds (BLA = 0) would be expected resulting in a D_{18h} cumulenic structure **A** (Figure 1.11). However one can imagine that cyclo[18]carbon can distort to a lower symmetry geometry due to second-order Jahn-Teller effects. Cyclo[18]carbon can either distort by introducing BLA, resulting in alternating C–C single and C≡C triple bonds giving a D_{9h} polyynic structure **B**. Or it can distort to have consecutive C=C bonds but with bond angle alternation (BAA) giving cumulenic D_{9h}

structure **C**. Lastly it can distort and introduce both BLA and BAA resulting in C_{9h} polyynic structure **D** (Figure 1.11).

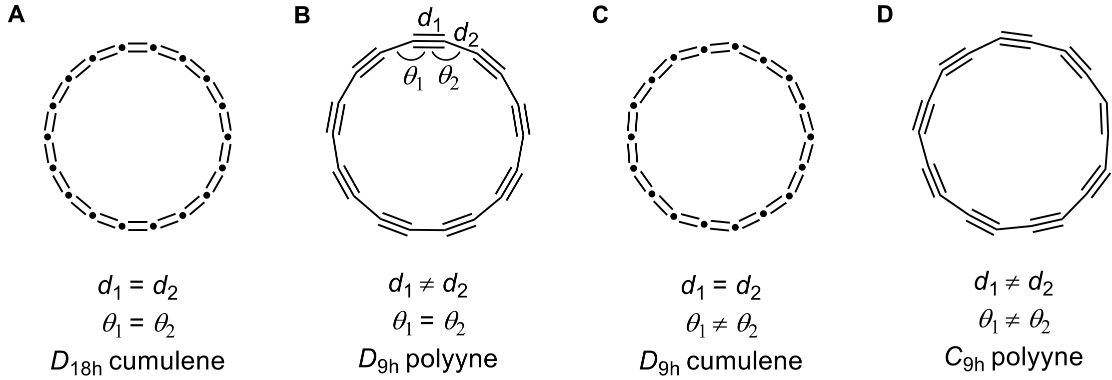

Figure 1.11 Four possible symmetries of cyclo[18]carbon **A**) cumulenic D_{18h}, **B**) polyynic D_{9h}, **C**) cumulenic D_{9h} ($\theta_1 \neq \theta_2$), **D**) polyynic C_{9h} ($\theta_1 \neq \theta_2$).

These possible symmetries have been extensively debated in the literature (Table 1.1) and different calculation types give different structures. These include self-consistent field (SCF), Hartree-Fock method (HF), second-order Møller-Plesset perturbation theory (MP2), coupled-cluster singles and doubles excitation theory (CCSD), density functional theory (DFT), local-density approximation (LDA) and quantum Monte Carlo (QMC). HF, MP2 and CCSD fall under the 'wavefunction'-based methods, that solve the Schrödinger equation using a product of one-electron wavefunctions. LDA, GGA, and hybrid DFT fall under the 'density'-based methods that use the electron density to obtain the energy of a system.

Table 1.1 Theoretical papers discussing the geometry of cyclo[18]carbon.

year	geometry	comment
1989[31]	D_{9h} **B**	Structure of C_{18} calculated using semi-empirical and ab initio molecular orbital calculations. Calculations optimised at HF level of theory give structure **B**.
1991[64]	D_{9h} **B**	**A** was optimised at MP2 level of theory, **B** and **C** were optimised at SCF level of theory as optimisation at MP2 level always led to **A**. At non correlated level **A** is the lowest energy structure. Upon introduction of electron correlation **B** becomes the energy minimum.
1992[90]	D_{9h} **B**	**B** was the energy minimum when analysed at SCF level of theory. If electron correlation is accounted for at MP2 level of theory **A** and **C** become lower in energy.
1994[91]	D_{18h} **A**	DFT study of different carbon ring sizes, conclude **A** is most stable structure.

1995[92]	C_{9h} **D**	DFT study demonstrates the tendency of DFT towards cumulenic structures. Carried out corrected DFT calculations with reduced symmetry to find **D** as the energy minimum.
1995[93]	D_{9h} **C**	Performed DFT calculations with exact exchange contributions. Find **C** to be the minimum energy structure. At the SCF level **D** is the energy minimum.
1998[94]	D_{18h} **A**	HF predicts a Peierls like transition and substantial BLA for $C_n \geq 14$ (structure **B**). Obtain **A** as the minimum energy structure for $C_n < C_{42}$ by LDA methods.
1999[95]	D_{9h} **C**	Implement a hybrid DFT method that includes electron many-body effects. For aromatic rings $C_n \leq C_{18}$ structure **C** is the energy minimum. Above C_{18} a second order Jahn-Teller transition is observed to **B**.
2000[66]	D_{9h} **B**	QMC calculations. Conclude that second-order Jahn-Teller effects result in geometry **B**.
2005[96]	D_{9h} **C**	DFT calculations found **C** as energy minimum.
2008[67]	C_{9h} **D**	CCSD calculations performed. Found that a Peierls distortion occurs at C_{14}. Conclude that **D** is the energy minimum structure for C_{18}.
2009[97]	D_{9h} **C**	DFT calculations found **C** as energy minimum. For C_{4n+2} ($n > 6$) then **D** is the energy minimum due to a second-order Jahn-Teller effects.
2010[98]	D_{9h} **B**	DFT calculations using rCAM-B3LYP exchange correlation functional which has minimal delocalisation error. Found that $C_n < C_{18}$ then structure **C** is the energy minimum and for $C_n \geq C_{18}$ structure **B** is energy minimum due to a second order Jahn-Teller effect.
2014[65]	D_{18h} **A**	DFT calculations where rings modelled as linear chains of carbon atoms within periodic boundary conditions with N_K unit cells. Up to C_{70} for C_{4n+2} rings structure **A** was energy minimum.
2016[99]	D_{18h} **A**	Performed *meta*-GGA DFT calculations and found **A** as the energy minimum.
2019[100]	D_{9h} **B**	Recognises challenge of using DFT to predict the structures of C_{18}. Found that all PBE-based functionals predicted **A** whereas RSX-based versions predicted **B**.
2019[101]	D_{9h} **B**	Carried out DFT calculations but varied the percentage of HF exchange to obtain geometry **B**.

The theoretical review in Table 1.1 demonstrates the difficulty in predicting the structure of cyclo[18]carbon as no structure appears to be a common energy minimum. In general HF[31,94] and SCF[64,90,93] calculations tend to give polyynic **B** as the energy minimum. DFT calculations seem to always tend toward a cumulenic structure (generally **C**[93,95–97] but also **A**[65,91,99]) however if the calculations are adjusted for electron correlation then polyynic, **B**[98,100,101] or **D**[92], are found as the energy minimum. High level CCSD calculations find polyynic **D**[67] as the energy minimum, however polyynic **B** is very close in energy. LDA calculations[94] give **A** as the energy minimum whereas QMC calculations give polyyne, **B**[66].

A distinctive feature of the structure of the cyclo[*n*]carbons is that they possess two perpendicular π-conjugated electron systems. This means they can exhibit two orthogonal ring currents, causing double aromatic stabilisation[31,97] (Figure 1.12). Double aromaticity was first introduced by Schleyer *et al.*[102] in the context of the 3,5-dehydrophenyl cation $C_6H_3^+$ which was detected by mass spectrometry. The system is a 6π electron system analogous to benzene, however there is also an in-plane 3-centre-2-electron interaction through overlap of the three σ-orbitals of the carbons with no hydrogens attached (Figure 1.12a).

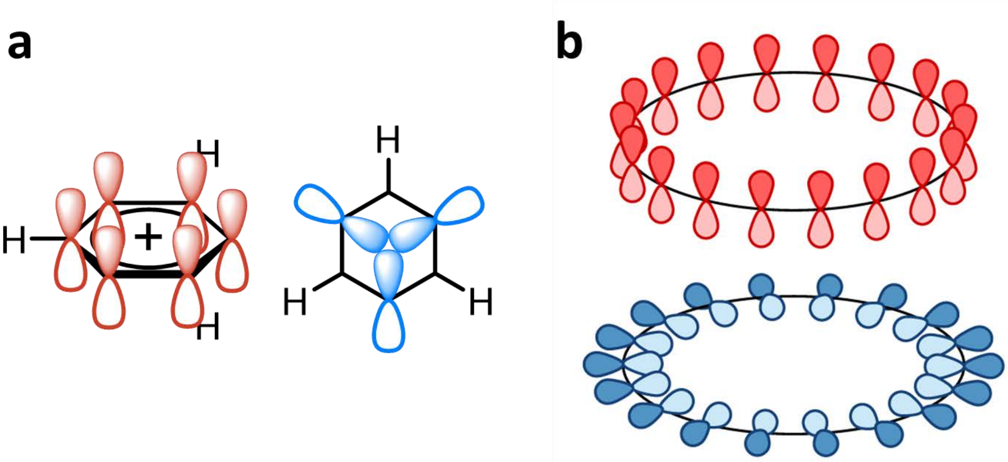

Figure 1.12 Visualisation of the perpendicular π-systems in **a**) 3,5-dehydrophenyl cation $C_6H_3^+$, **b**) cyclo[18]carbon.

The concept of double aromaticity in the context of all carbon rings was first applied to cyclo[*n*]carbons by Diederich[31], and developed by Fowler *et al.*[97] However the seminal paper to discuss cyclo[*n*]carbons by Pitzer and Clementi[33] in 1959 stated that for cyclic C_n molecules '*The pattern of ring orbitals is repeated for the* $2p_\pi$ *orbitals perpendicular to the plane and for those radially oriented in the plane of the ring'* which is essentially the principle of double aromaticity. Cyclo[*n*]carbon possess two sets of π-orbitals, a set of out of plane π-orbitals that are antisymmetric with respect to reflection in the molecular plane and a set of in plane π-orbitals that are symmetric with respect to reflection (Figure 1.12b). Hence cyclo[*n*]carbons can exhibit double aromaticity if both π_{in} and π_{out} contain $4n + 2$ electrons, or double antiaromaticity if both π_{in} and π_{out} contain $4n$ electrons. Or they can be of mixed character with π_{out} aromaticity and π_{in} antiaromaticity or vice versa. The magnitude of the magnetically induced ring current strength in cyclo[18]carbon was calculated using GIMIC calculations[101]. A diatropic ring current of 29 nA T^{-1} was calculated, for reference the calculated diatropic ring current in benzene is 12 nA T^{-1} thereby demonstrating that cyclo[18]carbon exhibits a strong diatropic ring current. The magnitude of the in-plane and out-of-plane rings currents were not found to be equal with I_{out} = 21.8 nA T^{-1} and I_{in} = 7.2 nA T^{-1} due to less efficient overlap of the π_{in} orbitals likely as a result of their angular arrangement.

Nested Frost-Musulin diagrams[103] can be used to depict the electron configuration in C_{4n+2} and C_{4n} rings (Figure 1.13). From this depiction it is clear that C_{4n+2} rings are doubly aromatic and C_{4n} rings are doubly antiaromatic. Current density maps have been used by Fowler *et al.*[104] to predict the magnitude of π_{in} and π_{out} ring currents. For cyclo[18]carbon the magnitude of the ring current in π_{in} and π_{out} was found to be approximately the same however for systems with alternative electron configurations (C_{4n+1}/C_{4n+3}) the interior current is stronger due to improved orbital overlap in the plane of the ring[104].

The discussion in this section has been predominantly focused on cyclo[18]carbon as this molecule is the focus of this thesis, however there are many interesting characteristics of the other sizes of C_n carbon clusters both from a theoretical perspective but also a spectroscopic one, this will be reviewed in the next section and extended in Section 4.2.

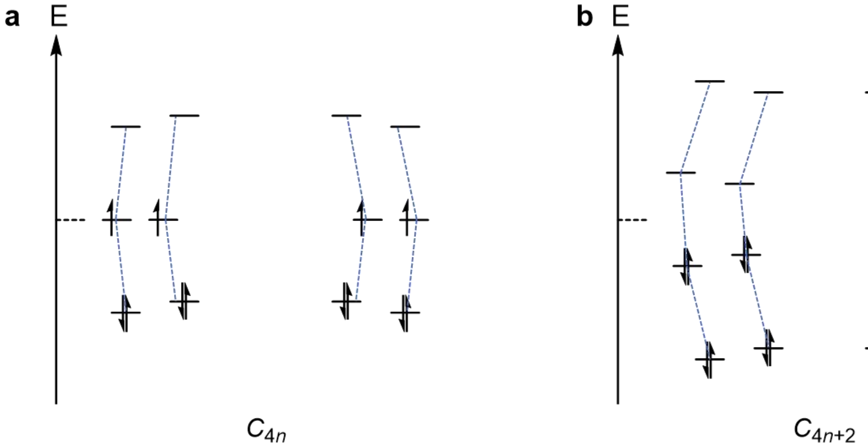

Figure 1.13 Nested Frost-Musulin diagram showing generalised frontier molecular orbitals for **a**) C_{4n} (before Jahn-Teller distortion), **b**) C_{4n+2}.

1.2.3 Detection and structure of carbon clusters, C_n

Carbon clusters C_n can exhibit many different structures, from linear chains to cyclo[*n*]carbons to cage type structures. These species garnered interest as it was suggested that they may be the origin of diffuse interstellar bands[105,106]. So far, most attention in the literature has focused on small carbon clusters[107–110]. Carbon clusters can be produced by laser vaporisation of graphite[111], the same process used in fullerene production[10], and be detected spectroscopically[81,112–114]. One would expect that as the size of the cluster increases then there will be a general trend for linear carbon chains up to a certain size due to ring strain, then a switch to cyclic structures for larger C_n and a final switch to cage structures for larger n. Photoelectron spectroscopy can be used to study carbon clusters. A study by Smalley *et al.*[112] observed a change in ionisation energy at C_{10} which they concluded to be due to a switch from linear to cyclic structures. This transition has since been supported by further photoelectron spectroscopy measurements[114] as well as ion chromatography[115] and more recently rotational spectroscopy[116]. From C_{10} onwards carbon clusters are predicted to be monocyclic ring structures. At a certain ring size a transition to fullerene type structures is predicted. Fullerenes must possess 12 pentagons in their structure, hence the smallest fullerene possible is C_{20}[117] however C_{20} is usually produced in ring form upon laser ablation of graphite[86] due to the strained nature of its fullerene form. However it has been produced in cage form from a brominated cage-like precursor $C_{20}H_{0-3}Br_{11-14}$[118]. Above C_{20} studies have shown that a mixture of ring and fullerene structures are formed in the gas phase[86,109]. For further details into the structures of C_n carbon clusters please see Section 4.2.

An interesting concept to consider is that of odd-numbered cyclo[*n*]carbons (Figure 1.14). Odd numbered cyclo[*n*]carbons C_{4n+1}/C_{4n+3} have been detected spectroscopically[112,113] and debated in the literature[91,97,104,119]. The structure they would adopt is not immediately obvious; one could imagine three potential structures. The first being a cumulenic geometry (Figure 1.14a) however the nature of the orbital overlap would mean that a 90° twist in the orbitals, in a Möbius type fashion, would be required for overlap to occur. Another possible structure is that of a cyclic structure that undergoes a Jahn Teller type distortion to C_{2v} symmetry with either a blunted or elongated C_{2v} structure[91,119] (Figure 1.14b). The third possible structure, proposed by Fowler *et al.*[97,104], is one in which C_{4n+1} and C_{4n+3} rings undergo an electron redistribution so that the π_{out} orbitals possess $4n + 2$ electrons and the π_{in} orbitals contain $4n$ electrons thus creating a system with mixed aromaticity with the aromatic component derived from the π_{out} electrons. The calculated structures corresponding to these mixed aromatic systems showed substantial bond angle distortion due to second order Jahn-Teller effects[97] as shown in Figure 1.14b.

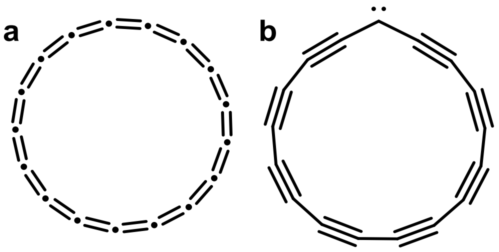

Figure 1.14 Two possible resonance forms of C_{17}.

Thus far the concept of carbon allotropes and the cyclo[*n*]carbons has been reviewed. The focus of the next section of this introduction will be the field of scanning probe microscopy (SPM) as this is the main technique used in this thesis for the study of cyclo[18]carbon.

1.3 Scanning Probe Microscopy

Scanning probe microscopy (SPM) is an unrivalled technique for exploring the world on the atomic scale. There are two main branches of SPM, scanning tunneling microscopy (STM) and atomic force microscopy (AFM). STM explores the tunneling current between the tip and the sample whereas AFM detects the force between the tip and the sample. Herein the field of SPM will be reviewed, as this was the main technique employed in this thesis for the study of cyclo[n]carbons.

1.3.1 Introduction to STM

The scanning tunneling microscope was the first SPM technique to be invented. Binnig and Rohrer at IBM–Research Zurich reported the first scanning tunneling measurements in 1982[120]. STM is carried out at very small tip-sample separations (a few Å), in this region electrons can tunnel through the gap between the tip and sample, despite electrons being classically forbidden in this region. Binnig's initial experiments exploited the change in tunnelling current with distance from the sample. The tunneling current I exponentially decays with distance z between the tip and the sample[120], Equation (3).

$$I(z) \cong I_0 e^{-2kz} \tag{3}$$

Where I_0 is a constant prefactor of the tunneling current and

$$k = \frac{\sqrt{2m_e\varphi_b}}{\hbar} \tag{4}$$

In a tunneling setup φ_b is the work function and is typically around 5 eV for the tip/sample materials generally used in STM measurements, m_e is the electron rest mass and ħ is the reduced Planck constant. This means k is of the order of 1/Å and thus altering the tip-sample distance by 1 Å causes an order of magnitude change in the tunneling current. A short time after Binnig and co-workers introduced the concept of tunneling through a controllable vacuum gap[120] they went on to produce the first atomic scale images of conducting surfaces using tunneling current[121]. The 1986 Nobel Prize in Physics was awarded to Binnig and Rohrer "for their design of the scanning tunneling microscope".

STM gives information about the electronic configuration of a conducting surface as well as providing insight into the topography of the surface. The major drawback of STM is that the measurements are limited to conducting surfaces whereas AFM allows measurements on non-conducting surfaces and therefore is more generally applicable. This led Binnig and co-workers to devise the atomic force microscope four years later in 1986[122], the concept of AFM will be introduced in the next section.

1.3.2 Introduction to AFM

AFM measures the local forces acting between a probe (the AFM tip) and a sample. The general setup for these measurements involves a probe attached to a flexible cantilever that is in close proximity to the sample surface. This can be described as a system of two coupled oscillators where k_0 is the spring constant of the cantilever, k_{ts} is the spring constant of the tip-sample interaction and m is the effective mass of the AFM tip (Figure 1.15).

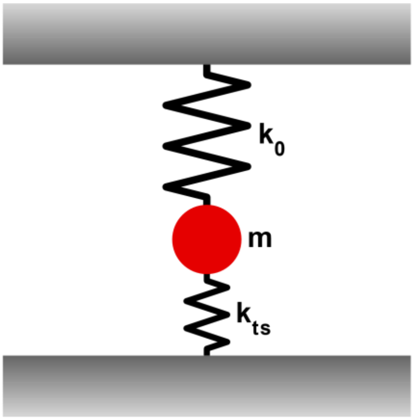

Figure 1.15 Depiction of an AFM setup as two coupled oscillators, k_0: spring constant of the cantilever, red ball: representation of AFM tip with effective mass m, k_{ts}: spring constant of the tip-sample interaction.

Hooke's law can then be used to describe the relationship between the spring constants and the forces acting on the tip[123]. The static form of this relationship is given by Equation (4) and the differential form by Equation (5).

$$\boldsymbol{F = -k \cdot z} \tag{4}$$

$$\boldsymbol{\partial F = -k \cdot \partial z} \tag{5}$$

There are two possible modes of operation in AFM, contact and non-contact mode. The first atomic force microscope developed by Binnig and co-workers in 1986[122] operated in contact mode. The probe is scanned over the sample surface and forces detected between the tip and sample cause a deflection of the cantilever. The deflections of the cantilever were very small and therefore an STM was used to detect the cantilever deflection z as the magnitude of the STM tunneling current has a very high sensitivity to the tip sample separation[122]. Hooke's law (Equation (4)) can then be used to extrapolate the force acting on the tip. This technique only allows the user to operate in contact mode as the total force between the tip and sample is attractive at typical tip-sample distances used for measurements which causes the cantilever to crash into the sample, a concept known as 'snap-in[124]'.

The problem of 'snap-in' can be solved by oscillating the AFM cantilever[125,126], this is known as dynamic mode or non-contact AFM (nc-AFM). nc-AFM can either be operated in amplitude modulation AFM (AM-AFM) mode whereby the cantilever is excited at a fixed frequency and the change in oscillation amplitude is recorded (ΔA). Or frequency-modulation AFM (FM-AFM) mode where the oscillation amplitude is constant and the change in the frequency of oscillation is recorded (Δf). Herein we will focus on FM-AFM as this is the main technique used in this thesis. If the maximum restoring force acting on the tip in the turning point near to the sample is greater than the attractive tip-sample force then 'snap-in' can be prevented. If the differential equation for two coupled oscillators

(Equation (5)) is solved then it is found that the resonance frequency of the cantilever depends both on the restoring force of the cantilever and the tip-sample interaction. Therefore, a change in the tip-sample interaction will change the resonance frequency of the cantilever. In the limit of small tip-sample forces and small oscillation amplitudes of the cantilever then the change in resonant frequency can be approximated by Equation (6)[126,127].

$$\Delta f \cong \frac{f_0 k_{ts}}{2k_0} \tag{6}$$

Where f_0 is the resonant frequency of the unperturbed cantilever (i.e. in the absence of tip-sample interaction). Using the differential form of Hooke's law (Equation 5) this means that Δf is given by Equation (7).

$$\Delta f \sim -\frac{\partial F}{\partial z} \tag{7}$$

Therefore, a change in the tip-sample interaction leads to a shift in the resonance frequency which is proportional to the negative gradient of the tip-sample force in the direction of oscillation[128]. The minimum detectable force gradient is given by Equation (8)[125].

$$\delta F_{min} = \sqrt{\frac{k_0 T B}{f_0 Q A^2}} \tag{8}$$

Where k_0 is the cantilever spring constant, T is the operation temperature, B is the bandwidth, f_0 is the resonant frequency of the cantilever, Q is the quality factor and A is the oscillation amplitude. Hence for the detection of small forces low temperatures, small bandwidths and a high resonant frequency and quality factor are beneficial.

The total tip-sample force is made up of many different contributions[128] (Figure 1.16) including long-range van der Waals and electrostatic forces (range of tens of nm) and short-range chemical forces[129] (range of several Å). Van der Waals forces consist of dipole-dipole interactions and London dispersion forces[130]. The main contribution to the total van der Waals forces between the tip and sample is usually London dispersion which is isotropic and always attractive. Electrostatic forces between the tip and sample are also attractive due to the potential difference between the tip and the sample. Lastly there are chemical forces between the tip and sample. When the tip and sample interact at small tip-sample separations there is a long-range attractive force (van der Waals) and a short-range repulsive force (chemical force). As the tip-sample separation is decreased a short-range repulsive force is generated as a result of overlap between the electronic orbitals of the tip and the sample. This overlap generates repulsive forces due to the Pauli exclusion principle. The sum of all the forces discussed above gives the force vs tip-sample distance curve shown in Figure 1.16. In the red region of the force curve the total force is repulsive. In the pale blue and grey regions the total force is attractive and the grey region is where AFM measurements are typically carried out. The corresponding Δf curve is shown which corresponds to the negative gradient of the tip-sample force.

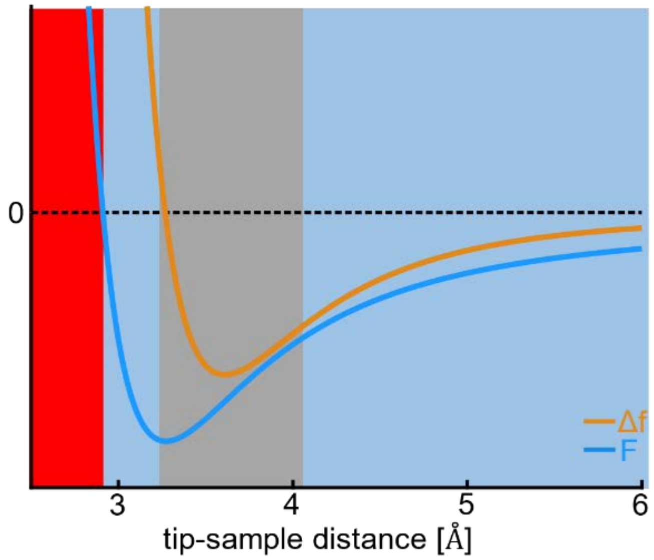

Figure 1.16 Representation of the total tip-sample force with tip-sample distance and Δf which is proportional to the negative force gradient. Red region: total force is repulsive, pale blue and grey region: total force is attractive, grey region: where AFM measurements are typically carried out.

Typically atomic resolution measurements are carried out in the grey section of the graph where the gradient of Δf changes sign and in which Pauli repulsive forces are observed. Pauli repulsive forces have been concluded to be the key contributor to obtaining atomic resolution[131], the van der Waals and electrostatic interactions only contribute a diffuse attractive background to images.

1.3.3 Experimental setup

The goal for any imaging technique is to improve the maximum resolution. Since the invention of the AFM in 1986 the technique has undergone many refinements until, in 2009, atomic resolution imaging of single molecules was achieved for the first time[132]. In order to achieve atomic resolution there are multiple criteria that must be fulfilled in the experimental setup.

All measurements described in this thesis were carried out in a homebuilt combined STM/AFM system. The system is operated under ultra-high vacuum conditions (base pressure of $p \approx 10^{-10}$ mbar) to minimise contamination of the sample surface and at low temperature ($T \approx 5$ K) to decrease thermal noise and to prevent thermally activated diffusion of surface adsorbates. A qPlus force sensor is used which consists of a quartz cantilever glued onto a substrate with a resonant frequency of $f_0 \approx 32$ kHz. qPlus sensors were introduced by Franz Giessibl[124,133] and the sensor design has multiple advantages. The first is due to the piezoelectricity of quartz, the cantilever oscillation is directly translated into an electrical signal and therefore no additional detection is needed. The high stiffness of the sensor ($k \approx 1800$ Nm^{-1}) allows for oscillation amplitudes below 1 Å (oscillation amplitudes of 0.5 Å are typically used for atomic resolution imaging[134]). Lastly, they possess a high Q-factor[133] ($Q \approx 100{,}000$) which enables low noise detection. In addition, a separate integrated tip electrode allows simultaneous STM and AFM operation. All STM measurements are carried out in constant current mode whereby the tip height is altered to maintain a constant tunneling current. All AFM images are carried out in constant height mode. Constant height mode is preferable to constant frequency mode as there is no additional feedback circuit in the measurements which enables more stable operation and improved signal-to-noise ratio. In addition, the gradient of $\Delta f(z)$ changes sign in the region where atomic resolution is obtained (Figure 1.16) meaning constant height measurements are preferred.

A key criterion in the experimental set up is the need to access very small tip-sample separations so contributions from Pauli repulsive forces can be detected. As the tip-sample distance is decreased the likelihood of picking up or reacting with the molecule under study increases. This problem was solved by Gross *et al.*[132] in 2009 at IBM Research–Zurich. They used atom manipulation to pick up small molecules from the surface and functionalise the AFM tip. This functionalisation meant that the AFM tip was chemically inert and thus small tip-sample separations were obtained while maintaining a stable system. They functionalised their AFM tip with Ag, CO, Cl and pentacene (structure shown in Figure 1.17b); the best resolution was obtained with a PtIr tip functionalised with CO. This led to atomic resolution of a single molecule (a pentacene molecule) for the first time (Figure 1.17). Atomic resolution was obtained due to Pauli repulsion, bright features in the constant height AFM images of pentacene arise from areas of increased electron density and increased Pauli repulsion. The van der Waals forces lead to an attractive background which is observed as a dark halo surrounding the molecule. The force-distance spectroscopy[135–137] of the pentacene molecule (Figure 1.17c) was obtained by recording $\Delta f(z)$ above each point in the molecule.

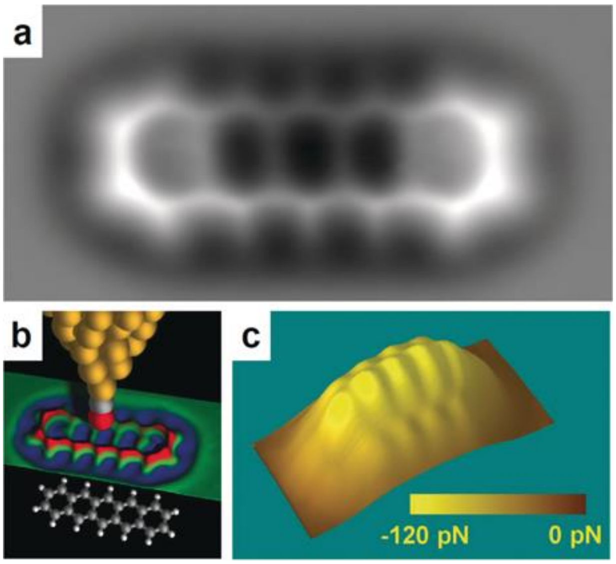

Figure 1.17 Imaging of pentacene with a CO-functionalised tip on Cu(111), **a**) constant height nc-AFM image obtained with a CO-tip, scale from $\Delta f = -2$ Hz (white) to –7 Hz (black) **b**) depiction of the measurement geometry and structure of pentacene **c**) forces measured in the plane above the molecule. Reprinted with permission from John Wiley and Sons Ltd: Angewandte Chemie International Edition[138].

Apart from being able to access small tip-sample separations CO tips possess other desirable characteristics. Firstly, they ensure the end of the tip has a high aspect ratio which increases the maximum possible resolution. Secondly, if the final tip geometry is known this aids interpretation and modelling of images[139]. Lastly, the CO tip can tilt laterally which can cause image sharpening due to contrast enhancement[140]. This effect must be treated with care as it can cause image artefacts that can appear as apparent bonds. However these effects are well-understood and can be corrected for[139–141]. Many different tip functionalisations have been reported since. Examples include metal atom tips such as Cu[132] or Au[142], however they were found to be highly reactive. Halogenated tips have also been demonstrated such as Cl[132,143] as well as noble gas tips such as Xe[144,145]. The more spherical and rigid nature of these tips means they suffer less from image distortion than CO tips; for example xenon tips work well for adsorption geometry measurements[145].

Lastly sample preparation is key for obtaining atomic resolution. A Cu(111) single crystal partially covered with NaCl is typically used as a substrate. Before measurements are carried out the single crystal is typically cleaned by repeated Ne-ion sputtering and annealing ($T \approx$

720 K) cycles and NaCl is then sublimed onto the clean Cu surface at 0 °C resulting in (100)-oriented predominantly double-layered NaCl islands[146]. The tip of the combined AFM/STM system consists of PtIr-wire with a diameter of 25 μm which is sharpened with a focused ion beam, followed by *in situ* indentations into the Cu surface to prepare an anatomically sharp tip. To enable tip functionalisation gaseous CO is allowed into the ultrahigh vacuum (UHV) chamber (partial pressure of $p = 2 \times 10^{-8}$ mbar) to adsorb onto the cold ($T \approx 10$ K) surface[132]. When all the factors detailed above are combined atomic resolution images of single molecules can be obtained. As well as chemical structure resolution many other exciting properties of molecules can be characterised by scanning probe microscopy. This will be reviewed in the next section.

1.3.4 Characterisation techniques

High resolution AFM and STM techniques provide unique insights into the characterisation of molecules such as bond orders and molecular orbitals. The bond order within carbon rich molecules is important and often debated. The concept of bond order was first introduced by Pauling in 1935[147] to describe covalent bond character. There are two main bond order contrast mechanisms in AFM: bonds can have different brightness or different length. In general, bonds of higher bond order have increased electron density and thus the Pauli repulsion above the bond is higher leading to brighter features in constant height AFM images[138]. CO tip tilting generally makes bonds appear longer than they actually are[139], this facilitates bond order analysis as the difference in bond length between higher and lower bonds order is enhanced. AFM has been used to discriminate the bond orders within multiple extended conjugated aromatic systems such as hexabenzocoronene[140] (HBC) as shown in Figure 1.18.

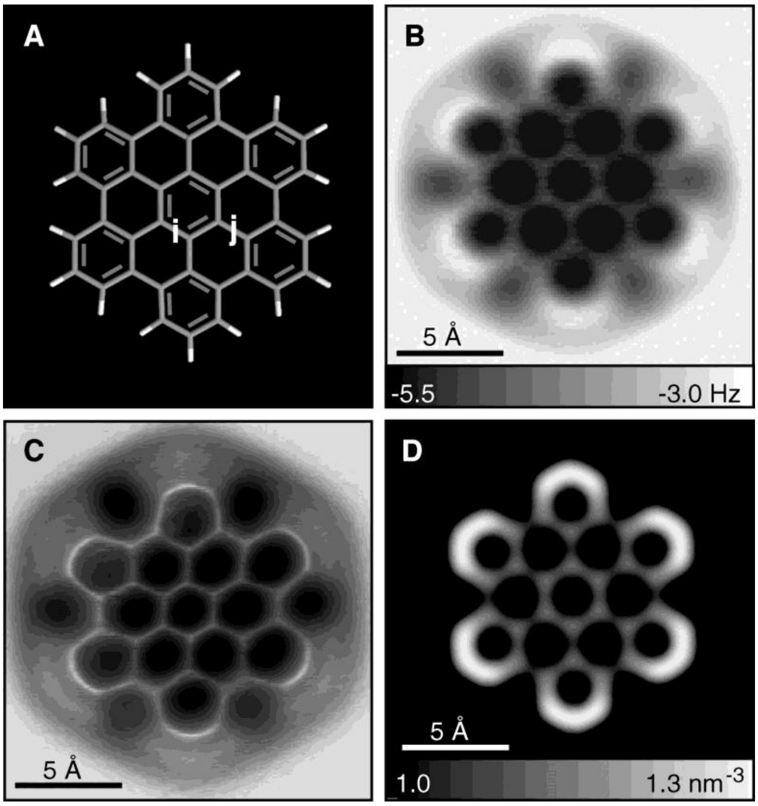

Figure 1.18 AFM images of hexabenzocoronene (HBC) **A**) molecular model of HBC, **B**) constant height AFM images of HBC on Cu(111) in B) tip height $z = 3.7$ Å and **C**) $z = 3.5$ Å with pseudo-3D representation, **D**) calculated electron density at 2.5 Å above the molecule. In all images the *i* bonds are shorter and brighter than the *j* bonds. Reprinted with permission from The American Association for the Advancement of Science Ltd: Science[140].

In HBC there are two types of internal bonds, labelled *i* and *j*. From the Kekulé structure *i* should have more double bond character than *j*. From the constant height AFM images, the *i* bonds appear brighter and shorter than the *j* bonds. However, one must be careful in interpreting bond order related contrast as it is often hard to deconvolute it from other effects such as non-planar absorption geometry or bonds in different chemical environments. In the case of HBC only bonds in the centre of the molecule could be compared as the contrast of the outer rings is complicated as a result of smaller van der Waals background forces at the edge of the molecule. This causes an apparent increase in Δf for the external rings and therefore bond order cannot be compared between the inner and outer sections of HBC.

Another characterisation technique possible using SPM is molecular orbital imaging by STM, a technique known as scanning tunneling spectroscopy[148] (STS). Orbital images are generally obtained on insulating films such as bilayer NaCl or xenon in order to electronically decouple the molecule from the metallic substrate. In order to image the frontier molecular orbitals (FMO) of a molecule a sufficiently high voltage must be applied to tunnel into or out of the FMO. The voltage is increased until a peak in the dI/dV curve is observed (Figure 1.19m) which corresponds to tunneling into a molecular orbital. At positive sample voltage the negative ion resonance is reached by temporarily attaching an electron to the LUMO and an image resembling the LUMO orbital density (ψ^2) is obtained. At negative sample voltage an electron is temporarily removed from the HOMO and the positive ion resonance is reached thus the HOMO orbital density is imaged.

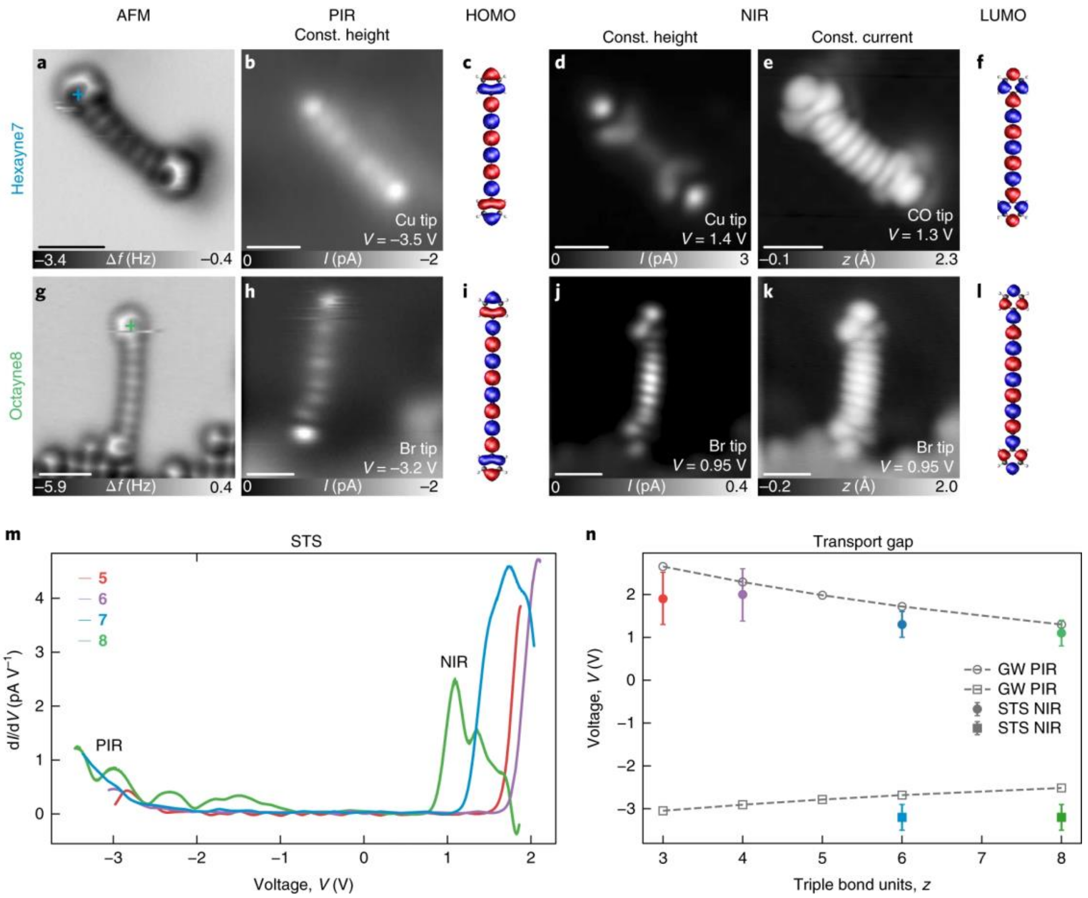

Figure 1.19 Polyyne characterisation using STS. **a,g**) CO-tip constant-height AFM images, **b,h**) STM of the PIR (HOMO orbital density), **d,e,j,k**) STM of the NIR (LUMO orbital density) with different tips and in constant height mode (d,j) and constant current mode (e,k), **c,i,f,l**) DFT calculations of the HOMO and LUMO orbital densities, **m**) differential conductance spectra (dI/dV) for polyynes, **n**) band gap measurements and calculated values using the GW approximation. Reprinted with permission from Springer Nature Ltd: Nature Chemistry[149].

HOMO and LUMO measurements on a range of different length of polyynes were performed by Pavliček *et al.*[149] (Figure 1.19). Comparison of the FMO energy in polyynes of varying length showed that as the length of the polyyne chain increases the HOMO-LUMO gap decreases as it tends to the infinite carbyne limit (Figure 1.19n). This is in agreement with the trend obtained *via* UV studies on polyyne chains by Tykwinski and co-workers[41,44].

Another useful characterisation technique is molecular charge state determination[150,151] which can crucially influence the structure of a molecule[152]. The charge state of molecules can be inferred *via* observation of the standing wave patterns of interface-state electrons. On NaCl/Cu(111), the Cu(111) surface state survives as an interface state. Scattering patterns of interface-state electrons can be made visible by STM imaging at low bias voltage[153]. The scattering of interface-state electrons serves as a hallmark for charged particles because charged adsorbates act as scattering centres, but neutral adsorbates do not[151,154].

The SPM toolkit for molecular characterisation provides exceptional insight into molecular structures. However, another facet of this technique is its ability to not only image molecules but also synthesise them on-surface. On-surface synthesis falls into two categories: atom manipulation and thermally induced surface reactions. These techniques will be reviewed in the next two sections.

1.3.5 Atom manipulation

Atom manipulation is the process by which chemical reactions on a molecule can be triggered with the tip of an AFM/STM[155]. The field was pioneered by Eigler and Schweizer[156] in 1990. Since then it has become unparalleled in its ability to generate molecules that are otherwise too reactive to be isolated above 5 K[149,157–159]. To carry out atom manipulation a precursor molecule is sublimed onto a surface, it is then manipulated using the AFM tip, by increasing the tip-sample voltage, which causes a rearrangement in the molecule. The resulting molecule can then be imaged by high resolution AFM (Figure 1.20).

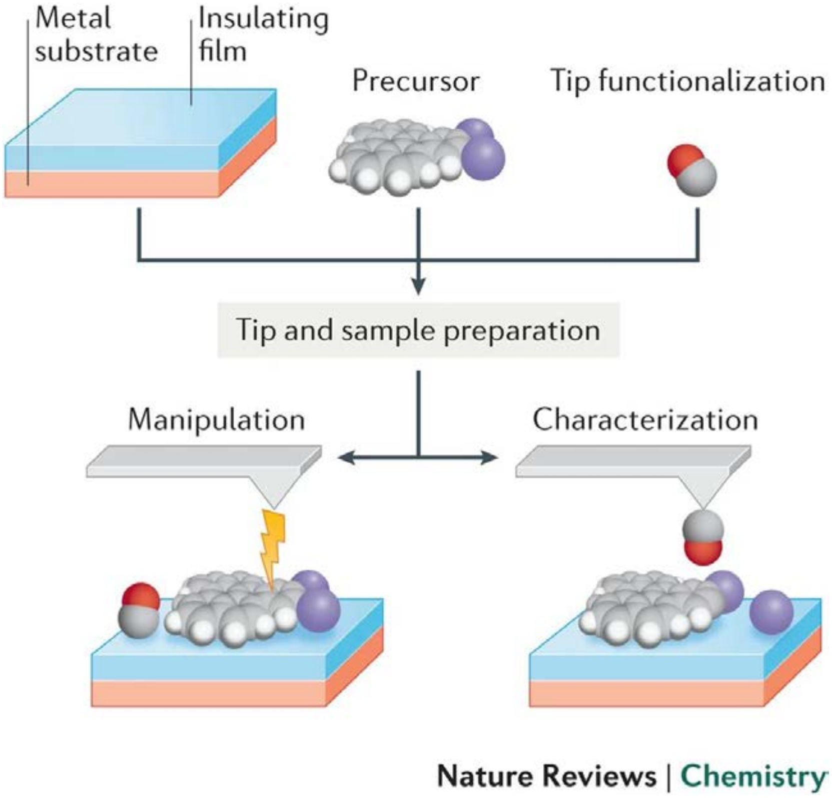

Figure 1.20 General procedure for atom manipulation on-surface. The precursor is deposited onto a thin insulating film on a metal substrate. Voltage is applied between the tip and sample to trigger a rearrangement; the resultant molecule is then imaged using CO-tip AFM. Reprinted with permission from Springer Nature Ltd: Nature Reviews Chemistry[128].

When the voltage between the tip and sample is increased, energy transfer to the molecule can occur *via* two methods[128]. The first method is due to inelastic electron tunneling (IET) between the tip and the sample. Electrons are removed from a state close to the electrochemical potential of the sample, upon tunneling between the sample and the tip they lose energy and end up in a state close to the electrochemical potential of the tip (or vice versa for opposite bias). The energy loss of the tunneling electrons can be transferred to the molecule and trigger a rearrangement. The second method is due to tunneling of hot electrons between the tip and sample that can generate hot carriers in the interface state[160,161]. Hot carriers are highly mobile across the surface and hence can remotely trigger reactions in molecules at a distance from the tip *via* an inelastic scattering event with the molecule. As the voltage is increased the energy of the electrons/ holes that are tunneling increases and thus the energy that can be transferred to the molecule is increased.

The electric field in the tip-sample junction can also cause reactions to be triggered by atom manipulation. Increasing the voltage between the tip and sample increases the strength of the electric field in the tip-sample junction. As the magnitude of the electric field increases the potential landscape of the system is altered. This can trigger changes in tunneling barriers within a molecule thus altering the activation energy for a chemical rearrangement and causing a reaction to occur.

The threshold voltage needed for a rearrangement to occur can be interpreted in two different ways depending on the process occurring. If energy is transferred into the vibrational modes of the molecule[162] then the threshold voltage corresponds to the energy of a vibrational mode[162]. If energy is injected into a vibronic molecular state[163] then the threshold voltage corresponds to the energy of a molecular orbital. In certain situations the mechanism can be deduced if the energy can be definitively assigned to, for example, excitation of an antibonding orbital or a vibrational excitation[164,165].

Bond dissociation is one of the most common atom manipulation mechanisms; energy transfer to the molecule causes the weakest molecular bond to break. Bonds must have a relatively low bond dissociation energy to be broken by atom manipulation such as C-X (X = halogen) or C-H bonds[149,157,158,166] and typical voltages applied are between 1.5 and 3 V. Molecular rearrangements can also be triggered by atom manipulation, an elegant example is that of a reversible Bergman cyclisation[158] (Figure 1.21). Two bromine atoms were removed from 9,10-dibromoanthracene (DBA) by voltage pulses from the AFM tip (1.6 V for the first bromine and 3.3 V for the second) to yield the diradical (Figure 1.21c). A further voltage pulse (1.7 V) triggered a Bergman rearrangement to the highly strained ten membered ring diyne (Figure 1.21d). This example demonstrates the utility of atom manipulation in the study of systems that are too reactive to access by any other means.

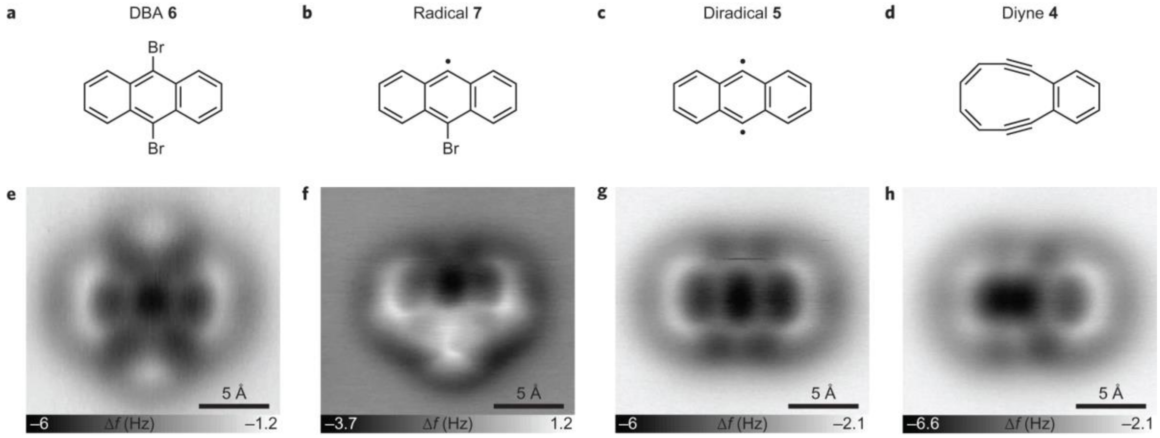

Figure 1.21 a–d) Chemical structures of reaction products produced by atom manipulation, a) 9,10-dibromoanthracene, b) 9-dehydro-10-bromoanthracene (radical **7**), c) 9,10-didehydroanthracene (diradical **5**), d) 3,4-benzocyclodeca-3,7,9-triene-1,5-diyne (**4**), **e–h**) Corresponding constant-height AFM images of molecules a–d on NaCl(2ML)/Cu(111) with a CO tip. Reprinted with permission from Springer Nature Ltd: Nature Chemistry[158].

Atom manipulation is well-suited to triggering reactions on single molecules whereas thermally induced surface reactions are better suited to the synthesis of larger molecular networks[138], this will be discussed in the next section.

1.3.6 Thermally induced surface reactions

Molecular synthesis by thermally induced surface reactions can be used to form polymers[138] or covalent networks[167]. Small molecule precursors are deposited onto a surface and then heated to trigger reactions between them to form extended networks. The field was pioneered by Grill *et al.*[167–169] and has been extensively employed in the synthesis of graphene nanoribbons[170–172] which are predicted to have exciting electronic properties but are poorly accessible in bulk due to low solubility. Jelínek and coworkers[173] exploited this technique to synthesise π-conjugated polymers. An anthracene precursor with $=CBr_2$

reactive centres was deposited on an Au(111) surface which was subsequently thermally annealed at 400 K (Figure 1.22). The molecule underwent dehalogenation and coupling of the reactive units to yield poly(p-anthracene ethynylene) molecular wires (Figure 1.22b) with coexisting bromine atoms. A final thermal annealing to 500 K removed any bromine atoms from the system and yielded high quality anthracene polymers (Figure 1.22h). The band gap of the system was studied by STM and found to be 1.5 eV.

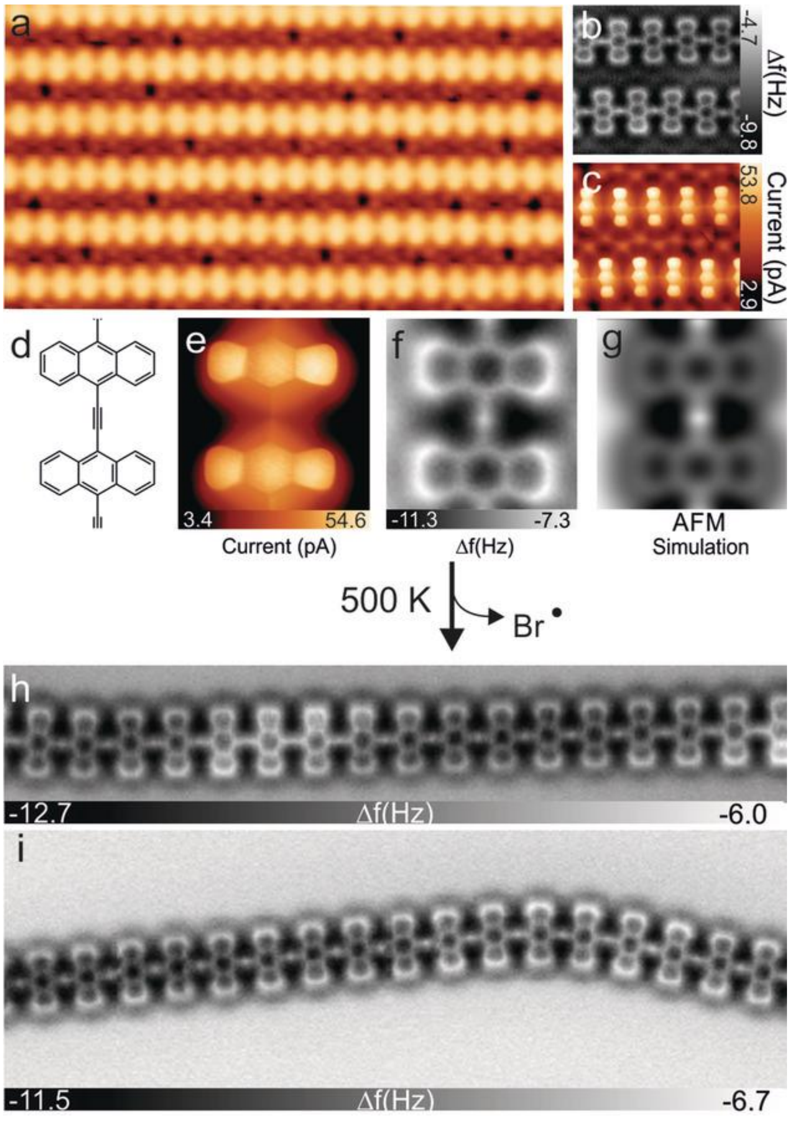

Figure 1.22 **a**) Large scale STM image of ethynylene linked polymers coexisting with bromine atoms after precursor deposition and annealing at 400 K on Au(111), **b**) magnified constant-height nc-AFM image, **c**) STM image of section of (a), **d**) chemical structure of anthracene polymer, **e)** constant height STM image of polymer, **f**) nc-AFM image with resolved ethylene bond, **g**) AFM simulation of f, **h**) and **i**) constant-height nc-AFM image of a linear and curved polymer segment respectively after annealing (a) to 500 K. Open access article.

Thermally induced surface reactions can also be applied within single molecules. A recent example is the synthesis of non-Kekulé π-extended triangulene, $C_{33}H_{15}$ from a molecular precursor[174]. The precursor was deposited onto an Au(111) surface and annealed to 320 °C which triggered a surface catalysed ring closure reaction to yield the highly reactive π-extended triangulene which was characterised by ultrahigh-resolution STM and its electronic properties explored by STS.

This section has demonstrated the utility of on-surface reactions in the synthesis of novel molecules. However, there can often be debate over the structure of products produced by atom manipulation. AFM simulations are useful tool to confirm the structure of possible reaction products and will be discussed in the next section.

1.3.7 Simulation of AFM images

AFM and STM imaging with CO functionalised tips has become common practice. However tip tilting effects can sometimes lead to image artefacts such as apparent bonds[175] and has caused controversy surrounding the imaging of hydrogen bonds[176,177]. This led Hapala and co-workers[139] to investigate the mechanism of tip-functionalised high-resolution STM/AFM imaging. They derived a numerical model to simulate the relaxation of the probe particle during AFM imaging (Figure 1.23). The probe particle experiences three different forces. The first F_{Surf} is the force between the probe particle and the molecular surface and can be modelled by a pairwise Lennard-Jones potential. The second $F_{Tip,R}$ is the force that ensures the probe particle stays attached to the tip and can be modelled by a radial Lennard-Jones potential. The third $F_{Tip,xy}$ is a lateral harmonic force due to the cylindrical attractive potential of the tip base. Using this model they found the probe particle relaxes away from areas of high Pauli repulsion at small tip-sample separations. This is the origin of image artefacts at small tip-sample separations however using this model these effects can be simulated and therefore distinguished from contrast due to actual bonding. In addition, image artefacts can be recognised by imaging at a variety of tip-sample distances and image artefacts due to tip-tilting will not be observed at larger tip-sample separations.

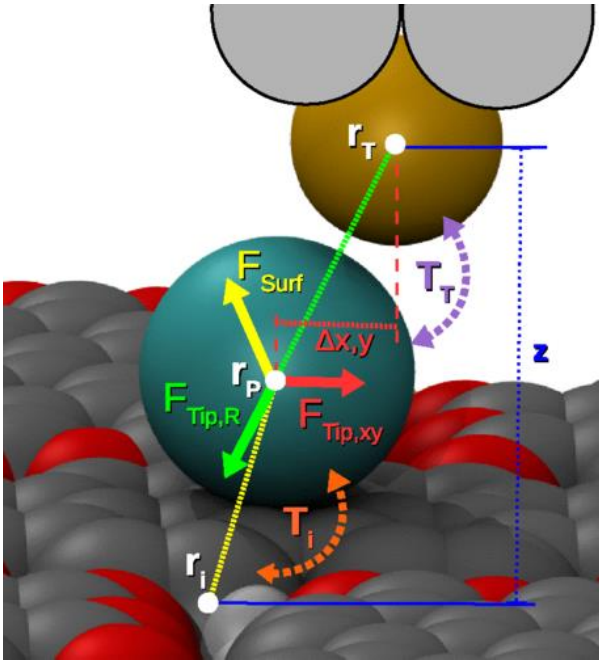

Figure 1.23 Schematic of the forces acting on the tip during AFM measurements. Sand coloured ball: last metal atom of the tip, cyan coloured ball: probe particle, grey and red balls: molecular layer. The forces acting on the probe particle are colour coded as green: radial tip force $F_{Tip,R}$, red: lateral tip force $F_{Tip,xy}$, yellow: force exerted by atoms of the sample F_{Surf}. STM hopping processes are probe particle tip T_t and probe particle sample T_i. Tip height denoted as *z*. Reprinted with permission from American Physical Society: Physical Review B[139].

1.4 Prospective

Thus far we have explored the concept of carbon allotropes, in particular the *sp* hybridised carbon allotropes with a specific focus on the cyclo[*n*]carbons. We have also reviewed the concept of SPM as the main technique used in this thesis for the study of cyclo[*n*]carbons (**Chapter 1**).

This thesis will herein detail the first example of structural characterisation of a cyclo[*n*]carbon. We will first explore the generation of cyclo[18]carbon from a cyclocarbon oxide $C_{24}O_6$ precursor (**Chapter 2**). The synthesis and properties of the $C_{24}O_6$ will be discussed before moving onto the on-surface synthesis, by atom manipulation, of cyclo[18]carbon. The characterisation of cyclo[18]carbon in its neutral and negative charge state by high-resolution atomic force microscopy will then be discussed. We will then explore the on-surface molecular fusion reactions of cyclo[18]carbon and its precursors.

We then move on to the synthesis and on-surface properties of a novel cyclo[18]carbon precursor bromocyclocarbon $C_{18}Br_6$ (**Chapter 3**). We will explore the synthesis of the *cis* halo-enediyne monomer unit and its subsequent deprotection and cyclisation to yield $C_{18}Br_6$. The crystal structure and properties of $C_{18}Br_6$ will then be discussed as well as the high yielding on-surface synthesis of cyclo[18]carbon from $C_{18}Br_6$. We will then explore the symmetry and bond length alternation in cyclo[18]carbon in greater depth.

Our attention will then turn to the synthesis and properties of a series of cyclocarbon oxides as precursors to antiaromatic cyclo[*n*]carbons. We will examine the synthesis and properties of these cyclocarbon oxides and their unfortunately unsuccessful sublimation attempts (**Chapter 4**).

1.5 References

[1] H. O. Pierson, *Handbook of Carbon, Graphite, Diamonds and Fullerenes*, Noyes Publications, **1993**.

[2] J. Berzelius, *Jahres-Bericht* **1841**, *20*, 7–13.

[3] W. B. Jensen, *J. Chem. Educ.* **2006**, *83*, 838–839.

[4] F. P. Bundy, W. A. Bassett, M. S. Weathers, R. J. Hemley, H. K. Mao, A. F. Goncharov, *Carbon N. Y.* **1996**, *34*, 141–153.

[5] W. Grochala, *Angew. Chem. Int. Ed.* **2014**, *53*, 3680–3683.

[6] J. Dong, Z. Yao, M. Yao, R. Li, K. Hu, L. Zhu, Y. Wang, H. Sun, B. Sundqvist, K. Yang, et al., *Phys. Rev. Lett.* **2020**, *124*, 065701.

[7] Z. Pan, H. Sun, Y. Zhang, C. Chen, *Phys. Rev. Lett.* **2009**, *102*, 055503.

[8] D. D. L. Chung, *J. Mater. Sci.* **2002**, *37*, 1475–1489.

[9] F. Diederich, *Nature* **1994**, *369*, 199–207.

[10] H. W. Kroto, J. R. Heath, S. C. O'Brien, R. F. Curl, R. E. Smalley, *Nature* **1985**, *318*, 162–163.

[11] H. Kroto, *Angew. Chem. Int. Ed. Engl.* **1997**, *36*, 1578–1593.

[12] W. Krätschmer, L. D. Lamb, K. Fostiropoulos, D. R. Huffman, *Nature* **1990**, *347*, 354–358.

[13] W. Krätschmer, K. Fostiropoulos, D. R. Huffman, *Chem. Phys. Lett.* **1990**, *170*, 167–170.

[14] G. Dennler, M. C. Scharber, C. J. Brabec, *Adv. Mater.* **2009**, *21*, 1323–1338.

[15] S. H. Friedman, D. L. DeCamp, G. L. Kenyon, R. P. Sijbesma, G. Srdanov, F. Wudl, *J. Am. Chem. Soc.* **1993**, *115*, 6506–6509.

[16] K. Holczer, O. Klein, S. M. Huang, R. B. Kaner, K. J. Fu, R. L. Whetten, F. Diederich, *Science* **1991**, *252*, 1154–1157.

[17] S. Iijima, *Nature* **1991**, *354*, 56–58.

[18] S. Iijima, T. Ichihashi, *Nature* **1993**, *363*, 603–605.

[19] H. Omachi, T. Nakayama, E. Takahashi, Y. Segawa, K. Itami, *Nat. Chem.* **2013**, *5*, 572–576.

[20] E. J. Leonhardt, R. Jasti, *Nat. Rev. Chem.* **2019**, *3*, 1–15.

[21] M. F. Yu, B. S. Files, S. Arepalli, R. S. Ruoff, *Phys. Rev. Lett.* **2000**, *84*, 5552–5555.

[22] W. A. De Heer, A. Châtelain, D. Ugarte, *Science* **1995**, *270*, 1179–1180.

[23] J. Hone, B. Batlogg, Z. Benes, A. T. Johnson, J. E. Fischer, *Science* **2000**, *289*, 1730–1733.

[24] K. S. Novoselov, A. K. Geim, S. V Morozov, D. Jiang, Y. Zhang, S. V Dubonos, I. V Grigorieva, A. A. Firsov, *Science* **2004**, *306*, 666–669.

[25] K. S. Novoselov, V. I. Fal′ko, L. Colombo, P. R. Gellert, M. G. Schwab, K. Kim, *Nature* **2012**, *490*, 192–200.

[26] A. S. Mayorov, R. V. Gorbachev, S. V. Morozov, L. Britnell, R. Jalil, L. A. Ponomarenko, P. Blake, K. S. Novoselov, K. Watanabe, T. Taniguchi, et al., *Nano Lett.* **2011**, *11*, 2396–2399.

[27] C. Lee, X. Wei, J. W. Kysar, J. Hone, *Science* **2008**, *321*, 385–388.

[28] J. S. Bunch, S. S. Verbridge, J. S. Alden, A. M. Van Der Zande, J. M. Parpia, H. G. Craighead, P. L. McEuen, *Nano Lett.* **2008**, *8*, 2458–2462.

[29] A. K. Geim, K. S. Novoselov, *Nat. Mater.* **2007**, *6*, 183–191.

[30] R. Hoffmann, *Tetrahedron* **1966**, *22*, 521–538.

[31] F. Diederich, Y. Rubin, C. B. Knobler, R. L. Whetten, K. E. Schriver, K. N. Houk, Y. Li, *Science* **1989**, *245*, 1088–1090.

[32] Y. Tobe, H. Matsumoto, K. Naemura, Y. Achiba, T. Wakabayashi, *Angew. Chem. Int. Ed. Engl.* **1996**, *35*, 1800–1802.

[33] K. S. Pitzer, E. Clementi, *J. Am. Chem. Soc.* **1959**, *81*, 4477–4485.

[34] R. Hayatsu, R. G. Scott, M. H. Studier, R. S. Lewis, E. Anders, *Science* **1980**, *209*, 1515–1518.

[35] A. E. Goresy, G. Donnay, *Science* **1968**, *161*, 363–364.

[36] F. J. M. Rietmeijer, *Meteoritics* **1993**, *28*, 242–245.

[37] P. Tarakeshwar, P. R. Buseck, H. W. Kroto, *J. Phys. Chem. Lett.* **2016**, *7*, 1675–1681.

[38] M. Liu, V. I. Artyukhov, H. Lee, F. Xu, B. I. Yakobson, *ACS Nano* **2013**, *7*, 10075–10082.

[39] B. Pan, J. Xiao, J. Li, P. Liu, C. Wang, G. Yang, *Sci. Adv.* **2015**, *1*, e1500857.

[40] R. J. Lagow, J. J. Kampa, H. C. Wei, S. L. Battle, J. W. Genge, D. A. Laude, C. J. Harper, R. Bau, R. C. Stevens, J. F. Haw, et al., *Science* **1995**, *267*, 362–367.

[41] W. A. Chalifoux, R. R. Tykwinski, *Nat. Chem.* **2010**, *2*, 967–971.

[42] C. Wang, A. S. Batsanov, K. West, M. R. Bryce, *Org. Lett.* **2008**, *10*, 3069–3072.

[43] W. A. Chalifoux, R. R. Tykwinski, *C. R. Chim.* **2009**, *12*, 341–358.

[44] Y. Gao, Y. Hou, F. Gordillo Gámez, M. J. Ferguson, J. Casado, R. R. Tykwinski, *Nat. Chem.* **2020**, *accepted*, 10.1038/s41557-020-0550–0.

[45] L. D. Movsisyan, M. Franz, F. Hampel, A. L. Thompson, R. R. Tykwinski, H. L. Anderson, *J. Am. Chem. Soc.* **2016**, *138*, 1366–1376.

[46] S. Schrettl, E. Contal, T. N. Hoheisel, M. Fritzsche, S. Balog, R. Szilluweit, H. Frauenrath, *Chem. Sci.* **2015**, *6*, 564–574.

[47] L. D. Movsisyan, D. V. Kondratuk, M. Franz, A. L. Thompson, R. R. Tykwinski, H.

L. Anderson, *Org. Lett.* **2012**, *14*, 3424–3426.

[48] S. L. Woltering, P. Gawel, K. E. Christensen, A. L. Thompson, H. L. Anderson, *J. Am. Chem. Soc.* **2020**, *142*, 13523–13532.

[49] L. Shi, P. Rohringer, K. Suenaga, Y. Niimi, J. Kotakoski, J. C. Meyer, H. Peterlik, M. Wanko, S. Cahangirov, A. Rubio, et al., *Nat. Mater.* **2016**, *15*, 634–639.

[50] M. Franz, J. A. Januszewski, D. Wendinger, C. Neiss, L. D. Movsisyan, F. Hampel, H. L. Anderson, A. Görling, R. R. Tykwinski, *Angew. Chem. Int. Ed.* **2015**, *54*, 6645–6649.

[51] J. A. Januszewski, D. Wendinger, C. D. Methfessel, F. Hampel, R. R. Tykwinski, *Angew. Chem. Int. Ed.* **2013**, *52*, 1817–1821.

[52] P. Gawel, Y.-L. Wu, A. D. Finke, N. Trapp, M. Zalibera, C. Boudon, J.-P. Gisselbrecht, W. B. Schweizer, G. Gescheidt, F. Diederich, *Chem. Eur. J.* **2015**, *21*, 6215–6225.

[53] R. Hoffmann, *Angew. Chem. Int. Ed. Engl.* **1987**, *26*, 846–878.

[54] H. A. Jahn, E. Teller, *Proc. R. Soc. Lond. A* **1937**, *161*, 220–235.

[55] K. Nakamura, Y. Osamura, S. Iwata, *Chem. Phys.* **1989**, *136*, 67–77.

[56] J. L. Bredas, *Mater. Horiz.* **2014**, *1*, 17–19.

[57] M. Kertesz, C. H. Choi, S. Yang, *Chem. Rev.* **2005**, *105*, 3448–3481.

[58] L. Shi, P. Rohringer, M. Wanko, A. Rubio, S. Waßerroth, S. Reich, S. Cambré, W. Wenseleers, P. Ayala, T. Pichler, *Phys. Rev. Mater.* **2017**, *1*, 075601.

[59] M. H. Garner, W. Bro-Jørgensen, P. D. Pedersen, G. C. Solomon, *J. Phys. Chem. C* **2018**, *122*, 26777–26789.

[60] D. Wendinger, R. R. Tykwinski, *Acc. Chem. Res.* **2017**, *50*, 1468–1479.

[61] J. A. Januszewski, R. R. Tykwinski, *Chem. Soc. Rev.* **2014**, *43*, 3184–3203.

[62] R. R. Tykwinski, *Chem. Rec.* **2015**, *15*, 1060–1074.

[63] H. Meier, U. Stalmach, H. Kolshorn, *Acta Polym.* **1997**, *48*, 379–384.

[64] V. Parasuk, J. Almlöf, M. W. Feyereisen, *J. Am. Chem. Soc.* **1991**, *113*, 1049–1050.

[65] C. Neiss, E. Trushin, A. Görling, *ChemPhysChem* **2014**, *15*, 2497–2502.

[66] T. Torelli, L. Mitas, *Phys. Rev. Lett.* **2000**, *85*, 1702–1705.

[67] S. Arulmozhiraja, T. Ohno, *J. Chem. Phys.* **2008**, *128*, 114301.

[68] M. C. Lasne, J. L. Ripoll, *Synth.* **1985**, *1985*, 121–143.

[69] U. E. Wiersum, *Recl. Trav. Chim. Pays-Bas* **2010**, *101*, 317–332.

[70] Y. Rubin, C. B. Knobler, F. Diederich, *J. Am. Chem. Soc.* **1990**, *112*, 1607–1617.

[71] Y. Rubin, F. Diederich, *J. Am. Chem. Soc.* **1989**, *111*, 6870–6871.

[72] Y. Rubin, S. S. Lin, C. B. Knobler, J. Anthony, A. M. Boldi, F. Diederich, *J. Am. Chem. Soc.* **1991**, *113*, 6943–6949.

[73] Y. Rubin, M. Kahr, C. B. Knobler, F. Diederich, C. L. Wilkins, *J. Am. Chem. Soc.* **1991**, *113*, 495–500.

[74] Y. Rubin, C. B. Knobler, F. Diederich, *J. Am. Chem. Soc.* **1990**, *112*, 4966–4968.

[75] F. Diederich, Y. Rubin, O. L. Chapman, N. S. Goroff, *Helv. Chim. Acta* **1994**, *77*, 1441–1457.

[76] J. Lewis, B. Lin, M. S. Khan, M. R. A. Al-Mandhary, P. R. Raithby, *J. Organomet. Chem.* **1994**, *484*, 161–167.

[77] D. R. Kohn, P. Gawel, Y. Xiong, K. E. Christensen, H. L. Anderson, *J. Org. Chem.* **2018**, *83*, 2077–2086.

[78] Y. Tobe, T. Fujii, H. Matsumoto, K. Naemura, Y. Achiba, T. Wakabayashi, *J. Am. Chem. Soc.* **1996**, *118*, 2758–2759.

[79] Y. Tobe, T. Fujii, K. Naemura, *J. Org. Chem.* **1994**, *59*, 1236–1237.

[80] Y. Tobe, T. Fujii, H. Matsumoto, K. Naemura, *Pure Appl. Chem.* **1996**, *68*, 239–242.

[81] T. Wakabayashi, M. Kohno, Y. Achiba, H. Shiromaru, T. Momose, T. Shida, K. Naemura, Y. Tobe, *J. Chem. Phys.* **1997**, *107*, 4783–4787.

[82] Y. Tobe, T. Fujii, H. Matsumoto, T. Kunihiro, D. Noguchi, N. Nakagawa, M. Sonoda, K. Naemura, Y. Achiba, T. Wakabayashi, *J. Am. Chem. Soc.* **2000**, *122*, 1792–1755.

[83] G. A. Adamson, C. W. Rees, *J. Chem. Soc. Perkin Trans. 1* **1996**, 1535–1543.

[84] Y. Tobe, R. Umeda, N. Iwasa, M. Sonoda, *Chem. Eur. J.* **2003**, *9*, 5549–5559.

[85] S. W. McElvany, M. M. Ross, N. S. Goroff, F. Diederich, *Science* **1993**, *259*, 1594–1596.

[86] G. von Helden, N. G. Gotts, M. T. Bowers, *Nature* **1993**, *363*, 60–63.

[87] N. S. Goroff, *Acc. Chem. Res.* **1996**, *29*, 77–83.

[88] D. Babić, N. Trinajstić, *J. Mol. Struct.* **1996**, *376*, 507–511.

[89] T. M. Chang, A. Naim, S. N. Ahmed, G. Goodloe, P. B. Shevlin, *J. Am. Chem. Soc.* **1992**, *114*, 7603–7604.

[90] M. Feyereisen, M. Gutowski, J. Simons, J. Almlöf, *J. Chem. Phys.* **1992**, *96*, 2926–2932.

[91] J. Hutter, H. P. Lüthi, F. Diederich, *J. Am. Chem. Soc.* **1994**, *116*, 750–756.

[92] D. A. Plattner, K. N. Houk, *J. Am. Chem. Soc.* **1995**, *117*, 4405–4406.

[93] J. M. L. Martin, J. El-Yazal, J.-P. François, *Chem. Phys. Lett.* **1995**, *242*, 570–579.

[94] E. J. Bylaska, J. H. Weare, R. Kawai, *Phys. Rev. B* **1998**, *58*, R7488–R7491.

[95] M. Saito, Y. Okamoto, *Phys. Rev. B* **1999**, *60*, 8939–8942.

[96] G. A. Rechtsteiner, C. Felix, A. K. Ott, O. Hampe, R. P. Van Duyne, M. F. Jarrold, K. Raghavachari, *J. Phys. Chem. A* **2001**, *105*, 3029–3033.

[97] P. W. Fowler, N. Mizoguchi, D. E. Bean, R. W. A. Havenith, *Chem. Eur. J.* **2009**, *15*,

6964–6972.

[98] T. Heaton-Burgess, W. Yang, *J. Chem. Phys.* **2010**, *132*, 234113.

[99] K. Remya, C. H. Suresh, *RSC Adv.* **2016**, *6*, 44261–44271.

[100] É. Brémond, Á. J. Pérez-Jiménez, C. Adamo, J. C. Sancho-García, *J. Chem. Phys.* **2019**, *151*, 211104.

[101] G. V. Baryshnikov, R. R. Valiev, A. V. Kuklin, D. Sundholm, H. Ågren, *J. Phys. Chem. Lett.* **2019**, *10*, 6701–6705.

[102] J. Chandrasekhar, E. D. Jemmis, P. von Ragué Schleyer, *Tetrahedron Lett.* **1979**, *20*, 3707–3710.

[103] A. A. Frost, B. Musulin, *J. Chem. Phys.* **1953**, *21*, 572–573.

[104] D. E. Bean, P. W. Fowler, A. Soncini, *Chem. Phys. Lett.* **2009**, *483*, 193–197.

[105] A. E. Douglas, *Nature* **1977**, *269*, 130–132.

[106] G. H. Herbig, D. R. Soderblom, *Astrophys. J.* **1982**, *252*, 610–615.

[107] W. Weltner, R. J. Van Zee, *Chem. Rev.* **1989**, *89*, 1713–1747.

[108] A. Van Orden, R. J. Saykally, *Chem. Rev.* **1998**, *98*, 2313–2357.

[109] N. G. Gotts, G. von Helden, M. T. Bowers, *Int. J. Mass Spectrom. Ion Process.* **1995**, *149*, 217–229.

[110] R. O. Jones, *J. Chem. Phys.* **1999**, *110*, 5189–5200.

[111] J. A. Van Vechten, D. A. Keszler, *Phys. Rev. B* **1987**, *36*, 4570–4573.

[112] S. Yang, K. J. Taylor, M. J. Craycraft, J. Conceicao, C. L. Pettiette, O. Cheshnovsky, R. E. Smalley, *Chem. Phys. Lett.* **1988**, *144*, 431–436.

[113] D. Zajfman, H. Feldman, O. Heber, D. Kella, D. Majer, Z. Vager, R. Naaman, *Science* **1992**, *258*, 1129–1131.

[114] H. Handschuh, G. Ganteför, B. Kessler, P. S. Bechthold, W. Eberhardt, *Phys. Rev. Lett.* **1995**, *74*, 1095–1098.

[115] G. Von Helden, P. R. Kemper, N. G. Gotts, M. T. Bowers, *Science* **1993**, *259*, 1300–1302.

[116] C. A. Rice, J. P. Maier, *J. Phys. Chem. A* **2013**, *117*, 5559–5566.

[117] H. W. Kroto, *Int. J. Mass Spectrom. Ion Process.* **1994**, *138*, 1–15.

[118] H. Prinzbach, A. Weller, P. Landenberger, F. Wahl, J. Wörth, L. T. Scott, M. Gelmont, D. Olevano, B. V. Issendorff, *Nature* **2000**, *407*, 60–63.

[119] J. M. L. Martin, J. P. François, R. Gijbels, J. Almlöf, *Chem. Phys. Lett.* **1991**, *187*, 367–374.

[120] G. Binnig, H. Rohrer, C. Gerber, E. Weibel, *Appl. Phys. Lett.* **1982**, *40*, 178–180.

[121] G. Binnig, H. Rohrer, C. Gerber, E. Weibel, *Phys. Rev. Lett.* **1982**, *49*, 57–61.

[122] G. Binnig, C. F. Quate, C. Gerber, *Phys. Rev. Lett.* **1986**, *56*, 930–933.

[123] W. Demtröder, *Mechanics and Thermodynamics*, Springer International Publishing, **2017**.

[124] F. J. Giessibl, *Rev. Mod. Phys.* **2003**, *75*, 949–983.

[125] T. R. Albrecht, P. Grütter, D. Horne, D. Rugar, *J. Appl. Phys.* **1991**, *69*, 668–673.

[126] F. J. Giessibl, *Phys. Rev. B* **1997**, *56*, 16010–16015.

[127] J. E. Sader, S. P. Jarvis, *Appl. Phys. Lett.* **2004**, *84*, 1801–1803.

[128] N. Pavliček, L. Gross, *Nat. Rev. Chem.* **2017**, *1*, 0005.

[129] Y. Sugimoto, P. Pou, M. Abe, P. Jelinek, R. Pérez, S. Morita, Ó. Custance, *Nature* **2007**, *446*, 64–67.

[130] J. P. Wagner, P. R. Schreiner, *Angew. Chem. Int. Ed.* **2015**, *54*, 12274–12296.

[131] N. Moll, L. Gross, F. Mohn, A. Curioni, G. Meyer, *New J. Phys.* **2010**, *12*, 125020.

[132] L. Gross, F. Mohn, N. Moll, P. Liljeroth, G. Meyer, *Science* **2009**, *325*, 1110–1114.

[133] F. J. Giessibl, *Appl. Phys. Lett.* **1998**, *73*, 3956–3958.

[134] F. J. Giessibl, H. Bielefeldt, S. Hembacher, J. Mannhart, *Appl. Surf. Sci.* **1999**, *140*, 352–357.

[135] H. Hölscher, S. M. Langkat, A. Schwarz, R. Wiesendanger, *Appl. Phys. Lett.* **2002**, *81*, 4428–4430.

[136] B. J. Albers, T. C. Schwendemann, M. Z. Baykara, N. Pilet, M. Liebmann, E. I. Altman, U. D. Schwarz, *Nat. Nanotechnol.* **2009**, *4*, 307–310.

[137] M. Z. Baykara, T. C. Schwendemann, E. I. Altman, U. D. Schwarz, *Adv. Mater.* **2010**, *22*, 2838–2853.

[138] L. Gross, B. Schuler, N. Pavliček, S. Fatayer, Z. Majzik, N. Moll, D. Peña, G. Meyer, *Angew. Chem. Int. Ed.* **2018**, *57*, 3888–3908.

[139] P. Hapala, G. Kichin, C. Wagner, F. S. Tautz, R. Temirov, P. Jelínek, *Phys. Rev. B* **2014**, *90*, 085421.

[140] L. Gross, F. Mohn, N. Moll, B. Schuler, A. Criado, E. Guitián, D. Peña, A. Gourdon, G. Meyer, *Science* **2012**, *337*, 1326–1329.

[141] J. Welker, F. J. Giessibl, *Science* **2012**, *336*, 444–449.

[142] L. Gross, B. Schuler, F. Mohn, N. Moll, N. Pavliček, W. Steurer, I. Scivetti, K. Kotsis, M. Persson, G. Meyer, *Phys. Rev. B* **2014**, *90*, 155455.

[143] N. Hauptmann, R. Robles, P. Abufager, N. Lorente, R. Berndt, *J. Phys. Chem. Lett.* **2016**, *7*, 1984–1990.

[144] P. Hapala, M. Švec, O. Stetsovych, N. J. Van Der Heijden, M. Ondráčk, J. Van Der Lit, P. Mutombo, I. Swart, P. Jelínek, *Nat. Commun.* **2016**, *7*, 1–8.

[145] B. Schuler, W. Liu, A. Tkatchenko, N. Moll, G. Meyer, A. Mistry, D. Fox, L. Gross, *Phys. Rev. Lett.* **2013**, *111*, 106103.

[146] R. Bennewitz, V. Barwich, M. Bammerlin, C. Loppacher, M. Guggisberg, A.

Baratoff, E. Meyer, H. J. Güntherodt, *Surf. Sci.* **1999**, *438*, 289–296.

[147] L. Pauling, L. O. Brockway, J. Y. Beach, *J. Am. Chem. Soc.* **1935**, *57*, 2705–2709.

[148] J. Repp, G. Meyer, S. M. Stojković, A. Gourdon, C. Joachim, *Phys. Rev. Lett.* **2005**, *94*, 026803.

[149] N. Pavliček, P. Gawel, D. R. Kohn, Z. Majzik, Y. Xiong, G. Meyer, H. L. Anderson, L. Gross, *Nat. Chem.* **2018**, *10*, 853–858.

[150] J. Repp, G. Meyer, S. Paavilainen, F. E. Olsson, M. Persson, *Phys. Rev. Lett.* **2005**, *95*, 225503.

[151] J. Repp, G. Meyer, S. Paavilainen, F. E. Olsson, M. Persson, *Science* **2006**, *312*, 1196–1199.

[152] T. Leoni, O. Guillermet, H. Walch, V. Langlais, A. Scheuermann, J. Bonvoisin, S. Gauthier, *Phys. Rev. Lett.* **2011**, *106*, 216103.

[153] J. Repp, G. Meyer, K. H. Rieder, *Phys. Rev. Lett.* **2004**, *92*, 4.

[154] I. Swart, T. Sonnleitner, J. Repp, *Nano Lett.* **2011**, *11*, 1580–1584.

[155] S. Hla, G. Meyer, K. Rieder, *ChemPhysChem* **2001**, *2*, 361–366.

[156] D. M. Eigler, E. K. Schweizer, *Nature* **1990**, *344*, 524–526.

[157] N. Pavliček, B. Schuler, S. Collazos, N. Moll, D. Pérez, E. Guitián, G. Meyer, D. Peña, L. Gross, *Nat. Chem.* **2015**, *7*, 623–628.

[158] B. Schuler, S. Fatayer, F. Mohn, N. Moll, N. Pavliček, G. Meyer, D. Peña, L. Gross, *Nat. Chem.* **2016**, *8*, 220–224.

[159] S. W. Hla, L. Bartels, G. Meyer, K. H. Rieder, *Phys. Rev. Lett.* **2000**, *85*, 2777–2780.

[160] J. N. Ladenthin, L. Grill, S. Gawinkowski, S. Liu, J. Waluk, T. Kumagai, *ACS Nano* **2015**, *9*, 7287–7295.

[161] V. Schendel, B. Borca, I. Pentegov, T. Michnowicz, U. Kraft, H. Klauk, P. Wahl, U. Schlickum, K. Kern, *Nano Lett.* **2016**, *16*, 93–97.

[162] Y. Kim, T. Komeda, M. Kawai, *Phys. Rev. Lett.* **2002**, *89*, 126104.

[163] X. H. Qiu, G. V. Nazin, W. Ho, *Phys. Rev. Lett.* **2004**, *92*, 206102.

[164] K. Huang, L. Leung, T. Lim, Z. Ning, J. C. Polanyi, *J. Am. Chem. Soc.* **2013**, *135*, 6220–6225.

[165] K. Huang, L. Leung, T. Lim, Z. Ning, J. C. Polanyi, *ACS Nano* **2014**, *8*, 12468–12475.

[166] N. Pavliček, A. Mistry, Z. Majzik, N. Moll, G. Meyer, D. J. Fox, L. Gross, *Nat. Nanotechnol.* **2017**, *12*, 308–311.

[167] L. Lafferentz, F. Ample, H. Yu, S. Hecht, C. Joachim, L. Grill, *Science* **2009**, *323*, 1193–1197.

[168] L. Grill, M. Dyer, L. Lafferentz, M. Persson, M. V. Peters, S. Hecht, *Nat. Nanotechnol.* **2007**, *2*, 687–691.

[169] L. Grill, S. Hecht, *Nat. Chem.* **2020**, *12*, 115–130.

[170] J. Cai, P. Ruffieux, R. Jaafar, M. Bieri, T. Braun, S. Blankenburg, M. Muoth, A. P. Seitsonen, M. Saleh, X. Feng, et al., *Nature* **2010**, *466*, 470–473.

[171] J. Van Der Lit, M. P. Boneschanscher, D. Vanmaekelbergh, M. Ijäs, A. Uppstu, M. Ervasti, A. Harju, P. Liljeroth, I. Swart, *Nat. Commun.* **2013**, *4*, 1–6.

[172] F. Schulz, P. H. Jacobse, F. F. Canova, J. Van Der Lit, D. Z. Gao, A. Van Den Hoogenband, P. Han, R. J. M. Klein Gebbink, M. E. Moret, P. M. Joensuu, et al., *J. Phys. Chem. C* **2017**, *121*, 2896–2904.

[173] A. Sánchez-Grande, B. de la Torre, J. Santos, B. Cirera, K. Lauwaet, T. Chutora, S. Edalatmanesh, P. Mutombo, J. Rosen, R. Zbořil, et al., *Angew. Chem. Int. Ed.* **2019**, *58*, 6559–6563.

[174] S. Mishra, D. Beyer, K. Eimre, J. Liu, R. Berger, O. Gröning, C. A. Pignedoli, K. Müllen, R. Fasel, X. Feng, et al., *J. Am. Chem. Soc.* **2019**, *141*, 10621–10625.

[175] N. Pavliček, C. Herranz-Lancho, B. Fleury, M. Neu, J. Niedenführ, M. Ruben, J. Repp, *Phys. Status Solidi B* **2013**, *250*, 2424–2430.

[176] J. Zhang, P. Chen, B. Yuan, W. Ji, Z. Cheng, X. Qiu, *Science* **2013**, *342*, 611–614.

[177] S. K. Hämäläinen, N. Van Der Heijden, J. Van Der Lit, S. Den Hartog, P. Liljeroth, I. Swart, *Phys. Rev. Lett.* **2014**, *113*, 186102.

Chapter 2

An *sp*-hybridised molecular carbon allotrope, cyclo[18]carbon

This chapter details the first structural characterisation of a cyclo[*n*]carbon. Carbon allotropes built from rings of two-coordinate atoms, known as cyclo[*n*]carbons, have fascinated chemists for many years, but until now they have not been isolated or structurally characterised, due to their high reactivity. We generated cyclo[18]carbon (C_{18}) using atom manipulation on bilayer NaCl on Cu(111) at 5 K by eliminating carbon monoxide from a cyclocarbon oxide molecule $C_{24}O_6$. Characterisation of cyclo[18]carbon by high-resolution atomic force microscopy revealed a polyynic structure with defined positions of alternating triple and single bonds. The high reactivity of cyclocarbon and the cyclocarbon oxides allows covalent coupling between molecules to be induced by atom manipulation, opening an avenue for the synthesis of other carbon allotropes and carbon-rich materials from the coalescence of cyclocarbon molecules.

2 An *sp*-hybridised molecular carbon allotrope, cyclo[18]carbon

2.1 Acknowledgements

Results from this chapter have been published[1]:

Katharina Kaiser,[1†] Lorel M. Scriven,[2†] Fabian Schulz,[1] Przemyslaw Gawel,[2]* Leo Gross,[1]* Harry L. Anderson[2]* *Science,* **2019**, *365*, 1299–1301.

[†] These authors contributed equally

The author carried out all the synthesis and characterisation of compounds listed in this chapter. All AFM experiments were performed by Katharina Kaiser, Dr Fabian Schulz, Dr Leo Gross and, in part, by the author upon visiting IBM Research-Zurich. Dr Fabian Schulz, Dr Przemyslaw Gawel and Katharina Kaiser carried out the DFT calculations. Dr Fabian Schulz performed the AFM simulations. The author, Katharina Kaiser, Dr Fabian Schulz, Dr Przemyslaw Gawel, Dr Leo Gross, and Professor Harry L. Anderson contributed to conceiving the research and writing the manuscript. The author wrote the first draft of the manuscript, parts of the text in this chapter are similar to the publication. Permission was granted for use of the full text from the American Association for the Advancement of Science Ltd: Science.

Dr Steffen L. Woltering is gratefully acknowledged for proofreading this chapter.

2.2 Introduction

The discovery of fullerenes[2], carbon nanotubes[3], and graphene[4], all of which consist exclusively of 3-coordinate carbon atoms, has sparked a new field of synthetic carbon allotropes[5,6]. The only molecular allotropes of carbon that have been isolated are the fullerenes[7]. Rings of 2-coordinate carbon atoms (cyclo[*n*]carbons, C_n) have been suggested as an alternative family of molecular carbon allotropes[5,6,8]. There is evidence for the existence of cyclocarbons in the gas phase[5,6,9,10], but these highly reactive species have not been structurally characterised or studied in condensed phases. The question of whether cyclocarbons are polyynic, with alternating single and triple bonds of different lengths, or cumulenic with consecutive double bonds (Figure 2.1) is fundamental and controversial[11–14].

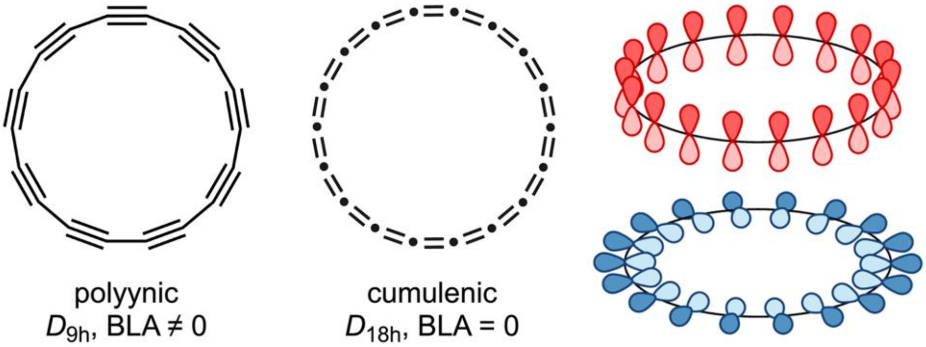

Figure 2.1 Two possible structures of cyclo[18]carbon. The polyynic form with D_{9h} symmetry and the cumulenic form with D_{18h} symmetry are shown, along with visualisations of their perpendicular π-systems. BLA: bond length alternation.

A distinctive feature of *sp*-hybridised carbon allotropes is that they possess two perpendicular π-conjugated electron systems (Figure 2.1). Hückel's rule predicts for planar, cyclic conjugated systems with $(4n + 2)$ π electrons an aromatic structure with no BLA[15]. Hoffmann discussed the stability of C_{18} in 1966[8], and later it was realised that this molecule could exhibit two orthogonal ring currents causing double aromatic stabilisation[5,16]. Since then, the structures of cyclo[*n*]carbons have been the topic of intense theoretical debate (see Section 1.2.2 and Section 4.2).

Most attempts at synthesising cyclocarbons have used a masked alkyne equivalent incorporated into a cyclic precursor designed to generate cyclo[*n*]carbon when activated by an external stimulus. Methods of unmasking included a retro-Diels-Alder reaction[5], decomplexation[17], decarbonylation[18] and [2+2] cycloreversion[19]. These attempts have given tantalising glimpses of cyclo[*n*]carbon in the gas phase. Cyclo[*n*]carbons may coalescence to form fullerenes[9,10], and gas-phase electronic spectra of C_{18}, formed by laser ablation of graphite, have been measured, but these studies did not reveal whether the structures are cumulenic or polyynic[20].

An alternative approach for studying highly reactive molecules is to isolate them on an inert surface at low temperature. Developments in the field of scanning tunneling microscopy (STM) and atomic force microscopy (AFM), in particular tip functionalisation, have enabled imaging of molecules with unprecedented resolution[21,22] and atom manipulation can trigger chemical reactions on surfaces[22–25]. Highly reactive molecules such as radicals[25,26] or arynes[27] have been generated and studied by this method. This led to the idea of generating a cyclo[*n*]carbon by atom manipulation on a low temperature surface and characterising it by high resolution atomic force microscopy.

The general requirements for a suitable cyclo[18]carbon precursor for on-surface atom manipulation are as follows[22,28]. The molecule needs to be of sufficiently low molecular weight to undergo sublimation. The acetylene masking group should have low enough bond dissociation energy to be removed by a voltage pulse. Lastly the precursor should be flat to facilitate study of the precursor and the reaction intermediates. Upon review of the cyclo[18]carbon precursors that have been synthesised previously[5,18,19,29–31], cyclocarbon oxides were selected as suitable candidates. The cyclocarbon oxides are relatively low molecular weight, flat molecules with a masked alkyne equivalent (MAE) that can be removed by flash vacuum pyrolysis. They were first proposed by Diederich *et al.* in 1989[32] who initially synthesised acetal protected cyclic precursors[33] (Figure 2.2, **7**–**9**). The acetal precursors **7**–**9** demonstrated remarkable stability however their deprotection to the cyclocarbon oxides proved challenging.

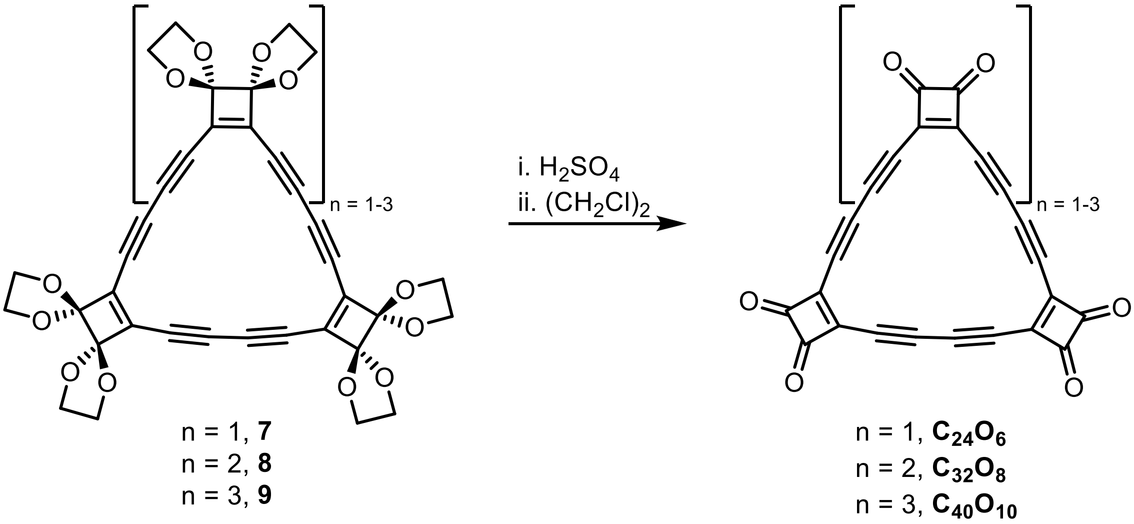

Figure 2.2 Initial preparation of the cyclocarbon oxides by Diederich *et al.*[33]

The first evidence[33] for the formation of the cyclocarbon oxides was obtained by dissolving **7** and **8** in D_2SO_4 which yielded $C_{24}O_6$ and $C_{32}O_8$ as light-sensitive solutions, however isolation in the bulk proved challenging. After optimisation of the acetal deprotection $C_{24}O_6$, $C_{32}O_8$ and $C_{40}O_{10}$ could be obtained in tens of milligram quantities from **7**–**9** in 70 to 99% yield[18] (Figure 2.2). In addition, the cyclobutenedione MAEs were used by Rubin[34] to synthesise $C_{60}H_6(CO)_{12}$ as a fullerene precursor.

Three methods have been reported for the unmasking of cyclobutenedione groups: laser-desorption mass spectrometry, photochemical irradiation and solution-spray flash vacuum pyrolysis (SS-FVP). Laser-desorption mass spectrometry was successfully used to detect C_{18}, C_{24} and C_{30} in the gas phase in analytical (very small) amounts from their corresponding cyclocarbon oxide precursors[18]. The second reported unmasking method is photochemical irradiation[35,36]. The photochemically activated [2+2] cycloreversion of the cyclobutenediones to 1,2-bisketenes was discovered in 1961[37,38]. 1,2-Bisketenes show a strong IR stretch at 2100 cm^{-1} and, upon further photochemical irradiation, can extrude two carbon monoxide moieties to generate an alkyne. Diederich *et al*[36] carried out low temperature FT-IR and UV spectroscopic experiments on the cyclocarbon oxides. A solution of $C_{24}O_6$ was injected onto a cold (15 K) CsI window. The change in the Fourier-transform IR transmittance upon UV irradiation was monitored. Irradiation at $\lambda > 338$ nm demonstrated loss of the strong band at 1792 cm^{-1} corresponding to the carbonyl of $C_{24}O_6$. A new signal was then observed at 2115 cm^{-1} which is likely due to a diketene moiety. Upon further irradiation, the band moved to 2136 cm^{-1} which was consistent with free CO. However, no IR absorption corresponding to cyclo[18]carbon was observed and thus no direct evidence for unmasking was obtained. The last reported unmasking method is SS-FVP; this is the process by which a compound is introduced as a sprayed aerosol into a hot quartz tube (at 600 °C) under a flow of low-pressure inert gas (~1.5 mbar) which triggers thermally activated reactions. Diederich used this method to prepare linear polyynes on a multigram scale[39]. These conditions are similar to the sublimation process used for on-surface study and thus we hoped that even if the cyclocarbon oxides could not be unmasked by atom manipulation that they might be thermally unmasked upon sublimation to reveal cyclo[*n*]carbons.

Encouraged by the unmasking characteristics of the cyclocarbon oxides and the seemingly straightforward synthesis of these molecules cyclocarbon oxides were selected as suitable candidates for on-surface cyclocarbon generation.

2.3 Methods

2.3.1 Synthesis of $C_{24}O_6$

Cyclo[18]carbon oxide $C_{24}O_6$ was prepared using modified procedures developed by Rubin and Diederich[18,34] (Figure 2.3). Liebeskind's methodology[40,41] was used to form siloxy ketone **10**, *via* attack of lithiated TIPS-acetylene into dimethyl squarate and subsequent quenching of the reaction with TMS-Cl (Figure 2.3). MeOTMS and TMSOTf converted **10** to **11** in a one pot reaction. TMS-acetylene was lithiated and added to **11** and the reaction was quenched with 3 M HCl to give the crude eneyne, which was subjected to acetal formation conditions (MeOTMS and TMSOTf) to yield stable bis(acetal) enediyne **12**. TBAF was used to deprotect **12** giving the unstable monomer **13**.

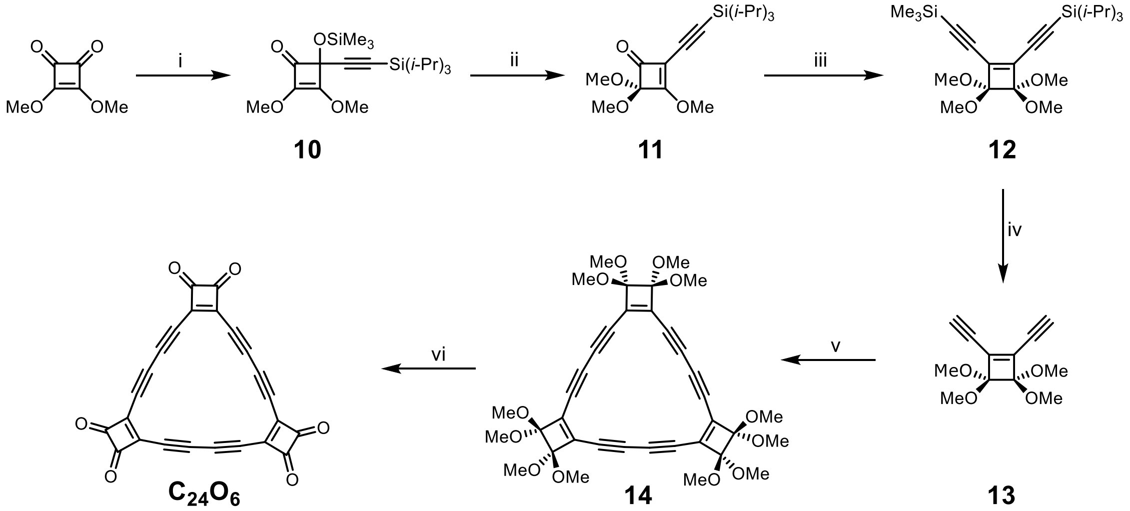

Figure 2.3 Synthesis of cyclo[18]carbon oxide $C_{24}O_6$. i) Li-C≡C-Si(i-Pr)$_3$, THF, 1 h, –78 °C; then TMS-Cl, 15 min, –78 °C to 21 °C, 96%; ii) MeOTMS then TMSOTf, THF, 30 min, 21 °C, 89%; iii) Li-C≡C-SiMe$_3$, Et_2O, 30 min, –45 °C; then HCl (3 M), –45 °C to 21 °C, 1 h; then MeOTMS then TMSOTf, 60 h, 21 °C, 75%; iv) TBAF, THF, 30 min, –78 °C, 93%; v) CuCl, TMEDA, acetone, O_2, 2 h, 21 °C, 7%; vi) conc. H_2SO_4, $(CH_2Cl)_2$, 10 min, 21 °C, 96%.

The monomer **13** was subjected to Hay coupling conditions[42] with stoichiometric pre-prepared Hay catalyst to give acetal protected cyclocarbon oxide **14** in 7% yield. Other ring sizes were also isolated and will be discussed in Chapter 4 (see Section 4.3.1). The cyclic trimer **14** was deprotected in the absence of light using H_2SO_4 and extracted with 1,2-dichloroethane to yield $C_{24}O_6$ as an unstable yellow solid. Our synthetic route prepared $C_{24}O_6$ in 6 steps from dimethyl squarate in 4% overall yield. Previously reported syntheses[18,33] prepared $C_{24}O_6$ in 5 steps from dichlorocyclobut-3-ene-1,2-dione in an overall yield of 6% however this starting reagent is prohibitively expensive and thus would need to have been prepared from 3,4-dimethoxy-3-cyclobutene-1,2-dione. In addition, our synthesis installed two orthogonal silyl protecting groups in **12** which can be used for a more stepwise synthesis that will be exploited in Chapter 4.

The acetal protected ring **14** showed remarkable stability both at room temperature and at –20 °C. **14** has been stored at –20 °C for up to a year without any notable decomposition. Single crystals of **14** were grown by layer diffusion of CH_2Cl_2/hexane (Figure 2.4). The crystals are orthorhombic (*PBcn* space group) with four molecules per unit cell and half a molecule of **14** in the asymmetric unit.

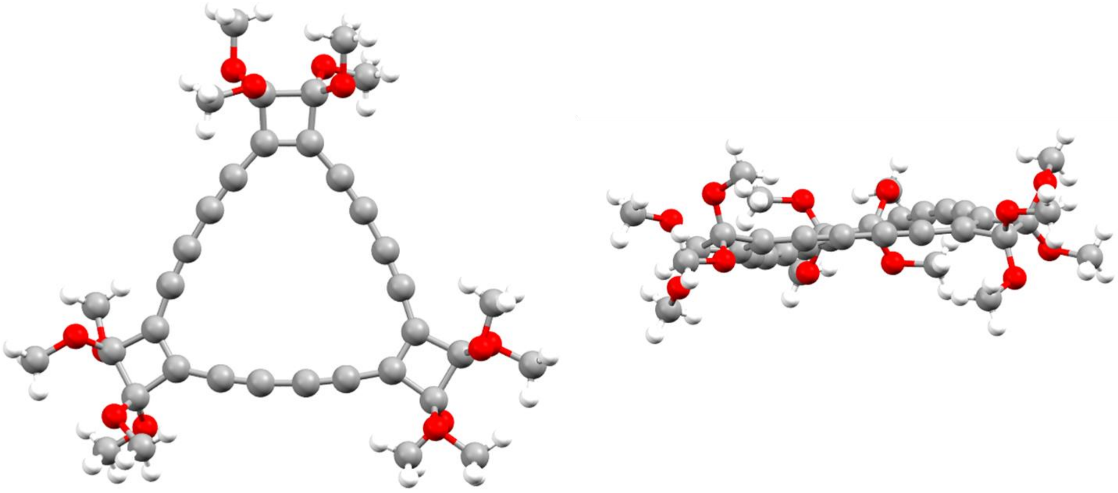

Figure 2.4 Single crystal X-ray structure of **14** showing front facing and side view.

The crystal structure confirmed that **14** has a nearly planar geometry with OMe groups above and below the plane of the ring. There is slight bending in the acetylene units away from the ideal 180° geometry (acetylene angles recorded as 172.7°, 171.8°, 172.8°, 175.3°, 174.0°

and 174.4°) presumably to relieve strain in the cyclobutenedione moieties. Further analysis of bond order and strain effects in these rings will be discussed in Chapter 4.

Acetal **14** was deprotected to $C_{24}O_6$ by dropping concentrated sulphuric acid onto the ketal and extraction with 1,2-dichloroethane. $C_{24}O_6$ was found to have higher stability than that reported by Diederich[18] who stated that the cyclocarbon oxides were "*too unstable for sending out for elemental analysis*[18]". Thermal stability studies were carried out using UV to monitor the change in intensity upon leaving $C_{24}O_6$ in different environmental conditions for four days (Figure 2.5). The change in intensity of the peak at 380 nm was used as a crude measure of the relative decomposition of the sample.

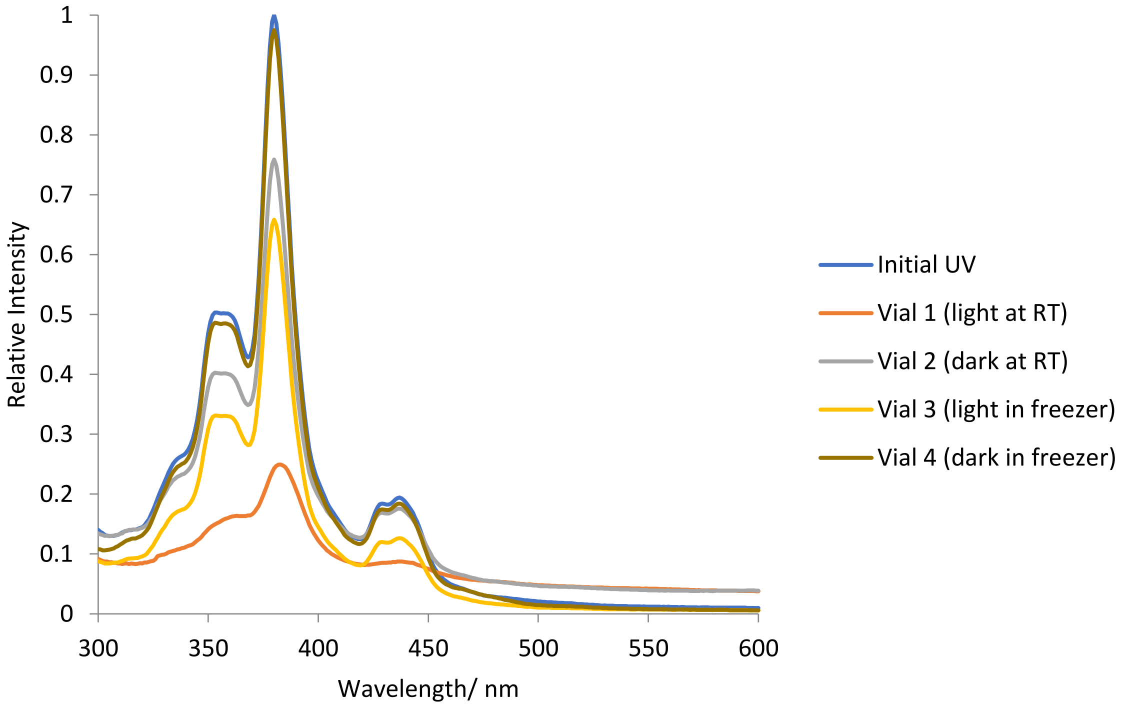

Figure 2.5 UV spectra of $C_{24}O_6$ (spectra recorded at 13 µM in 1,2-dichloroethane) after exposure to different environmental conditions. 1 mg of $C_{24}O_6$ was transferred to each vial, an initial UV spectrum at 13 µM was recorded. The solvent was then blown down and the vials left in different environments for four days. After four days a UV spectrum at the same concentration was recorded and the change in intensity of the UV relative to the initial UV was measured.

76% decomposition was observed for the sample left at 21 °C in low level ambient light in the laboratory (vial 1). Whereas the sample left at 21 °C in the dark (wrapped in aluminium foil) only showed 24% decomposition (vial 2) thus demonstrating the light-sensitivity of these compounds. A sample left at –20 °C with no aluminium wrapping and that was exposed to low level ambient light when the freezer was opened showed 34% decomposition whereas the sample left at –20 °C in the dark only showed 2% decomposition over four days. While these measurements only give a rough indication of the thermal stability of $C_{24}O_6$, they demonstrated the high sensitivity of these compounds to light and, to a lesser extent, temperature.

These results demonstrated that if $C_{24}O_6$ is handled correctly and always stored in the dark at –20 °C then these compounds could be stable for weeks and therefore be shipped to IBM Research–Zurich *via* courier without significant decomposition.

2.3.2 Sample and tip preparation

As a substrate, a Cu(111) single crystal was partially covered with NaCl. The Cu single crystal was cleaned *in situ* by repeated Ne-ion sputtering and annealing ($T \approx 720$ K) cycles[43]. NaCl was sublimed onto the clean Cu surface that was kept at $T \approx 270$ K, resulting in (100)-oriented, mostly double-layered NaCl islands[44]. The microscope tip (PtIr-wire with a diameter of 25 μm) was sharpened using a focused ion beam, followed by *in situ* indentations into the Cu surface to prepare an atomically sharp tip. For tip functionalisation, we used single CO molecules that were picked up from the surface[21,45]. To this end, gaseous CO was allowed into the UHV chamber (partial pressure of $p = 2 \times 10^{-8}$ mbar) for about 20 seconds to adsorb on the cold ($T \approx 10$ K) surface. The cyclocarbon oxide precursors were deposited on the cold ($T \approx 10$ K) sample *via* sublimation from a Si-wafer that was flash-annealed to approximately 900 K within a few seconds[46].

2.3.3 STM/AFM Measurements

For the characterisation with STM and AFM, we used a home-built combined STM/AFM system, operating at ultra-high vacuum conditions ($p \approx 1 \cdot 10^{-10}$ mbar) and low temperatures ($T = 5$ K). The microscope employs a qPlus force sensor[47] with a resonance frequency $f_0 \approx 30$ kHz, quality factor $Q \approx 100.000$ at $T = 5$ K and a spring constant $k \approx 1.800$ Nm^{-1} and is operated in frequency-modulation mode[48]. The bias voltage V was applied to the sample. The lower end of the tip-height colour scale bar (corresponding to black) in constant-current STM images is defined as 0 Å. AFM images were acquired in constant-height mode at $V = 0$ V and an oscillation amplitude of $A = 0.5$ Å. The tip-height offsets Δz for constant-height AFM images are defined as the offset in tip-sample distance relative to the STM set point at the top centre of the acquired image, with positive (negative) values indicating that the tip-sample distance increased (decreased) with respect to the STM set point.

2.4 Results and Discussion

2.4.1 On-surface synthesis of cyclo[18]carbon

This section details the synthesis and structural characterisation of cyclo[18]carbon. A low temperature STM-AFM was used to sequentially remove masking CO groups from the precursor $C_{24}O_6$ by atom manipulation (Figure 2.6). We resolved the structure of cyclo[18]carbon and observed BLA in its ground state.

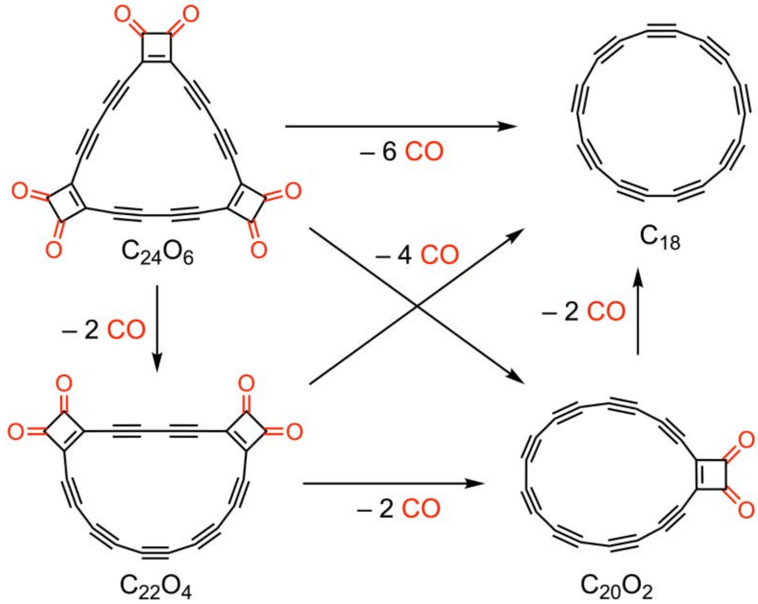

Figure 2.6 Reaction scheme for the on-surface formation of C_{18}. Decarbonylation was achieved *via* voltage pulses that resulted in the loss of two, four or six CO moieties.

$C_{24}O_6$ was sublimed according to the procedure listed in Section 2.3.2. All molecules were studied on bilayer NaCl, providing an inert surface on which radicals and polyynes[25] are stable and can be imaged. The experiments were carried out in a combined STM/AFM system equipped with a qPlus force sensor[47] operating at $T = 5$ K in frequency-modulation mode[48]. We used CO tip functionalisation to improve the resolution[21]. AFM images were acquired at constant height, with the offset Δz applied to the tip-sample distance with respect to the STM setpoint above the bare NaCl surface. We simulated AFM images using the probe particle model[49] based on the structures relaxed in the gas phase, calculated by DFT (see Section 2.4.8 for further discussion of AFM simulations).

After deposition, we found molecules of the precursor $C_{24}O_6$ on the NaCl surface, as well as some fragmented or (partially) decarbonylated molecules and single CO molecules (Figure 2.7). This result indicated that partial decarbonylation and dissociation took place during sublimation.

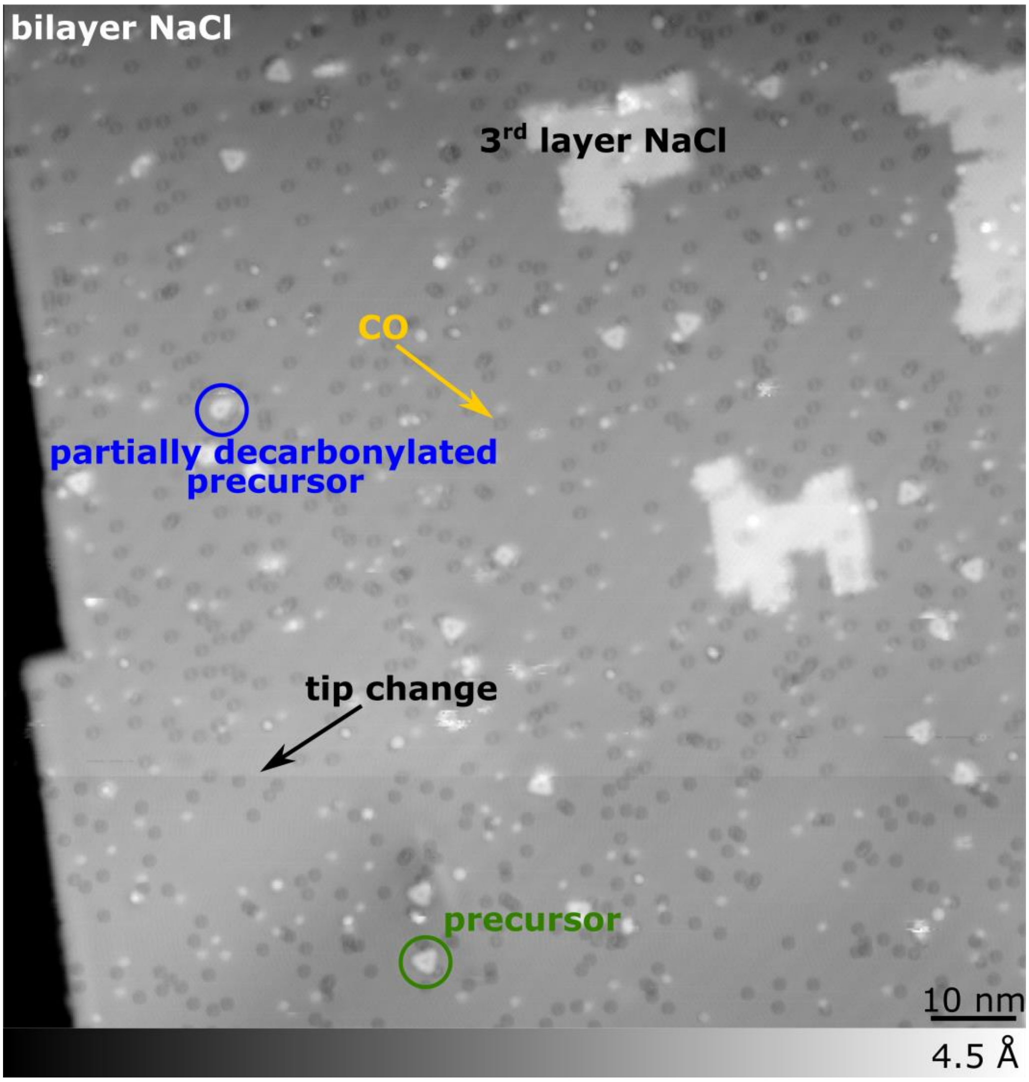

Figure 2.7 Overview image. STM overview recorded at a set point of $V = 0.4$ V, $I = 0.5$ pA. Most of the image shows bilayer NaCl on Cu(111), a few islands of third layer NaCl are visible (3rd layer NaCl). The small depressions are single CO molecules. The overview shows mainly intact $C_{24}O_6$ precursor molecules (example shown in the green circle) and a few partially decarbonylated intermediates (example shown in the blue circle). In the lower part of the image, the contrast changes abruptly, which can be attributed to a tip change.

Figure 2.8 shows AFM data and corresponding simulations for $C_{24}O_6$ and products created by atom manipulation. $C_{24}O_6$ molecules appeared as triangular objects with dark features at the corners and two bright protrusions at each side (Figure 2.8B). The dark contrast, characteristic of ketone groups[50] was explained by a reduced adsorption height and a relatively small electron density in the region imaged above the O atoms, which have high electron affinity. Both effects led to comparably small Pauli repulsive forces above the O atoms. Figure 2.8B was recorded at moderate tip height ("AFM far", $\Delta z = +0.3$ Å), at which differences in bond order were visible in the Δf signal, with high brightness, i.e., high Δf indicating high bond order[51]. The two bright features at each side of the molecule were assigned to triple bonds[25,52]. At decreased tip-sample distance ("AFM close", Figure 2.8C, $\Delta z = -0.1$ Å), repulsive forces made greater contributions and tip relaxations, i.e., tilting of the CO at the tip apex, affected the AFM images substantially. These effects led to apparent sharpening of the bonds, and pronounced differences in apparent bond lengths[49,51,53]. The different contrasts of the three different sides of $C_{24}O_6$ (Figure 2.8B) suggest an adsorption geometry not parallel to the surface[50].

To decarbonylate $C_{24}O_6$, the tip was positioned in the vicinity (a few nanometres) of the molecule, retracted by about 3 Å from the STM setpoint (typically $V = 0.2$ V and $I = 0.5$ pA) and the sample bias voltage V was increased to about $V = +3$ V, for a few seconds. This procedure often led to the removal of two, four, or six CO moieties. The most abundant products were $C_{22}O_4$ (Figure 2.8F) and $C_{20}O_2$ (Figure 2.8K). The removal of a masking group (2 CO) resulted in the formation of a longer bent polyynic segment. Assigning the bright features in the "AFM far" images to the location of triple bonds, we observed curved polyyne segments with the expected number of triple bonds: 5 in $C_{22}O_4$ (Figure 2.8G) and 8 in $C_{20}O_2$ (Figure 2.8L). At small tip height (Figure 2.8, H and M), we observed sharp bond-like features with corners at the assigned positions of triple bonds and straight lines in between. This contrast was explained by CO tip relaxation, in that maxima in the potential energy landscape, from which the tip apex was repelled, were located above the triple bonds because of their high electron density. In between these maxima, ridges in the potential landscape led to straight bond-like features[49,54,55]. The assignment of the intermediates was further supported by AFM simulations (Figure 2.8, 4th and 5th column).

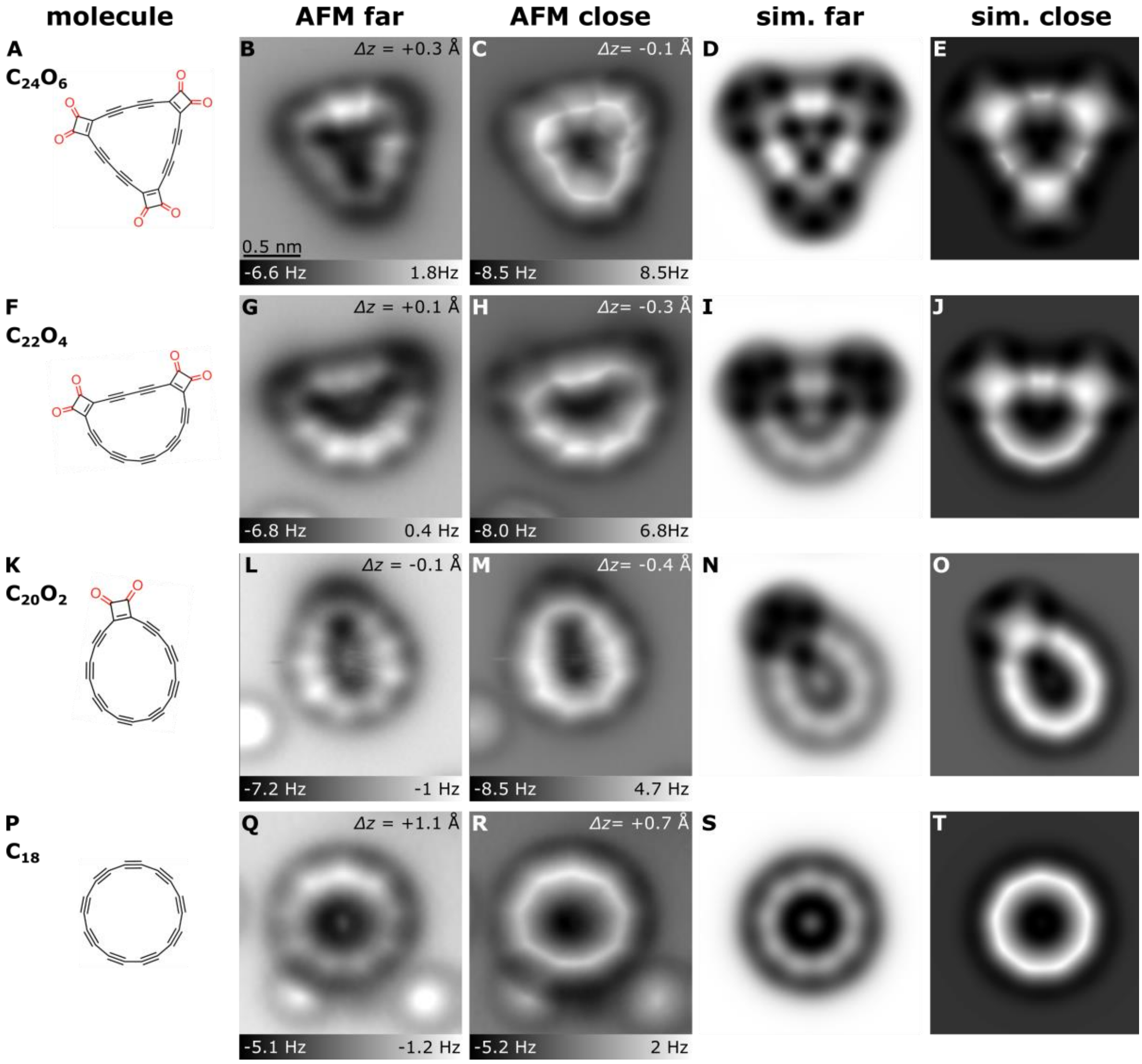

Figure 2.8 Precursor and products generated by tip-induced decarbonylation. Structures (1st column) and AFM images (2nd and 3rd column) recorded with a CO-functionalised tip at different tip offsets Δz, with respect to an STM set point of I = 0.5 pA, V = 0.2 V above the NaCl surface, showing (**A**–**E**) precursor, (**F**–**J** and **K**–**O**) most frequently observed intermediates and (**P**–**T**) cyclo[18]carbon. The bright features at the lower part in (L), (M), (Q) and (R) correspond to individual CO molecules. Simulated AFM images (4th and 5th column) based on gas-phase DFT calculated geometries. The difference in probe height in "sim. far" to "sim. close" corresponds to the respective differences in "AFM far" and "AFM close". The same scale bar as in (B) applies to all experimental and simulated AFM images.

We removed all six CO moieties from $C_{24}O_6$ typically resulting in circular molecules (Figure 2.8 Q and R). At moderate tip heights (Figure 2.8Q) the resulting molecule exhibited a cyclic arrangement of nine bright lobes. For smaller tip heights (Figure 2.8R), the molecule appeared as a nonagon with corners at the positions of the bright lobes that were observed at larger tip-sample distance (Figure 2.8Q). The contrast can be explained in analogy to the precursors: The bright lobes in Figure 2.8Q and the corresponding corners in Figure 2.8R were observed above triple bonds. The molecule was thus identified as cyclo[18]carbon. The AFM contrast provided evidence for a polyynic structure of cyclo[18]carbon on NaCl with the defined positions of triple bonds supported by AFM simulations (Figure 2.8, S and T). Further insight into the structural determination of cyclo[18]carbon will be detailed in the next section.

2.4.2 Structural determination of cyclo[18]carbon

These measurements provided the first insight into the bonding characteristics of cyclo[18]carbon. They revealed a nine-fold symmetric polyynic structure. In the case of a cumulenic structure, no BLA and an 18-fold symmetry of the molecule would be expected, in contrast to the experimental result. Figure 2.9 shows additional AFM images of the fully decarbonylated cyclo[18]carbon at different tip-height offsets Δz. For large tip-sample distances (Figure 2.9A), the molecules show bright features (increased Δf values) that can be attributed to the triple bonds due to their large exposed electron density. For decreasing tip-sample distances, the brightness contrast between single and triple bonds gradually disappears and bright, bond-like features appear, with corners above the positions of triple bonds and straight lines connecting them (Figure 2.9D). As explained for the precursors, this contrast results from the tilting of the CO molecule at the tip apex[49,53,54,56,57] and leads to the nonagon shape of the molecule. The AFM contrast indicates that cyclo[18]carbon molecules adsorbed in a non-planar geometry, i.e., not parallel with respect to the NaCl surface. The maxima related to the triple bonds appear with different brightness. From the different contrast of the triple bonds within AFM images and the contrast evolution as a function of tip height, we estimate maximal height differences of 0.1 Å to 0.3 Å within an individual molecule[50]. Thus, we estimate tilts of the molecular plane with respect to the surface plane of about 1–2 degrees, varying for different molecules. These angles are calculated assuming a diameter for cyclo[18]carbon of approximately 7.4 Å and height difference of 0.1 Å (1 degree tilt) and 0.3 Å (2 degree tilt). The non-planar adsorption could be related to the mismatch in symmetry of the nine-fold symmetric cyclo[18]carbon with the fourfold symmetric NaCl surface. Such slight tilt of the molecular plane with respect to the surface can also be observed for $C_{24}O_6$ and most of the intermediates (Figure 2.8).

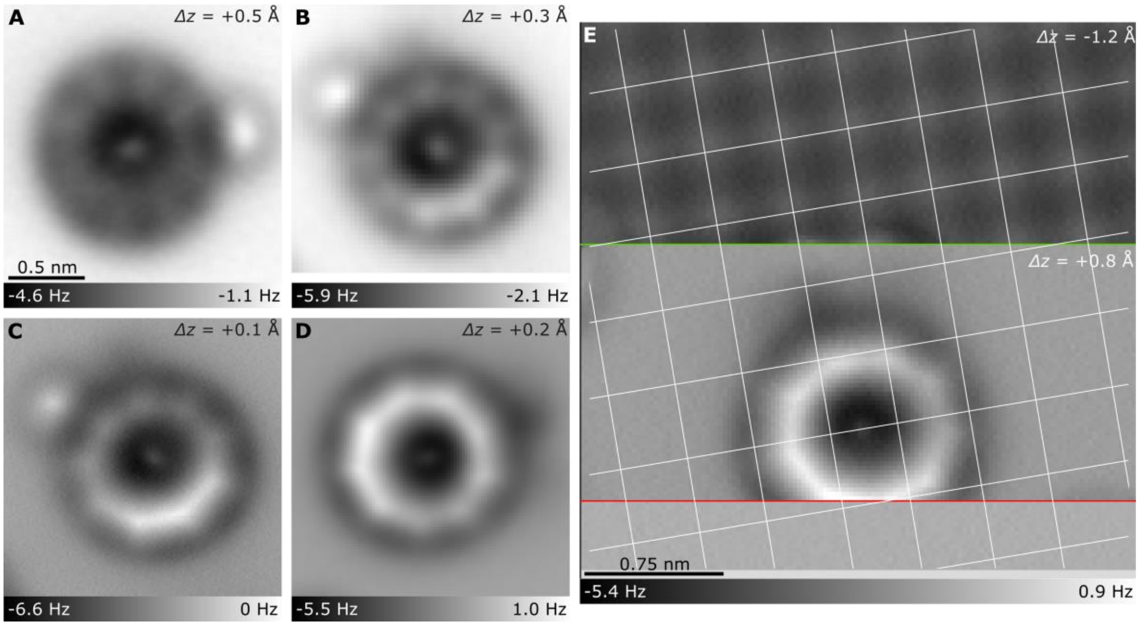

Figure 2.9 Additional AFM data of cyclo[18]carbon. (**A**–**D**) Constant-height AFM images of different cyclo[18]carbon molecules recorded at different tip-sample distances, decreasing from (A) to (D). (B) and (C) show the same molecule. (**E**) AFM image of cyclo[18]carbon to determine the adsorption position. The slow scan direction was from top to bottom. In the upper part of the image, a small tip height ($\Delta z = -1.2$ Å) was used to resolve the NaCl surface atomically. The Cl anions appear as bright features and are indicated by the overlaid grid. At the green line, the tip height was increased to $\Delta z = 0.8$ Å. At the red line, the tip lost the CO molecule. The measurement shows cyclo[18]carbon adsorbed on a Cl-Cl bridge site. In (A, D, E), Δz is given with respect to an STM set point of $V = 0.1$ V and $I = 0.5$ pA, in (B, C), Δz is given with respect to an STM set point of $V = 0.2$ V and $I = 0.5$ pA.

The AFM images shown in Figure 2.9, C and D are taken at tip sample distances where a part of the molecule shows the contrast for small tip heights (cf. “AFM close” in Figure 2.8), i.e., sharp lines with corners above the positions of triple bonds, while on the opposing side of the ring the contrast for large tip heights is visible (“AFM far” in Figure 2.8), i.e., bright lobes above positions of triple bonds. These images visualise the non-planar adsorption geometry of the molecules and the evolution of the contrast as a function of tip-sample distance. Moreover, they corroborate that the corners observed at small tip height are at the locations of the bright lobes at large tip height, and thus correspond to the locations of the triple bonds.

Figure 2.9E shows a constant-height AFM image in which the tip height was changed to determine the adsorption position of cyclo[18]carbon. In the top part of the image, a small tip-height offset of $\Delta z = -1.2$ Å (setpoint $V = 0.1$ V and $I = 0.5$ pA) was chosen to atomically resolve the NaCl lattice. The bright features in this part of the image correspond to Cl-atoms[58]. In the part of the image below the green line the tip-height offset was increased to $\Delta z = +0.8$ Å. Extrapolating the Cl lattice sites, we find that this cyclo[18]carbon is adsorbed with the centre on a Cl-Cl bridge site. At the red line the CO-functionalised tip lost the CO.

During charge-state switching, tip-induced decarbonylation, and STM imaging, the molecules often jumped[59] to different locations on the surface, indicating a very small diffusion barrier on NaCl. Cyclo[18]carbon moved more frequently than the other molecules observed, and it was often found adjacent to step edges or individual CO molecules adsorbed on the surface, pinning the molecule (Figure 2.8, Q and R). This is visible in Figure 2.9, A to C, where the bright contrast directly next to the cyclo[18]carbon stems from adjacently adsorbed CO molecules. We conclude that these CO molecules were not covalently bound to cyclo[18]carbon, due to the following observations: i) The adjacent CO molecules show the same contrast and adsorption site (on top of Na cations) as single isolated CO molecules, indicating they are also adsorbed in a vertical geometry on the NaCl surface. ii) If a cyclo[18]carbon jumped to a different adsorption site, the previously adjacent CO molecules did not move in conjunction with it. iii) The typical observed distance between cyclo[18]carbon and adjacent CO molecules, determined from the separation of Δf maxima in AFM images (Figure 2.9, A to C), is about 4 Å, which is too large for a covalent bond, even when taking into account possible image distortions for tip relaxations. Presumably, the CO molecules interact with the cyclo[18]carbon *via* van der Waals forces and stabilise the cyclo[18]carbon molecule such that it can be imaged without moving. However, the presence of the closely adsorbed CO molecules can affect the tilting of the CO tip and thus lead to distortions during constant-height imaging at small tip-sample distances, affecting also the contrast observed above cyclo[18]carbon in the vicinity of CO molecules.

A key question that needed to be answered for full characterisation of cyclo[18]carbon was that of its charge state which can crucially influence the structure of a molecule[60]. This will be discussed in the next section.

2.4.3 Charge state of cyclo[18]carbon

In the nine-fold symmetric form described above, the cyclo[18]carbon molecule was uncharged (neutral). We found that cyclo[18]carbon exhibited charge bistability[55] on this surface and it changed to a less symmetric and less planar geometry in the negatively charged state. The molecule could be reversibly switched between its two charge states and associated geometries. The charge state of molecules can be inferred *via* observation of the standing wave patterns of interface-state electrons[61,62]. On NaCl/Cu(111), the Cu(111) surface state survives as an interface state. Scattering patterns of interface-state electrons can be made visible by imaging at low bias voltage[63]. The scattering of interface-state electrons serves as a hallmark for charged particles because charged adsorbates act as scattering centres, but neutral adsorbates do not[55,61] (Figure 2.10).

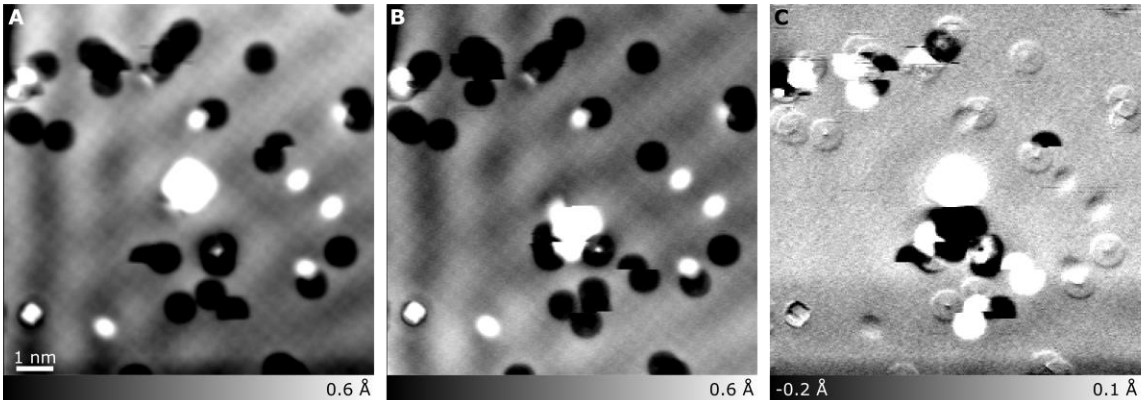

Figure 2.10 Interface state scattering behavior of neutral cyclo[18]carbon. (**A**, **B**) STM images acquired at I = 0.7 pA, V = 0.1 V before and after moving the (charge neutral) cyclo[18]carbon, in the centre of the image, laterally on the surface, respectively. (**C**) Difference image (A) – (B), exhibiting almost no contrast of standing wave pattern.

Figure 2.10A shows a STM image with a standing wave pattern of the interface state visible. Because of scattering at step edges and island edges[63] it is not obvious if the cyclo[18]carbon molecule in the centre of the image acts as a scattering centre. The molecule was moved laterally, and the same area was imaged again, using the same set point (Figure 2.10B). To emphasise changes in the scattering pattern, caused by moving the molecule, both images were subtracted from each other (Figure 2.10C). For a charged molecule a pronounced standing wave pattern would be expected in the difference image. The resulting difference image does not exhibit such a standing wave pattern, which evidences that this cyclo[18]carbon is not acting as a scattering centre for interface-state electrons and thus is charge neutral.

However, cyclo[18]carbon can be charged and exhibits charge bistability on this surface. This behaviour is demonstrated in Figure 2.11. A change in the charge state of the molecule was deliberately triggered by STM imaging at V = +0.6 V and is evidenced by the change in standing wave pattern of the interface-state electrons. Figure 2.11A shows an STM image of a neutral cyclo[18]carbon, acquired at a set point of I = 0.4 pA, V = 0.1 V. By imaging the same molecule at a bias voltage of $V = +0.6$ V (Figure 2.11B), an abrupt change in shape occurred, during the scan line indicated by the arrow. Subsequent imaging of the same area, shown in Figure 2.11C, recorded with the same set point as in Figure 2.11A, shows a change in the standing wave pattern around the molecule compared to Figure 2.11A. This change is emphasised in the difference image Figure 2.11D, where the interference pattern around the molecule indicates a change in charge state between Figure 2.11A and Figure 2.11C.

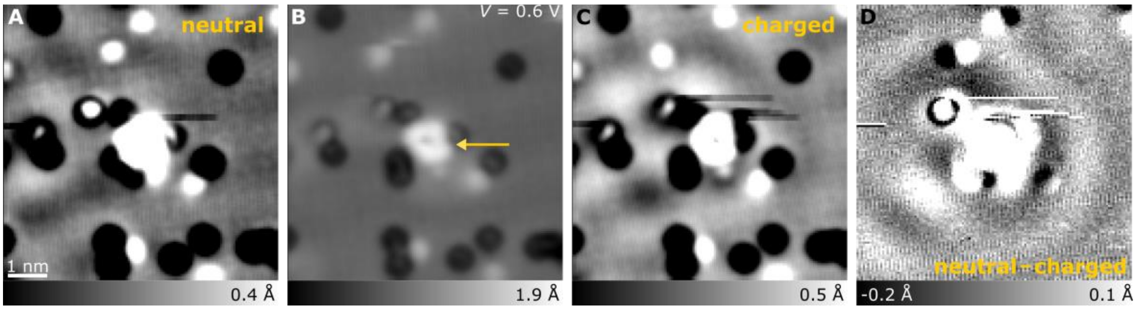

Figure 2.11 Interface state scattering behaviour of charged cyclo[18]carbon. (**A**) Image of the neutral cyclo[18]carbon acquired at $I = 0.4$ pA, $V = 0.1$ V. (**B**) Image of the same cyclo[18]carbon acquired at $I = 0.4$ pA, $V = 0.6$ V, leading to a change in charge state at the scan line indicated by the arrow. (**C**) Image of the charged cyclo[18]carbon acquired at $I = 0.4$ pA, $V = 0.1$ V. (**D**) Difference image of (A) – (C) showing an interference pattern, indicating charge-state switching of the molecule.

Figure 2.12 shows a series of charging and discharging events of an individual cyclo[18]carbon molecule. The molecule was charged by imaging it at voltages $V > 0.6$ V. Presumably, cyclo[18]carbon is charged negatively by resonantly attaching a long-lived electron to its LUMO, in analogy to the reported charge-state switching of CuPc[55]. In contrast to neutral cyclo[18]carbon, the charged molecule exhibits a distorted, less circular geometry (see Figure 2.12, D, E and H). Its structural characterisation is even more challenging than for neutral cyclo[18]carbon, as it often changed its adsorption geometry and site, leading to the stripy images observed in Figure 2.12, D, E and H. At voltages $V < -0.2$ V, the molecule was switched back to the neutral charge state reestablishing the nine-fold symmetric geometry of neutral cyclo[18]carbon. Often a change in the charge state of the molecule was accompanied by lateral displacement of the molecule and sometimes chemical reactions with surrounding molecules. The charge bistability and the high reactivity render imaging of the orbital densities of cyclo[18]carbon with STM extremely challenging. As a result of the charging of cyclo[18]carbon at positive bias voltages, the LUMO related resonance cannot be spatially imaged. The threshold for charging the molecule at about $V = 0.6$ V gives an indication for the onset of the negative ion resonance (NIR), related to the LUMO, at this voltage. Once the molecule has been charged negatively, the corresponding state remains occupied and is therefore not available as a tunneling path. The next-higher unoccupied state of the singly negatively charged molecule lies higher in energy by the Coulomb energy and can therefore only be addressed by applying markedly higher voltages. Applying voltages larger than 1.5 V for imaging of cyclo[18]carbon has resulted in this molecule reacting with other molecules on the surface in all attempts. Imaging the HOMO density at negative bias voltages was also not possible since imaging at elevated negative bias voltages ($V < -1.5$ V) led to the molecule jumping away.

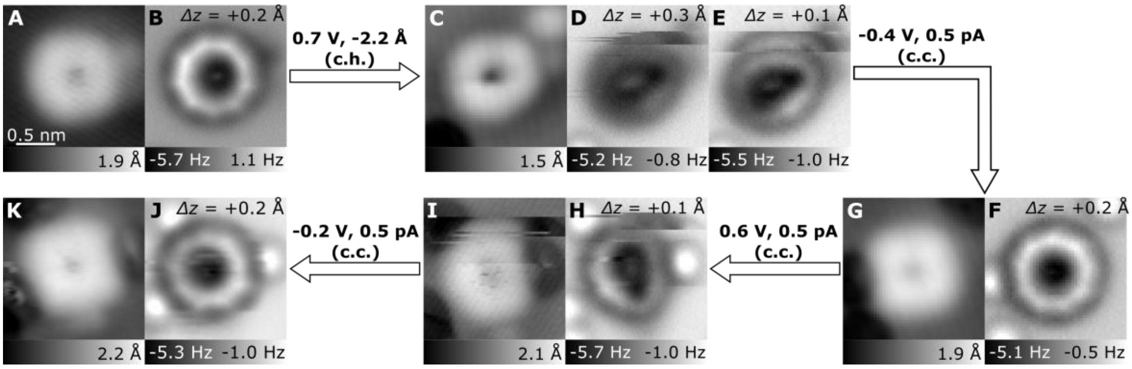

Figure 2.12 Reversible charge-state transitions of cyclo[18]carbon. Series of STM (**A**, **C**, **G**, **I**, **K**) and AFM (**B**, **D**, **E**, **F**, **H**, **J**) images recorded after charging and discharging events of a cyclo[18]carbon molecule, starting with the neutral molecule (A, B). Upon applying positive bias voltages $V > 0.6$ V, the molecule could be charged (C–E), upon applying negative voltages the molecule could be switched back into its neutral state (G, F). It was charged again (I, H) and switched back to neutral again (K, J). The arrows indicate how the charge state was manipulated, 'c.h.' indicates that the change in charge state happened during a constant-height image with the given parameters, 'c.c.' indicates that the change occurred during a constant-current STM image at the given parameters. Note the markedly different, less symmetric and less stable AFM contrast of the charged cyclo[18]carbon compared to the neutral one. STM images displayed were recorded at a set point of $V = 0.1$ V and $I = 0.5$ pA and Δz for the constant-height AFM images displayed is given with respect to that set point.

Structural determination of cyclo[18]carbon required its synthesis from $C_{24}O_6$ or other commonly observed intermediates. The atom manipulation and reaction statistics for the synthesis of cyclo[18]carbon will be detailed in the next section.

2.4.4 Yield and mechanism for the synthesis of cyclo[18]carbon

The yield of formation of cyclo[18]carbon was calculated by evaluation of 90 atomic manipulation events. Table 2.1 summarises the outcome of all tip-induced decarbonylation attempts, starting from either the intact precursor or one of the intermediates. The two most abundant intermediates are listed separately and denoted by their chemical formula $C_{22}O_4$ and $C_{20}O_2$, respectively.

Table 2.1 Reaction statistics for on-surface reactions by atom manipulation. Educts were the intact precursor $C_{24}O_6$, the two most abundant intermediates, $C_{22}O_4$ and $C_{20}O_2$ (structures shown in Figure 2.8) and other seldomly observed intermediates (rare intermediates). Reaction products were the two most abundant intermediates, $C_{22}O_4$ and $C_{20}O_2$, seldomly observed intermediates (rare intermediates), cyclo[18]carbon (C_{18}), chain-like structures due to breaking of a bond within the cyclic system (non-cyclic products) and other rare cyclic reaction products that could not be further manipulated (rare final products; see Figure 2.13). For the table in total $N = 90$ single molecule reactions induced by atom manipulation were evaluated.

Product / Educt	$C_{22}O_4$	$C_{20}O_2$	rare intermediates	C_{18}	non-cyclic products	rare final products
$C_{24}O_6$	17%	28%	4%	4%	26%	21%
$C_{22}O_4$	/	31%	6%	13%	31%	19%
$C_{20}O_2$	/	/	19%	13%	38%	31%
rare intermediates	/	20%	/	20%	20%	40%

We evaluated a total of 90 atomic manipulation events, in which the initial and final product were characterised. The resulting yield for the generation of cyclo[18]carbon from the precursor $C_{24}O_6$ by atom manipulation, including its synthesis *via* intermediates, was 13%. This yield was calculated by summing the measured individual yields for the different pathways, shown in Table 2.1. The pathways with different intermediates observed and their determined respective yields are:

$C_{24}O_6$ → C_{18} (4% yield),

$C_{24}O_6$ → $C_{20}O_2$ → C_{18} (3.6% yield),

$C_{24}O_6$ → $C_{22}O_4$ → C_{18} (2.2% yield),

$C_{24}O_6$ → rare intermediate → C_{18} (0.8% yield),

$C_{24}O_6$ → $C_{22}O_4$ → $C_{20}O_2$ → C_{18} (0.7% yield),

$C_{24}O_6$ → $C_{20}O_2$ → rare intermediate → C_{18} (1.1% yield),

$C_{24}O_6$ → $C_{22}O_4$ → rare intermediate → C_{18} (0.2% yield),

$C_{24}O_6$ → rare intermediate → $C_{20}O_2$ → C_{18} (0.1% yield).

Total yield of C_{18}: 12.7%.

Atom manipulation was carried out by positioning the tip in the vicinity of a precursor molecule and then holding at that position while the absolute value of the bias voltage was increased. We found that decarbonylation was rather delocalised and hence also possible for lateral distances of several nm between tip and molecule. Because of the nonlocality of the process, we tentatively propose that it is mediated by hot interface-state charge carriers[22,64–66], without excluding an influence of the electric field on the dissociation barriers. A detailed study of the reaction mechanisms of the different induced reactions goes beyond the scope of this chapter. For different reactions we observed different voltage thresholds that increased with the number of decarbonylated groups. The voltage threshold for decarbonylation, at positive voltage polarity and typical currents on the order of pA, increased from about +1.5 V for the first decarbonylation ($C_{24}O_6$ → $C_{22}O_4$) to about +2.5 V for the final, third decarbonylation ($C_{20}O_2$ → C_{18}).

The most successful conditions for decarbonylation involved large tip-sample distances (small currents, i.e., $I < 1$ pA) and bias voltages of about +3 V. In most cases, two, four or six CO molecules were removed with one voltage pulse, such that either the product cyclo[18]carbon or an intermediate, with an even number of COs still attached, was formed. The most abundantly formed intermediates were those with either one or two intact masking groups still attached. Other molecules less frequently created from $C_{24}O_6$ by voltage pulses are shown in Figure 2.13. Less common intermediates in which the AFM image suggests that in two masking groups a single CO unit was removed to generate two monoketenes and subsequent rearrangement of the polyynic region to reveal an additional triple bond are summarised as 'rare intermediates' (Figure 2.13, A to H). Rare cyclic reaction products that could not be further manipulated are indicated as 'rare final products' (Figure 2.13, I to L). Reactions in which the cyclic unit was broken are indicated as 'non-cyclic products' (Figure 2.13, M to O).

Atom manipulation of the $C_{24}O_6$ and its intermediates not only led to the formation C_{18} or rare intermediates but also led to covalent fusion between molecules, this will be discussed in the next section.

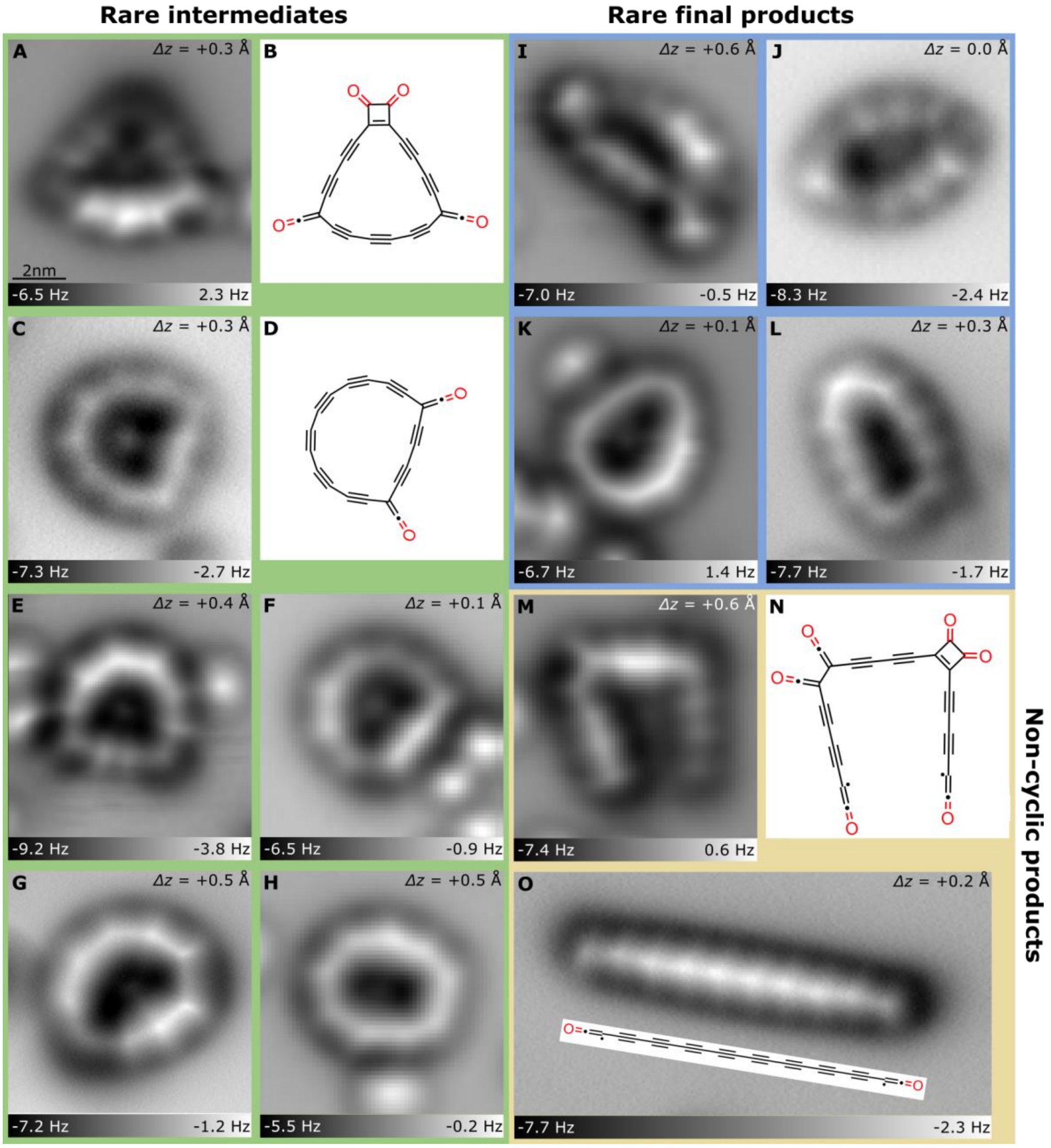

Figure 2.13 Molecules less commonly formed by atom manipulation. (**A**, **C**, **E**–**M**, **O**) AFM images and (**B**, **D**, **N**, **O**) chemical structures. (A–H) Less common intermediates, summarised as 'rare intermediates' in the reaction statistics (Table 2.1). B and D show the assigned structure of the molecules shown in A and C. In these the removal of 2 CO and 4 CO from $C_{24}O_6$, generated different $C_{22}O_4$ and $C_{20}O_2$ isomers compared to the ones described above. (I–L) AFM images of cyclic molecules that did not react further upon voltage pulses. In the reaction statistics, molecules of this kind are summarised as 'rare final products'. (M–O) Products in which a bond within the cyclic unit was broken. (N) shows the assigned structure to the molecule shown in M. (O) shows an AFM image of a linear polyyne chain with the assigned structure shown in the inset. In the reaction statistics, molecules of this kind are summarised as 'non-cyclic products'. Δz is given with respect to the STM set point of $V = 0.2$ V and $I = 0.5$ pA in A, F, H, K and O; $V = 0.2$ V and $I = 0.8$ pA in C and L; $V = 0.15$ V and $I = 0.6$ pA in E; $V = 0.2$ V and $I = 1$ pA in G; $V = 0.1$ V and $I = 0.7$ pA in I; $V = 0.3$ V and $I = 0.5$ pA in J; $V = 0.1$ V and $I = 0.5$ pA in M.

2.4.5 Covalently fused molecules

The high reactivity of cyclo[18]carbon and its oxides makes them promising candidates for on-surface covalent molecular fusion by atom manipulation, of which very few previous examples have been reported[23]. Applying an elevated bias voltage near two proximate molecules led to their fusion. For example, the two neighboring cyclocarbon oxide intermediates, $C_{20}O_2$ and $C_{22}O_4$ (Figure 2.14A), were fused in this way. After constant-current imaging at a set point of $V = 3$ V and $I = 0.5$ pA, the molecules reacted through a [4+2] cycloaddition, as revealed by the AFM resolved structure of the product shown in Figure 2.14C.

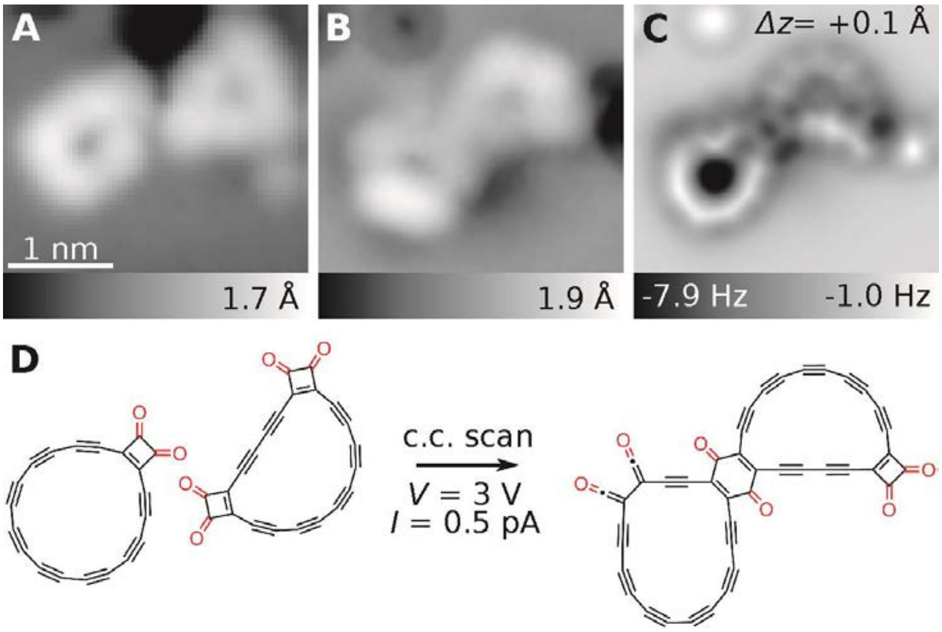

Figure 2.14 Molecular fusion by atom manipulation. (**A**) STM image of two neighbouring intermediates, identified as $C_{22}O_4$ and $C_{20}O_2$. Imaging the area at constant current (c.c.) with a set point of $V = 3$ V, $I = 0.5$ pA resulted in the reaction between the molecules. (**B**, **C**) STM and AFM image of the resulting fused molecule, respectively. (**D**) Proposed reaction scheme.

The nonlocality of the process suggests that it is mediated by hot interface-state charge carriers[22,64–66].We hypothesise that the potential mechanism for the reaction shown in Figure 2.14 involves one of the cyclobutene-1,2-dione groups of $C_{22}O_4$ undergoing a 4-electron electrocyclic ring opening to form a bisketene moiety (Figure 2.15). This then undergoes a [4+2] cycloaddition with the triple bond of $C_{20}O_2$ to form the benzoquinone product.

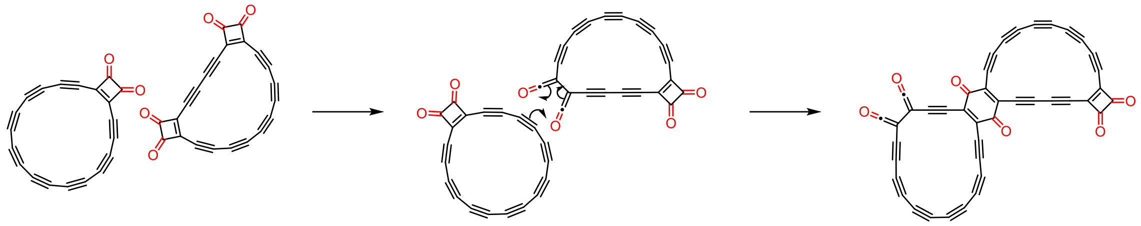

Figure 2.15 . Proposed mechanism for the fusion reaction between $C_{20}O_2$ and $C_{22}O_4$.

Figure 2.16 depicts the formation of a large ring with at least one unknown side group by atom manipulation. Figure 2.16A shows an STM overview image before the ring was formed. The employed $C_{24}O_6$ precursor (Figure 2.16B) is highlighted by a yellow box. Voltage pulses of $V = 2.4$ V and $V = 3.5$ V, respectively, were applied atop the molecule, resulting in partial decarbonylation (Figure 2.16, C to F). Eventually, the molecule shown in Figure 2.16, G and H was found in the area marked by the green box in Figure 2.16A. Upon scanning with an elevated bias voltage ($V = 3.7$ V, $I = 1$ pA), the molecule jumped away. The fused molecule shown in Figure 2.16, I to N was found close to the molecule marked by the red circle in Figure 2.16A. Figure 2.16, I to K show STM images and AFM images at two different tip-sample distances, from which the suggested structure shown in Figure 2.16 L is inferred. HOMO and LUMO densities of the fused cyclic molecule are shown in Figure 2.16, M and N.

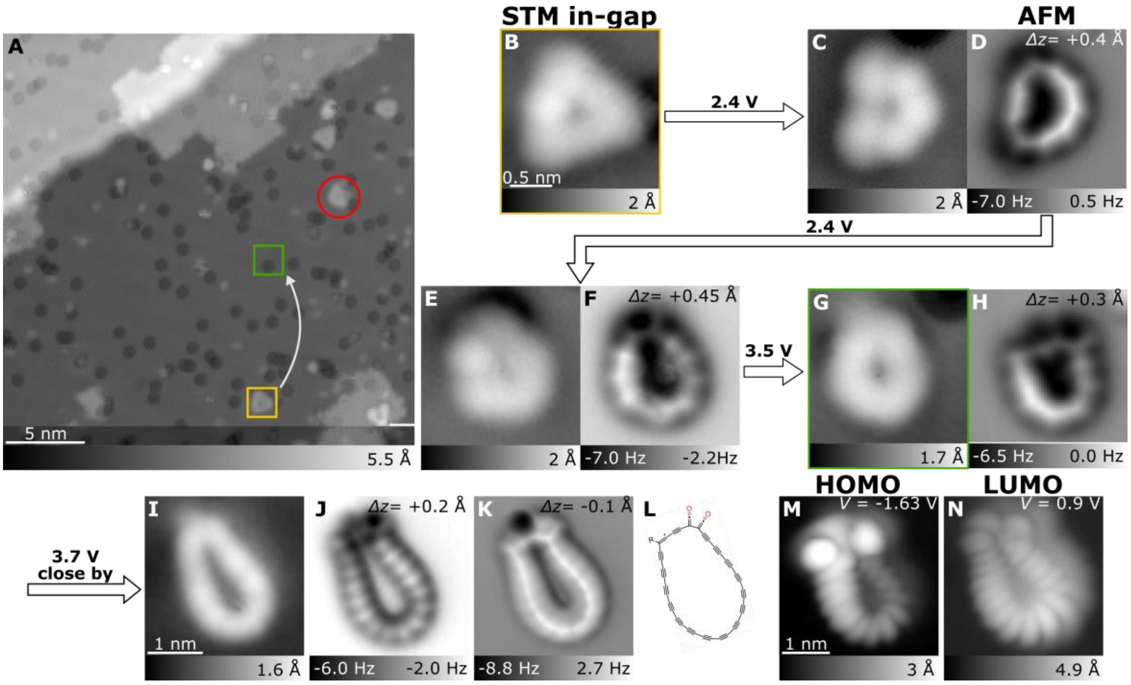

Figure 2.16 Pathway for the reaction of two adjacent molecules. (**A**) STM overview (V = 0.6 V and I = 0.5 pA). The yellow box marks the $C_{24}O_6$ precursor, shown in (**B**) that was chemically altered by applying voltage pulses/scanning at elevated bias voltages. Upon applying elevated bias voltages, the molecule was partially decarbonylated, as indicated by the consecutive STM and AFM images (**C**–**H**). The voltages used to chemically alter the molecule are indicated above the arrows. During decarbonylation, the molecule jumped several times and eventually landed in the area marked by the green box in (A). In the last step, the molecule jumped and most likely reacted with the molecule marked by the red circle in (A), yielding the molecule shown in (**I**–**K**). (**L**) Suggested structure and (**M**, **N**) STM orbital density maps recorded at the PIR and NIR (at I = 1 pA), respectively, of the molecule shown in (I–K). The scale bars in (B, I, M) apply to all following images, respectively. (B–F) and (I–K) were recorded using a set point of V = 0.2 V and I = 0.5 pA, for (G–H) V = 0.2 V, I = 1 pA was used.

In addition to molecules fused by atom manipulation, we also found fused molecules on the surface which had likely reacted during the sublimation and adsorption process. Figure 2.17 shows a molecule that was found on the surface, where no voltage pulses had been applied. The AFM contrast suggests that this molecule was formed by coalescence of three partially decarbonylated precursor molecules. STM orbital density images (Figure 2.17, C and D) reveal that the π-system is delocalised over the entire molecule.

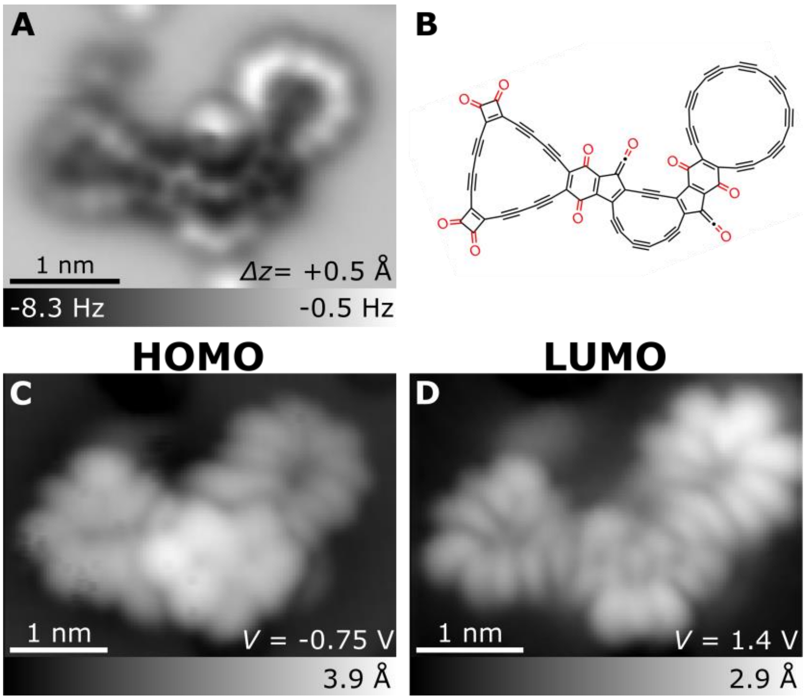

Figure 2.17 Larger fused molecule. (**A**) AFM image of molecule found like this on the surface. Δz is given with respect to the STM set point of $V = 0.2$ V and $I = 0.7$ pA. (**B**) Tentatively assigned structure of the molecule with a molecular formula of $C_{64}O_{10}$. The molecule could have resulted from the reaction $C_{24}O_6 + C_{20}O_2 + C_{20}O_2$. (**C**, **D**) STM orbital density images of the same molecule recorded at the PIR and NIR, respectively, at $I = 0.7$ pA. Delocalisation of the orbital densities over the entire molecule indicate a delocalised π-system.

These results demonstrated that the strained polyynic moieties of cyclo[18]carbon and its oxide intermediates allowed covalent coupling by atom manipulation. Further molecular characterisation of products formed *via* atom manipulation was obtained via STM images within the fundamental gap and at the ion resonances, as discussed in the next section.

2.4.6 STM Data

For electronic structure characterisation, STM images were recorded within the fundamental gap (denoted as in-gap), see Figure 2.18. For the $C_{24}O_6$ precursor, the in-gap STM image (Figure 2.18C) shows a bright feature in the centre of the upper left side. This protrusion in the in-gap STM image was found in all imaged $C_{24}O_6$ molecules. It always corresponded to the bright side visible in the AFM images and therefore probably relates to the side of the molecule that has the largest adsorption height. For cyclo[18]carbon, the in-gap STM shows four-fold symmetry with four protrusions, leading to a square-like shape (Figure 2.18L). The diagonals of the square were always aligned with non-polar directions of the (100)-oriented NaCl surface. The four-fold contrast we assign to the influence of the underlying four-fold symmetric NaCl surface.

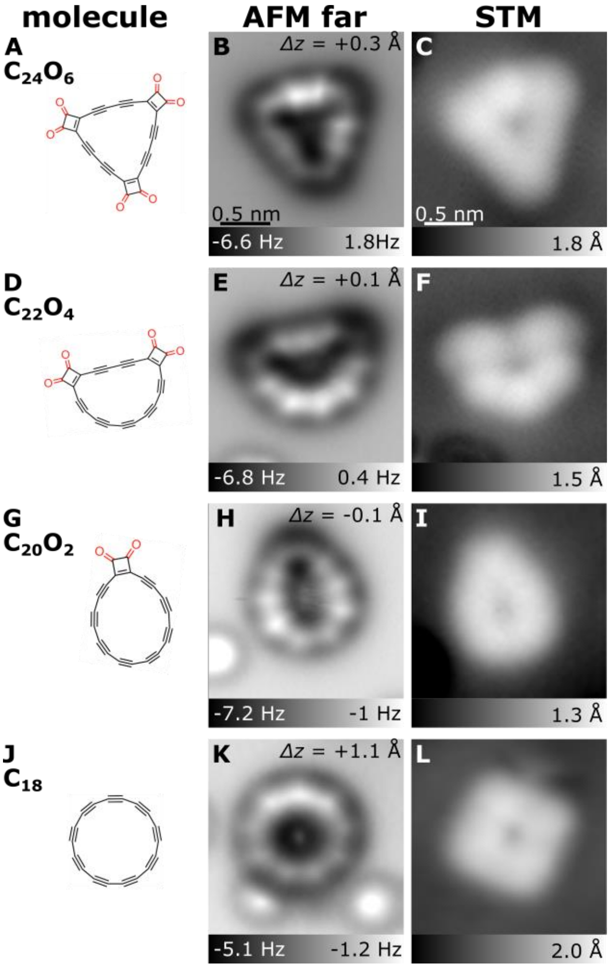

Figure 2.18 STM contrast of precursors and products. The structures (1st column) and AFM data (2nd column) are reproduced from Figure 2.8. The 3rd column shows complementary STM data of the same molecules in that row, respectively. STM images were recorded in constant-current mode at $I = 0.5$ pA, $V = 0.2$ V (C, F, I) and $I = 0.7$ pA, $V = 0.1$ V (L). The same scale bar as in (B) and (C) applies to all AFM and all STM images, respectively. All measurements are obtained with CO-functionalised tips.

The positive and negative ion resonances (PIR/NIR) for the precursor and two most abundant intermediates were recorded, Figure 2.19. The orbital density images of precursor and intermediates (Figure 2.19) show qualitatively different contrast and different nodal planes for PIR and NIR, indicating that these molecules are in a closed shell configuration and thus charge neutral when imaging within the gap. Thus, we can assign the STM image recorded at the PIR to the density of the HOMO (recorded at negative bias voltage) and the NIR to the density of the LUMO (at positive bias voltage). For cyclo[18]carbon, imaging of the ion resonances was not possible due to its charge bistability. Charge-state switching to the negative charge state was observed for positive bias, $V > 0.6$ V. At negative bias we did not observe a resonance for cyclo[18]carbon up to sample voltages of $V < -1.5$ V and the molecule was not stable (jumped on the surface) for increased negative voltages.

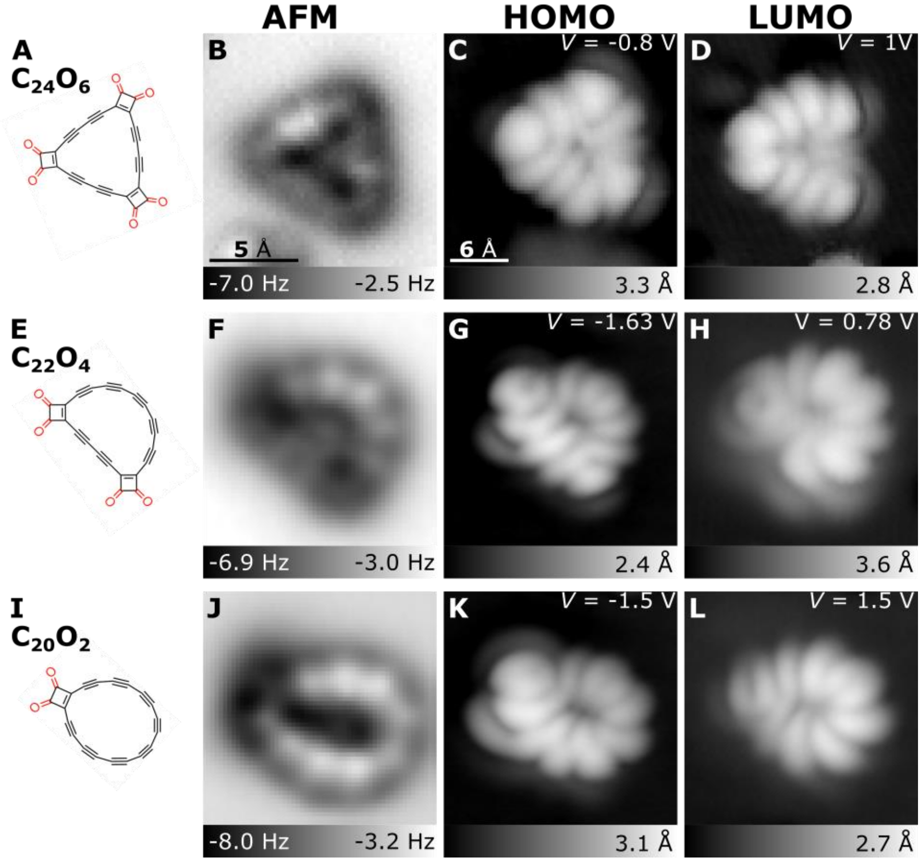

Figure 2.19 Orbital density maps. Molecular structures (first column), AFM images (second column) and STM orbital density images (third and fourth column) of the cyclo[18]carbon precursors (**A**–**D**) $C_{24}O_6$ (STM at $I = 1$ pA), (**E**–**H**) $C_{22}O_4$ (STM at $I = 0.5$ pA) and (**I**–**L**) $C_{20}O_2$ (STM at $I = 0.5$ pA). The images acquired at the first resonance at negative bias voltage are interpreted as density of the HOMO, while the images acquired at the first resonance at positive bias voltage are interpreted as density of the LUMO.

The orbital densities of the precursor and two most abundant intermediates were calculated (Figure 2.20) using DFT calculations with the HSE hybrid functional. They show qualitative agreement with the observed orbital density images.

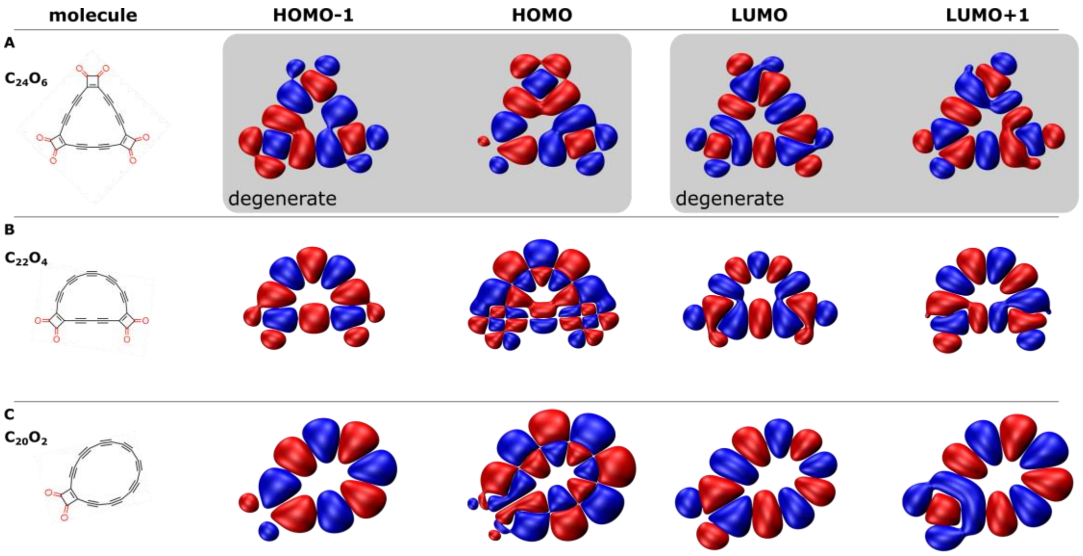

Figure 2.20 Calculated orbital density maps. Electron densities of the two highest occupied molecular orbitals (HOMO-1 and HOMO) and lowest unoccupied molecular orbitals (LUMO and LUMO+1) of the cyclo[18]carbon precursors (**A**) $C_{24}O_6$, (**B**) $C_{22}O_4$ and (**C**) $C_{20}O_2$ in the gas phase. The DFT calculations were carried out using the HSE hybrid functional.

Figure 2.21 shows a cyclo[18]carbon molecule adsorbed directly next to a $C_{24}O_6$ precursor molecule. Both molecules are not covalently linked, as is apparent from the AFM images at different tip-sample distances (Figure 2.21, A to C). At $V = -0.8$ V ($V = +1.3$ V), the onset of the PIR (NIR) of $C_{24}O_6$ is reached, leading to an increase in tunneling current at this voltage at the positions of large densities of the HOMO (LUMO) above the $C_{24}O_6$ molecule in constant-height STM images (Figure 2.21, E to F). No contrast (no tunneling current) is measured above cyclo[18]carbon in these image demonstrating that the onset of PIR and NIR for cyclo[18]carbon lies outside of these voltage limits.

Further structural characterisation of cyclo[18]carbon and its intermediates was obtained *via* DFT calculations of their structures and analysis of the symmetry and bond length alternation obtained. This will be discussed in the next section.

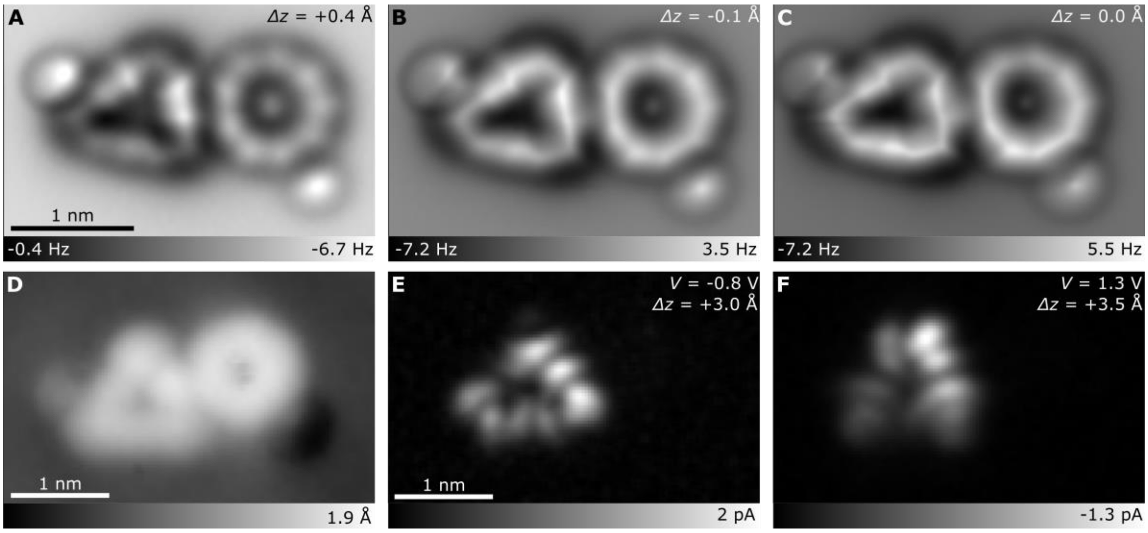

Figure 2.21 Comparative measurements of $C_{24}O_6$ precursor and cyclo[18]carbon. (**A**–**C**) AFM and (**D**–**F**) STM images of a $C_{24}O_6$ precursor and a cyclo[18]carbon molecule adsorbed adjacent to each other. The bright features in the AFM images next to the molecule stem from adjacently adsorbed CO molecules. (D) In-gap constant-current STM image at $V = 0.13$ V and $I = 0.5$ pA. (E, F) Constant-height STM images obtained at the onset of the PIR and NIR of the $C_{24}O_6$ precursor, respectively. In the images recorded in constant-height mode (A–C, E, F), Δz corresponds to the tip-height offset with respect to an STM set point of $V = 0.2$ V and $I = 0.5$ pA.

2.4.7 DFT Calculations

Density functional theory (DFT) calculations were carried out using the all-electron code FHI-aims[67]. Two different approximations to the exchange-correlation (x-c) functional were used; the Perdew–Burke-Ernzerhof (PBE) generalised gradient approximation[68] and the Heyd–Scuseria–Ernzerhof (HSE) hybrid functional[69]. The mixing parameter that controls the amount of exact exchange in HSE was set to 0.8. The Tkatchenko-Scheffler correction[70] was used to account for van der Waals interactions. For calculations using PBE, we employed the default 'very tight' settings for the atomic basis sets, while for HSE the default 'tight' settings were employed. All molecules were calculated in the gas phase, and the structures were relaxed until the forces acting on atoms were smaller than 10^{-3} e V Å^{-1}.

We obtained different results using the two different x-c functionals. Independent of the starting geometry, the PBE calculations for cyclo[18]carbon converged to a cumulenic structure with 18-fold symmetry and equal bond length of all C=C bonds of 1.284 Å. In contrast, the HSE calculations for cyclo[18]carbon always converged to a nine-fold symmetry with alternating short (1.195 Å) and long (1.343 Å) bonds, i.e., a polyynic structure.

For the intermediates ($C_{22}O_4$, $C_{20}O_2$) we obtained different results with the two x-c functionals as well. The HSE functional yielded similar bond-length alternation (BLA) for the different length polyynic segments in the different molecules ($C_{24}O_6$, $C_{22}O_4$, $C_{20}O_2$, C_{18}) and larger BLA compared to calculations with PBE. For the PBE functional, we observed that the BLA monotonically decreases with the length of the polyynic chain in the molecules $C_{24}O_6$, $C_{22}O_4$, $C_{20}O_2$ and vanishes for cyclo[18]carbon.

The atomic coordinates from these DFT calculations were used as the input for AFM simulations that were used to confirm the structures of cyclo[18]carbon and the most common intermediates by comparison with their high-resolution AFM images.

2.4.8 AFM Simulations

AFM images acquired with CO-functionalised tips can be efficiently simulated *via* a well-established molecular-mechanics model (see Section 1.3.7) that takes into account the flexibility of the CO molecule at the tip apex[49,56]. The interaction of the tip with the sample is modelled *via* classical force fields and the CO at the tip is relaxed. We simulated AFM images for the precursor $C_{24}O_6$, the partially decarbonylated intermediates ($C_{22}O_4$, $C_{20}O_2$) as well as the final product cyclo[18]carbon using the Probe-Particle code implemented by Hapala *et al.*[49]. This code also allows electrostatic interactions to be included by assigning a charge to the CO molecule and letting it interact with the Hartree potential of the sample.

As input for the AFM simulation, we used the atomic coordinates from the DFT gas-phase structure optimisation as well as the corresponding DFT Hartree potential. For all AFM simulations, we used a lateral spring constant for the CO at the tip of 0.2 N/m and an electrostatic monopol on the oxygen of –0.05 e[71] and the experimental oscillation amplitude $A = 50$ pm.

Figure 2.22 shows simulated AFM images for the various molecules at different tip-sample distances, where Δz is defined as previously, i.e., positive Δz values correspond to an increase in the tip-sample distance. All images have been calculated using the results obtained from the HSE x-c functional as input, except the bottom row which was calculated based on the PBE x-c functional results. The (HSE-based) simulated images for the pristine precursor $C_{24}O_6$ (Figure 2.22A) show very good agreement with the experimental images, with two bright lobes on each of the three sides of the triangular carbon backbone. Each of the bright lobes can be ascribed to one of the triple bonds. For the two intermediates $C_{22}O_4$ and $C_{20}O_2$ (Figure 2.22B and Figure 2.22C, respectively) the agreement with experimental data is very good as well. At large and medium tip-sample distances ($\Delta z > 0.3$ Å), the AFM simulations show five bright lobes at the longer bend part of the molecule for $C_{22}O_4$ and eight lobes for $C_{20}O_2$, which again correspond to the triple bonds. Because for the AFM simulations the optimised gas-phase geometry was used as an input, the simulation does not account for non-planar adsorption geometries. Therefore, all sides of the molecule exhibit equal contrast. Additionally, the CO moieties appear brighter compared to the experimental AFM images since they are not bent down towards the surface in the geometry that was used for simulating the AFM images.

The simulated HSE-based AFM images for the final product cyclo[18]carbon (Figure 2.22D) show nine lobes at large and medium tip-sample distances (see Figure 2.22D, $\Delta z >$ 0.3 Å), which form a ring and can be associated with the nine triple bonds of the polyynic structure. At small tip-sample distances (Figure 2.22D, $\Delta z < 0.3$ Å), the AFM image of the molecule resembles a nonagon due to bending of the CO at the tip apex[49,56] (a similar change in contrast at small tip-sample distances occurs for the other molecules shown in Figure 2.22, A to C). The AFM contrast for all molecules and all tip heights, using the results of the HSE x-c functional as inputs, are in excellent agreement with the experimental observations. Again, the simulation does not account for a non-planar adsorption geometry. Hence, the differences in brightness between two opposing sites of the molecules resulting from the non-planarity of the molecule with respect to the surface are not reproduced in the simulations. For comparison, Figure 2.22E shows simulated AFM images based on the results obtained with the PBE x-c functional, i.e., for cumulenic cyclo[18]carbon. They show only a featureless ring, independent of the tip-sample distance, in contrast to the experimental images. Thus, the AFM simulations confirm our interpretation of the experimental data that cyclo[18]carbon adopts a polyynic structure on NaCl.

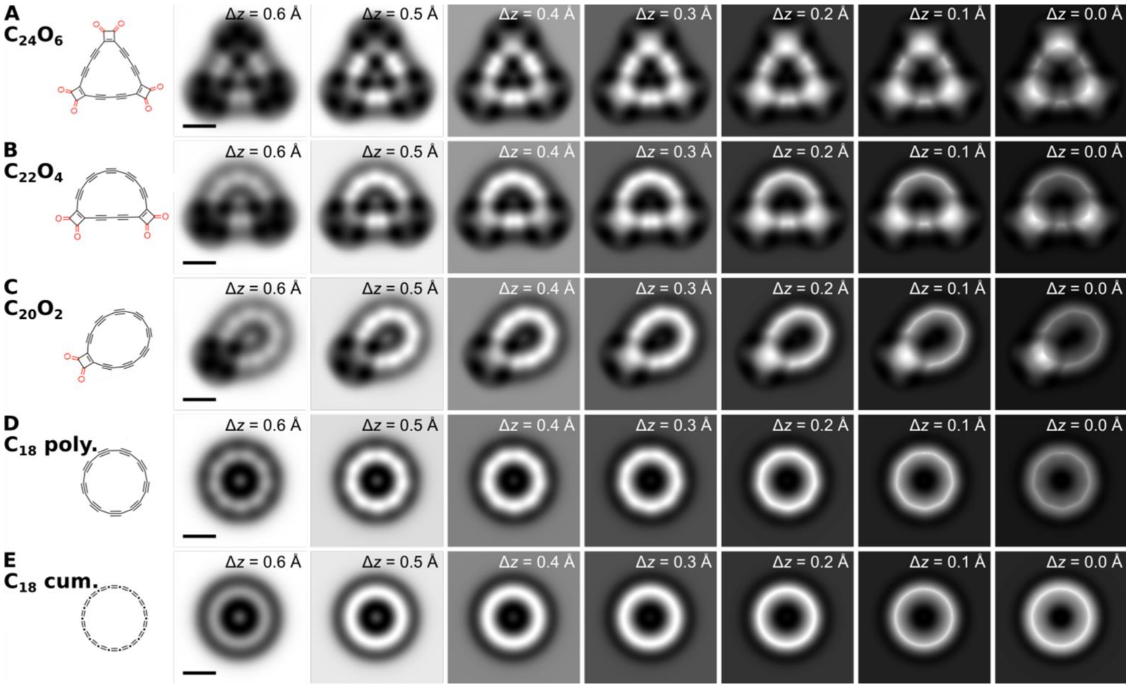

Figure 2.22 AFM simulations. Chemical structure and simulated AFM images at different tip-sample distances for the pristine precursor $C_{24}O_6$ (**A**), the intermediates $C_{22}O_4$ (**B**) and $C_{20}O_2$ (**C**) as well as polyynic cyclo[18]carbon (**D**) and cumulenic cyclo[18]carbon (**E**). The molecular structure was optimised by DFT using either the HSE x-c functional (A–D) or the PBE x-c functional (E). Δz values correspond to the increase in tip-sample distance. The scale bar is 5 Å and all images have the same scale.

2.5 Conclusions

Our results provide the first direct experimental insight into the structure of a cyclo[18]carbon. Cyclo[18]carbon was generated using atom manipulation on bilayer NaCl on Cu(111) at 5 K by eliminating carbon monoxide from a cyclocarbon oxide molecule, $C_{24}O_6$. Characterisation of cyclo[18]carbon by high-resolution atomic force microscopy revealed a nine-fold symmetric polyynic structure with alternating triple and single bonds. We confirmed that in the nine-fold symmetric form cyclo[18]carbon is uncharged but that it is able to exhibit charge bistability on this surface. The yield of formation of cyclo[18]carbon by atom manipulation was calculated as 13%. The high reactivity of cyclocarbon and cyclocarbon oxides allowed covalent coupling between molecules to be induced by atom manipulation, opening an avenue for the synthesis of other carbon allotropes and carbon-rich materials from the coalescence of cyclocarbon molecules. We confirmed the characterisation of $C_{24}O_6$ and its intermediates and the reaction product cyclo[18]carbon by STM imaging in the fundamental gap and at the ion resonances for $C_{24}O_6$ and its intermediates. We performed DFT calculations and AFM simulations to further confirm the identity of these species. In conclusion, our results provide direct experimental insights into the structure of a cyclocarbon and open the way to create other elusive carbon-rich molecules by atom manipulation.

2.6 Experimental Data

2.6.1 Synthetic General Methods

Reagents (Alfa Aesar, Aldrich, Acros, Fluorochem, Fisher Scientific) were used without further purification. Dry solvents (THF, Et_2O) for reactions were purified by a MBraun MB-SPS-5-Bench Top under nitrogen (H_2O content < 20 ppm). All other solvents used were HPLC grade. Reactions, unless otherwise stated, were carried out in oven-dried glassware under a N_2 atmosphere. Flash column chromatography was carried out on a Biotage Isolera One with a 200–400 nm UV detector. Analytical thin layer chromatography (TLC) was performed on aluminum sheets coated with silica gel 60 F254 (Merck). UV light (254 nm) was used for visualisation. Evaporation under reduced pressure was performed at 15–40 °C and 5–1010 mbar. Reported yields refer to pure compounds dried under high vacuum (< 0.1 mbar). ^1H and ^{13}C nuclear magnetic resonance (NMR) spectra were recorded on Bruker AVIII HD 400 spectrometer at 400 MHz (^1H) and 101 MHz (^{13}C) at 21 °C. Chemical shifts, δ, reported in ppm downfield from tetramethylsilane using residual deuterated solvent signals as internal reference ($CDCl_3$: $\delta_H = 7.26$ ppm, $\delta_C = 77.16$ ppm; $C_6D_5NO_2$: $\delta_C = 148.50$ ppm). High-resolution mass spectrometry (HR-MS) measurements were performed by the mass spectrometry service at the University of Oxford on a Waters GTC classic.

2.6.2 Synthetic Protocols

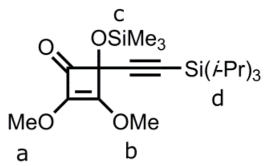

Synthesis of compound 10: *n*-BuLi (4.6 mL, 1.6 M in hexanes, 7.4 mmol) was added to a solution of TIPS-acetylene (1.7 mL, 7.4 mmol) in THF (8 mL) at 0 °C. The clear solution was stirred for 30 minutes and then added over 15 minutes to a dimethyl squarate (1.0 g, 7.0 mmol) solution in THF (30 mL) at –78 °C. After stirring for 1 h at –78 °C, TMS-Cl (1.2 mL, 9.2 mmol) was added and the solution was allowed to warm to 21 °C. The reaction was quenched with a sat. aqueous solution of $NaHCO_3$ (50 mL) and extracted with CH_2Cl_2 to yield **10** as a yellow oil (2.7 g, 6.8 mmol, 95%). ^{1}**H NMR** (400 MHz, $CDCl_3$): 4.17 (s, 3H; **a**/**b**), 3.95 (s, 3H; **a**/**b**), 1.07 (m, 21H; **d**), 0.25 ppm (s, 9H; **c**). ^{13}**C NMR** (101 MHz, $CDCl_3$): 180.3, 165.7, 135.3, 102.6, 91.5, 79.8, 59.8, 58.6, 18.7, 11.3, 1.4 ppm. ^{1}H and ^{13}C NMR were in accordance with reported values[34].

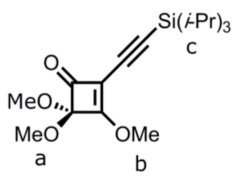

Synthesis of compound 11: MeOTMS (0.98 mL, 7.1 mmol) was added to a solution of **10** (2.7 g, 6.8 mmol) in THF (3 mL). TMSOTf (73 µL, 0.41 mmol) was added dropwise to avoid overheating (an exothermic reaction occurs). The mixture was stirred for 30 minutes at 21 °C and then quenched with a sat. aqueous solution of $NaHCO_3$ (5 mL). The aqueous phase was extracted with CH_2Cl_2 and the organic layer was dried over $MgSO_4$ to yield **11** as a yellow oil (2.0 g, 6.0 mmol, 89%). ^{1}**H NMR** (400 MHz, $CDCl_3$): 4.37 (s, 3H; **b**), 3.52 (s, 6H; **a**), 1.08 ppm (s, 21H; **c**). ^{13}**C NMR** (101 MHz, $CDCl_3$): 186.4, 184.2, 112.6, 99.8, 95.2, 92.1, 61.3, 53.5, 18.7, 11.4 ppm. ^{1}H NMR and ^{13}C NMR were in accordance with reported values[34].

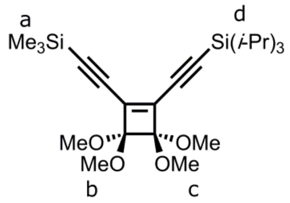

Synthesis of compound 12: *n*-BuLi (4.0 mL, 1.6 M in hexanes, 6.4 mmol) was added to a TMS-acetylene (0.88 mL, 6.4 mmol) solution in Et_2O (15 mL) at 0 °C and stirred for 30 minutes. The resulting clear solution was cooled to –78 °C and a solution of **11** (2.0 g, 6.0 mmol) in Et_2O (25 mL) was added dropwise over 30 minutes and the resulting solution was stirred for 1 h at –45 °C to give a dark red solution. Aqueous HCl (3 M, 20 mL) was added and the solution was stirred vigorously at 25 °C for 1 h. The reaction was quenched with a sat. aqueous solution of $NaHCO_3$ (50 mL) and the resulting organic layer dried over $MgSO_4$ to yield the enediyne as a yellow oil (2.39 g, 5.91 mmol) which was used without further purification. MeOTMS (2.9 mL, 21.3 mmol) was added to enediyne (2.39 g, 5.91 mmol) followed by addition of

TMSOTf (0.13 mL, 0.74 mmol). The resulting brown solution was stirred for 60 h at 21 °C. The reaction was quenched with a sat. aqueous solution of $NaHCO_3$ (5 mL). The aqueous phase was extracted with CH_2Cl_2 and the organic layer was dried over $MgSO_4$ and purified by column chromatography, SiO_2 (petroleum ether/ethyl acetate 8:2) to yield **12** as a yellow oil (2.0 g, 4.5 mmol, 75% over two steps). **^{1}H NMR** (400 MHz, $CDCl_3$): 3.51 (s, 6H; **c**/**b**), 3.50 (s, 6H; **b**/**c**), 1.08 (s, 21H; **d**), 0.18 ppm (s, 9H; **a**). **^{13}C NMR** (101 MHz, $CDCl_3$): 136.3, 136.0, 110.1, 108.3, 108.2, 107.5, 98.1, 96.0, 52.2, 52.1, 18.7, 11.3, –0.3 ppm. **HR-ESI-MS**: 419.24251 (mass corresponds to $(M+H)^+$–MeOH, $C_{23}H_{39}O_3Si_2^+$: 419.24322) **IR (ATR): $\tilde{\nu}$** = 678, 761, 846, 883, 896, 919, 985, 1039, 1081, 1179, 1206, 1258, 1384, 1463, 1771, 2138, 2836, 2866, 2943 cm^{-1}.

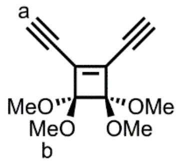

Synthesis of compound 13: Tetrabutylammonium fluoride (2.2 mL, 1.0 M in THF, 2.2 mmol) was added to a solution of **12** (1.0 g, 2.2 mmol) in THF (40 mL) and water (0.5 mL) at –78 °C. The resulting dark red solution was then stirred for 30 minutes. The reaction was quenched with water and the aqueous phase extracted with Et_2O (50 mL). The organic layer was washed with brine (50 mL) and dried over $MgSO_4$ to yield the crude product as a red oil. Purification by column chromatography, SiO_2 (petroleum ether/ethyl acetate 7:3) gave **13** (456 mg, 2.05 mmol, 93%) as an unstable red oil that was used immediately in the next step. **^{1}H NMR** (400 MHz, $CDCl_3$): 3.73 (s, 2H; **a**), 3.50 (s, 12H; **b**) ppm. **^{13}C NMR** (101 MHz, $CDCl_3$): 136.3, 108.2, 91.2, 74.9, 52.1 ppm. **HR-ESI-MS:** 245.07852 (mass corresponds to $C_{12}H_{14}O_4Na^+$: 245.07843). **IR (ATR): $\tilde{\nu}$** = 650, 812, 870, 983, 1030, 1078, 1179, 1199, 1257, 1440, 2103, 2838, 2944, 3243 cm^{-1}.

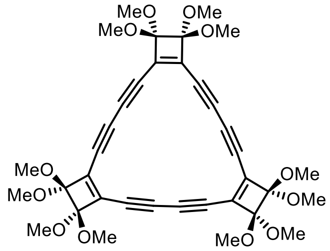

Synthesis of compound 14: Freshly prepared CuCl[72] (5.0 g, 51 mmol) was stirred in acetone (50 mL) under N_2. TMEDA (2.7 mL, 18 mmol) was added to this suspension and the resulting opaque, pale blue solution was stirred for 30 minutes. The solid was allowed to settle and the supernatant solution (15.0 mL, 5.29 mmol) withdrawn and immediately added to a vigorously stirred solution of **13** (1.15 g, 5.17 mmol) in acetone (300 mL) at 21 °C with a $CaCl_2$ drying tube and under an O_2 atmosphere for 2 h. Upon completion the reaction was diluted with $CHCl_3$ (300 mL) and the organic phase washed with water (2 × 600 mL). The organic extracts were combined and dried over $MgSO_4$ and the solvent removed *in vacuo* at 30 °C. The crude was purified by column chromatography, SiO_2 (petroleum ether/ethyl acetate 8:2) to yield **14** as a yellow solid (76 mg, 0.12 mmol, 7%). Single crystals of **14** were grown by layer diffusion of CH_2Cl_2/ hexane to yield yellow, needle like, crystals. **^{1}H NMR** (400 MHz, $CDCl_3$): 3.70 (s, 36H) ppm. **^{13}C NMR** (101 MHz, $CDCl_3$): 139.7, 109.9, 90.3, 82.1, 52.6 ppm. **MALDI-TOF m/z:** 629.308, (mass corresponds to $C_{35}H_{33}O_{11}^+$: 629.202). **IR (ATR):** $\tilde{\nu}$ = 625, 881, 982, 1034, 1083, 1180, 1209, 1252, 1457, 1560, 1742, 2836, 2940 cm^{-1}. **M.p.:** decomposes at ≈ 200 °C. **UV/vis ($CHCl_3$): λ_{max} (ε) =** 403 (16100), 393 (12900), 345 (78100), 328 nm (42200 M^{-1} cm^{-1}).

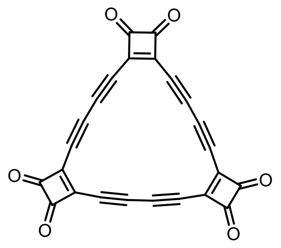

Synthesis of compound $C_{24}O_6$: All reaction vessels were kept under nitrogen and wrapped with aluminum foil to exclude light. Concentrated H_2SO_4 (0.2 mL) was dropped onto **14** (10 mg, 0.015 mmol) to form a dark orange emulsion which was stirred for 5 minutes at 21 °C. Then, $(CH_2Cl)_2$ (10 mL) was added and the resulting solution stirred vigorously for 10 minutes. The clear orange organic phase was transferred *via* syringe to a flask containing $CaCO_3$ (0.4 g). The extraction with $(CH_2Cl)_2$ was repeated until the organic extracts were colourless. The combined organic phases were filtered with 0.45 μm PTFE syringe filters to yield a clear orange solution. The solvent was removed *in vacuo* and crude material was dried under high vacuum in the dark to yield $C_{24}O_6$ as an unstable, light sensitive yellow solid which was stored in the dark at –20 °C (5.6 mg, 0.014 mmol, 96%). The crude could be recrystallised from a mixture of 1,2-dichloroethane, pentane to yield

$C_{24}O_6$ as a brown crystalline solid. **^{13}C NMR** (101 MHz, $C_6D_5NO_2$): 192.3, 180.7, 107.7, 84.5 ppm. **IR (ATR): $\tilde{\nu}$** = 804, 1028, 1103, 1403, 1541, 1788 (strong), 2117 cm^{-1}. **M.p.:** decomposes at ≈ 200 °C (Note this compound has been previously reported to explode violently above 85 °C). **UV/vis ($CHCl_3$): λ_{max} (ε)** = 438 (19300), 430 (19300), 381 (98600), 360 (50400), 355 (50400), 335 (26300), 316 (15200), 271 nm (31900 M^{-1} cm^{-1}). ^{13}C NMR, IR and UV-Vis spectra match that of the literature[18].

2.6.3 Selected NMR Spectra

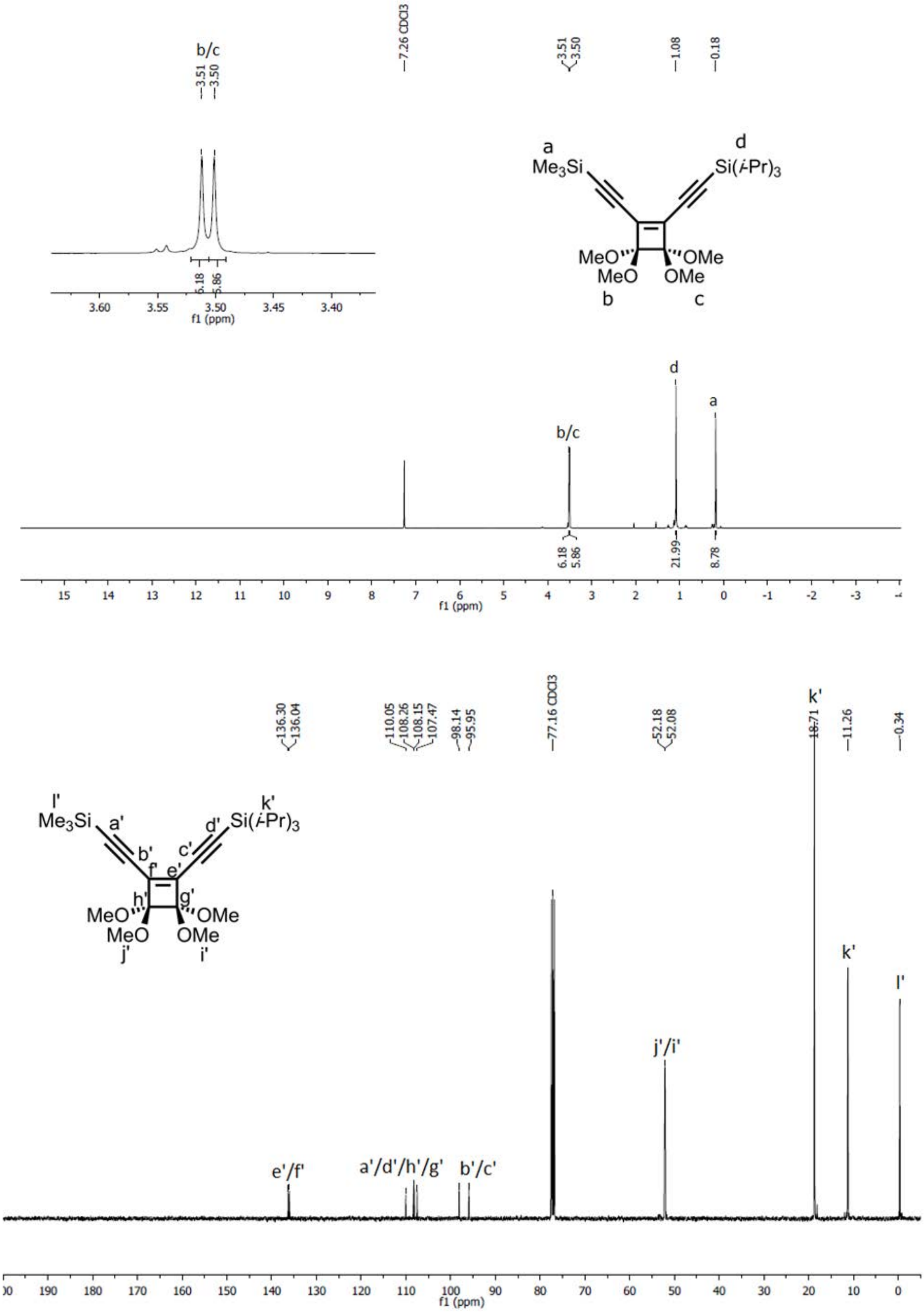

Figure 2.23 ^{1}H NMR (400 MHz, CDCl$_3$, 294 K) and ^{13}C NMR (101 MHz, CDCl$_3$, 294 K) spectra of **12**.

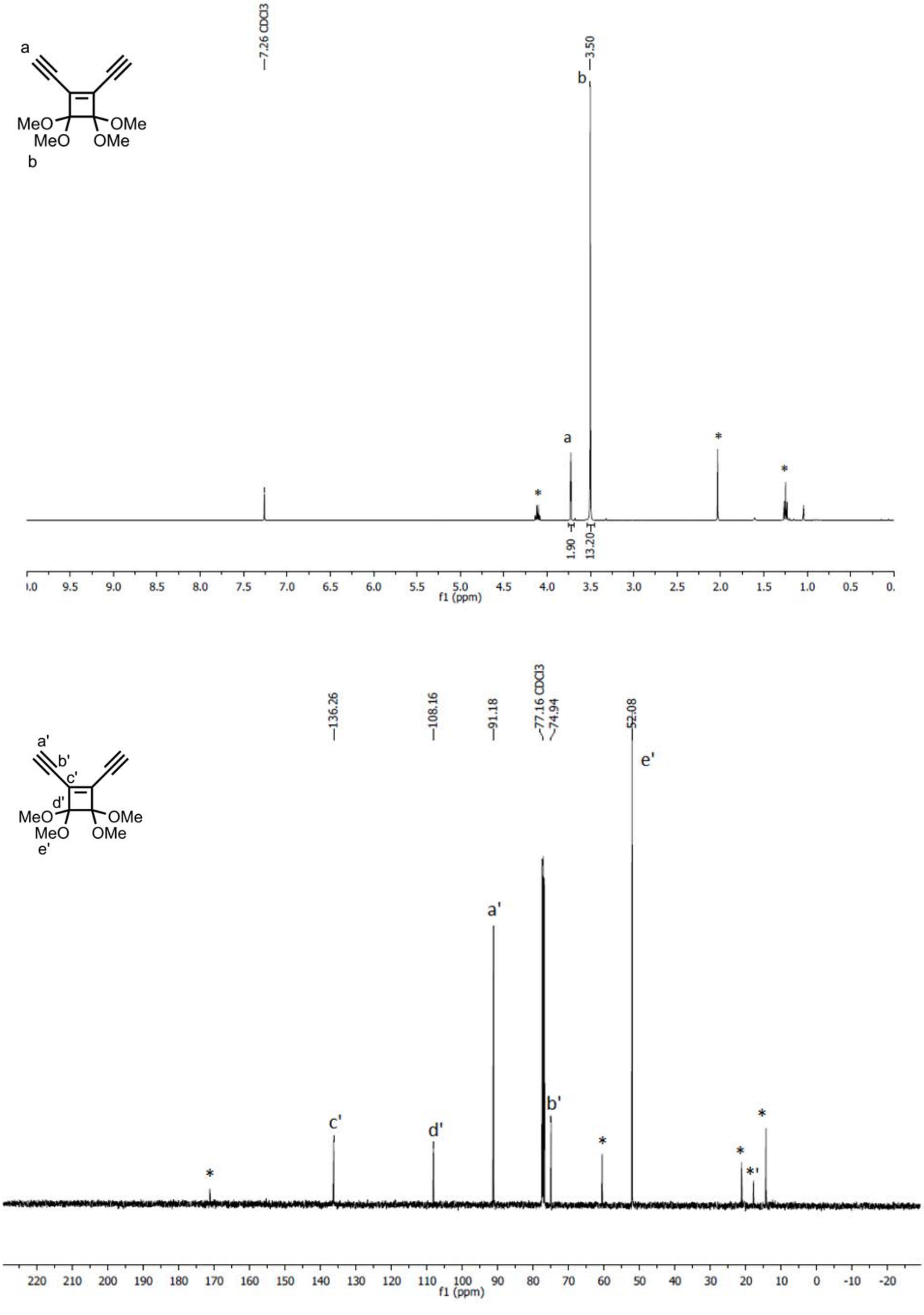

Figure 2.24 ^{1}H NMR (400 MHz, $CDCl_3$, 294 K) and ^{13}C NMR (101 MHz, $CDCl_3$, 294 K) spectra of **13**. Residual ethyl acetate solvent signals as samples were not completely dried to avoid decomposition. Reaction yield corrected accordingly.

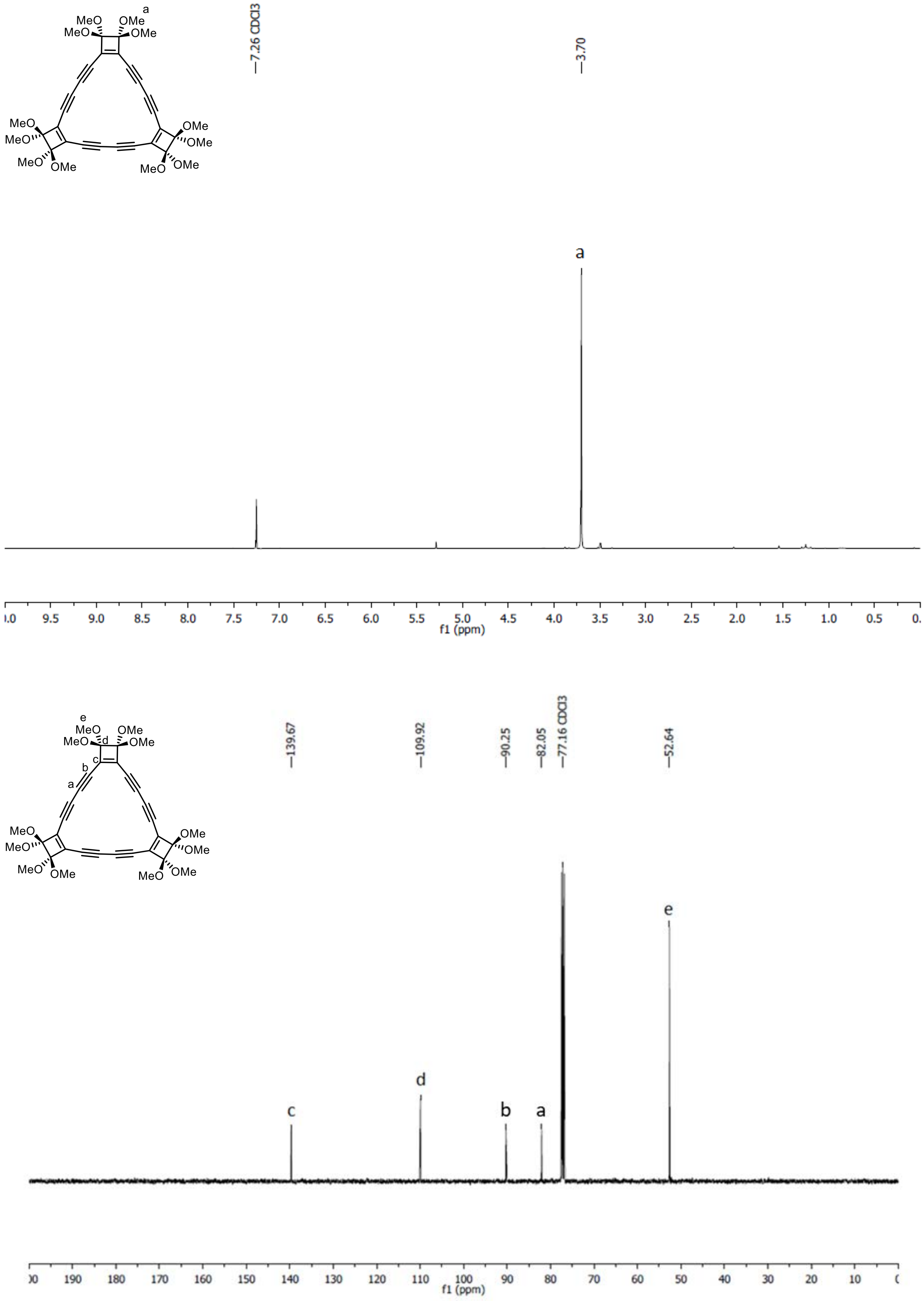

Figure 2.25 ^{1}H NMR (400 MHz, $CDCl_3$, 294 K) and ^{13}C NMR (101 MHz, $CDCl_3$, 294 K) spectra of **14**.

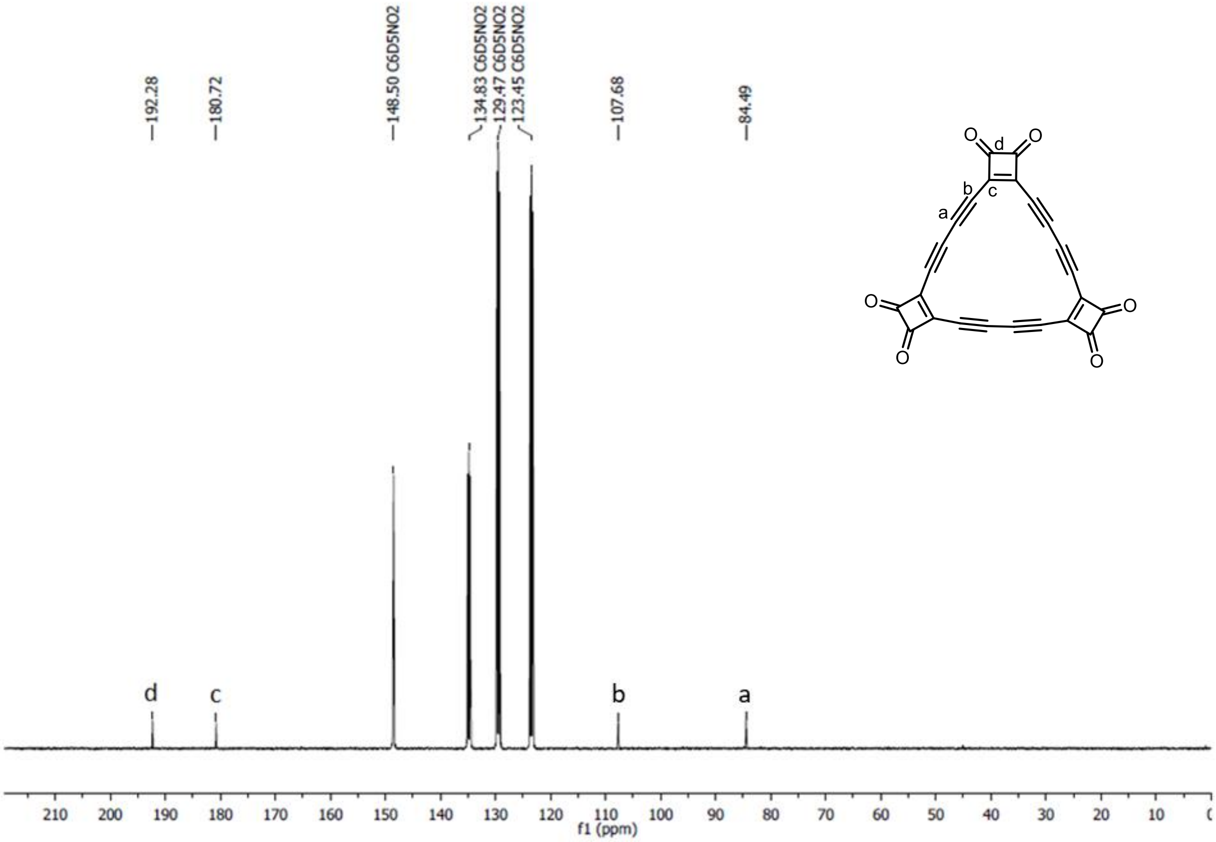

Figure 2.26 ^{13}C NMR spectrum of $C_{24}O_6$ (101 MHz, $C_6D_5NO_2$, 294 K).

2.7 References

[1] K. Kaiser, L. M. Scriven, F. Schulz, P. Gawel, L. Gross, H. L. Anderson, *Science* **2019**, *365*, 1299–1301.

[2] H. W. Kroto, J. R. Heath, S. C. O'Brien, R. F. Curl, R. E. Smalley, *Nature* **1985**, *318*, 162–163.

[3] S. Iijima, T. Ichihashi, *Nature* **1993**, *363*, 603–605.

[4] K. S. Novoselov, A. K. Geim, S. V Morozov, D. Jiang, Y. Zhang, S. V Dubonos, I. V Grigorieva, A. A. Firsov, *Science* **2004**, *306*, 666–669.

[5] F. Diederich, Y. Rubin, C. B. Knobler, R. L. Whetten, K. E. Schriver, K. N. Houk, Y. Li, *Science* **1989**, *245*, 1088–1090.

[6] F. Diederich, M. Kivala, *Adv. Mater.* **2010**, *22*, 803–812.

[7] W. Krätschmer, L. D. Lamb, K. Fostiropoulos, D. R. Huffman, *Nature* **1990**, *347*, 354–358.

[8] R. Hoffmann, *Tetrahedron* **1966**, *22*, 521–538.

[9] S. W. McElvany, M. M. Ross, N. S. Goroff, F. Diederich, *Science* **1993**, *259*, 1594–1596.

[10] G. von Helden, N. G. Gotts, M. T. Bowers, *Nature* **1993**, *363*, 60–63.

[11] V. Parasuk, J. Almlöf, M. W. Feyereisen, *J. Am. Chem. Soc.* **1991**, *113*, 1049–1050.

[12] C. Neiss, E. Trushin, A. Görling, *ChemPhysChem* **2014**, *15*, 2497–2502.

[13] T. Torelli, L. Mitas, *Phys. Rev. Lett.* **2000**, *85*, 1702–1705.

[14] S. Arulmozhiraja, T. Ohno, *J. Chem. Phys.* **2008**, *128*, 114301.

[15] E. Hückel, *Zeitschrift für Phys.* **1932**, *76*, 628–648.

[16] P. W. Fowler, N. Mizoguchi, D. E. Bean, R. W. A. Havenith, *Chem. Eur. J.* **2009**, *15*, 6964–6972.

[17] Y. Rubin, C. B. Knobler, F. Diederich, *J. Am. Chem. Soc.* **1990**, *112*, 4966–4968.

[18] Y. Rubin, M. Kahr, C. B. Knobler, F. Diederich, C. L. Wilkins, *J. Am. Chem. Soc.* **1991**, *113*, 495–500.

[19] Y. Tobe, T. Fujii, H. Matsumoto, K. Naemura, Y. Achiba, T. Wakabayashi, *J. Am. Chem. Soc.* **1996**, *118*, 2758–2759.

[20] A. E. Boguslavskiy, H. Ding, J. P. Maier, *J. Chem. Phys.* **2005**, *123*, 034305.

[21] L. Gross, F. Mohn, N. Moll, P. Liljeroth, G. Meyer, *Science* **2009**, *325*, 1110–1114.

[22] N. Pavliček, L. Gross, *Nat. Rev. Chem.* **2017**, *1*, 0005.

[23] S. W. Hla, L. Bartels, G. Meyer, K. H. Rieder, *Phys. Rev. Lett.* **2000**, *85*, 2777–2780.

[24] J. Repp, G. Meyer, S. Paavilainen, F. E. Olsson, M. Persson, *Science* **2006**, *312*,

1196–1199.

[25] N. Pavliček, P. Gawel, D. R. Kohn, Z. Majzik, Y. Xiong, G. Meyer, H. L. Anderson, L. Gross, *Nat. Chem.* **2018**, *10*, 853–858.

[26] B. Schuler, S. Fatayer, F. Mohn, N. Moll, N. Pavliček, G. Meyer, D. Peña, L. Gross, *Nat. Chem.* **2016**, *8*, 220–224.

[27] N. Pavliček, B. Schuler, S. Collazos, N. Moll, D. Pérez, E. Guitián, G. Meyer, D. Peña, L. Gross, *Nat. Chem.* **2015**, *7*, 623–628.

[28] L. Gross, B. Schuler, N. Pavliček, S. Fatayer, Z. Majzik, N. Moll, D. Peña, G. Meyer, *Angew. Chem. Int. Ed.* **2018**, *57*, 3888–3908.

[29] Y. Rubin, C. B. Knobler, F. Diederich, *J. Am. Chem. Soc.* **1990**, *112*, 4966–4968.

[30] G. A. Adamson, C. W. Rees, *J. Chem. Soc. Perkin Trans. 1* **1996**, 1535–1543.

[31] Y. Tobe, R. Umeda, N. Iwasa, M. Sonoda, *Chem. Eur. J.* **2003**, *9*, 5549–5559.

[32] Y. Rubin, F. Diederich, *J. Am. Chem. Soc.* **1989**, *111*, 6870–6871.

[33] Y. Rubin, C. B. Knobler, F. Diederich, *J. Am. Chem. Soc.* **1990**, *112*, 1607–1617.

[34] Y. Rubin, T. C. Parker, S. J. Pastor, S. Jalisatgi, C. Boulle, C. L. Wilkins, *Angew. Chem. Int. Ed.* **1998**, *37*, 1226–1229.

[35] A. D. Allen, J. D. Colomvakos, F. Diederich, I. Egle, X. Hao, R. Liu, J. Lusztyk, J. Ma, M. A. McAllister, Y. Rubin, et al., *J. Am. Chem. Soc.* **1997**, *119*, 12125–12130.

[36] F. Diederich, Y. Rubin, O. L. Chapman, N. S. Goroff, *Helv. Chim. Acta* **1994**, *77*, 1441–1457.

[37] F. B. Mallory, J. D. Roberts, *J. Am. Chem. Soc.* **1961**, *83*, 393–397.

[38] A. T. Blomquist, E. A. LaLancette, *J. Am. Chem. Soc.* **1961**, *83*, 1387–1391.

[39] Y. Rubin, S. S. Lin, C. B. Knobler, J. Anthony, A. M. Boldi, F. Diederich, *J. Am. Chem. Soc.* **1991**, *113*, 6943–6949.

[40] L. S. Liebeskind, R. W. Fengl, K. R. Wirtz, T. T. Shawe, *J. Org. Chem.* **1988**, *53*, 2482–2488.

[41] L. S. Liebeskind, K. R. Wirtz, *J. Org. Chem.* **1990**, *55*, 5350–5358.

[42] A. S. Hay, *J. Org. Chem.* **1962**, *27*, 3320–3321.

[43] X. D. Zhu, E. Nabighian, *Appl. Phys. Lett.* **1998**, *73*, 2736–2738.

[44] R. Bennewitz, V. Barwich, M. Bammerlin, C. Loppacher, M. Guggisberg, A. Baratoff, E. Meyer, H. J. Güntherodt, *Surf. Sci.* **1999**, *438*, 289–296.

[45] L. Bartels, G. Meyer, K. H. Rieder, *Appl. Phys. Lett.* **1997**, *71*, 213–215.

[46] B. Schuler, G. Meyer, D. Peña, O. C. Mullins, L. Gross, *J. Am. Chem. Soc.* **2015**, *137*, 9870–9876.

[47] F. J. Giessibl, *Appl. Phys. Lett.* **1998**, *73*, 3956–3958.

[48] T. R. Albrecht, P. Grütter, D. Horne, D. Rugar, *J. Appl. Phys.* **1991**, *69*, 668–673.

[49] P. Hapala, G. Kichin, C. Wagner, F. S. Tautz, R. Temirov, P. Jelínek, *Phys. Rev. B* **2014**, *90*, 085421.

[50] B. Schuler, W. Liu, A. Tkatchenko, N. Moll, G. Meyer, A. Mistry, D. Fox, L. Gross, *Phys. Rev. Lett.* **2013**, *111*, 106103.

[51] L. Gross, F. Mohn, N. Moll, B. Schuler, A. Criado, E. Guitián, D. Peña, A. Gourdon, G. Meyer, *Science* **2012**, *337*, 1326–1329.

[52] D. G. De Oteyza, P. Gorman, Y. C. Chen, S. Wickenburg, A. Riss, D. J. Mowbray, G. Etkin, Z. Pedramrazi, H. Z. Tsai, A. Rubio, et al., *Science* **2013**, *340*, 1434–1437.

[53] A. Riss, S. Wickenburg, P. Gorman, L. Z. Tan, H. Z. Tsai, D. G. De Oteyza, Y. C. Chen, A. J. Bradley, M. M. Ugeda, G. Etkin, et al., *Nano Lett.* **2014**, *14*, 2251–2255.

[54] N. Pavliček, B. Fleury, M. Neu, J. Niedenführ, C. Herranz-Lancho, M. Ruben, J. Repp, *Phys. Rev. Lett.* **2012**, *108*, 086101.

[55] I. Swart, T. Sonnleitner, J. Repp, *Nano Lett.* **2011**, *11*, 1580–1584.

[56] S. K. Hämäläinen, N. Van Der Heijden, J. Van Der Lit, S. Den Hartog, P. Liljeroth, I. Swart, *Phys. Rev. Lett.* **2014**, *113*, 186102.

[57] A. J. Weymouth, T. Hofmann, F. J. Giessibl, *Science* **2014**, *343*, 1120–1122.

[58] M. Ellner, N. Pavliček, P. Pou, B. Schuler, N. Moll, G. Meyer, L. Gross, R. Peréz, *Nano Lett.* **2016**, *16*, 1974–1980.

[59] E. El koraychy, K. Sbiaai, M. Mazroui, R. Ferrando, Y. Boughaleb, *Chem. Phys. Lett.* **2017**, *669*, 150–155.

[60] T. Leoni, O. Guillermet, H. Walch, V. Langlais, A. Scheuermann, J. Bonvoisin, S. Gauthier, *Phys. Rev. Lett.* **2011**, *106*, 216103.

[61] J. Repp, G. Meyer, F. E. Olsson, M. Persson, *Science* **2004**, *305*, 493–495.

[62] J. Repp, G. Meyer, S. Paavilainen, F. E. Olsson, M. Persson, *Phys. Rev. Lett.* **2005**, *95*, 225503.

[63] J. Repp, G. Meyer, K. H. Rieder, *Phys. Rev. Lett.* **2004**, *92*, 4.

[64] V. Schendel, B. Borca, I. Pentegov, T. Michnowicz, U. Kraft, H. Klauk, P. Wahl, U. Schlickum, K. Kern, *Nano Lett.* **2016**, *16*, 93–97.

[65] J. N. Ladenthin, L. Grill, S. Gawinkowski, S. Liu, J. Waluk, T. Kumagai, *ACS Nano* **2015**, *9*, 7287–7295.

[66] N. Pavliček, Z. Majzik, S. Collazos, G. Meyer, D. Pérez, E. Guitián, D. Peña, L. Gross, *ACS Nano* **2017**, *11*, 10768–10773.

[67] V. Blum, R. Gehrke, F. Hanke, P. Havu, V. Havu, X. Ren, K. Reuter, M. Scheffler, *Comput. Phys. Commun.* **2009**, *180*, 2175–2196.

[68] J. P. Perdew, K. Burke, M. Ernzerhof, *Phys. Rev. Lett.* **1996**, *77*, 3865–3868.

[69] J. Heyd, G. E. Scuseria, M. Ernzerhof, *J. Chem. Phys.* **2003**, *118*, 8207–8215.

[70] A. Tkatchenko, M. Scheffler, *Phys. Rev. Lett.* **2009**, *102*, 073005.

[71] J. Van Der Lit, F. Di Cicco, P. Hapala, P. Jelinek, I. Swart, *Phys. Rev. Lett.* **2016**, *116*, 096102.

[72] R. Keller, H. Wycoff, L. E. Marchi, *Inorg. Synth.* **1946**, *2*, 1–4.

Chapter 3

Synthesis of cyclo[18]carbon *via* debromination of $C_{18}Br_6$

This chapter details the synthesis of the molecular carbon allotrope cyclo[18]carbon by dehalogenation of a bromocyclocarbon precursor $C_{18}Br_6$ in 64% yield, by atomic manipulation on a sodium chloride bilayer on Cu(111) at 5 K. This method of generating C_{18} gives a higher yield than that discussed previously from the cyclocarbon oxide $C_{24}O_6$ (Chapter 2). The experimental images of C_{18} were compared with simulated images for four theoretical model geometries, including possible bond-angle alternation: D_{18h} cumulene, D_{9h} polyyne, D_{9h} cumulene and C_{9h} polyyne. Cumulenic structures with (D_{9h}) and without (D_{18h}) bond-angle alternation can be excluded. Polyynic structures with (C_{9h}) and without (D_{9h}) bond-angle alternation both show a good agreement with the experiment and are challenging to differentiate.

3 Synthesis of cyclo[18]carbon *via* debromination of $C_{18}Br_6$

3.1 Acknowledgements

Results from this chapter have been published[1]:

Lorel M. Scriven,[1†] Katharina Kaiser,[2†] Fabian Schulz,[2] Alistair J. Sterling,[1] Steffen L. Woltering,[1] Przemyslaw Gawel,[1] Kirsten E. Christensen,[1] Harry L. Anderson,[1*] Leo Gross[2*] *J. Am. Chem. Soc.* **2020**, *142*, 12921–12924.

[†] These authors contributed equally

The author carried out all synthesis and characterisation of the compounds discussed in this chapter. All AFM images in this chapter were performed by Katharina Kaiser, Dr Fabian Schulz, Dr Leo Gross and, in small part, by the author upon visiting IBM Research-Zurich. DFT calculations were carried out by Alistair Sterling and Katharina Kaiser. AFM simulations were performed by Katharina Kaiser. Interpretation and analysis of images was carried out by the author, Katharina Kaiser, Dr Fabian Schulz, Dr Leo Gross and Professor Harry Anderson. The author wrote the first draft of the manuscript and subsequently all authors contributed to writing the manuscript. Parts of the text in this chapter are similar to this publication.

Dr Steffen L. Woltering is gratefully acknowledged for proofreading this chapter.

3.2 Introduction

The previous chapter described the synthesis of cyclo[18]carbon *via* elimination of carbon monoxide from $C_{24}O_6$ on a bilayer of sodium chloride on Cu(111) at 5 K[2], and the characterisation of this molecular carbon allotrope by high resolution atomic force microscopy (AFM). This study achieved the first structural characterisation of any cyclo[*n*]carbon. Molecules of C_{18} showed nine-fold symmetry, indicating a polyyne structure. However, many questions remain unanswered about the structure and properties of cyclo[*n*]carbons[3–7].

A key question that was triggered by this research is that of the bond-shift valence tautomerisation[8], also referred to as automerisation[3], in cyclo[18]carbon. Bond-shift valence tautomerisation is the process by which π-bonds interconvert in molecule with alternating bond lengths. The concept is well understood[9] in antiaromatic systems such as cyclobutadiene, pentalene and heptalene (Figure 3.1). These antiaromatic molecules have alternating bond lengths due to symmetry breaking Jahn-Teller distortions (there is debate[8,10] as to whether they are pseudo-Jahn-Teller distortions or first-order Jahn-Teller distortions however this is not critical in this discussion). Alternating bond lengths are required for a molecule to exhibit valence bond-shift tautomerism, aromatic molecules generally have equal bond lengths and are at resonance and therefore valence bond-shift tautomerisation does not apply. The energy surface of a molecule that exhibits valence tautomerism is expected to have a symmetrical double-well potential with a transition state in between. Shifting of the π-bonds between the two wells in the energy potential is thought to occur predominantly *via* quantum mechanical tunneling of the carbon atoms[9,11–14]. The criteria for carbon atom tunneling are a low activation energy for the process ($\Delta E^{\ddagger}$) and a narrow barrier width (i.e. a small change in bond length/molecular structure upon rearrangement).

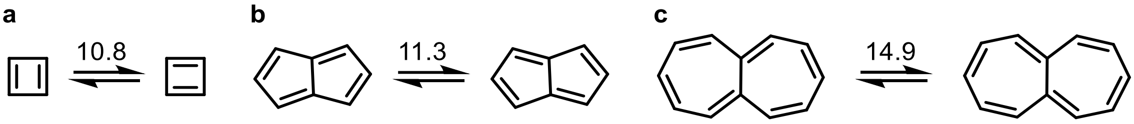

Figure 3.1 Examples of bond-shift valence tautomerism in **a**) cyclobutadiene[11] **b**) pentalene[9] **c**) heptalene[9]. Calculated $\Delta E^{\ddagger}$ shown above the arrows in kcal mol^{-1}. For simplicity bond length alternation is not shown in these representations.

Quantum mechanical tunneling of carbon atoms has been predicted to occur in cyclo[18]carbon[3,5]. For the polyynic geometry of cyclo[18]carbon (with either D_{9h} or C_{9h} symmetry) there are two possible arrangements of the triple bonds that could exist in a symmetrical double well potential with the D_{18h} cumulenic geometry as the transition state between them (Figure 3.2). Usually valence bond tautomerism is only considered in antiaromatic systems due to the bond length alternation (BLA) in these systems. However, in cyclo[18]carbon, BLA is thought to occur due to second-order Jahn-Teller effects[3,15–18] and therefore it can undergo valence bond-shift tautomerisation. The rearrangements discussed above involve double bond shifting (which can be considered as a single π bond-shift) whereas in cyclo[18]carbon triple bond shifting can occur (which can be considered as a double π bond-shift). The difference in bond length between the polyynic and cumulenic geometries of cyclo[18]carbon is small (see Section 3.4.2) and therefore the process has a narrow barrier width. Theoretical investigations[3,5] predict a very high rate of quantum mechanical tunneling in cyclo[18]carbon, the calculated activation energy[3] for the process (9.6 kcal mol^{-1}) is smaller than that calculated for the antiaromatic systems described in Figure 3.1. Thus, an average image corresponding to the D_{18h} geometry would be expected for AFM imaging. This is in contrast to the experimental result and raises the question as to how much the geometry of the molecule is influenced by interactions with the substrate. A recent theoretical study concluded that the interaction of C_{18} with the NaCl surface is unlikely to substantially change the molecular geometry[4] however it could exert a subtle effect by breaking the symmetry of double well potential of cyclo[18]carbon thereby causing one polyynic geometry to be favoured over the other.

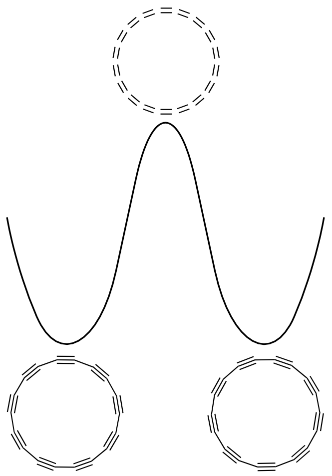

Figure 3.2 Representation of the potential energy surface for bond-shift valence tautomerisation in cyclo[18]carbon. Calculated $\Delta E^{\ddagger} = 9.6$ kcal mol^{-1}[3].

This debate surrounding the structure of cyclo[18]carbon led us to investigate further the symmetry of cyclo[18]carbon on bilayer sodium chloride. Second-order Jahn-Teller effects have been proposed to cause both bond-length alternation (BLA) and bond-angle alternation (BAA) in cyclo[*n*]carbons[3,15–18], whereas Hückel aromaticity should favour a high-symmetry structure in C_n rings with $n = 4k + 2$, such as C_{18}[19,20]. Theoretical studies have suggested four possible geometries for C_{18}: D_{18h} cumulene, D_{9h} polyyne, D_{9h} cumulene and C_{9h} polyyne[3,15–18] (Figure 3.3 and 1.2.2).

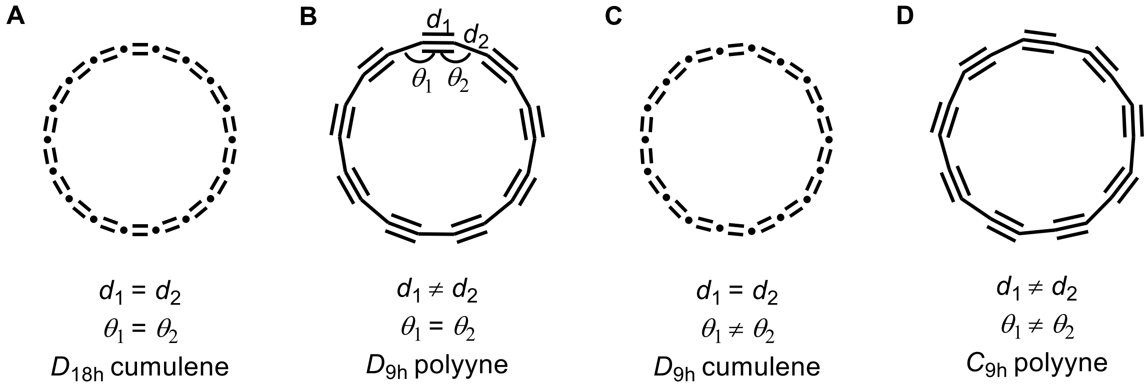

Figure 3.3 Possible geometries of cyclo[18]carbon, **A**–**D**.

Many theoretical studies have calculated the BLA and BAA for cyclo[18]carbon and the calculated values are reviewed in Table 3.1. The geometries generally show good agreement however different calculations show different exact values.

Table 3.1 Literature review of the calculated geometries of cyclo[18]carbon using various calculation types.

year	**A**	**B**	**C**	**D**
1989[19]	$\theta = 160$ ° $d_1 = 1.265$ Å	$\theta = 160$ ° $d_1 = 1.362$ Å $d_2 = 1.199$ Å	$\theta_1 = 170.4$ ° $\theta_2 = 149.6$ ° $d = 1.271$ Å	-
1991[15]	$\theta = 160$ ° $d_1 = 1.277$ Å	$\theta = 160$ ° $d_1 = 1.375$ Å $d_2 = 1.194$ Å	$\theta_1 = 175$ ° $\theta_2 = 145$ ° $d = 1.277$ Å	-
1992[21]	$\theta = 160$ ° $d_1 = 1.270$ Å	$\theta = 160$ ° $d_1 = 1.360$ Å $d_2 = 1.120$ Å	-	-
1994[22]	$\theta = 160$ ° $d_1 = 1.270$ Å	-	-	-
1995[16]	$\theta = 160$ ° $d_1 = 1.271$ Å	$\theta = 160$ ° $d_1 = 1.380$ Å $d_2 = 1.198$ Å	$\theta_1 = 167.1$ ° $\theta_2 = 152.9$ ° $d = 1.294$ Å	$\theta_1 = 156.7$ ° $\theta_2 = 163.3$ ° $d_1 = 1.198$ Å $d_2 = 1.379$ Å
1995[23]	$\theta = 160$ ° $d_1 = 1.287$ Å	$\theta = 160$ ° $d_1 = 1.380$ Å $d_2 = 1.202$ Å	-	$\theta_1 = 158.0$ ° $\theta_2 = 162.0$ ° $d_1 = 1.202$ Å $d_2 = 1.380$ Å
1999[24]	$\theta = 160$ ° $d_1 = 1.280$ Å	-	-	-
2000[17]	$\theta = 160$ ° $d_1 = 1.285$ Å	-	-	-
2005[25]	$\theta = 160$ ° $d_1 = 1.285$ Å	-	$\theta_1 = 167.6$ ° $\theta_2 = 152.5$ ° $d = 1.285$ Å	$\theta_1 = 152.4$ ° $\theta_2 = 167.6$ ° $d_1 = 1.2854$ Å $d_2 = 1.2852$ Å
2008[18]	**$\theta = 160$ °** **$d_1 = 1.2971$ Å**	**$\theta = 160$ °** **$d_1 = 1.3828$ Å** **$d_2 = 1.2381$ Å**	**$\theta_1 = 162.85$ °** **$\theta_2 = 157.15$ °** **$d = 1.2971$ Å**	**$\theta_1 = 156.73$ °** **$\theta_2 = 163.27$ °** **$d_1 = 1.2379$ Å** **$d_2 = 1.3827$ Å**

The geometries calculated in 2008[18] (bold values in Table 3.1) were chosen as the most accurate geometries as they were calculated using coupled-cluster singles and doubles excitation theory (CCSD) with different basis sets and the energy minima values are quoted in the table. These values were used to calculate the radial coordinates for cyclo[18]carbon in its four possible symmetries (see Section 3.4.2).

To facilitate further study into the structure and properties of cyclo[18]carbon it was necessary to design a cyclo[18]carbon precursor that would unmask more reliably and in higher yield than $C_{24}O_6$. Previous studies[26–28] have shown that dehalogenation typically requires low energy pulses ($V \approx 2$ V) and thus a target precursor based on dehalogenation was selected. The chosen synthetic target were the bromocyclocarbons, $C_{6n}Br_{2n}$ as their molecular weight is sufficiently low for sublimation (a strict requirement for on-surface study) and their unmasking was predicted to be achieved under mild conditions. This chapter presents a synthesis of C_{18} *via* a new route: dehalogenation of $C_{18}Br_6$, which occurs under milder conditions, and in five times higher yield (64%) compared to the yield of formation from $C_{24}O_6$ (13%, Figure 3.4).

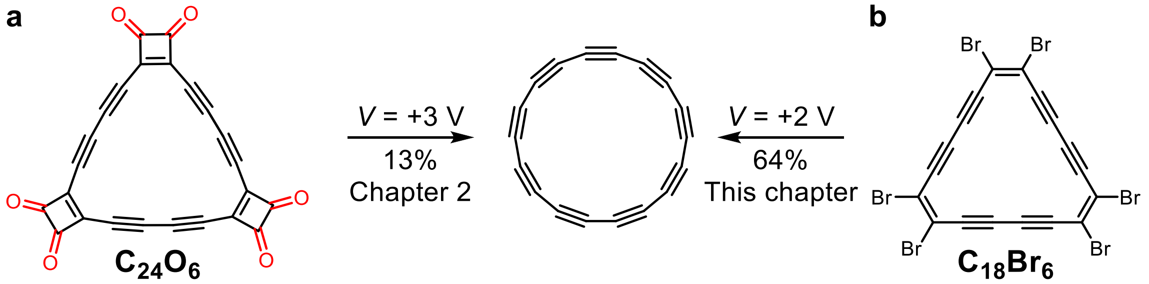

Figure 3.4 Synthesis of cyclo[18]carbon from **a**) cyclocarbon oxide precursor, $C_{24}O_6$ **b**) bromocyclocarbon precursor, $C_{18}Br_6$.

This chapter will review the synthetic strategy towards $C_{18}Br_6$ before moving on to the on-surface atom manipulation of $C_{18}Br_6$ and further structural characterisation of cyclo[18]carbon.

3.3 Methods

The key requirement for the synthesis of $C_{18}Br_6$ was the synthesis of the monomer for cyclisation **15** (Scheme 3.1).

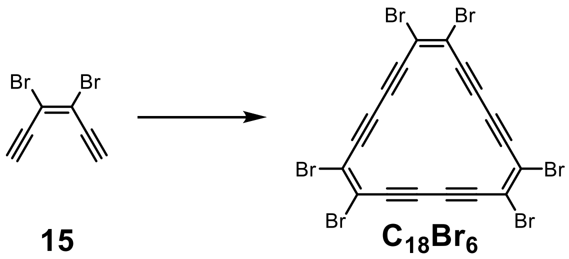

Scheme 3.1 Proposed monomer **15** for formation of $C_{18}Br_6$.

15 is a (*Z*)-halo-enediyne and compounds of this type are challenging to access synthetically as they must be formed in a stereospecific manner[29–32]. Multiple different approaches were pursued towards the synthesis of **15** and will be detailed in the following sections. The cyclisation of **15** to $C_{18}Br_6$ will then be described along with characterisation of the structure and properties of $C_{18}Br_6$.

3.3.1 Linking silyl protecting group

The first approach pursued was based on an intramolecular carbenoid coupling[32,33]. A synthetic route was designed, based on a linking silyl protecting group, to force the stereochemistry of the halo-enediyne into a (*Z*)-configuration (Scheme 3.2). Propargylaldehyde diethyl acetal was lithiated and added to 1,2-bis(chlorodimethylsilyl)ethane to generate **16**. Sulfuric acid was used to remove the acetal protecting groups to reveal the propargyl dialdehyde **17**. Bromination of propargyl dialdehyde **17** to the tetrabromo precursor to carbenoid coupling **18** required significant optimisation as the propargyl aldehyde is a strong Michael acceptor and has a high tendency to undergo unwanted side reactions.

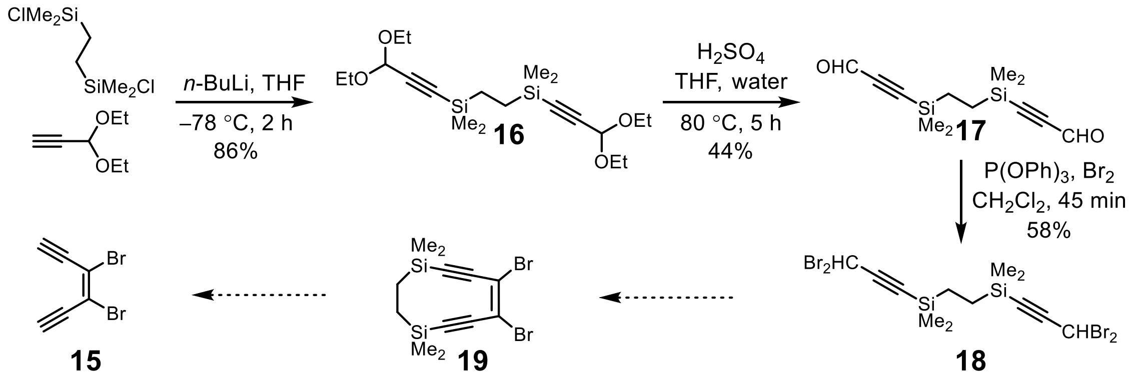

Scheme 3.2 Attempted synthesis of **15** *via* an intramolecular carbenoid coupling.

In order to achieve tetrabromination of **17** multiple different bromination conditions were screened (Table 3.2). It was found that any nucleophilic bases, such as pyridine or triethylamine, led to decomposition of the starting material, presumably due to deprotection of the linking silyl protecting group. Decomposition was also observed upon use of BBr_3, likely due to the harsh nature of this reagent. Successful bromination conditions were found *via* the preformation of a $P(OPh)_3Br_2$ complex which gave clean conversion to the propargyl tetrabromide **18**.

Table 3.2 Various bromination conditions attempted on the propargyl aldehyde **17**.

Bromination conditions	Outcome
PCl_3 (2 eq), Br_2 (2 eq), pyridine (0.2 eq)[34]	Multiple aldehyde and brominated species in ^1H NMR spectrum, no clear conversion to product
Zn (4 eq), PPh_3 (4 eq), CBr_4 (4 eq)[35]	Dibromoolefin formation
$P(OPh)_3$ (2.2 eq), Br_2 (2.2 eq), Et_3N (6 eq)[36]	Decomposition of **17**
BBr_3[37]	Decomposition of **17**
$P(OPh)_3$, Br_2[38]	Successful conversion to **18** in 58% yield

The carbenoid coupling of **18** was then attempted. The initial conditions used were identical to those attempted by Jones and co-workers[33] which used LiHMDS as a base and HMPA as an electron donor to destabilise the carbenoid[39] and promote the coupling reaction. However, these conditions led to complete decomposition of the starting material (Table 3.3). Modifications of these conditions were attempted however all conditions resulted in the recovery of starting material or multiple peaks in the protecting group region but no clear conversion to the desired product **19**. It is likely that the protecting group is sensitive to the basic conditions required for the reaction and thus leads to partial deprotection of the silyl linking group creating a complex mixture of species.

Table 3.3 Various conditions attempted for carbenoid coupling of **18**.

Conditions[33]	Outcome
LiHMDS (2.2 eq), HMPA (10 eq), –45 °C	Decomposition of **18**, no clear product peaks in ^{1}H NMR spectrum
LiHMDS (1.1 eq), no HMPA, –78 °C	Recovery of **18**
LiHMDS (1.1 eq), HMPA (1.1 eq), –78 °C	Multiple product and starting material peaks in ^{1}H NMR spectrum, no clear conversion to desired product
LiHMDS (2.2 eq), HMPA (2.2 eq), –78 °C	Multiple product and starting material peaks in ^{1}H NMR spectrum, no clear conversion to desired product
LDA (2.2 eq), HMPA (2.2 eq), –78 °C	Multiple product and starting material peaks in ^{1}H NMR spectrum, no clear conversion to desired product

After the lack of success of the linking silyl protecting group, the synthesis of **15** was attempted *via* an untethered halo-enediyne formation designed to yield the desired protected compound **21** that could then be deprotected to **15**. There is literature precedent for untethered stereocontrolled enediyne formation with high *Z*/*E* ratios[32,33,40]; *Z*/*E* ratios of 1.2/1 have been reported[32]. A tri*iso*propylsilyl (TIPS) protecting group was selected as this is one of the most robust acetylene protecting groups. Therefore, TIPS-aldehyde was brominated using the preformed $P(OPh)_3Br_2$ complex to yield the dibromo species **20**. The carbenoid coupling of **20** was attempted (Scheme 3.3). The starting material of the reaction was consumed however analysis of the crude reaction products, by their ^{1}H and ^{13}C NMR spectra, did not clearly correspond to either of the predicted products **21** and **22**.

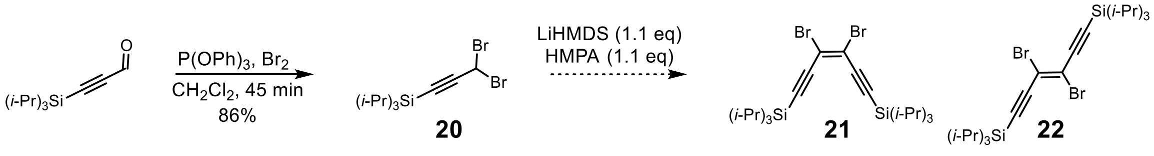

Scheme 3.3 Attempted untethered halo-enediyne formation to yield desired product **21**.

As the reaction products could not be identified this route was not pursued further. At this point it was decided a carbenoid coupling synthetic strategy was not feasible and thus stereocontrolled bromination of an acetylene was pursued as an alternative strategy.

3.3.2 Stereocontrolled bromination

Stereocontrolled bromination of acetylenes presents a synthetic challenge as (*E*)-dihaloalkenes are often formed in preference to (*Z*)-dihaloalkenes, due to steric effects[41–44]. However, encouraging examples of the synthesis of (*Z*)-dihaloalkenes from alkynes[45] led us to pursue this route (Scheme 3.4).

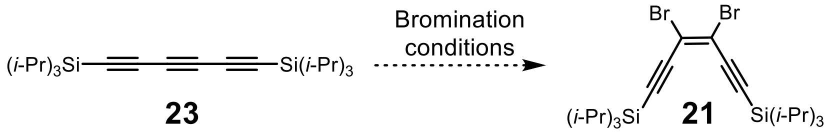

Scheme 3.4 Proposed formation of **21** *via* sterecontrolled bromination of **23**.

Triyne **23** was synthesised *via* a previously reported route[46] as shown in Scheme 3.5. Lithiated TIPS-acetylene was added to ethyl formate to give the alcohol **23a** which was oxidised to give the diacetylene ketone **23b**. The ketone was converted to the dibromoolefin **23c** with a modified version of the Wittig reaction[47]. **23c** was converted to TIPS-triyne **23** *via* the Fritsch-Buttenberg-Wiechell rearrangement[48].

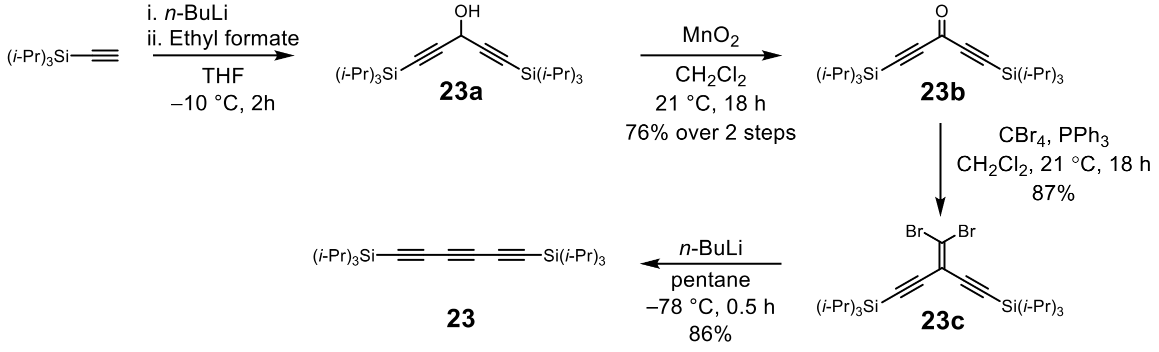

Scheme 3.5 Synthesis of **23**[46].

There is literature precedence for the stereoselective synthesis of (*Z*)-dihaloalkenes adjacent to TIPS groups[45] using TMS-Br and N-bromosuccinimide (NBS). It was hoped that steric considerations would ensure bromination of the central bond of **23**. Full conversion of **23** to two different products, **24a** and **24b**, was observed upon reaction with TMS-Br and NBS (Scheme 3.6). Small amounts of **24a** could be purified on silica whereas **24b** could not be separated from residual **24a**. The structure of **24a** was determined *via* single crystal X-ray analysis. Single crystals of **24a** were grown from a slowly cooled saturated solution of **24a** in methanol to reveal (*Z*)-selective bis bromination adjacent to the TIPS units of **23** (Scheme 3.6b). Presumably **24b** is an intermediate in the formation of **24a**.

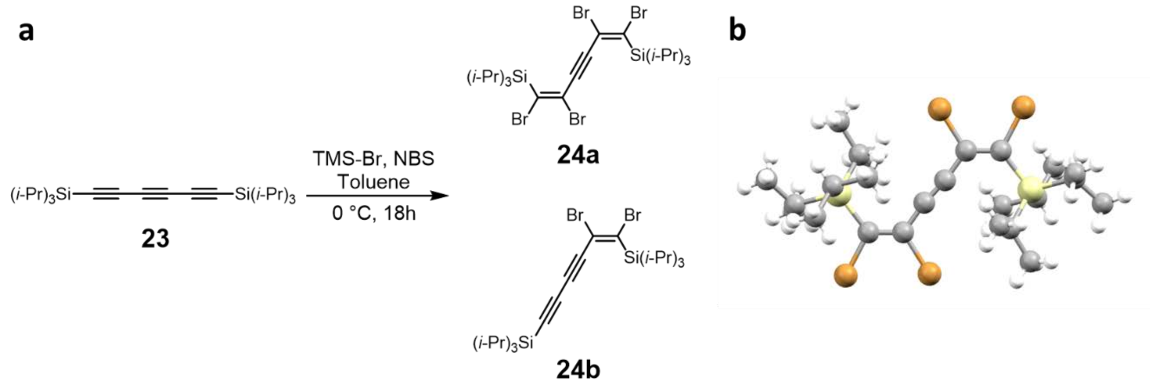

Scheme 3.6 a) Stereoselective bromination of **23** to yield (*Z*)-dibromoalkene units adjacent to the TIPS units in products **24a** and **24b**. **b**) Single crystal X-ray structure of **24a**.

Bromination adjacent to the TIPS group is likely due to the electronic stabilisation of the β-silicon effect which outweighs the steric considerations in this case[49]. It was also found that upon treatment of **23** with Br_2 that the same products were detected as for the TMS-Br and NBS conditions however the reaction proceeded much less cleanly and the products could not be fully isolated. It was concluded that any reaction involving the attack of an alkyne into an electrophile would yield products **24a** and **24b** instead of **21** due to electronic considerations.

Due to the failure to form the desired product *via* electrophilic bromination, our attention turned towards reliable methods of stereoselectively installing units on the central bond of **23** that could be converted to **21** upon further reaction. Hence our attention turned towards a halodeboronation strategy[50].

3.3.3 Halodeboronation strategy

Literature precedent[51] for the synthesis of internal (*Z*)-dibromoalkenes from acetylenes *via* their bis-boryl adducts encouraged investigation of halodeboronation as a potential synthetic route. It was found that, upon optimisation of the reaction conditions, **23** could undergo *syn*-selective diboration of its central C≡C triple bond, using a platinum-catalysed reaction, developed by Suzuki *et al*[52], to give the (*Z*)-bis(boryl)enediyne **25**. This intermediate was stereoselectively bromodeboronated using copper(II) bromide, to yield the TIPS-protected (*Z*)-dibromo-enediyne **21** in 53% yield over two steps

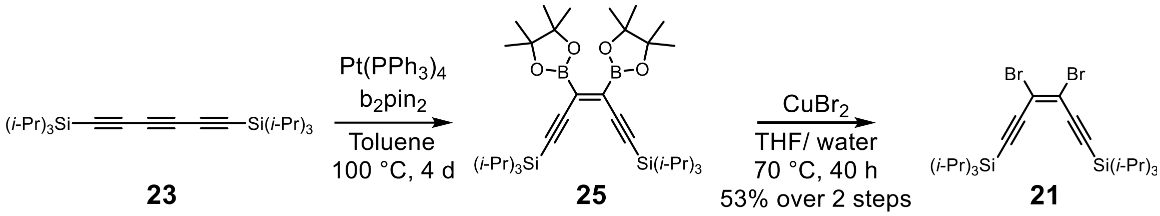

Scheme 3.7 Synthesis of **21** *via* a halodeboronation strategy.

Suzuki and co-workers[52] first reported the diboration of alkynes to pure (*Z*)-bis(boryl)alkenes in 1993. It was hoped that borylation of **23** would lead to bis-borylation of the central triple bond due to steric constraints analogous to the regioselective addition of cobalt across **23** as shown by Diederich and co-workers[53]. Suzuki and co-workers[52] found that only platinum catalysts, such as $Pt(PPh_3)_4$, were active for the diboration of alkynes. In addition, it was found that more polar solvents accelerated the reaction rate with DMF > CH_3CN > toluene. Therefore, the first conditions attempted were the optimised conditions used by Suzuki and co-workers whereby the reaction was heated to 80 °C for 24 h in DMF (Table 3.4). These conditions appeared to result in the decomposition of **23**, with no clear conversion to the desired product. Upon extension of the reaction time to 24 h and increasing the temperature from 80 °C to 100 °C in DMF some conversion to a species with a ^{13}C NMR spectrum consistent with the desired product **25** (Figure 3.5) was detected, however significant baseline decomposition was also observed. The reaction time was then increased to 2 days at 100 °C, however this led to complete decomposition of the reaction mixture. At this point the solvent was switched from DMF to toluene and the reaction time increased from 24 h to 4 days and full conversion to **25** was observed with limited baseline decomposition (Table 3.4, Figure 3.5).

Table 3.4 Optimisation of diboration of **23**.

Conditions	Temp	Time	Solvent	Outcome
B_2pin_2 (1.1 eq), $Pt(PPh)_3$ (0.03 eq)	80 °C	24 h	DMF	Only **23** and baseline decomposition
B_2pin_2 (1.1 eq), $Pt(PPh)_3$ (0.03 eq)	80 °C	5 h	DMF	Only **23** and baseline decomposition
B_2pin_2 (1.1 eq), $Pt(PPh)_3$ (0.03 eq)	100 °C	24 h	DMF	Some conversion to **25**, baseline decomposition, **23** still detected
B_2pin_2 (1.1 eq), $Pt(PPh)_3$ (0.03 eq)	100 °C	2 d	DMF	Only baseline decomposition
B_2pin_2 (1.1 eq), $Pt(PPh)_3$ (0.03 eq)	100 °C	24 h	Toluene	Some conversion to **25**, still **23** but no baseline decomposition
B_2pin_2 (1.1 eq), $Pt(PPh)_3$ (0.03 eq)	100 °C	4 d	Toluene	Full conversion to **25**

The only reliable method to monitor the reaction progress was *via* ^{13}C NMR analysis of aliquots of the reaction mixture as the R_F of the starting material and product are very similar and the ^{1}H NMR spectrum only contains Bpin and TIPS signals. Moreover **25** could never be detected by any form of mass spectrometry, presumably due to fragmentation of the Bpin units upon ionisation. Upon conversion of **23** to **25** loss of the three acetylene signals of **23** was observed and evolution of a new set of, downfield shifted, acetylene signals in **25** were observed (Figure 3.5). There was uncertainty in the structure of the product as the C=C signal in the spectrum of **25** had very low intensity, however most ^{13}C spectra of bis-boryl alkenes do not report a signal corresponding to signal **c** of **25** in Figure 3.5[52], presumably due to very long relaxation times of this carbon atom.

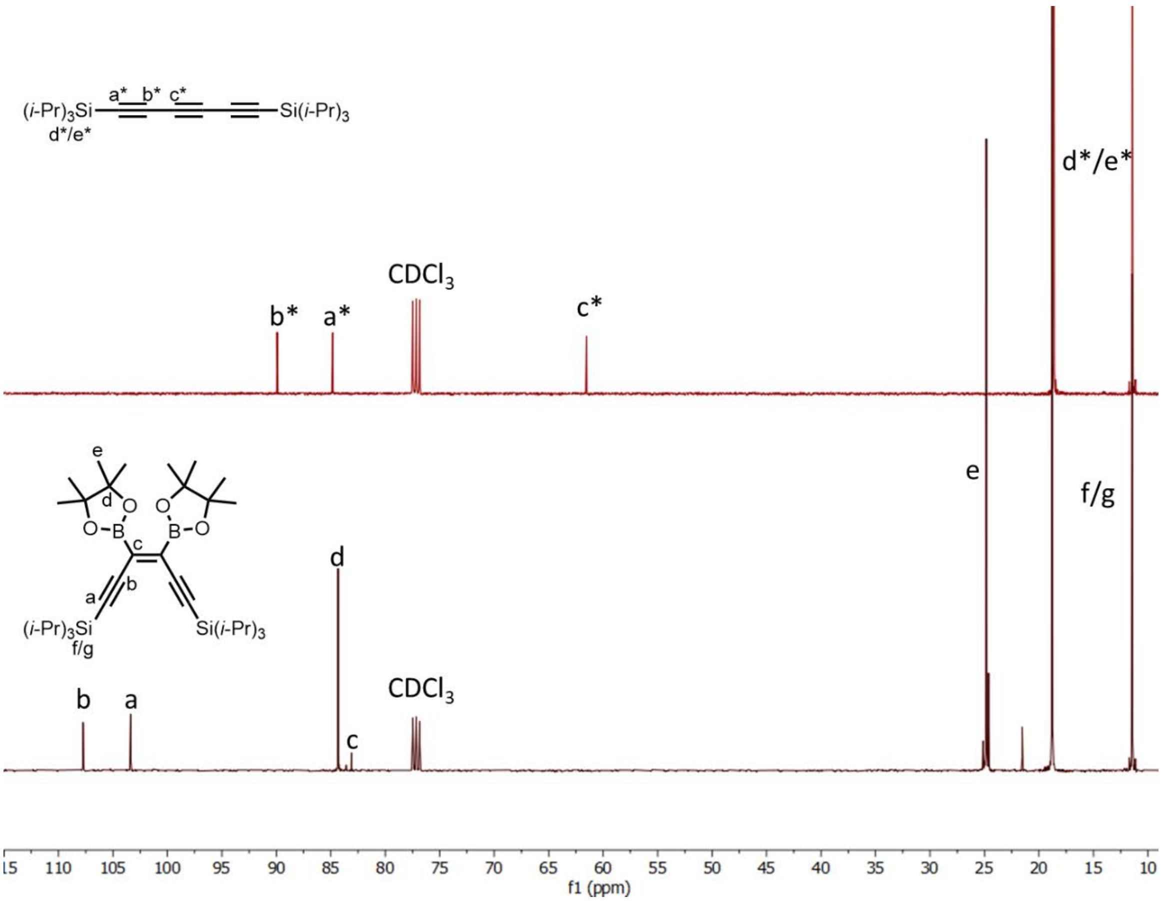

Figure 3.5 ^{13}C spectra of **23** and **25** (101 MHz, $CDCl_3$, 294 K) demonstrating the chemical shift change upon borylation of **23**. *: atom labels of **23**.

From the spectra shown in Figure 3.5 it was concluded that the desired product had been formed. The stereochemistry of the central bond was unknown however, from the stereocontrolled platinum catalysed reaction conditions used[52], it was expected that the (*Z*)-isomer had been formed. **25** shows limited stability on silica and thus was subjected to bromodeboronation conditions without further purification. There is literature precedence[51] for stereocontrolled bromodeboronation *via* conversion of the Bpin groups to potassium organotrifluoroborates, using KHF_2, which then undergo facile bromodeboronation with tetrabutylammonium tribromide (TBATB). However, these conditions were not compatible with the TIPS groups of **25** due to exposure to KHF_2 which can cause desilylation. Instead stereoselective bromodeboronation conditions reported by Ge and co-workers[50] were attempted. **25** and $CuBr_2$ were heated to reflux at 70 °C in a 1:1 mixture of THF and water. Full conversion to **21** was observed after 24 h in 53% yield over two steps (Scheme 3.7).

Reaction completion was determined by loss of the Bpin derived signals in the ^{1}H NMR spectrum. Furthermore, analysis by HR-APCI-MS confirmed the expected mass. At this stage in the synthesis the stereochemistry of the central double bond of **21** was still not definitively known. However, the deprotection of **21** and cyclisation was attempted as, if $C_{18}Br_6$ was detected in the reaction mixture, this would confirm the stereochemistry of the double bond.

3.3.4 First detection of $C_{18}Br_6$

The first stage in the synthesis of $C_{18}Br_6$ from **15** required the deprotection of **21**. Tetrabutylammonium fluoride (TBAF) was used to deprotect **21** to give **15** as a yellow solution that was unstable to solvent removal and was always deprotected immediately before use and kept in solution. Cyclisation of **15** was carried out using the same conditions as for the cyclisation to the cyclocarbon oxide precursors (the solvent was switched from acetone to CH_2Cl_2 due to the apolar nature of these compounds). A solution of Hay catalyst[54] was prepared under nitrogen in CH_2Cl_2 and added to a vigorously stirred solution of **15** (approximately 15 mM) in CH_2Cl_2 under oxygen (Scheme 3.8).

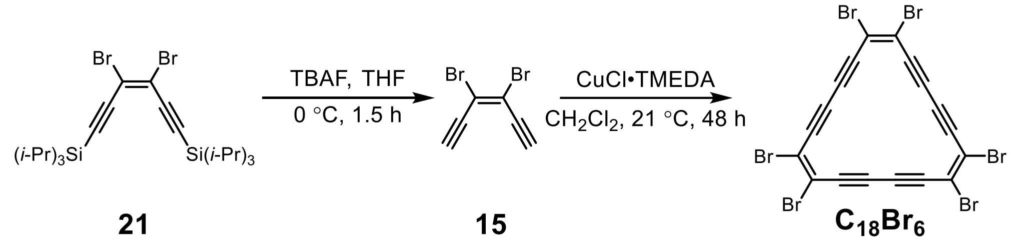

Scheme 3.8 Synthesis of $C_{18}Br_6$ from **21**.

Upon analysis of the reaction mixture by TLC, **15** was completely consumed and a mixture of highly apolar species were detected. The crude reaction mixture was found to be explosive and therefore care was taken to always work on a small scale and non-flammable solvents were used where possible. Size exclusion chromatography (Bio-Beads SX3, $CHCl_3$) was carried out and the retention time of the fractions was analysed using analytical gel permeation chromatography (GPC) as shown in Figure 3.6. The GPC traces were highly dependent on the chosen wavelength of observation as the different components of the reaction mixture show a large variation in absorbance upon changing the wavelength. The wavelength of absorption chosen in Figure 3.6 was 360 nm. At longer wavelengths the intensity of absorption of larger species was greater compared to $C_{18}Br_6$.

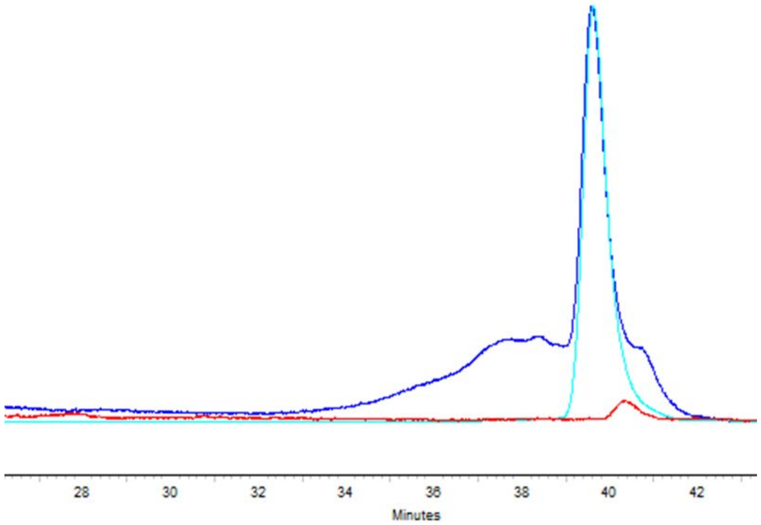

Figure 3.6 Typical GPC trace of the retention time of a cyclisation mixture. Dark blue trace: crude reaction mixture. Light blue trace: peak with a retention time corresponding to $C_{18}Br_6$ (shoulder of peak due to solvent impurities). Red trace: peak with a retention time corresponding to **15**. Wavelength of absorption = 360 nm.

Formation of $C_{18}Br_6$ was confirmed by mass spectrometry; the GPC peak with a retention time corresponding to $C_{18}Br_6$ (pale blue line in Figure 3.6) presents a radical M^{-} ion in APCI ($C_{18}Br_6^{-}$) with the expected isotope pattern (Figure 3.30). Further positive characterisation was obtained *via* the UV-Vis spectrum of the fraction corresponding to $C_{18}Br_6$ which gave an absorption profile very similar to those of Tobe's propellane-annelated dehydro[18]annulene derivative[55] **4** which has a comparable conjugated system (Figure 3.7).

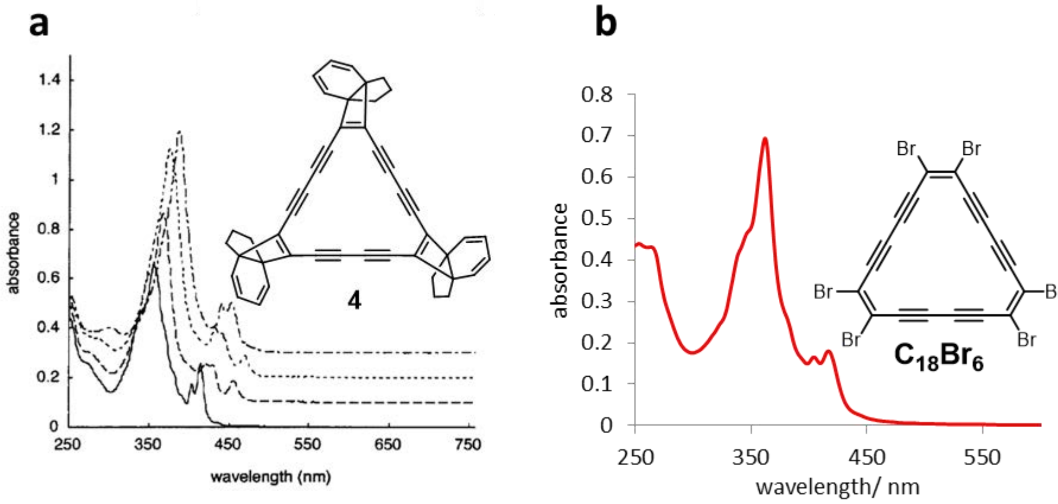

Figure 3.7 Comparison of UV-Vis of **a**) Tobe's propellane-annelated dehydro[18]annulene derivative **4** solid line (1.09×10^{-5} M) and **b**) $C_{18}Br_6$, red line (1.44×10^{-5} M) which show similar absorption profiles. Absorption profile of **4** was modified with permission from American Chemical Society: Journal of the American Chemical Society[55].

Other ring sizes, $C_{12}Br_4$ and $C_{24}Br_8$, were tentatively detected in the reaction mixture by their radical M^{-} ions in APCI (Figure 3.31, Figure 3.32 and Figure 3.8). $C_{12}Br_4$ presents as a red band on the size exclusion column and gives pale pink solutions however upon solvent removal it decomposes to an insoluble black solid and thus was not investigated further. $C_{24}Br_8$ exhibited significant overlap with $C_{18}Br_6$ and larger species upon purification by small column size exclusion chromatography. Recycling GPC was used to purify $C_{24}Br_8$ (< 1 mg) and it was characterised by a M^{-} ion in APCI-MS ($C_{24}Br_8^{-}$). Isolation and characterisation of $C_{24}Br_8$ was not pursued further as the relatively large molecular weight of this compound is likely to result in its decomposition upon sublimation for on-surface analysis.

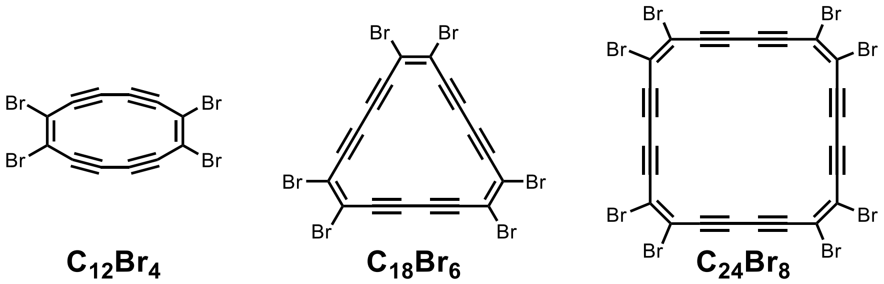

Figure 3.8 Ring sizes detected from the cyclisation mixture.

Using these conditions only very small amounts of $C_{18}Br_6$ and other ring sizes could be isolated, the initial yield of formation of $C_{18}Br_6$ was around 2% over two steps from **21**, however this was not reproducible and a maximum of 1–2 mg per cyclisation reaction could be isolated which hindered further purification attempts such as recrystallisation. Therefore, optimisation of the reaction conditions was carried out and will be discussed in the next section.

3.3.5 Optimised synthesis of $C_{18}Br_6$

In order to optimise the yield of formation of $C_{18}Br_6$ multiple cyclisation conditions were attempted (Table 3.5). The original conditions attempted were 1 eq of Hay catalyst in CH_2Cl_2 with vigorous stirring under oxygen (Table 3.5**A**) and gave $C_{18}Br_6$ in 2% yield over two steps from **21** however these conditions were not reproducible. Any conditions involving pyridine (Table 3.5 **B** and **C**) led to decomposition of $C_{18}Br_6$, likely due to the sensitivity of $C_{18}Br_6$ to nucleophilic bases. Upon increasing the equivalents of Hay catalyst (Table 3.5**D** and **E**) only larger species were detected by analytical GPC and no peak corresponding to $C_{18}Br_6$ was detected. Upon reduction in the equivalents of Hay catalyst (Table 3.5**F**) a two-fold increase in the yield to 4% over two steps from **21** was obtained. Lastly upon use of palladium, benzoquinone conditions (Table 3.5**G**) a 4% yield was once again detected. Due to the ease of experimental set up **F** was selected as the optimum conditions for formation of $C_{18}Br_6$.

Table 3.5 Optimisation of conditions for cyclisation of $C_{18}Br_6$.

	Conditions	Observations
A	1 eq Hay Catalyst CH_2Cl_2, vigorous stirring, O_2	$C_{18}Br_6$ formed in 2% yield over two steps from **21** but not reproducible
B	7 eq $Cu(OAc)_2$ Pyridine: THF: MeOH (1:1:2)	Decomposition of **15**
C	10 eq CuCl Pyridine, vigorous stirring, O_2	Decomposition of **15**

D	20 eq Hay Catalyst CH_2Cl_2, vigorous stirring, O_2	Larger species detected by analytical GPC, no $C_{18}Br_6$ detected
E	5 eq Hay Catalyst CH_2Cl_2, vigorous stirring, O_2	Larger species detected by GPC, no $C_{18}Br_6$ detected
F	0.2 eq Hay Catalyst CH_2Cl_2, vigorous stirring, O_2	$C_{18}Br_6$ formed in 4% yield over two steps from **21**
G	0.33 eq $PdCl_2(PPh_3)_2$, 7 eq benzoquinone, 1.7 eq CuI, $CHCl_3$ 0.1% DIPA	$C_{18}Br_6$ formed in 4% yield over two steps from **21**

Additionally, it was possible to optimise the purification of $C_{18}Br_6$. Instead of separation of $C_{18}Br_6$ by the lengthy process of size exclusion chromatography, which often needed to be repeated multiple times to get a pure sample, $C_{18}Br_6$ was isolated from the reaction mixture by crashing it out of solution. The crude cyclisation mixture was passed through a plug, SiO_2 (petroleum ether) and then concentrated to approximately 10 mL. Upon concentration a red solid crashed out of solution which was found to be predominantly $C_{18}Br_6$ by GPC analysis of the retention time. Upon trituration of the red solid in CH_2Cl_2 pure $C_{18}Br_6$ could be obtained as a highly insoluble red crystalline solid. By this method $C_{18}Br_6$ could be isolated in approximately 6 mg batches with a 4% yield over two steps from **21**. The reaction was not significantly scaled up due to the explosive nature of the crude reaction mixture. Details of the structure and properties of $C_{18}Br_6$ will be discussed in the next section.

3.3.6 Structure and properties of $C_{18}Br_6$

$C_{18}Br_6$ is stable under ambient conditions in solution and in the solid state, with no significant decomposition over several days at room temperature, and the solid can be stored for weeks at –20 °C. However, it explodes when scratched and care was taken to work on a small scale. Differential scanning calorimetry was carried out on 0.6 mg of $C_{18}Br_6$ which was sealed into an aluminum pan and heated relative to an empty reference (Figure 3.9). The sample was held for 1 minute at 50 °C, heated from 50 °C to 250 °C at 10 °C/min, held for 1 minute at 250 °C and then cooled from 250 °C to 50 °C at 10 °C/min. A large exotherm was observed during the heating cycle, from 85 °C to 125 °C, corresponding to an enthalpy of ΔH = –109 kJ/mol. An additional scan was then carried out on the same sample and no further exotherms were observed, presumably due to decomposition of the sample. This data implies that $C_{18}Br_6$ is thermally stable up to approximately 85 °C but decomposes in an exothermic fashion above this temperature.

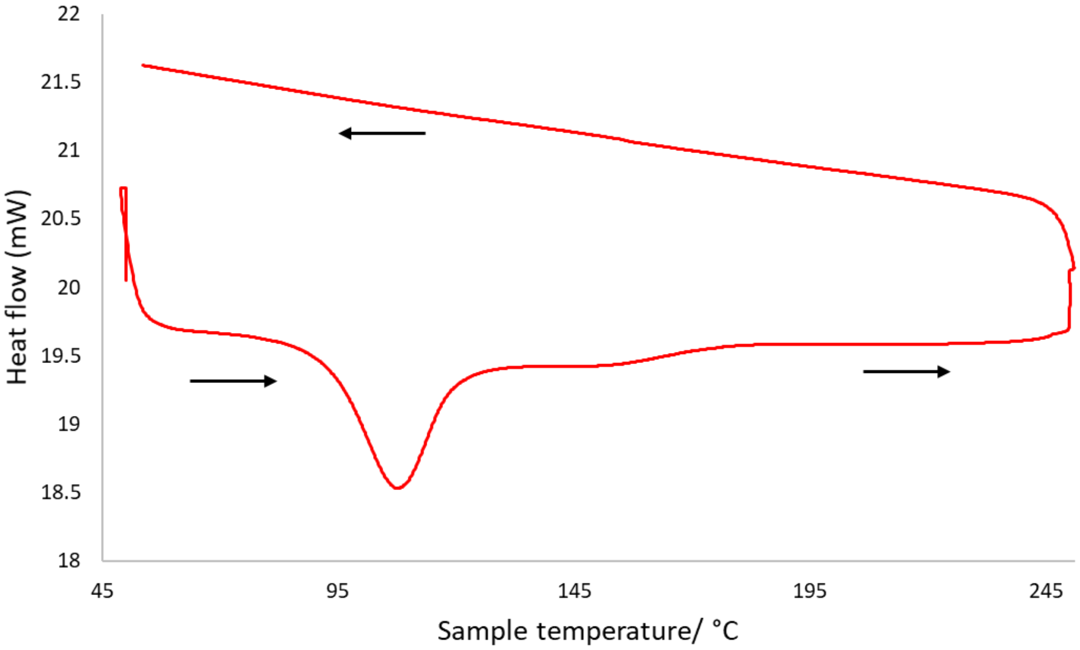

Figure 3.9 DSC curve of $C_{18}Br_6$ with a heating rate of 10 °C/min.

$C_{18}Br_6$ is sparingly soluble in CH_2Cl_2, $CHCl_3$, chlorobenzene, toluene and soluble to a very small extent in hexane and pentane. It has very low solubility in MeOH and EtOH. The best solvent for $C_{18}Br_6$ was found to be CS_2 with a solubility of approximately 0.4 mM. Due to its low solubility a ^{13}C NMR spectrum of $C_{18}Br_6$ could not be obtained despite multiple attempts. $C_{18}Br_6$ is a challenging compound to characterise due to the lack of proton resonances and very limited solubility. Conclusive structural determination was obtained *via* single crystal X-ray analysis. Single crystals suitable for X-ray analysis were grown from a saturated solution of $C_{18}Br_6$ in CS_2 at 4 °C (Figure 3.10). The crystals are orthorhombic (*Fdd*2 space group) with eight molecules per unit cell, and half a molecule of $C_{18}Br_6$ in the asymmetric unit. The compound adopts a layer structure, with a layer spacing of 3.412(1) Å, and the packing arrangement resembles that in the corresponding hydrocarbon, $C_{18}H_6$[56].

The intermolecular Br···Br distances within each layer (3.458, 3.478 and 3.500 Å) are significantly shorter than twice the van der Waals radius of bromine (3.70 Å)[57], however these distances should not be taken as absolute as there is a relatively high degree of disorder in the crystal structure (R-factor = 13%).

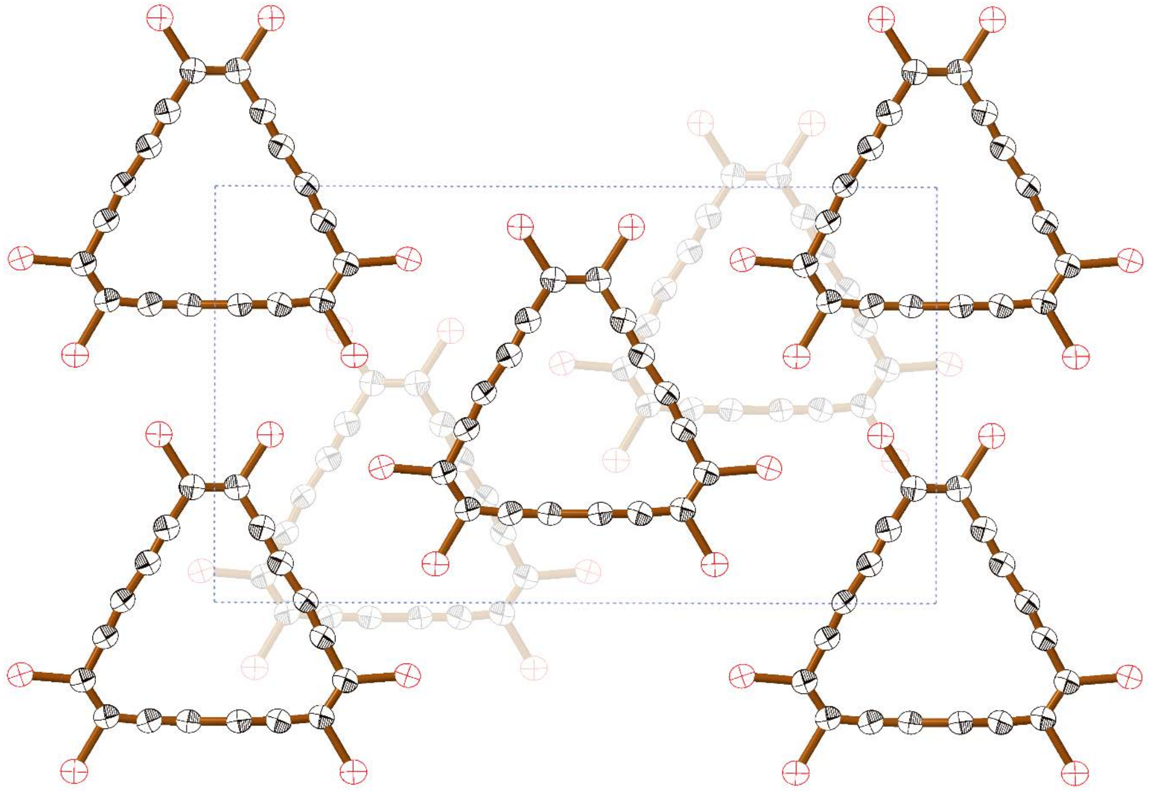

Figure 3.10 Crystal structure of $C_{18}Br_6$, viewed along the crystallographic *b*-axis, showing two layers of molecules. The central rectangle is the unit cell (thermal ellipsoids: 50% probability level).

An interesting question to consider when contemplating the structure of $C_{18}Br_6$ is that of the extent of BLA. Analysis of BLA in $C_{18}Br_6$ will be discussed in the next section.

3.3.7 Investigations into the structure of $C_{18}Br_6$

For the 18π aromatic system of $C_{18}Br_6$ one could imagine two possible resonance forms, acetylenic and cumulenic (Figure 3.11). Chemical intuition would suggest that the acetylenic resonant form will be dominant. The resonance between these two forms might be probed by ^{13}C NMR analysis of the chemical shifts of the compound however due to the low solubility of $C_{18}Br_6$ this method was not possible. Crystal structure and computational analysis were used to determine the extent of BLA in $C_{18}Br_6$. Herein BLA is defined as the total difference in length of adjacent C–C bonds. For the cyclic structures under consideration the BLA was calculated as the difference in length between the central single bond and the average length of the adjacent triple bonds.

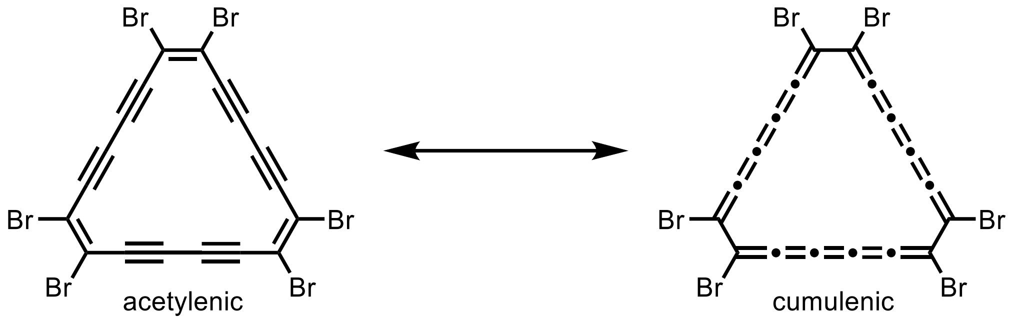

Figure 3.11 Two possible resonance forms of $C_{18}Br_6$.

The crystal structure of $C_{18}Br_6$ showed a relatively high degree of disorder and asymmetry within the $C_{18}Br_6$ molecule. However, upon analysis of the asymmetric unit, clear BLA can be observed along the long side of the asymmetric unit; C–C bond lengths of 1.470, 1.206, 1.368, 1.194 and 1.452 Å and BLA = 0.168 Å. The shorter side of the asymmetric unit does not show the expected BLA and therefore only the long side was considered in the bond order analysis (Figure 3.12).

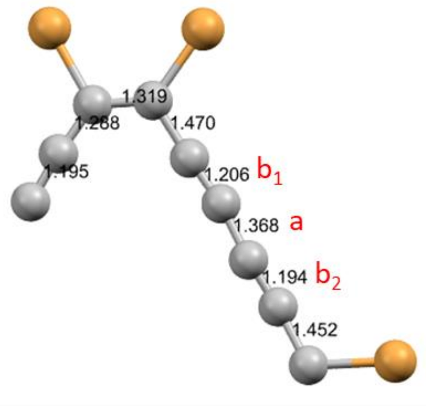

$$\mathrm{BLA} = a - (b_1 + b_2/2) = 0.168\ \text{Å}$$

Figure 3.12 Bond length analysis of the asymmetric unit of the crystal structure of $C_{18}Br_6$.

Due to the uncertainty surrounding the asymmetry in the crystal structure of $C_{18}Br_6$ its molecular structure was calculated by DFT for comparison (Figure 3.13). Structures were calculated at the ωB97X-D3/def2-TZVP level of theory and were verified to be minima by the absence of imaginary frequencies upon calculation of the Hessian. This method has also been shown to reproduce the correct symmetry and BLA of C_{18} compared with the CCSD/def2-TZVP level of theory[58]. As a calibration for the DFT calculations the DFT structure of $C_{18}H_6$ was also calculated as this compound has two reported, well refined, crystal structures[56,59]. BLA in these structures was calculated as described above, the difference in BLA between the calculated and crystal structure is defined as the ΔBLA_{xtal}.

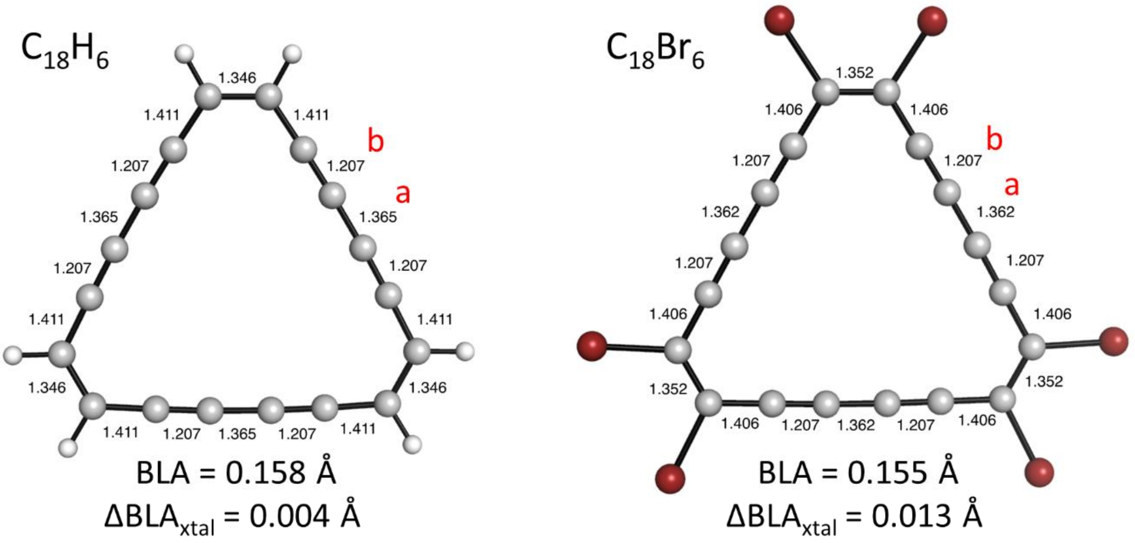

Figure 3.13 Calculated structures of $C_{18}H_6$ and $C_{18}Br_6$, the BLA in the calculated structure of $C_{18}H_6$ was found to have good agreement with its crystal structure.

Both $C_{18}H_6$ and $C_{18}Br_6$ were calculated to have a similarly large BLA (0.158 Å for $C_{18}H_6$ and 0.155 Å for $C_{18}Br_6$) consistent with a preference for the acetylenic resonance form over the cumulenic form. The BLA in $C_{18}H_6$ was only compared to one of the reported crystal structures[56] (R-factor < 4) due to its measurement at lower temperature (100 K vs 173.1 K[59]) in an attempt to minimise any potential thermal effects as the calculated structure has no thermal energy correction to the geometry. For $C_{18}H_6$ the $\Delta BLA_{xtal}(C_{18}H_6) = 0.004$ Å is significantly smaller than the $\Delta BLA_{xtal}(C_{18}Br_6) = 0.013$ Å. The larger ΔBLA_{xtal} for $C_{18}Br_6$ is likely due to disorder in the crystal structure of $C_{18}Br_6$ affecting the BLA value. The crystal structure of $C_{18}Br_6$ was recorded at 150 K however crystal structure disorder is likely to have a larger effect on the calculated BLA than thermal effects.

These calculated structures were used to attempt to quantify the extent of BLA in these systems. Typical C–C bond lengths in butadiynes and cumulenes from crystallographic data are as shown below (each distance is averaged from at least 5 structures with low R factors in the Cambridge crystallographic database) and a molecule that is between these two extremes (Figure 3.14).

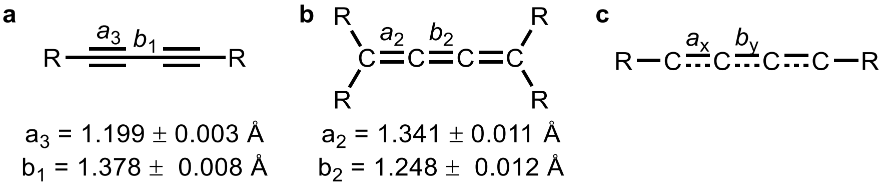

Figure 3.14 Typical CC bond lengths in **a**) butadiynes **b**) cumulenes and **c**) a theoretical molecule between the two extremes.

The level of polyyne character can be defined as a variable *P* ranging from *P* = 1 if it is a polyyne to *P* = 0 if it is a cumulene. Values of *P* can be estimated from a_x and b_y.

$$P_a = \frac{(a_2 - a_x)}{(a_2 - a_3)} \quad (1) \qquad \text{and} \qquad P_b = \frac{(b_y - b_2)}{(b_1 - b_2)} \quad (2)$$

This method can be used to calculate the level of polyyne character in the following structures (Figure 3.15). The bond lengths quoted for the crystal structure of $C_{18}Br_6$ are the mean crystallographic bond lengths from the long side of the asymmetric unit.

Calculations *via* this method gives

a) $P_a = 0.94 \pm 0.02$; $P_b = 0.90 \pm 0.06$
b) $P_a = 0.94 \pm 0.02$; $P_b = 0.88 \pm 0.06$
c) $P_a = 0.94 \pm 0.02$; $P_b = 0.88 \pm 0.06$
d) $P_a = 0.99 \pm 0.02$; $P_b = 0.92 \pm 0.06$

These calculations imply that there is a small but detectable contribution of the cumulenic form of approximately 1–12%.

The errors in P_a and P_b were estimated using equations (3) and (4).

$$\sigma_{P_a} = \frac{\sqrt{\sigma_{a_2}^2 (a_x - a_3)^2 + \sigma_{a_3}^2 (a_2 - a_x)^2}}{(a_2 - a_3)^2} \tag{3}$$

$$\sigma_{P_b} = \frac{\sqrt{\sigma_{b_1}^2 (b_y - b_2)^2 + \sigma_{b_2}^2 (b_y - b_1)^2}}{(b_1 - b_2)^2} \tag{4}$$

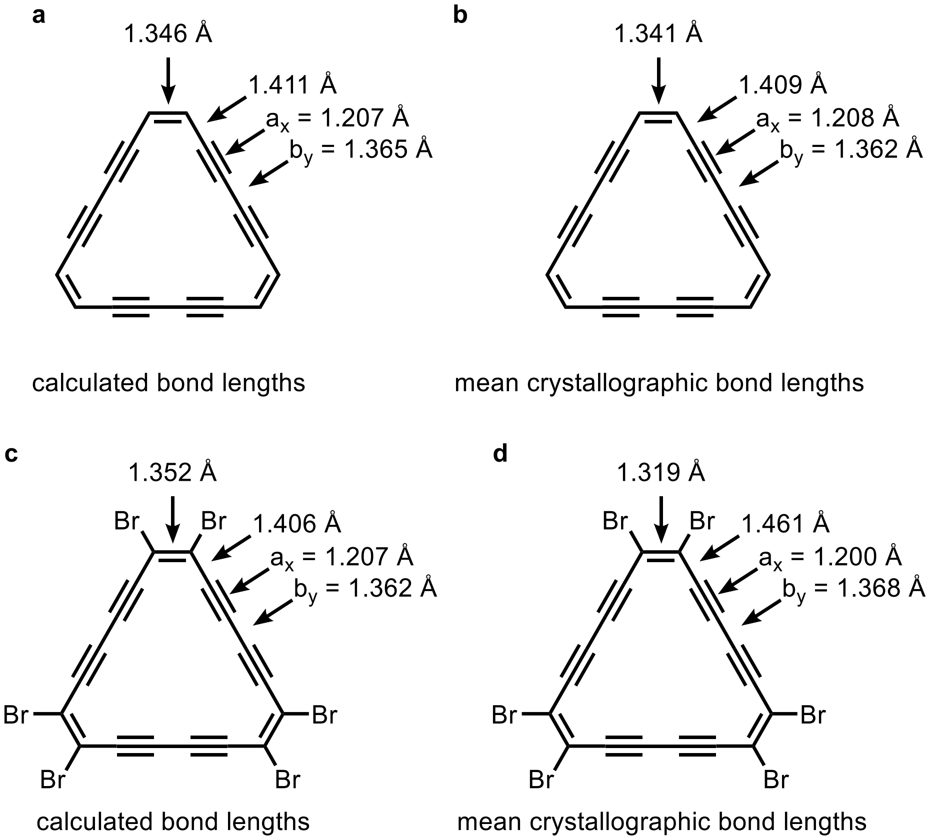

Figure 3.15 Bond lengths used in calculations regarding the level of polyyne character in $C_{18}H_6$ and $C_{18}Br_6$. **a**) Calculated $C_{18}H_6$, **b**) crystallographic $C_{18}H_6$, **c**) calculated $C_{18}Br_6$ and **d**) crystallographic $C_{18}Br_6$.

From this analysis it was concluded that $C_{18}Br_6$ was likely to be mainly acetylenic in character and show bright lobes for the triple bonds in AFM images. This section has detailed the synthesis and properties of $C_{18}Br_6$, the next section of this chapter will discuss the on-surface unmasking of $C_{18}Br_6$ to cyclo[18]carbon and further insights into the structure of cyclo[18]carbon obtained from these measurements.

3.4 Results and Discussion

This section discusses the synthesis of C_{18} *via* a new route: dehalogenation of $C_{18}Br_6$, which occurs under milder conditions, and with a five times higher yield (64%) compared to the yield of formation from $C_{24}O_6$ (13%). The dissociated Br atoms are immobile on the NaCl surface under our imaging conditions and hinder motion of the C_{18} molecules, which facilitated high-resolution AFM imaging at different tip heights. We compared the AFM data for C_{18} with simulated images for the four possible symmetries of cyclo[18]carbon, cumulenic D_{18h}, polyynic D_{9h}, cumulenic D_{9h} and polyynic C_{9h}.

3.4.1 Synthesis of cyclo[18]carbon *via* debromination of $C_{18}Br_6$

The synthesis and characterisation of cyclo[18]carbon was carried out in a low-temperature combined STM/AFM system (for more details see 2.3.2 and 2.3.3). The $C_{18}Br_6$ precursor was thermally sublimed onto a cold Cu(111) surface ($T \approx 5$ K) partially covered with NaCl bilayer islands, yielding a sub-monolayer coverage of well-dispersed molecules. No intact $C_{18}Br_6$ molecules were observed on the bare Cu(111) surface, possibly due to its high reactivity and all atom-manipulation experiments were carried out on bilayer NaCl. The tip was functionalised with carbon monoxide (CO) to enhance the AFM contrast[60,61]. AFM measurements were recorded in constant-height mode, where Δz denotes the tip height offset with respect to the STM set-point (a positive Δz corresponds to an increase in tip-sample distance).

Sublimation of $C_{18}Br_6$ yielded exclusively intact $C_{18}Br_6$ molecules with no appearance of C_{18} or partially debrominated intermediates. This indicates that, unlike the cyclocarbon oxide precursor $C_{24}O_6$[2], unmasking did not take place during sublimation and adsorption. Figure 3.16a-d shows AFM images of the intact $C_{18}Br_6$ precursor recorded at different tip-sample distances, revealing a characteristic triangular shape. The six bright features at the corners relate to the Br atoms and the bright features along the edges of the triangular core correspond to C≡C triple bonds[2,28,62]. The non-uniform brightness of Br atoms and triple bonds within the molecule results from a non-planar adsorption geometry, with the brighter parts of the molecule indicating their greater height[63]. These differences are most distinct in the AFM images recorded at large tip-sample distances (Figure 3.16a,b). At small tip-sample distances (Figure 3.16c,d), tip relaxations, such as tilting of the CO, cause image distortions and detrimentally affect the AFM images[60,61,64,65].

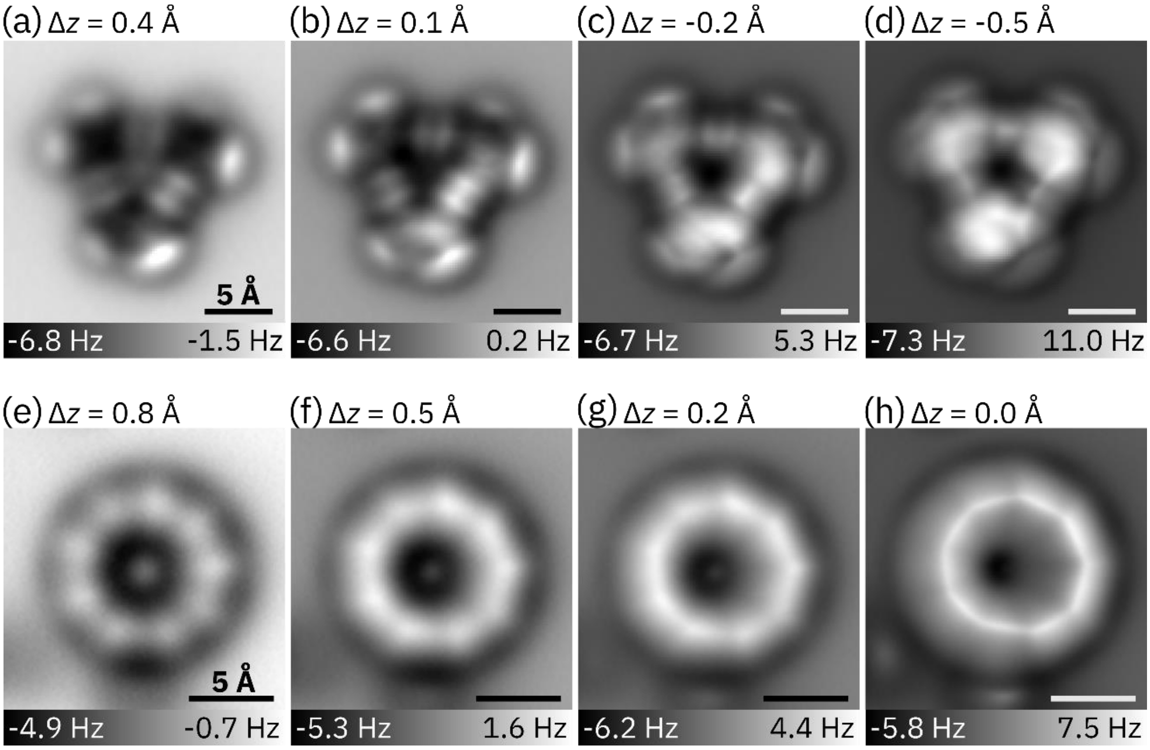

Figure 3.16 AFM images of (a)–(d) $C_{18}Br_6$ and (e)–(h) cyclo[18]carbon recorded at different Δz. In (e)–(h), the scan angle was adjusted such that the scanned plane was parallel to the molecule instead of the underlying surface. Δz denotes the difference in tip-sample distance with respect to the set-point of $I = 0.5$ pA, $V = 0.2$ V. All scale bars 5 Å.

Debromination of $C_{18}Br_6$ was typically achieved by positioning the tip a lateral distance of 1–3 nm from the centre of the molecule, retracting it by 2–3 Å from the STM set-point (typically $I = 0.5$ pA, $V = 0.2$ V) to minimise the tunneling current ($I < 50$ fA) and increasing the bias voltage to 2 V for up to 5 s. With this procedure, we could remove one to six bromine atoms and ultimately generate cyclo[18]carbon from $C_{18}Br_6$ in a yield of ~64% (see Section 3.4.3 for further details). Thus cyclo[18]carbon could be generated more reliably and in higher yield than in previous work, from a cyclocarbon oxide precursor[2]. The increased yield of formation of cyclo[18]carbon is probably a consequence of the lower voltage required for unmasking. AFM images of cyclo[18]carbon synthesised from $C_{18}Br_6$ were recorded at several different tip-sample distances (Figure 3.16e-h). Cyclo[18]carbon adsorbs in a non-planar geometry on bilayer NaCl[2]. To correct for this the plane for constant-height imaging was adjusted by 4° with respect to the NaCl surface to tilt the imaging plane approximately parallel to the molecular plane, so as to obtain a uniform contrast across the molecule. The dark features next to the cyclo[18]carbon molecule in Figure 3.16e (bottom and left), which become bright in Figure 3.16h, can be assigned to the dissociated bromine atoms. Further examples are shown in Figure 3.17.

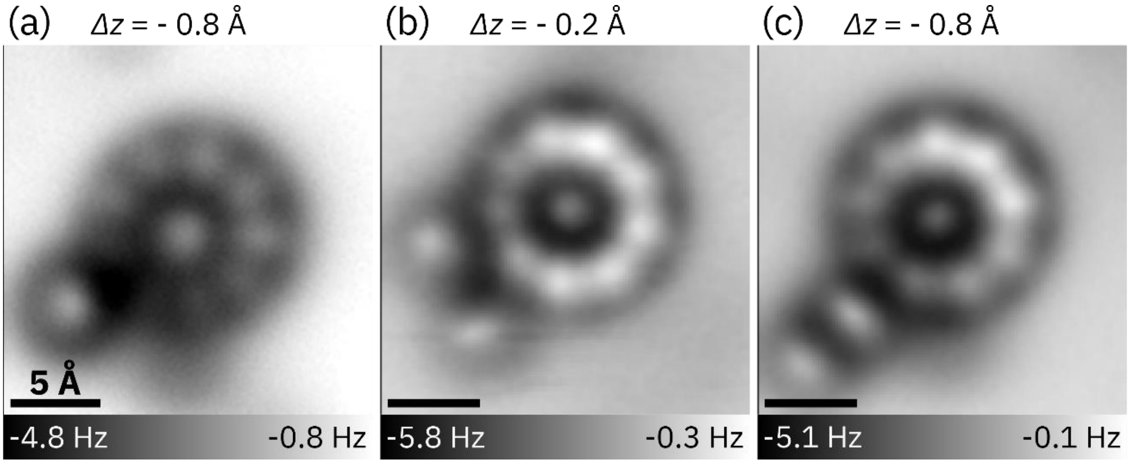

Figure 3.17 AFM images of different of different C_{18} molecules generated by atom manipulation of $C_{18}Br_6$. The bright features next to the molecules can be assigned to dissociated Br atoms. Δz denotes the tip-height offset from an STM set-point of $I = 0.5$ pA, $V = 0.2$ V. All scale bars correspond to 5 Å.

These dissociated Br atoms were found to stabilise and prevent motion of the cyclo[18]carbon molecules, which is advantageous for high-resolution AFM imaging: it enabled us to obtain AFM data for C_{18} with improved resolution and data sets with different tip heights on the same molecule without moving it (Figure 3.16e-h). As reported for cyclo[18]carbon formed from $C_{24}O_6$, the molecule shows nine bright lobes in the AFM images recorded at larger tip-sample distances (Figure 3.16e,f) that transition into nine corners for smaller tip-sample distances (Figure 3.16g,h). The nine bright lobes are assigned to the triple bonds. These data sets obtained on the same molecule for different tip heights allowed further insights into the structural characterisation of cyclo[18]carbon to be obtained, this will be discussed in the next section.

3.4.2 Structural characterisation of cyclo[18]carbon

The experimental AFM images of C_{18} (Figure 3.16e-h) were compared with simulated images of C_{18} using the probe particle model based on the four different symmetries **A**–**D** (Figure 3.3) with different degrees of BLA and BAA. AFM images of the different calculated geometries of cyclo[18]carbon were simulated using the probe-particle model (PPM) implemented by Hapala *et al*[61] (see Section 1.3.7). In this code, the interaction between (functionalised) tip and sample is calculated using classical force fields to determine the relaxation of the probe particle (CO) in the presence of the molecule. Electrostatic interactions between the CO at the tip apex and the molecule are modelled by assigning a charge and charge distribution to the CO and calculating its interactions with the Hartree potential of the molecule. For the simulations we used an oscillation amplitude of A = 50 pm, a lateral spring constant of the CO of 0.2 N/m and an electrostatic monopole on the oxygen of –0.05 e[2,66].

As input for the AFM simulations we used the atomic coordinates (Figure 3.18 and Table 3.1) from high level *ab initio* CCSD theory calculations with the cc-pVDZ basis set[18] (C_{18h} cumulene: $d_1 = d_2 = 1.30$ Å, $\theta_1 = \theta_2 = 160°$; D_{9h} polyyne: $d_1 = 1.38$ Å, $d_2 = 1.24$ Å, $\theta_1 = \theta_2 = 160°$; D_{9h} cumulene: $d_1 = d_2 = 1.30$ Å, $\theta_1 = 157.1°$, $\theta_2 = 162.9°$; C_{9h} polyyne: $d_1 = 1.38$ Å, $d_2 = 1.24$ Å, $\theta_1 = 156.7°$, $\theta_2 = 163.3°$), as well as related coordinates with up to a factor of four increase in BAA.

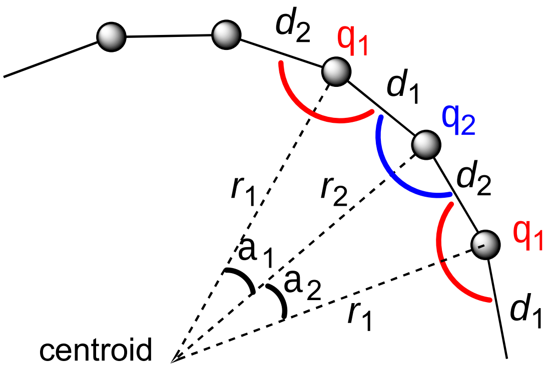

Figure 3.18 Definition of the radial coordinates r_1, r_2, α_1 and α_2 for a molecule of C_{18} ($\alpha_1 + \alpha_2 = 40°$).

Polar atomic coordinates, r_1, r_2, α_1 and α_2 were calculated from bond lengths d_1 and d_2 and bond angles θ_1 and θ_2 using equations (5)–(8):

$$r_1 = \frac{\sqrt{d_1^2 + d_2^2 - d_1 d_2 \cos\theta_1}}{2\sin(20°)} \tag{5}$$

$$r_2 = \frac{\sqrt{d_1^2 + d_2^2 - d_1 d_2 \cos\theta_2}}{2\sin(20°)} \tag{6}$$

$$\alpha_1 = \cos^{-1}\left(\frac{r_1^2 + r_2^2 - d_1^2}{2r_1 r_2}\right) \tag{7}$$

$$\alpha_2 = \cos^{-1}\left(\frac{r_1^2 + r_2^2 - d_2^2}{2r_1 r_2}\right) \tag{8}$$

The corresponding Hartree potentials were calculated using the all-electron density functional theory (DFT) code FHI-aims[67] by letting the electronic structure relax while constraining the atomic coordinates. The same settings as in Chapter 2 were used. We used the Heyd-Scuseria-Ernzerhof (HSE) hybrid functional[68] as the exchange-correction functional, with a mixing parameter of 0.8. The Tkatchenko-Scheffler correction[69] was used to account for van der Waals interactions. For all calculations the default 'tight' settings for the atomic basis set were used. The tip-height offsets of the simulated AFM images were adjusted to match the experimental data.

The simulated AFM images of cyclo[18]carbon with a D_{18h} cumulene geometry (Figure 3.19) show a uniform circular shape, without contrast modulations for all tip-sample distances. Figure 3.20 shows simulated AFM images of the D_{9h} polyyne geometry with the theoretically predicted BLA[18] (Figure 3.20b) as well as geometries with half (Figure 3.20a) and twice (Figure 3.20c) this predicted BLA. The AFM simulations of the different D_{9h} polyyne geometries illustrate how the AFM contrast evolves with different BLA: The differences in the Δf signal between the neighbouring single and triple bonds in cyclo[18]carbon relate to their respective differences in electron density. The larger the BLA the greater are the differences in electron density between formal single and triple bonds (bond order alternation) and thus, the more pronounced are the differences in the AFM contrast above single and triple bonds. In agreement with this, the bright lobes atop the triple bonds in the AFM simulations at large tip-sample distances ($0.8\ \text{Å} \geq \Delta z \geq 0.5\ \text{Å}$) are most pronounced in Figure 3.20c (largest BLA) and least pronounced in Figure 3.20a (smallest BLA). With the parameters that we used in the PPM simulations, Figure 3.20b fits best to our experimental data.

Figure 3.21a–c shows simulated AFM images of the D_{9h} cumulene geometry with different degrees of BAA. AFM simulations of the theoretically predicted geometry[18] with bond angles of $\theta_1 = 162.85°$ and $\theta_2 = 157.15°$ (BAA = 5.7°) are shown in Figure 3.21a. The simulated AFM images are almost identical to those of the D_{18h} cumulene geometry (Figure 3.19). For twice the theoretically predicted BAA (11.4°) the changes in the bond angles become apparent as corners in the AFM simulations for small Δz (Figure 3.21b). However, at larger Δz the contrast still resembles that of the D_{18h} geometry. For the BAA of 22.8° (Figure 3.21c) a nine-fold symmetry is already visible at large Δz, *i.e.*, $\Delta z = 0.7$ Å, where corners can be seen. In contrast to the polyyne geometries, the magnitude of the Δf contrast is uniform above the ring. Interestingly, the simulations at small tip-sample distances, *i.e.*, $\Delta z = 0.1$ Å and $\Delta z = 0.2$ Å, are very similar to the contrast of the polyyne geometries exhibiting a nonagon, although the origin of the nonagonal contrast is quite different for cumulene and polyyne. In the D_{9h} polyyne, the nonagonal shape arises because of the different electron densities above single and triple bonds and the corners of the nonagon are located above the positions of triple bonds. In D_{9h} cumulenes the nonagon relates to the geometry of the molecule and the corners are located above the atom positions at more acute bond angles.

Figure 3.22 shows simulated AFM images of the C_{9h} polyyne geometry with different magnitude of BAA. The theoretically predicted geometry[18] with bond angles of θ_1 = 163.27° and θ_2 = 156.73° is shown in Figure 3.22a. Geometries with twice and four times the BAA are shown in Figure 3.22b,c, respectively. The AFM simulations of all three geometries show nine-fold symmetry with bright lobes atop the triple bonds at larger tip-sample distances (0.8 Å ≥ Δz ≥ 0.4 Å) that transition into corners for smaller Δz, similar to the D_{9h} geometry. At larger tip-sample distances (0.8 Å ≥ Δz ≥ 0.5 Å) the lobes appear slightly asymmetric (droplet-shaped rather than oval), with the larger end pointing towards the more acute bond angle, reflecting the prochirality of the molecule. The C_{9h} geometries with different BAA look very similar in the simulated AFM images.

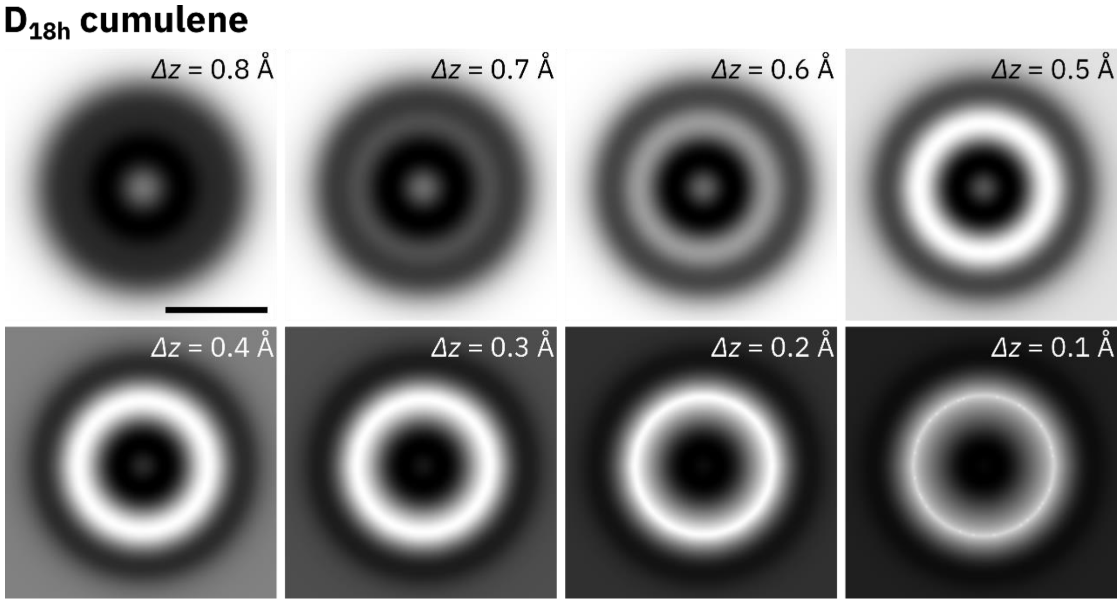

Figure 3.19 Calculated AFM images of C_{18} with a D_{18h} cumulene geometry at decreasing tip-sample distances from top left to bottom right (geometry **A**: $d_1 = d_2 = 1.297$ Å, $\theta_1 = \theta_2 = 160°$).

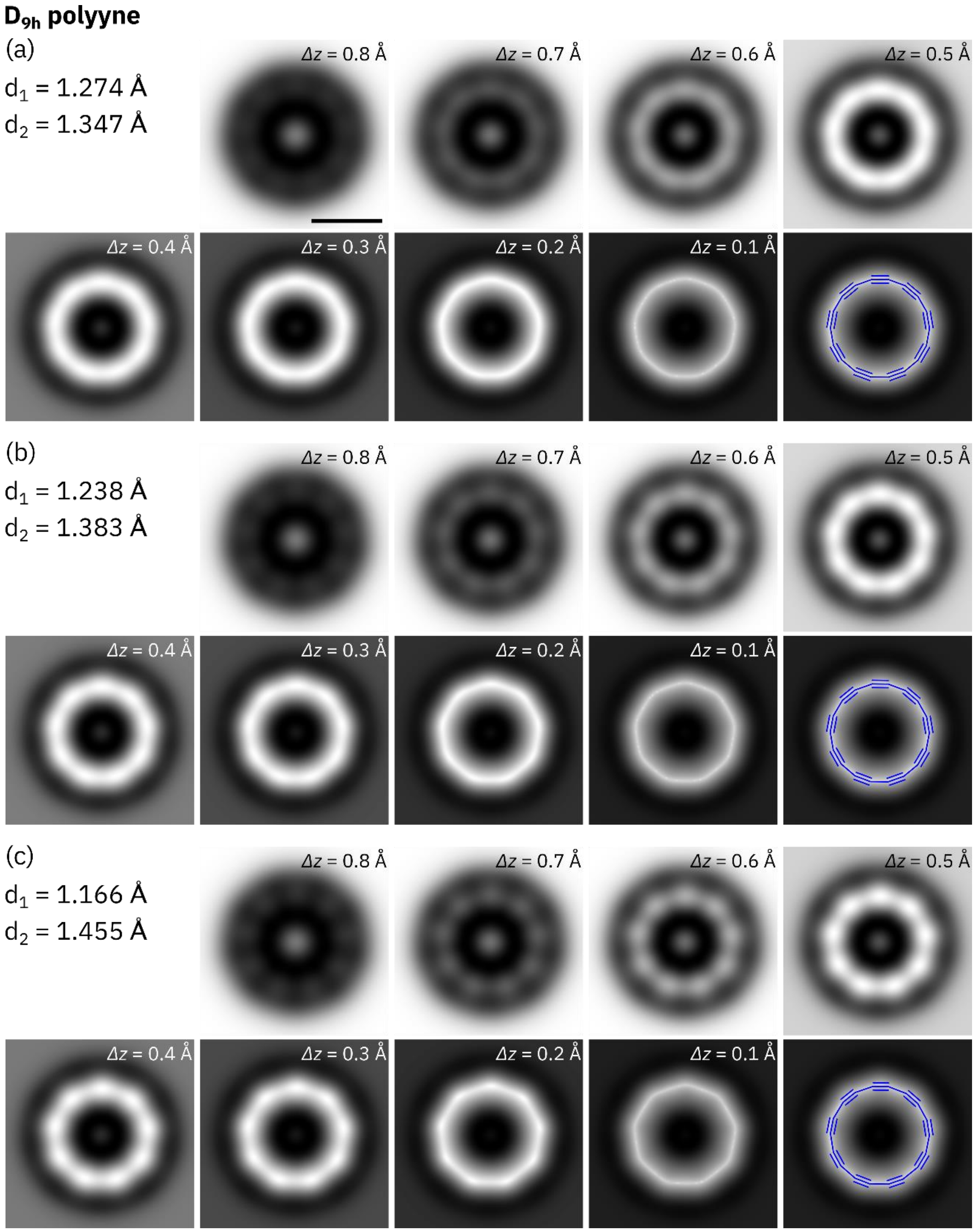

Figure 3.20 Calculated AFM images of C_{18} with a *D*$_{9h}$ polyyne geometry with different degrees of BLA at decreasing tip-sample distances from top left to bottom right. The BLA corresponds to half the theoretically predicted value (**a**, BLA = 0.073 Å), the predicted geometry[18] (**b**, BLA = 0.145 Å) and twice the predicted value (**c**, BLA = 0.289 Å). The images in the respective bottom right panels show again the AFM simulation for Δ*z* = 0.1 Å, but overlaid with the corresponding molecular structure model.

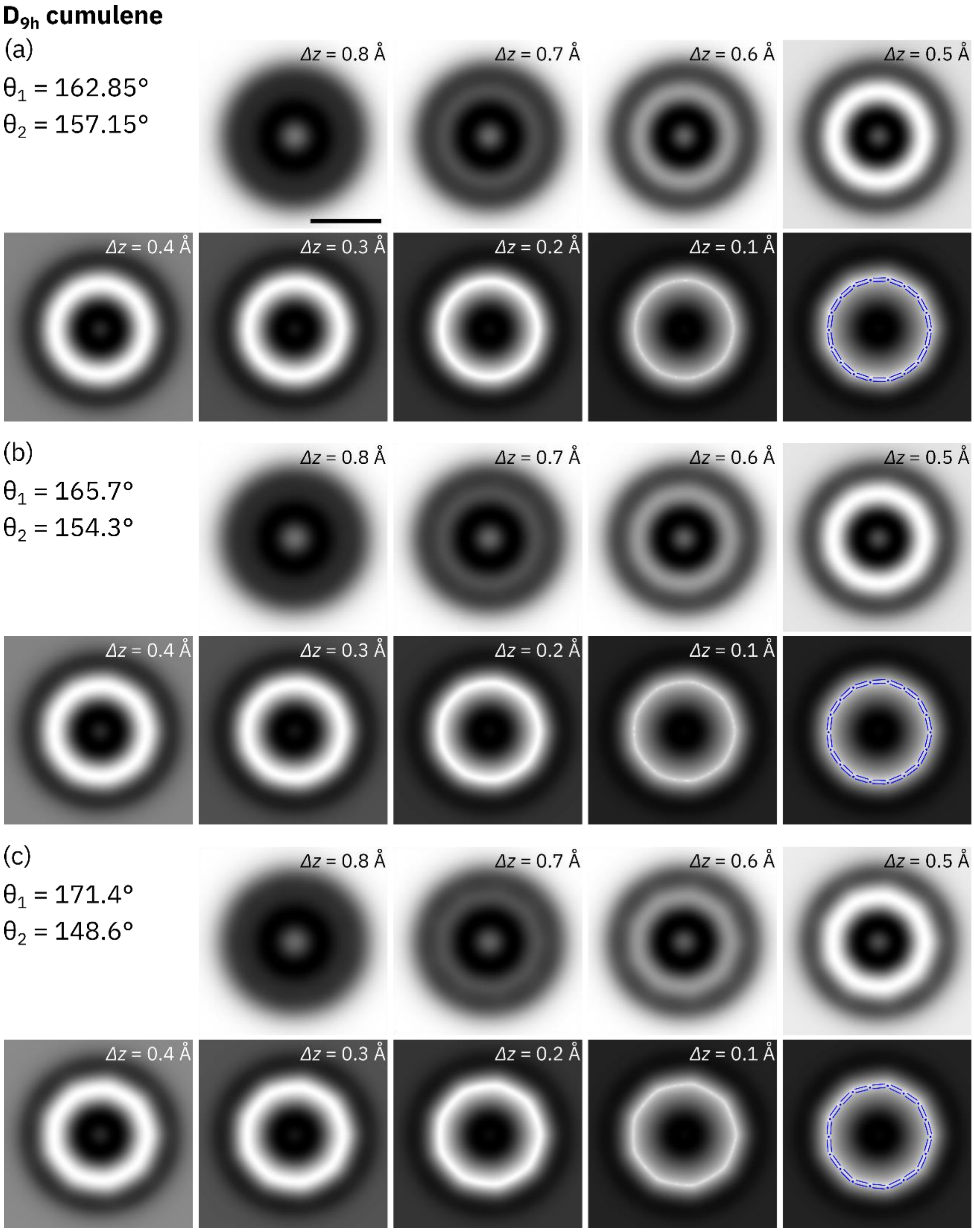

Figure 3.21 Calculated AFM images of C_{18} with a D_{9h} cumulene geometry with different degrees of BAA at decreasing tip-sample distances. The BAA corresponds to the calculated geometry[18] (**a**, BAA = 5.7°) as well as twice (**b**, BAA = 11.4°) and four times the theoretically predicted value (**c**, BAA = 22.8°). The images in the respective bottom right panels show again the AFM simulation for Δz = 0.1 Å, but overlaid with the corresponding molecular structure model.

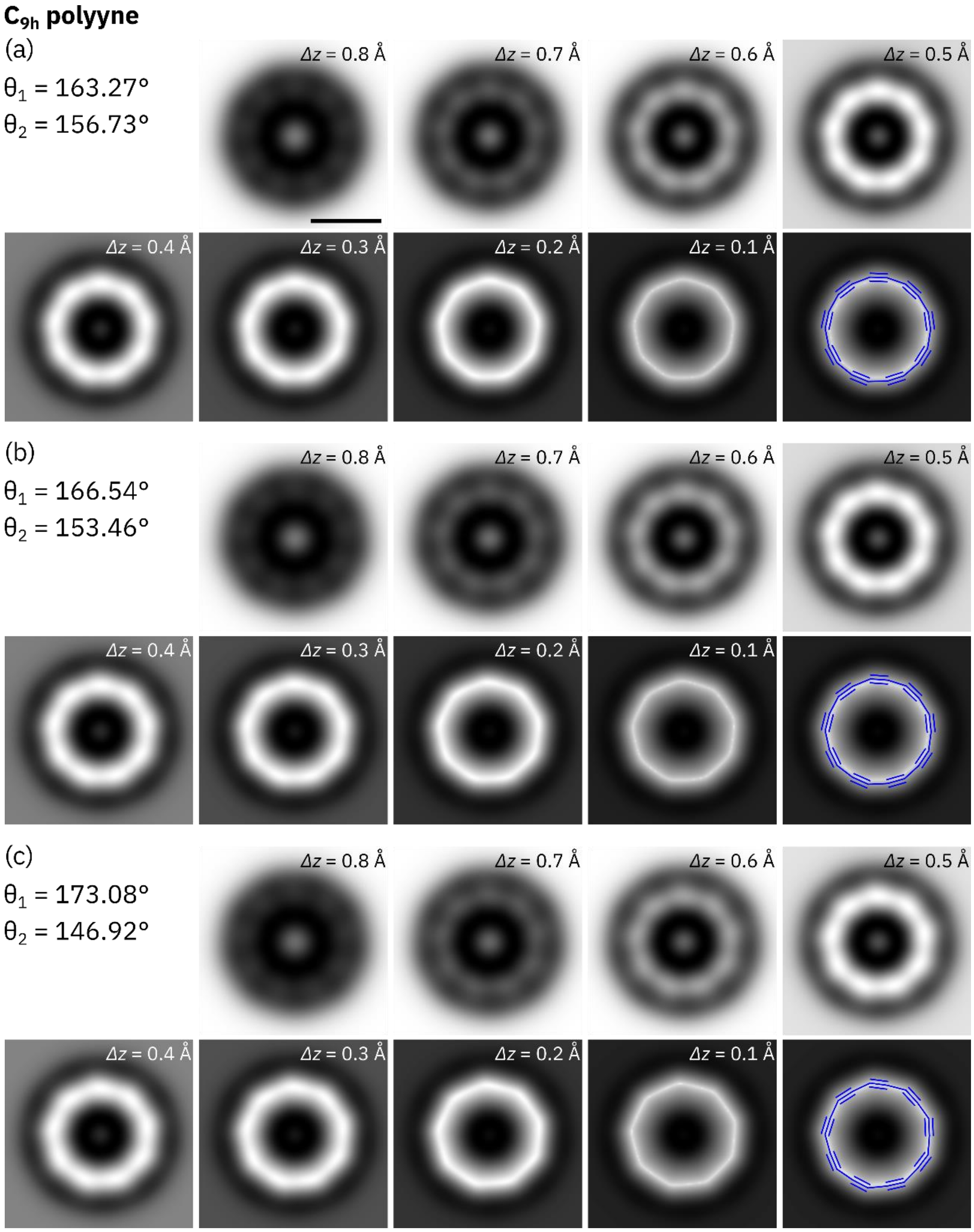

Figure 3.22 Calculated AFM images of C_{18} with a C_{9h} polyyne geometry with different degrees of BAA at decreasing tip-sample distances from top left to bottom right. The BAA corresponds to the calculated geometry[18] (**a**, BAA = 6.54°) as well as twice (**b**, BAA = 13.08°) and four times this value (**c**, BAA = 26.16°). The images in the respective bottom right panels show again the AFM simulation for Δz = 0.1 Å, but overlaid with the corresponding molecular structure model.

In order to compare the effect of BAA on the AFM contrast in the four different geometries we will examine a selection of simulated AFM images (Figure 3.23) at two different tip-sample distances for the calculated geometries[18] of the $D_{18\mathrm{h}}$ cumulene and $D_{9\mathrm{h}}$ polyyne geometries, as well as the $D_{9\mathrm{h}}$ cumulene and $C_{9\mathrm{h}}$ polyyne with four times the calculated BAA[18] (**C**: $\theta_1 = 171.4°$, $\theta_2 = 148.6°$; **D**: $\theta_1 = 173.1°$, $\theta_2 = 146.9°$).

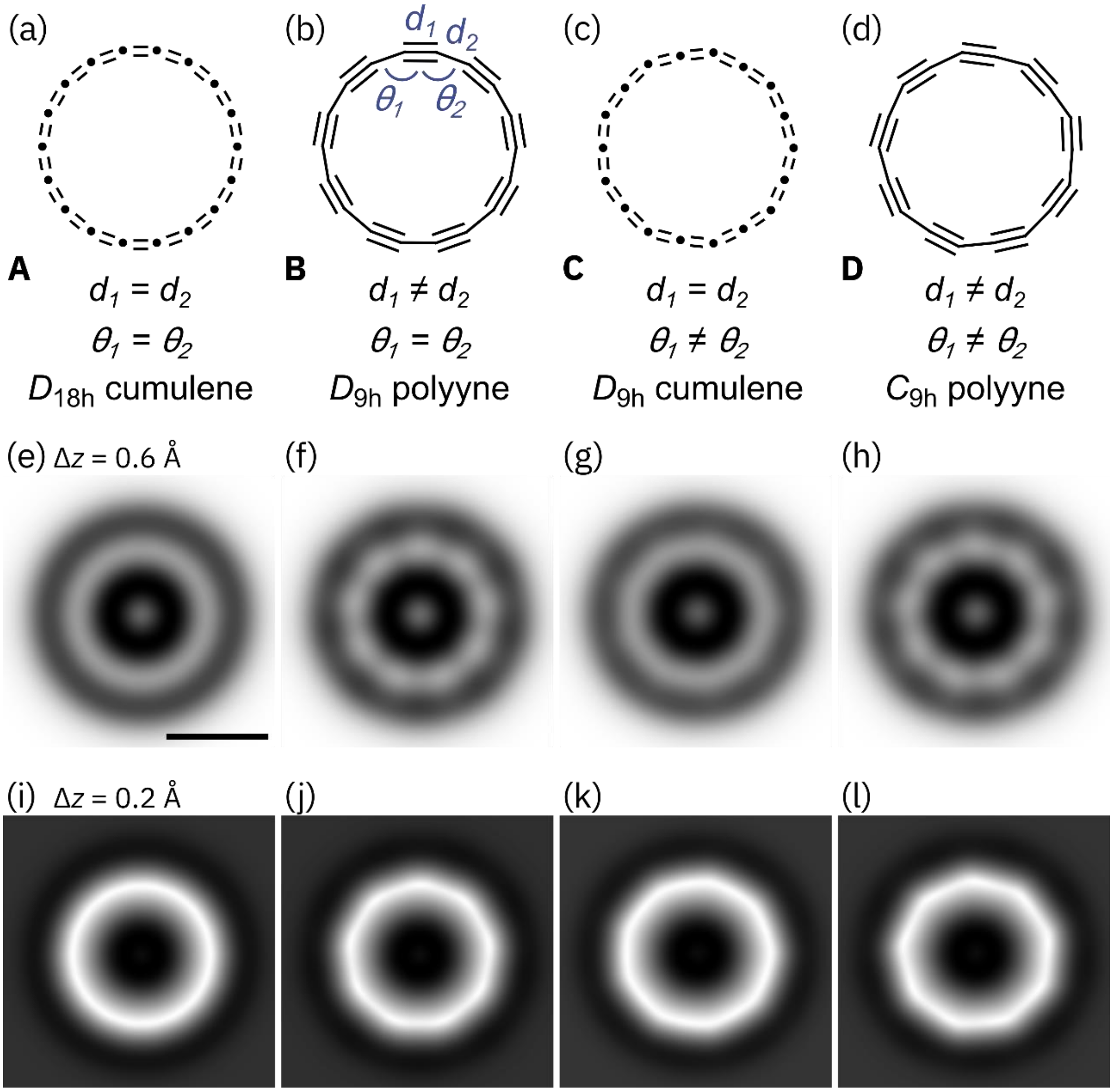

Figure 3.23 Possible geometries of cyclo[18]carbon, **A**–**D**, together with respective simulated AFM images at two different tip-sample distances, (e)–(h): $\Delta z = 0.6$ Å; (i)–(l): $\Delta z = 0.2$ Å. The AFM simulations correspond to geometries with **A**: $d_1 = d_2 = 1.30$ Å, $\theta_1 = \theta_2 = 160°$; **B**: $d_1 = 1.38$ Å, $d_2 = 1.24$ Å, $\theta_1 = \theta_2 = 160°$; **C**: $d_1 = d_2 = 1.30$ Å, $\theta_1 = 171.4°$, $\theta_2 = 148.6°$; **D**: $d_1 = 1.38$ Å, $d_2 = 1.24$ Å, $\theta_1 = 173.1°$, $\theta_2 = 146.9°$. The scale bar in A is 5 Å and applies to all simulated AFM images.

BAA strongly affects the simulated contrast of the D_{9h} cumulene for small tip heights (Figure 3.23k) and the contrast of the cumulene with large BAA becomes very similar to those of the polyynes (Figure 3.23j,l), showing a characteristic nonagon. The corners of the D_{9h} cumulene are located above atom positions, while the corners of the D_{9h} polyyne are above triple bonds. Importantly, the polyyne models can be distinguished from both cumulene models at larger tip height (see Figure 3.23e,g); only the polyynes exhibit nine bright lobes (Figure 3.23f,h) in agreement with the experiment (Figure 3.16e,f). Thus, both cumulenic geometries of cyclo[18]carbon (D_{18h} and D_{9h}) can be excluded. However, the polyyne geometries (D_{9h} and C_{9h}) show almost no change in contrast variations as we varied the BAA which implies that for polyyne geometries it is challenging to resolve or quantify the extent of BAA from AFM images. Two factors may contribute to this effect: (i) In the cumulenic geometries, the introduction of BAA corresponds to a significant change in symmetry from D_{18h} to D_{9h} (i.e. from eighteen-fold to nine-fold symmetry). However, in the polyyne geometries, the introduction of BAA corresponds to a more subtle change in symmetry from D_{9h} to C_{9h}, both of which are nine-fold symmetric. (ii) The AFM contrast of the polyynic geometries is dominated by strong modulations around the carbon ring, due to the large differences in the electron density between triple and single bonds, which are enhanced in AFM by relaxations of the CO tip. On the other hand, BAA affects the position and orientation of the bonds without causing large changes in the electron densities of bonds, resulting in relatively subtle contrast modulations.

These simulations provided further insight into the structure of cyclo[18]carbon by conclusively excluding cumulenic geometries and demonstrating that cyclo[18]carbon can possess either a C_{9h} or D_{9h} symmetry. Not only did the synthesis of cyclo[18]carbon from $C_{18}Br_6$ allow these further insights into the structural characterisation of cyclo[18]carbon it also proceeded in much higher yield than that previously reported, which will be discussed in the next section.

3.4.3 Reaction statistics for on-surface synthesis of cyclo[18]carbon

$C_{18}Br_6$ was found to unmask to cyclo[18]carbon in a five times greater yield than from the $C_{24}O_6$ precursor[2]. The on-surface debromination of $C_{18}Br_6$ was possible at both bias polarities but was found to be more successful at positive sample voltages. The voltage threshold for debromination at positive voltage polarity was found to be around 1.2 V and dissociation of single bromine atoms already occurred before reaching the negative ion resonance of the precursor molecule. Debromination was found to be most successful for lateral distances between tip and precursor molecule of 1–3 nm, relatively large tip-sample distances (tip retracted by 2–3 Å from the STM set-point, i.e., $I < 50$ fA) and sample voltages of around 2 V. In most cases, this procedure resulted in the dissociation of less than 6 Br from the precursor. Two examples of observed intermediates are shown in Figure 3.24a and b. However, for intermediate molecules it was often not possible to determine the exact number of dissociated Br atoms from AFM images as they often stayed next to the intermediate and obscured the contrast in their vicinity. When we observed the characteristic nine-fold symmetric contrast of C_{18}, we concluded that all six Br were dissociated. Table 3.6 summarises the outcome of all tip-induced debromination attempts starting from the intact precursor or an intermediate. The total on-surface reaction yield for cyclo[18]carbon formation was 64% *i.e.*, in 64% of cases we generated C_{18} from an intact $C_{18}Br_6$ precursor by applying one of more successive voltage pulses, and in 36% we generated another final product.

Table 3.6 Reaction statistics for on-surface debromination of $C_{18}Br_6$. Educts were the intact precursor and partially debrominated intermediates. Reaction products were cyclo[18]carbon (C_{18}), partially debrominated intermediates (Figure 3.24a,b), chain-like structures due to breaking of a bond within the cyclic system (non-cyclic products, Figure 3.24c) and other rare cyclic reaction products that could not be further manipulated (rare final products, Figure 3.24d). A total of 21 single molecule reactions induced by atom manipulation were evaluated.

Product Educt	C_{18}	intermediates	non-cyclic products	rare final products
$C_{18}Br_6$	21%	43%	7%	29%
intermediate	100%			

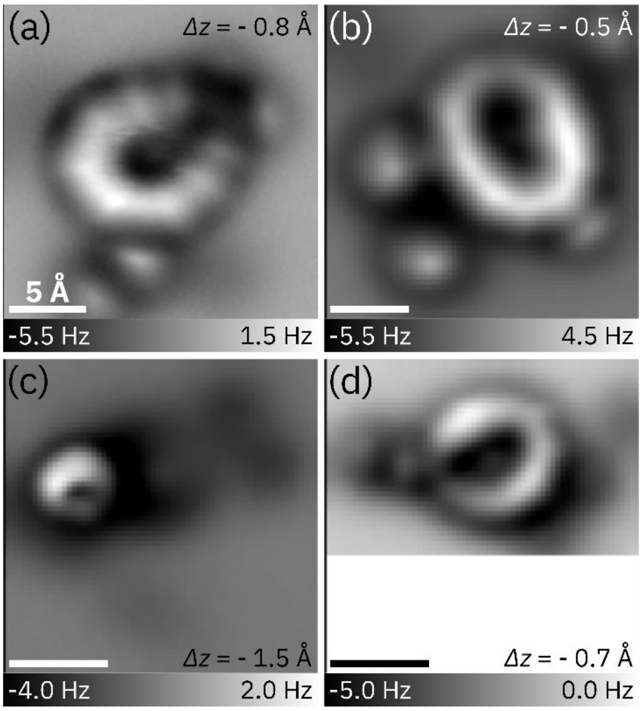

Figure 3.24 AFM images of different reaction products generated *via* atom manipulation of $C_{18}Br_6$. (a) and (b) show intermediates with at least four Br masking groups already dissociated. (c) shows a non-cyclic product and (d) a rare final product. Δz denotes the tip-height offset from an STM set-point of $I = 0.5$ pA, $V = 0.2$ V. All scale bars correspond to 5 Å.

It had been hoped that the mild unmasking of $C_{18}Br_6$ could be used to generate cyclo[18]carbon molecules in close proximity and generate a different size of cyclo[*n*]carbon, such as cyclo[36]carbon by molecular fusion. However, sublimation of $C_{18}Br_6$ always led to well dispersed molecules. One instance of two cyclo[18]carbons being generated in close proximity was recorded but the resultant molecules were too far apart for fusion to occur (Figure 3.25). Nonetheless this example demonstrates the ease and reliability of cyclo[18]carbon synthesis from $C_{18}Br_6$.

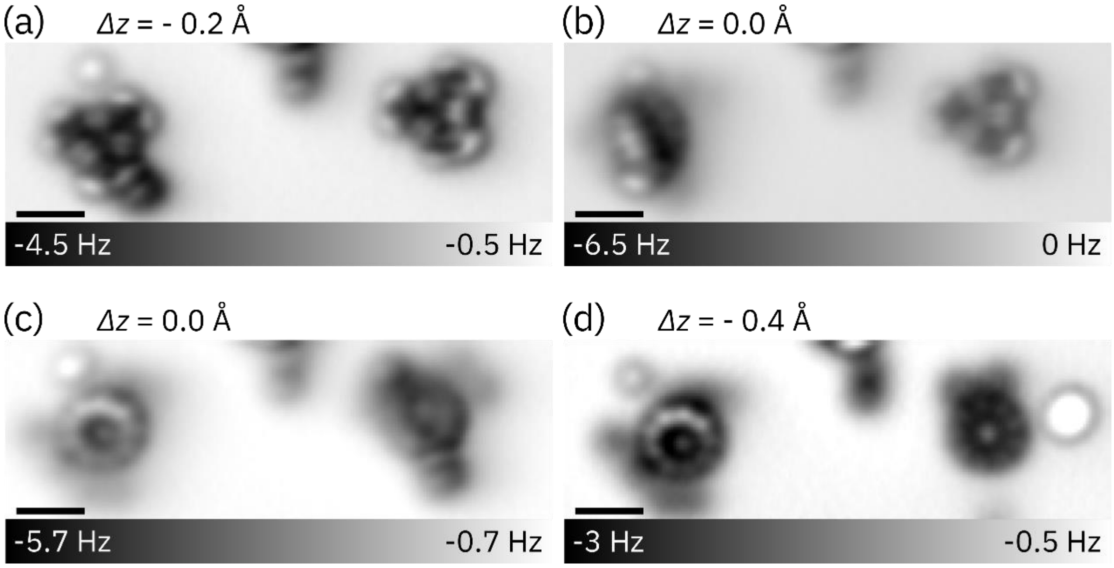

Figure 3.25 AFM images of two $C_{18}Br_6$ precursors prior to and after applying bias voltage pulses of 2–3 V with the tip positioned in close proximity of the molecules. (a) shows both intact precursors prior to atom manipulation. In (b), the precursor on the left has reacted to an intermediate while the precursor on the right remained intact. In (c) the precursor on the left has reacted to C_{18} and the precursor on the right has reacted to an intermediate. (d) shows two cyclo[18]carbon molecules generated by atom manipulation from the precursors shown in (a). The dark features next to the molecules can be assigned to dissociated Br atoms. They hinder motion of the molecules such that the intermediates and cyclo[18]carbon molecules are held in place during voltage pulsing. Δz denotes the tip-height offset from an STM set-point of $I = 0.5$ pA, $V = 0.2$ V. All scale bars correspond to 5 Å.

The reliable synthesis of cyclo[18]carbon from $C_{18}Br_6$ led us to contemplate the reaction mechanism of debromination which will be discussed in the next section.

3.4.4 Reaction mechanism of debromination

As discussed in the previous section, upon debromination of $C_{18}Br_6$ several partly debrominated reaction intermediates (see Figure 3.24 and Figure 3.25) were observed. Thus it was concluded that the debromination of $C_{18}Br_6$ occurs in several steps. Dissociated Br atoms were often observed as individual Br atoms on the NaCl surface near the molecule (see, *e.g.*, Figure 3.17). Because the debromination can be induced even with the tip laterally displaced a few nanometers from the molecule, we assume that the reaction is mediated by hot interface state charge carriers. The bond is likely broken by inelastic energy transfer from charge carriers to the molecule[70,71]. Surface state charge carriers have been shown to induce nonlocal reactions[72,73] on Cu(111). The Cu(111) surface state survives as an interface state[74] for bilayer NaCl on Cu(111). Interface-state charge carriers have been proposed to mediate halogen dissociation reactions[75] and unmasking of the $C_{24}O_6$ precursor of cyclo[18]carbon[2], see Section 2.4.4.

Previous studies into the debromination of a dibromo-alkene on Cu(111) as a function of bias voltage and tunnel current[28] concluded a single-electron process for both Br dissociation reactions with an electron yield of 10^{-9}. However in the case of debromination of $C_{18}Br_6$ on NaCl bilayer on Cu(111), a quantification of the electron yield and determination of the voltage thresholds for the individual debromination reactions was not feasible. This is due to the fact that the bias threshold does not increase for successive reaction steps and many different intermediates, which are challenging to assign, are possible after a pulse (see Figure 3.24).

For $C_{18}Br_6$ on bilayer NaCl on Cu(111), our observations and comparison with previous results[2,28,75–77] point towards successive debromination reactions, induced stepwise by single electrons with a voltage threshold of 2 V or less for each individual C-Br dissociation. For the first Br dissociation from $C_{18}Br_6$ the voltage threshold was approximately 2 V. Because of the observation that we often dissociated several Br within one 2 V voltage pulse until we formed C_{18}, we conclude that the debromination reactions after the first debromination exhibit voltage thresholds of approximately 2 V or less. However, for these subsequent Br dissociations, we cannot exclude that some of them occur spontaneously or that their bias threshold is significantly smaller than 2 V. The dissociated Br atoms (examples shown in Figure 3.24) exhibit a similar contrast to single Br adatoms observed previously[28,78]. There is a possibility that some of the Br atoms could have recombined to form Br_2 however the contrast of Br_2 on the surface is not known and therefore it cannot be determined whether this occurred in these experiments.

The reliability of the synthesis of cyclo[18]carbon from $C_{18}Br_6$ led us to investigate the synthesis of cyclo[18]carbon from $C_{18}Br_6$ on alternative substrates, this will be discussed in the next section.

3.4.5 $C_{18}Br_6$ on xenon

The extent of valence bond-shift tautomerisation is a key question that has been raised in the context of cyclo[*n*]carbons. Theoretical investigations[3,5] of the polyynic form predict a fast rate of quantum mechanical tunneling and therefore one might expect this interconversion between polyyne forms to be fast leading to an apparent D_{18h} symmetry in contrast to the experimental AFM images. This leads to the question of whether the interaction of C_{18} with the NaCl substrate increases the barrier to bond-shift valence tautomerisation.

We planned to address this issue by attempting to form C_{18} on an alternative substrate, a layer of xenon. For the preparation of Xe/Cu(111), the clean Cu sample was cooled, in the microscope, to below 15 K, Xe was then dosed into the UHV chamber up to a partial pressure of 2×10^{-5} mbar. Subsequently, the shutter to the microscope was opened for 35 s resulting in partial coverage with single layer xenon. The $C_{18}Br_6$ precursor molecules were then sublimed onto the cold Xe/Cu(111). The $C_{18}Br_6$ molecules were found to be very mobile on the xenon surface. AFM imaging with a Xe- or CO-terminated tip was not possible, but STM images of $C_{18}Br_6$ in the fundamental gap on Xe could be recorded (Figure 3.26a). Attempts to remove bromine atoms using bias voltage pulses of up to 3 V were unsuccessful and only resulted in lateral movement of the precursor. Higher bias voltages resulted in the molecules jumping away, adsorbing onto the tip, or bonds within the cyclic system being broken, and it was not possible to evaluate whether tip-induced dehalogenation was successful.

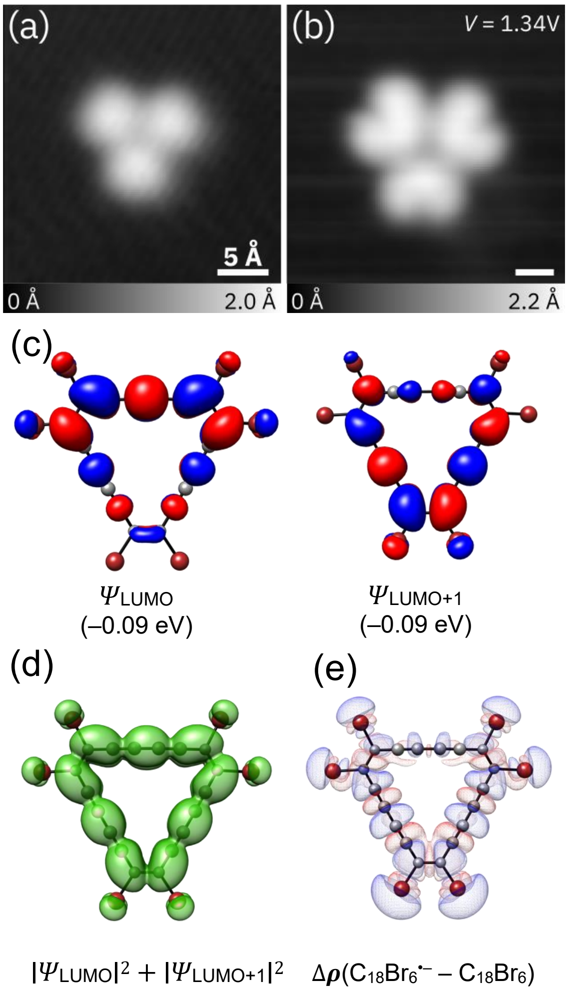

Figure 3.26 STM images of $C_{18}Br_6$ on Xe/Cu(111) recorded at different bias voltages. (a) In-gap STM image, recorded at a set point of $I = 1$ pA, $V = 0.4$ V (b) STM image showing the orbital density of the LUMO, recorded at a set point of $I = 1.2$ pA, $V = 1.34$ V. (c) Degenerate LUMO and LUMO + 1 of $C_{18}Br_6$ (isovalue = 0.02 a.u.) calculated at the DLPNO-CCSD(T)/cc-pVTZ level of theory. (d) $|\Psi_{\text{LUMO}}|^2 + |\Psi_{\text{LUMO+1}}|^2$ (isovalue = 0.0004 e Å^{-3}) calculated at the same level of theory. (e) Difference in electron density ($\Delta\boldsymbol{\rho}$) between $C_{18}Br_6^{\bullet-}$ and $C_{18}Br_6$ (isovalue = 0.0004 e Å^{-3}), at the same level of theory; blue (red) denotes an increase (decrease) in electron density.

However, while attempts to attain orbital density images on NaCl/Cu(111) resulted in (partial) dehalogenation, it was possible to address the negative ion resonance of $C_{18}Br_6$ on Xe/Cu(111). STM images of $C_{18}Br_6$ recorded at its negative ion resonance ($V = 1.34$ V) relate to the density of the LUMO (Figure 3.26b), providing additional evidence that the precursors remained intact upon sublimation. In the case of $C_{18}Br_6$, the comparison of the NIR image and the LUMO is complicated by the degeneracy of the LUMO and LUMO + 1 (Figure 3.26c). However, the sum of the probability densities of the LUMO and LUMO + 1

($|\Psi_{\mathrm{LUMO}}|^2 + |\Psi_{\mathrm{LUMO+1}}|^2$, Figure 3.26, d) can be used to account for this degeneracy once this electron density is convoluted with the tip orbital[79]. A plot of the difference in the electron density between the radical anion and neutral $C_{18}Br_6$ (Figure 3.26e) is asymmetric which suggests that the molecule undergoes a Jahn-Teller distortion upon charging resulting in the asymmetric electron distribution shown in Figure 3.26e in analogy to the charging of copper(II)phthalocyanine[80] and cyclo[18]carbon[2]. Further to this the plot demonstrates that electron density is transferred from the carbocycle onto each bromine atom in the negative charge state (Figure 3.26e), in line with the observation that full electron attachment leads to C–Br bond cleavage.

Unfortunately cyclo[18]carbon could not be generated on the xenon surface as all attempts to remove bromines were unsuccessful and therefore the behaviour of cyclo[18]carbon on an alternative substrate remains still to be examined.

3.5 Conclusions

In conclusion, C_{18} is generated by debromination of $C_{18}Br_6$ on bilayer NaCl on Cu(111) at 5 K, with a five times greater yield than from $C_{24}O_6$ precursors. The synthesis of $C_{18}Br_6$ was achieved *via* a halodeboronation strategy after initial attempts *via* carbenoid coupling and stereoselective bromination were not successful. $C_{18}Br_6$ was definitively characterised by its single crystal X-ray structure and its properties were analysed, including its thermal behaviour. The synthesis of cyclo[18]carbon from $C_{18}Br_6$ enabled high resolution AFM images at a range of different tip heights for the same C_{18} molecule to be obtained. These images were compared with AFM simulations of different geometries of C_{18} and demonstrated that BAA can have a considerable effect on the simulated AFM images for the cumulenic structure but is barely visible for the polyyne. The simulations confirm that the cumulene geometries, even those with extreme BAA, can be excluded, and therefore the polyynic structure of C_{18} on NaCl was corroborated. We found that it is challenging to rule out or quantify BAA in the polyynic geometry. We attempted to study cyclo[18]carbon on a xenon substrate however unmasking of $C_{18}Br_6$ was not possible on the alternative substrate. In the future, we plan to use the debromination of cyclocarbon precursors to explore other cyclo[*n*]carbons.

3.6 Experimental Data

3.6.1 Synthetic General Methods

Reagents (Alfa Aesar, Aldrich, Acros, Fluorochem, Fisher Scientific) were used without further purification. Dry solvents (THF, toluene, CH_2Cl_2) for reactions were purified by a MBraun MB-SPS-5-Bench Top under nitrogen (H_2O content < 20 ppm). All other solvents used were HPLC grade. Reactions, unless otherwise stated, were carried out in oven-dried glassware under a N_2 atmosphere. Flash column chromatography was carried out on a Biotage Isolera One with a 200–400 nm UV detector. Analytical thin layer chromatography (TLC) were performed on aluminium sheets coated with silica gel 60 F254 (Merck). UV light (254 nm) was used for visualisation. Evaporation *in vacuo* was performed at 15–40 °C and 5–1010 mbar. Reported yields refer to pure compounds dried under high vacuum (< 0.1 mbar). ^1H and ^{13}C nuclear magnetic resonance (NMR) were recorded on Bruker AVIII HD 400 spectrometer at 400 MHz (^1H) and 101 MHz (^{13}C) at 294 K. Chemical shifts, δ, reported in ppm downfield from tetramethylsilane using residual deuterated solvent signals as internal reference ($CDCl_3$: $\delta_H = 7.26$ ppm, $\delta_C = 77.16$ ppm). High-resolution mass spectrometry (HR-MS) measurements were performed by the mass spectrometry service at the University of Oxford on a Waters GTC classic. Differential scanning calorimetry was carried out on a Perkin Elmer DSC 4000. Analytical GPC was carried out on a VWR system with a JAIGEL H-P pre-column, a JAIGEL 4H-A column (8 mm × 500 mm) in series with THF/1% pyridine containing 0.1% BHT stabiliser as eluent with a flow rate of 1 mL/min. Semi-preparative recycling GPC was performed on a Shimadzu recycling GPC system equipped with a JAIGEL H-P pre-column, a JAIGEL 3H (20 mm × 600 mm) and a JAIGEL 4H column (20 mm × 600 mm) in series with toluene as eluent with a standard flow rate of 3.5 mL/min.

3.6.2 Synthetic Protocols

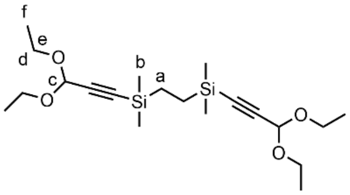

Synthesis of compound 16[81]: *n*-BuLi (0.64 mL, 1.6 M in hexanes, 1.02 mmol) was added to a solution of propargylaldehyde diethyl acetal (147 µL, 1.02 mmol) in THF (3 mL) at –78 °C and the resulting colourless solution stirred for 1 h. 1,2-Bis(chlorodimethylsilyl)ethane (100 mg, 0.47 mmol) in THF (1 mL) was added and the resulting clear yellow solution warmed to 21 °C and stirred for 2 h. The reaction was quenched with a sat. aqueous solution of NH_4Cl (5 mL) and the aqueous phase extracted with Et_2O (3 × 10 mL) and dried over $MgSO_4$ to yield **16** as a pale yellow oil (159 mg, 0.40 mmol, 86%). **^{1}H NMR** (400 MHz, $CDCl_3$): 5.25 (s, 2H; **c**), 3.75 (dq, J = 7.2 and 9.6 Hz, 4H; **d**/**e**), 3.59 (dq, J = 7.2 and 9.6 Hz, 4H; **d**/**e**), 1.24 (t, J = 7.2 Hz, 12H; **f**), 0.60 (s, 4H; **a**), 0.16 (s, 12H; **b**) ppm. **^{13}C NMR** (101 MHz, $CDCl_3$): 100.8, 91.4, 89.6, 61.0, 15.2, 8.3, –2.4 ppm. **HR-ESI-MS m/z:** 421.21964 (Mass corresponds to $C_{20}H_{38}O_4{}^{23}Na^{28}Si_2{}^+$: 421.22008). **IR (ATR):** $\tilde{\nu}$ = 650, 713, 783, 821, 836, 1011, 1055, 1098, 1116, 1251, 1326, 1352, 1404, 1445, 2885, 2976 cm^{-1}.

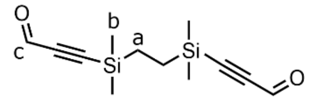

Synthesis of compound 17[82]: A solution of **16** (159 mg, 0.40 mmol) in THF (4 mL) and water (4 mL) was prepared. Concentrated H_2SO_4 (0.17 mL) was added and the resulting opaque solution heated to reflux (80 °C) for 5 h. The reaction mixture was diluted with ethyl acetate (20 mL) and washed with a sat. aqueous solution of Na_2CO_3 (20 mL) and the organic phase dried over $MgSO_4$. The crude was purified by column chromatography, SiO_2 (petroleum ether/ethyl acetate 8:2) to yield **17** as a yellow oil (44 mg, 0.18 mmol, 44%). **^{1}H NMR** (400 MHz, $CDCl_3$): 9.18 (s, 2H; **c**), 0.69 (s, 4H; **a**), 0.26 (s, 12H; **b**) ppm. **^{13}C NMR** (101 MHz, $CDCl_3$): 176.8, 102.9, 102.0, 7.8, –2.9 ppm. ^{1}H NMR and ^{13}C NMR were in accordance with reported values[83].

Synthesis of compound 18[38]: A solution of bromine (0.40 mL, 7.8 mmol) in CH_2Cl_2 (4 mL) was added to triphenyl phosphite (2.05 mL, 7.8 mmol) under N_2 at 0 °C and the resulting clear yellow solution stirred for 5 minutes. A solution of **17** (500 mg, 2.0 mmol) in CH_2Cl_2 (2 mL) was added and the resulting orange solution stirred for 45 minutes. The reaction mixture was diluted with petroleum ether (20 mL) and passed through a plug of silica (petroleum ether/ ethyl acetate 9:1) to yield the crude as a yellow solid which was purified by column chromatography, SiO_2 (petroleum ether) to give **18** as a white solid (620 mg, 1.2 mmol, 58%). **^{1}H NMR** (400 MHz, $CDCl_3$): 6.06 (s, 2H; **a**), 0.64 (s, 4H; **c**), 0.21 (s, 12H; **b**) ppm. **^{13}C NMR** (101 MHz, $CDCl_3$): 101.2, 97.0, 16.4, 7.9, –2.8 ppm. **HR-ESI/APCI/MALDI-MS:** Could not be obtained. **IR (ATR): $\tilde{\nu}$** = 644, 719, 780, 821, 842, 1046, 1120, 1137, 1205, 1249, 1404, 2916, 2961, 2987 cm^{-1}. **Melting point:** 92–94 °C.

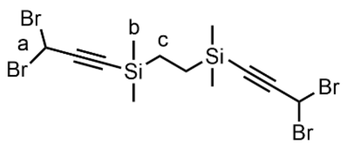

Synthesis of compound 20[38]: A solution of bromine (95 µL, 1.85 mmol) in CH_2Cl_2 (1 mL) was added to triphenyl phosphite (0.49 mL, 1.85 mmol) under N_2 at 0 °C. and the resulting clear yellow solution stirred for 5 minutes. A solution of TIPS-aldehyde (100 mg, 0.48 mmol) in CH_2Cl_2 (0.5 mL) was added and the resulting orange solution stirred for 45 minutes. The reaction mixture was diluted with petroleum ether (5 mL) and passed through a plug of silica (petroleum ether/ ethyl acetate 9:1) to yield the crude as a yellow oil which was purified by column chromatography, SiO_2 (petroleum ether) to yield **20** as a yellow oil (145 mg, 0.41 mmol, 86%). **^{1}H NMR** (400 MHz, $CDCl_3$): 6.08 (s, 1H; **a**), 1.10 (s, 21H; **b**) ppm. **^{13}C NMR** (101 MHz, $CDCl_3$): 102.9, 95.8, 18.6, 16.6, 11.3 ppm. **HR-ESI/APCI/MALDI-MS**: Unable to obtain. **IR (ATR): $\tilde{\nu}$** = 651, 678, 882, 919, 996, 1018, 1049, 1123, 1205, 1385, 1463, 2866, 2943 cm^{-1}.

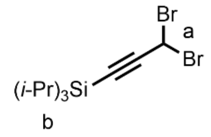

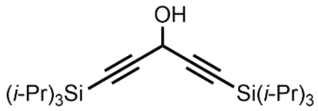

Synthesis of compound 23a[84]: *n*-BuLi (6.85 mL, 1.6 M in hexanes, 11.0 mmol) was added to a solution of TIPS-acetylene (2.46 mL, 11.0 mmol) in THF (30 mL) at –10 °C under N_2 and the resulting clear yellow solution was stirred for 15 minutes. Ethyl formate (0.44 mL, 5.48 mmol) was added over 1.5 h at –10 °C and the solution was then warmed to 0 °C and stirred for 30 minutes. The solution was quenched with a sat. aqueous solution of NH_4Cl (40 mL) and extracted with Et_2O (100 mL). The organic phase was washed with brine (100 mL), dried over $MgSO_4$ and passed through a plug, SiO_2 (petroleum ether) to yield **23a** as an impure orange oil which was used in the next step without further purification (assume 100% yield 2.15 g, 5.48 mmol). **^{1}H NMR** (400 MHz, $CDCl_3$): 5.10 (d, *J* = 7.9 Hz, 1H; C-H), 2.24 (m, 1H; OH), 1.07 (s, 42H; TIPS) ppm. **^{13}C NMR** (101 MHz, $CDCl_3$): 104.4, 85.8, 53.2, 18.7, 11.3 ppm. ^{1}H and ^{13}C NMR were in accordance with reported values[84].

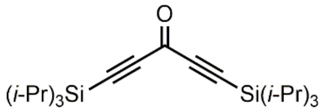

Synthesis of compound 23b[84]: MnO_2 (7.15 g, 82.1 mmol) was added to a solution of **23a** (2.15 g, 5.48 mmol) in dry CH_2Cl_2 (90 mL) and the resulting black suspension stirred for 18 h. The reaction was filtered through a plug of $MgSO_4$ and the crude purified by column chromatography, SiO_2 (petroleum ether/ethyl acetate 9:1) to yield **23b** as a yellow oil (1.64 g, 4.20 mmol, 76% over two steps). **^{1}H NMR** (400 MHz, $CDCl_3$): 1.11 (m, 42H; TIPS) ppm. **^{13}C NMR** (101 MHz, $CDCl_3$): 160.1, 105.4, 97.8, 18.6, 11.2 ppm. ^{1}H and ^{13}C NMR were in accordance with reported values[84].

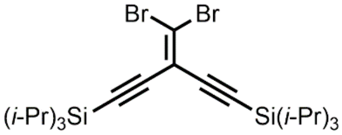

Synthesis of compound 23c[46]: A solution of CBr_4 (2.78 g, 8.39 mmol) in dry CH_2Cl_2 (150 mL) was transferred *via* cannula to a flask containing PPh_3 (4.40 g, 16.8 mmol) under N_2 and stirred at 21 °C for 1 h. A solution of **23b** (1.64 g, 4.20 mmol) in CH_2Cl_2 (40 mL) was then added and the resulting orange solution stirred for 18 h. The reaction mixture was concentrated to 10 mL and petroleum ether (200 mL) was added to precipitate Ph_3PO. The supernatant was decanted and filtered through a silica plug (petroleum ether/ ethyl acetate 95:5) to yield **23c** as an opaque yellow oil (2.0 g, 3.7 mmol, 87%). **^{1}H NMR** (400 MHz, $CDCl_3$): 1.10 (s, 42H; TIPS) ppm. **^{13}C NMR** (101 MHz, $CDCl_3$): 115.1, 108.9, 102.5, 99.6, 18.7, 11.3 ppm. ^{1}H and ^{13}C NMR were in accordance with reported values[46].

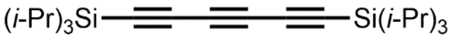

Synthesis of compound 23[46]: *n*-BuLi (2.86 mL, 1.6 M in hexanes, 4.57 mmol) was added over 10 minutes to a solution of **23c** (2.0 g, 3.67 mmol) in pentane (65 mL) at –78 °C under N_2. The solution was then warmed to 21 °C over 30 minutes. The reaction was quenched with a sat. aqueous solution of NH_4Cl (65 mL) and the organic phase collected and dried over $MgSO_4$. The crude was purified by column chromatography, SiO_2 (petroleum ether) to yield **23** as off-white needles (1.22 g, 3.15 mmol, 86%). **^{1}H NMR** (400 MHz, $CDCl_3$): 1.08 (s, 42H; TIPS) ppm. **^{13}C NMR** (101 MHz, $CDCl_3$): 89.9, 84.9, 61.5, 18.7, 11.4 ppm. ^{1}H and ^{13}C NMR were in accordance with reported values[46].

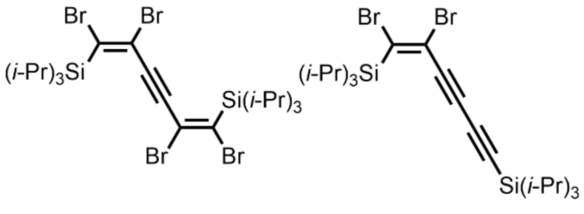

Synthesis of compound 24a/b[45]: TMSBr (56 µL, 0.43 mmol) in CH_2Cl_2 (0.4 mL) was added dropwise to **23** (150 mg, 0.39 mmol) in anhydrous toluene (1.2 mL) at 0 °C. Once the addition was complete NBS (76 mg, 0.43 mmol) in CH_3CN (0.8 mL) was added dropwise to the mixture and the resulting solution heated to 60 °C and stirred for 18 h. The reaction mixture was cooled to 0 °C and quenched with a sat. aqueous solution of $Na_2S_2O_3$ (5 mL) and the two-phase mixture stirred vigorously for 10 minutes. The aqueous phase was extracted with Et_2O (10 mL), washed with brine (10 mL) and dried over $MgSO_4$. The crude was purified by column chromatography, SiO_2 (petroleum ether) to yield **24a** as a white solid (47 mg, 0.09 mmol, 22%), **24b** could not be fully purified due to residual impurities of **24a**. Single crystals of **24a** were grown from a slowly cooled saturated solution of **24a** in MeOH to yield white, needle-like crystals. **24a**: **^{1}H NMR** (400 MHz, CDCl$_3$): 1.14 (m, 42H; TIPS) ppm. **^{13}C NMR** (101 MHz, CDCl$_3$): 142.7, 111.6, 92.4, 18.7, 13.1 ppm. **HR-APCI-MS m/z**: Unable to obtain. **IR (ATR): $\tilde{\nu}$** = 616, 641, 665, 680, 692, 799, 839, 883, 920, 998, 1021, 1204, 1260, 1385, 1463, 1535, 2359, 2866, 2926, 2944 cm^{-1}. **24b**: **^{1}H NMR** (400 MHz, CDCl$_3$): 1.12 (m, 42H; TIPS) ppm. **^{13}C NMR** (101 MHz, CDCl$_3$ values taken from an impure spectrum contaminated with **11a**): 138.4, 130.0, 122.6, 105.8, 103.8, 102.3, 19.2 (broad), 13.3 (broad) ppm. **HR-APCI-MS m/z**: 547.12393 (Mass corresponds to $C_{24}H_{43}Br_2Si_2^+$: 547.12441). IR was not recorded as a pure sample could not be obtained.

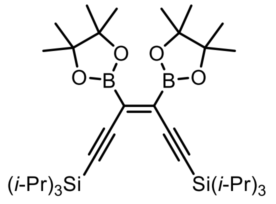

Synthesis of compound 25: 23 (5.14 g, 13.3 mmol), Pt(PPh$_3$)$_4$ (496 mg, 0.40 mmol) and bis(pinacoloto)diboron (3.71 g, 14.6 mmol) were dissolved in dry toluene (26 mL) under N$_2$ and the clear orange solution was freeze-pump-thaw degassed. The solution was then heated to 100 °C for 90 h. The solvent was removed *in vacuo* to yield crude **25** as an orange oil that was unstable to silica and thus the crude was carried through to the next step without further purification. **^{1}H NMR** (400 MHz, CDCl$_3$): 1.29 (24H, s; Bpin), 1.10 (s, 42H; TIPS) ppm. **^{13}C NMR** (101 MHz, CDCl$_3$): 107.7, 103.4, 84.3, 83.1, 24.8, 18.8, 11.4 ppm. **HR-ESI/APCI/MALDI-MS m/z**: Could not obtain. **IR (ATR): $\tilde{\nu}$ =** 633, 660, 674, 695, 756, 811, 850, 882, 923, 971, 996, 1062, 1144, 1214, 1271, 1332, 1358, 1462, 1535, 2130, 2865, 2942 cm^{-1}.

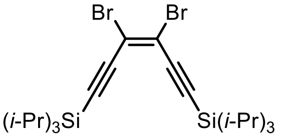

Synthesis of compound 21: Copper(II) bromide (17.8 g, 79.7 mmol) was added to a solution of crude **25** in THF (45 mL) and water (30 mL). The resulting dark brown solution was heated to 70 °C with a reflux condenser for 18 h. An additional aliquot of CuBr$_2$ (6.0 g, 26.9 mmol) in THF (20 mL) was added and the reaction heated to 80 °C for an additional 20 h. The reaction was monitored by NMR and quenched upon loss of the Bpin signals in the crude NMR.

Upon completion of the reaction the solution was diluted with water (50 mL) and extracted with diethyl ether (3 × 50 mL) and the organic phase dried over $MgSO_4$. The crude was purified by column chromatography, SiO_2 (petroleum ether) to yield **21** as a red oil (3.84 g, 7.03 mmol, 53% from **23**). **^{1}H NMR** (400 MHz, $CDCl_3$): 1.04 (s, 42H; TIPS) ppm. **^{13}C NMR** (101 MHz, $CDCl_3$): 112.2, 105.1, 102.7, 18.8, 11.3 ppm. **HR-APCI-MS m/z**: 547.1246 (mass corresponds to $C_{24}H_{43}Br_2Si_2^+$, m/z: 547.1245). **IR (ATR):** $\tilde{\nu}$ = 619, 664, 678, 818, 883, 920, 997, 1018, 1042, 1176, 1242, 1367, 1384, 1463, 2137, 2866, 2891, 2943 cm^{-1}.

Synthesis of $C_{18}Br_6$:

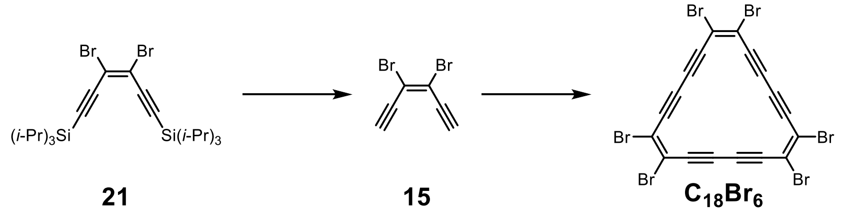

(**Note:** The crude reaction mixture from this cyclisation reaction was found to be explosive if scratched. Care should be taken to work on a small scale. Monomer **15** should not be fully dried and non-flammable solvents used where possible.)

Synthesis of compound 15: Tetrabutylammonium fluoride (1.61 mL, 1.0 M in THF, 1.61 mmol) was added to a solution of compound **21** (400 mg, 0.73 mmol) in THF (25 mL) and water (0.25 mL) at 0 °C. The resulting clear orange solution was stirred and monitored by TLC until the reaction had reached completion, approximately 1.5 h. Water (25 mL) was added and the aqueous phase was extracted with Et_2O (2 × 20 mL) and dried over $MgSO_4$. The crude was purified by column chromatography, SiO_2 (petroleum ether) to yield **15** as a yellow solution in petroleum ether (2 mL) that was diluted with dry CH_2Cl_2 for use directly in the next step. **^{1}H NMR** (400 MHz, $CDCl_3$): 3.75 (s, 2H) ppm. **^{13}C NMR** (101 MHz,

$CDCl_3$): 112.9, 87.6, 80.2 ppm. **GC-EI-MS m/z**: 231.8523 (calc m/z $C_6H_2Br_2$: 231.8518) **IR (ATR):** $\tilde{\nu}$ = 1464 (C=C), 2928 (C≡C-H/ potentially solvent) cm^{-1}.

Synthesis of $C_{18}Br_6$ *via* cyclisation conditions F: (Optimal conditions) The Glaser-Hay catalyst was prepared by addition of TMEDA (0.12 mL, 0.81 mmol) to a solution of CuCl (189 mg, 1.91 mmol) in dry CH_2Cl_2 (1.9 mL) under N_2. The resulting pale green suspension was stirred for 30 min and then allowed to settle and 0.39 mL of the supernatant solution was withdrawn and added to the vigorously stirred solution of **15** in dry CH_2Cl_2 (50 mL) under O_2. An immediate colour change was observed after addition of the catalyst from clear yellow to deep red. An insoluble brown precipitate slowly formed over the course of the reaction. The mixture was stirred for 48 h and the end point was determined by consumption of the starting material, determined by TLC analysis. The reaction mixture was diluted with CH_2Cl_2 (200 mL) and washed with water (200 mL). A brown emulsion was formed in the aqueous layer, which was extracted with CH_2Cl_2 (2 × 200 mL) until all brown emulsion had been removed from the pale blue aqueous layer. The organic layer was combined, washed with water (500 mL) and dried over $MgSO_4$ to yield a clear orange solution. The solution was concentrated to approximately 10 mL and diluted with petroleum ether (350 mL) to form a dark brown solution, which was filtered through a SiO_2 plug to yield a clear yellow solution. This solution was concentrated to approximately 20 mL and a red insoluble solid formed which stuck to the sides of the flask. The solution was diluted with $CHCl_3$ (100 mL) and sonicated to suspend the red solid in solution, the solution was then concentrated again to approx. 10 mL to give a red solid suspended in an orange solution, the red solid was collected using syringe filtration. Analytical GPC analysis revealed the red solid to be predominantly $C_{18}Br_6$ with some slightly larger species. The crude was triturated with CH_2Cl_2 (25 mL) and then washed with pentane (25 mL) to yield $C_{18}Br_6$ as a bright red crystalline solid (6.0 mg, 8.6 µmol, 4%) Crystalline material suitable for X-ray diffraction was obtained by cooling of a saturated solution of $C_{18}Br_6$ in CS_2 to 4 °C for 4 days to yield red parallelepipeds. **$C_{18}Br_6$: M.p.:** decomposes to black solid around 145 °C, no further change seen up to 300 °C **^{1}H NMR** (400 MHz, $CDCl_3$): no signals. **^{13}C NMR:** too insoluble to obtain. **HR-APCI-MS m/z:** 689.5104 (mass corresponds to $C_{18}{}^{79}Br_6^-$, m/z: 689.5106), 691.5077 (mass corresponds to $C_{18}{}^{79}Br_5{}^{81}Br^-$, m/z: 691.5086), 693.5058 (mass corresponds to $C_{18}{}^{79}Br_4{}^{81}Br_2^-$, m/z: 693.5065), 695.5035 (mass corresponds to $C_{18}{}^{79}Br_3{}^{81}Br_3^-$, m/z: 695.5046), 697.5015 (mass corresponds to $C_{18}{}^{79}Br_2{}^{81}Br_4^-$, m/z: 697.5026), 699.4994 (mass corresponds to $C_{18}{}^{79}Br{}^{81}Br_5^-$, m/z: 699.5007), 701.4978 (mass corresponds to $C_{18}{}^{81}Br_6^-$, m/z: 701.4986). **UV/vis ($CHCl_3$): λ_{max} (ε)** = 416 (13808), 403 (26114), 362 (52239), 347 (35154), 340 (31695), 265 (32394), 253 (33143 M^{-1} cm^{-1}). **IR (ATR): $\tilde{\nu}$** = 2112 (weak C≡C), 1048, 872, 858.

Cyclisation conditions A: (original conditions) The Glaser-Hay catalyst was prepared *via* addition of TMEDA (0.21 mL, 1.38 mmol) to a solution of CuCl (378 mg, 3.82 mmol) in dry CH_2Cl_2 (3.8 mL). The resulting pale green suspension was stirred for 30 minutes and then allowed to settle. 1.69 mL of the supernatant solution was withdrawn and added to a vigorously stirred solution of **15** (assume 100% yield, 144 mg, 0.62 mmol) in dry CH_2Cl_2 (25 mL) under O_2. An immediate colour change was observed after addition of the catalyst from clear yellow to opaque orange-brown. The solution was stirred for 2 h until the reaction had reached completion. The reaction mixture was then diluted with CH_2Cl_2 (200 mL) and washed with water (200 mL). The brown emulsion that forms in the aqueous layer was then extracted with CH_2Cl_2 (2 × 200 mL) and the organic layers combined and dried over $MgSO_4$ to yield a clear orange solution. The solvent was removed *in vacuo* to yield a brown solid containing multiple apolar components by TLC analysis. The mixture was purified by size exclusion chromatography (Bio-Beads SX3, $CHCl_3$) to yield multiple fractions containing different products. The desired ring was identified *via* analysis of the retention time by analytical GPC to yield $C_{18}Br_6$ as a highly insoluble yellow solid (3.3 mg, 4.7 µmol, 2%).

Cyclisation conditions G: $PdCl_2(PPh_3)_4$ (99 mg, 0.14 mmol), benzoquinone (314 mg, 2.91 mmol) and CuI (135 mg, 0.71 mmol) were dissolved in dry $CHCl_3$ (500 mL) and freshly distilled diisopropylamine (0.74 mL) to form a clear orange solution. **15** (assuming 100% yield 100 mg, 0.43 mmol) was added in $CHCl_3$ (25 mL) and the resulting solution stirred vigorously under air for 18 h. Upon completion of the reaction the crude mixture was passed through an alumina plug. The crude mixture was concentrated to 10 mL and then diluted into petroleum ether (200 mL) and passed through a silica plug. The relative yield of $C_{18}Br_6$ was obtained *via* quantitative analytical GPC analysis.

3.6.3 Selected NMR Spectra

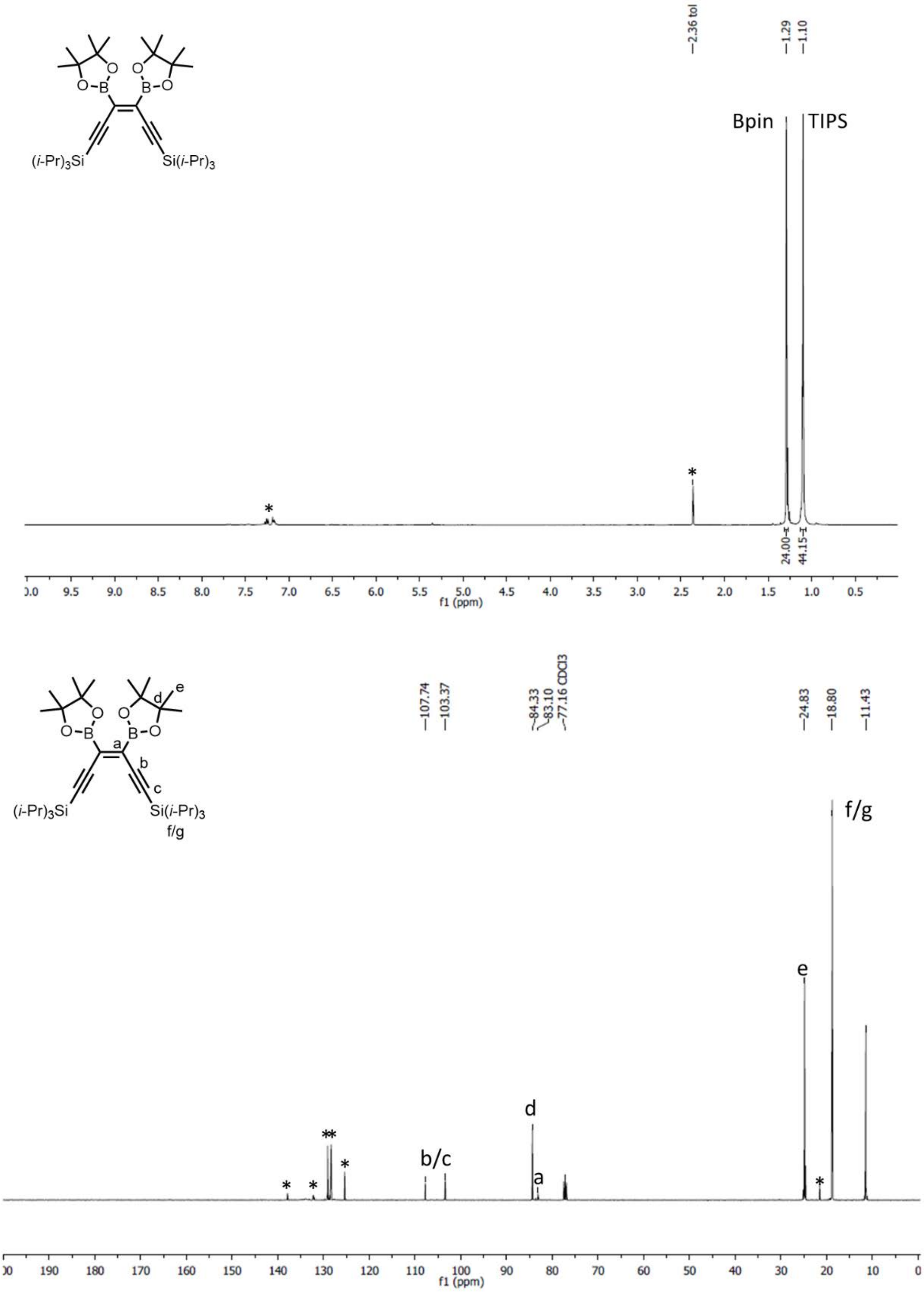

Figure 3.27 ^{1}H NMR (400 MHz, $CDCl_3$, 294 K) and ^{13}C NMR (101 MHz, $CDCl_3$, 294 K) spectra of **25**. *: Residual toluene and PPh_3 signals are present as the product is not stable on silica.

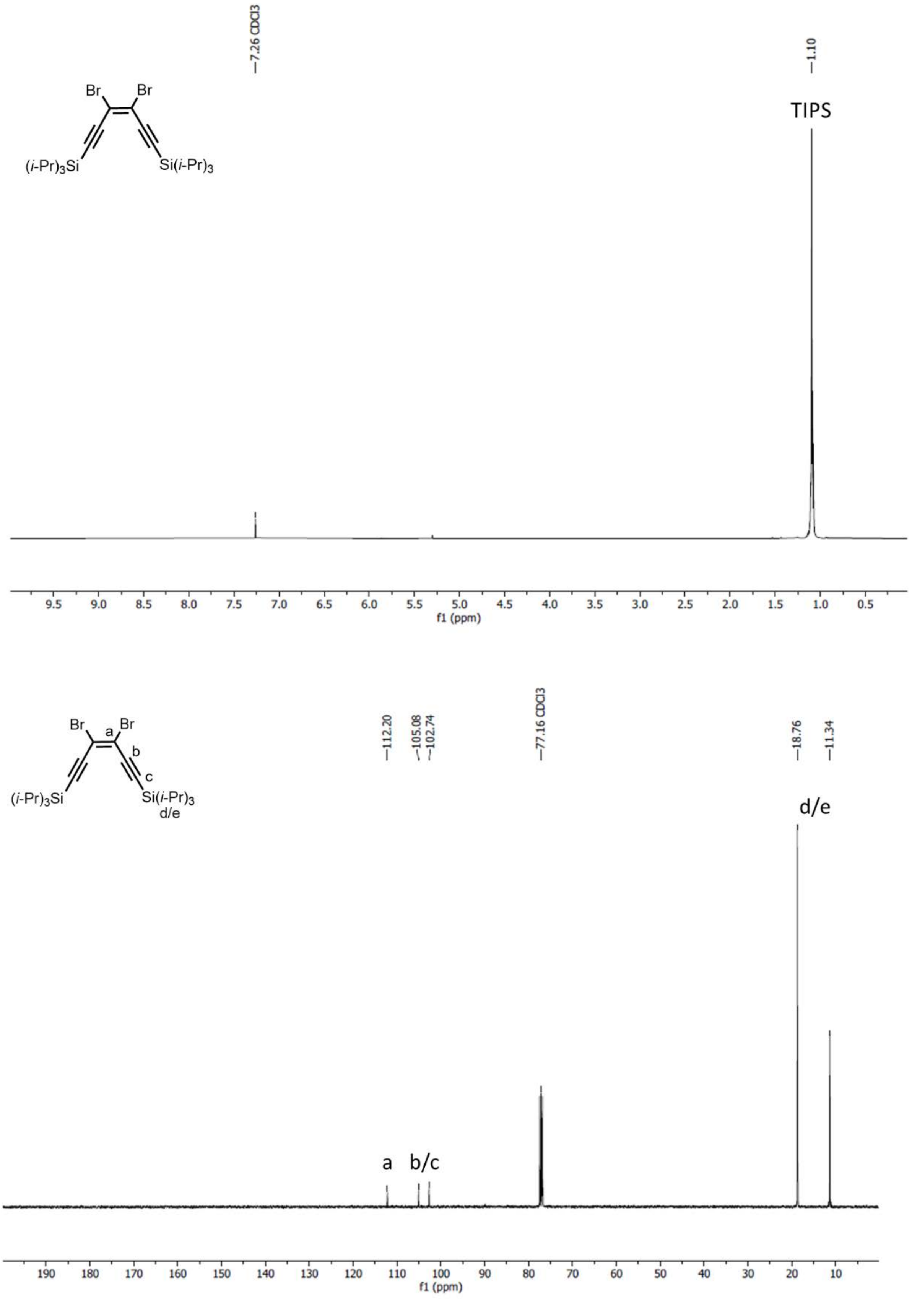

Figure 3.28 ^{1}H NMR (400 MHz, $CDCl_3$, 294 K) and ^{13}C NMR (101 MHz, $CDCl_3$, 294 K) spectra of **21**.

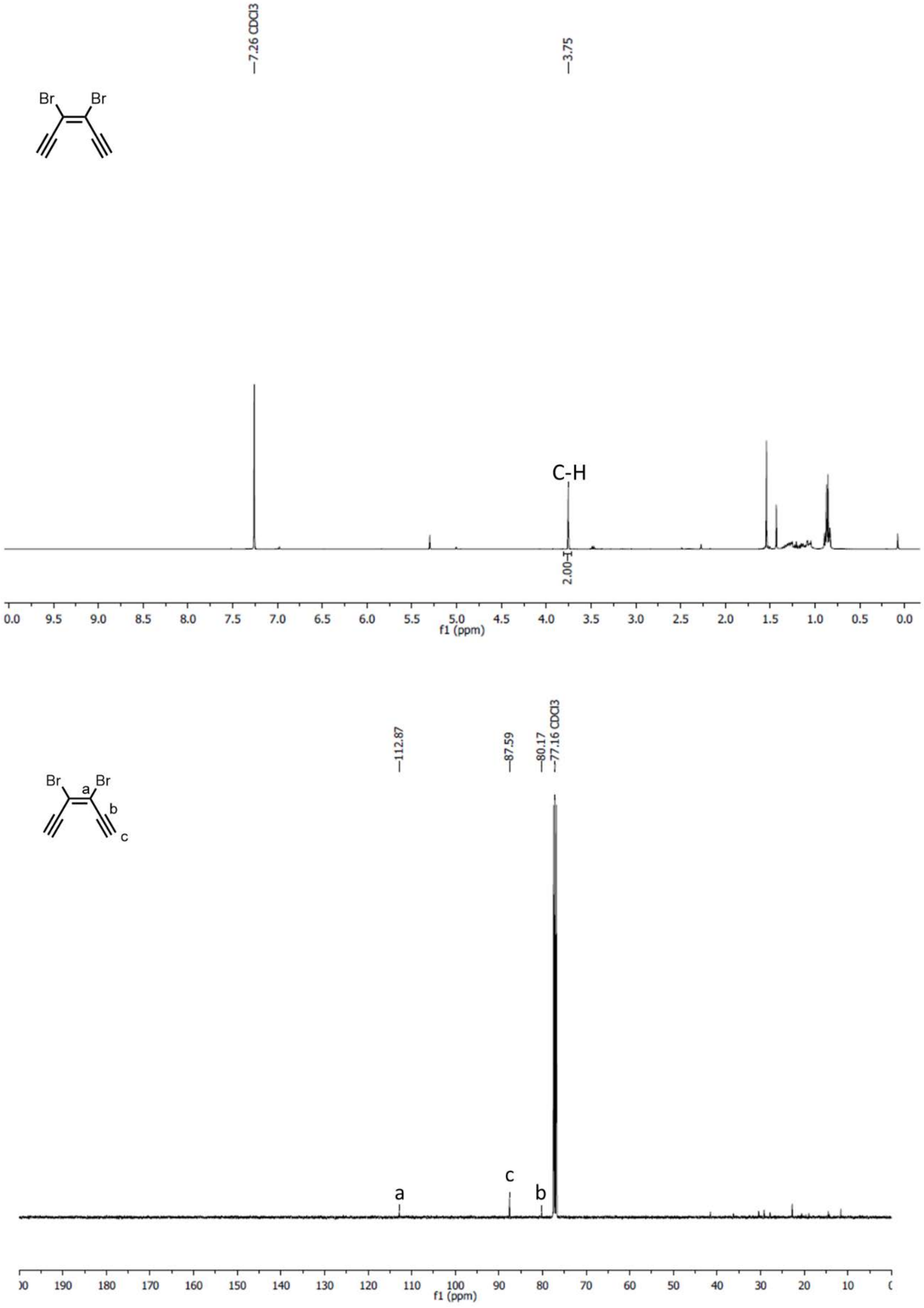

Figure 3.29 ^{1}H NMR (400 MHz, $CDCl_3$, 294 K) and ^{13}C NMR (101 MHz, $CDCl_3$, 294 K) spectra of **15**. Residual petroleum ether signals are present as the sample was not completely dried to avoid decomposition.

$C_{18}Br_6$:

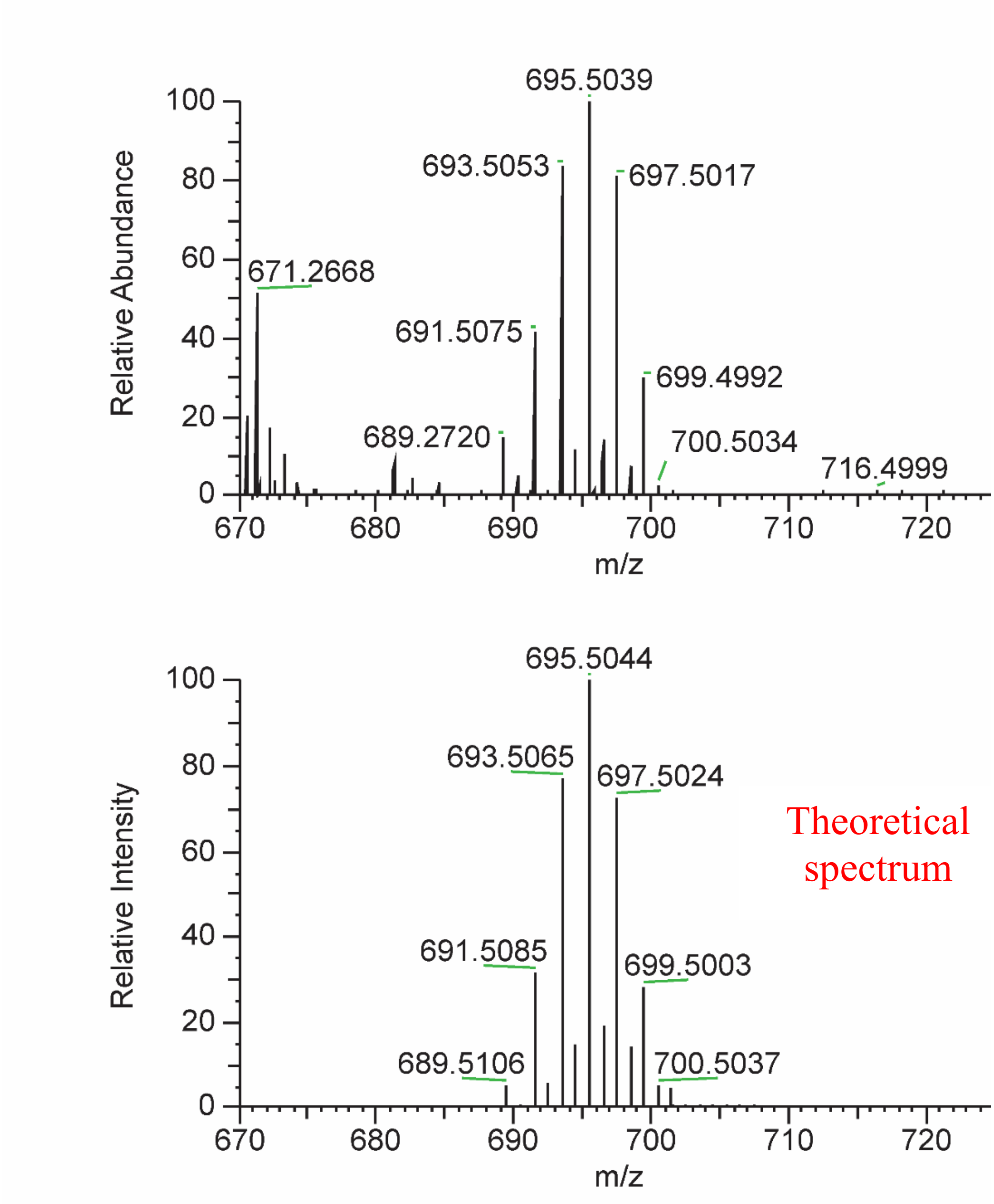

Figure 3.30 Radical M^- ion of $C_{18}Br_6$ detected in APCI. Theoretical patterns were generated using the Thermo XCalibur program.

$C_{24}Br_8$:

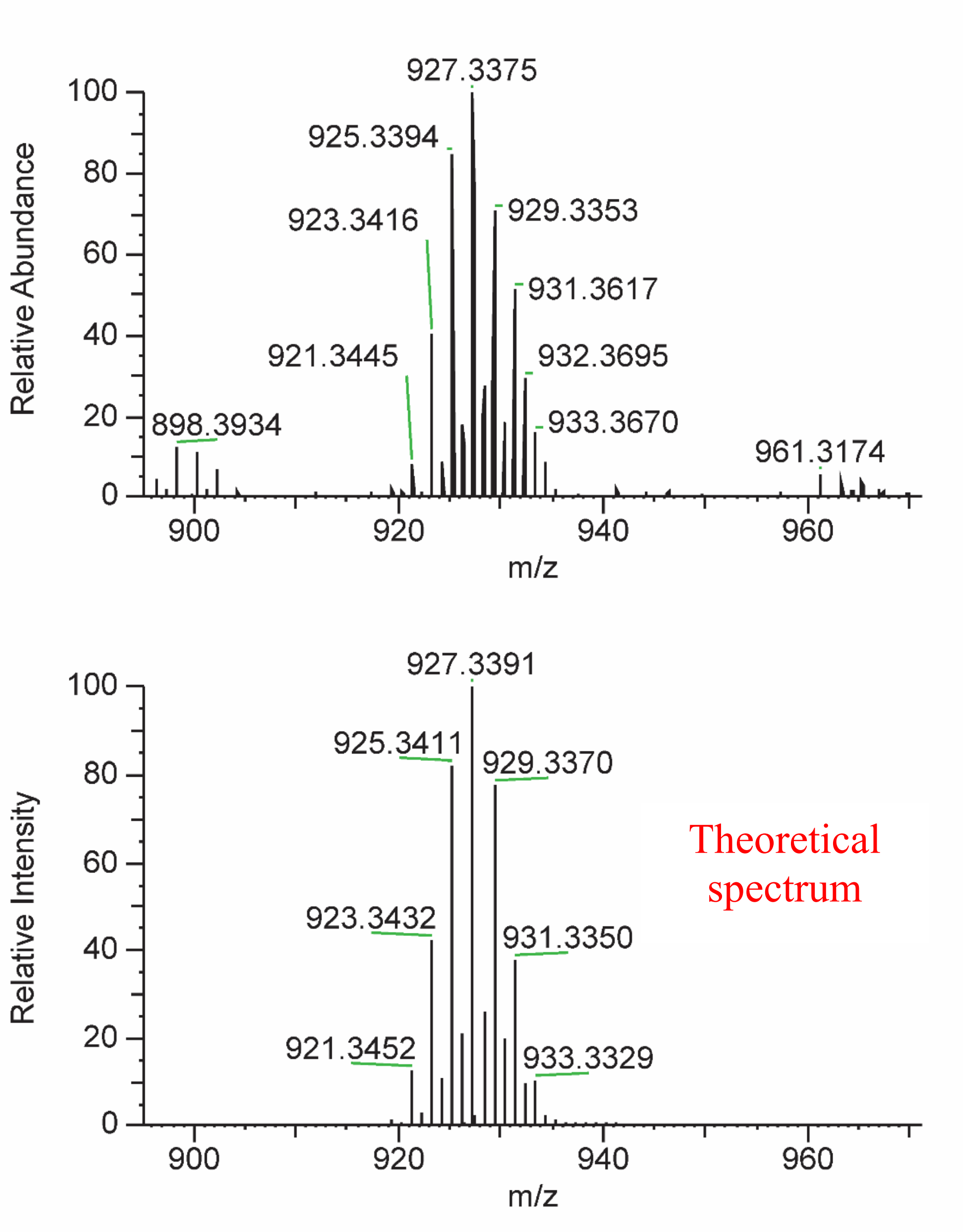

Figure 3.31 Radical M^{-} ion of $C_{24}Br_8$ detected in APCI. Theoretical patterns were generated using the Thermo XCalibur program.

$C_{12}Br_4$:

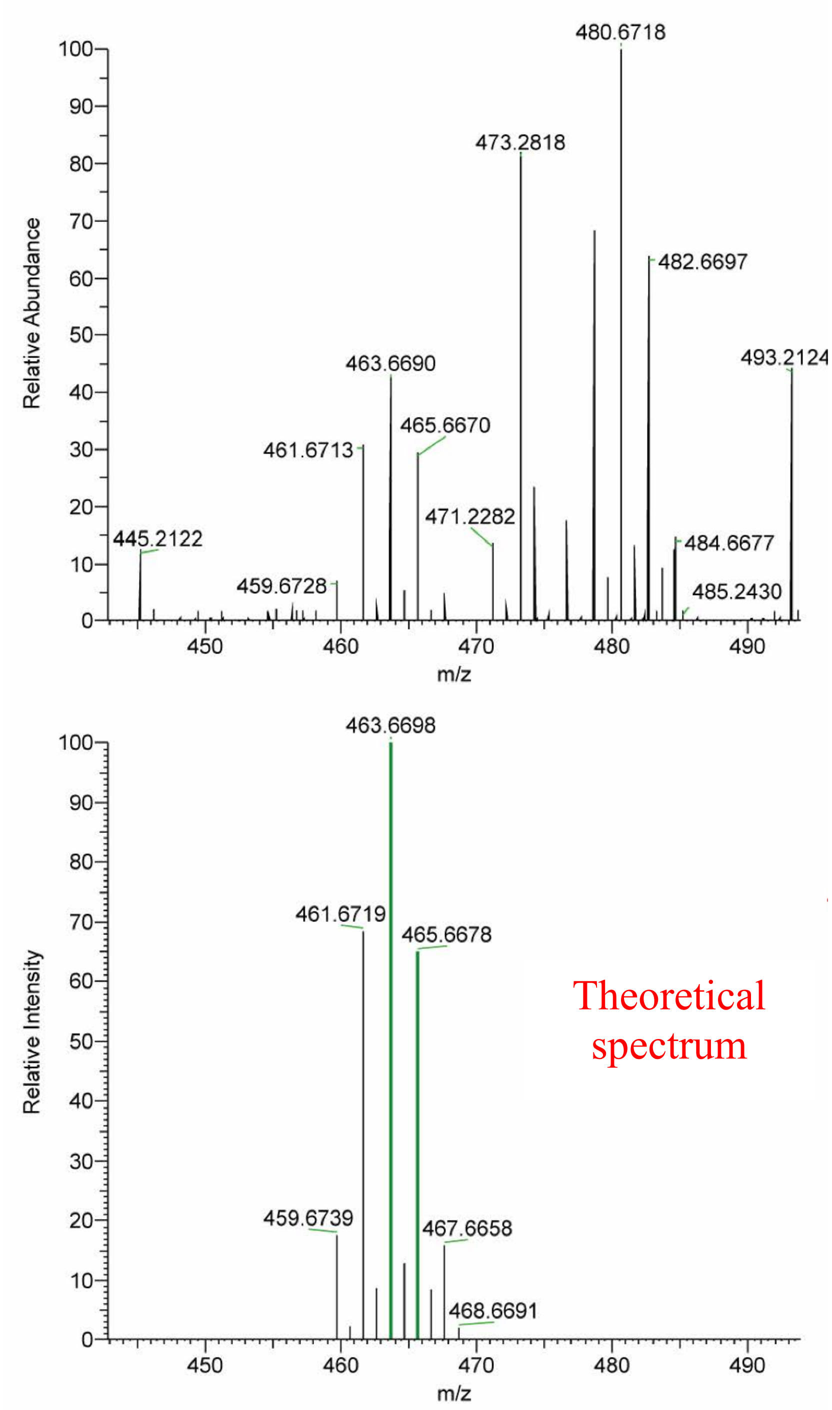

Figure 3.32 Radical M⁻ ion of $C_{12}Br_4$ detected in APCI. Mass at 480.6718 with the expected isotope distribution suggest the partial oxidation of $C_{12}Br_4$. Theoretical patterns were generated using the Thermo XCalibur program.

3.7 References

[1] L. M. Scriven, K. Kaiser, F. Schulz, A. J. Sterling, S. L. Woltering, P. Gawel, K. E. Christensen, H. L. Anderson, L. Gross, *J. Am. Chem. Soc.* **2020**, *142*, 12921–12924.

[2] K. Kaiser, L. M. Scriven, F. Schulz, P. Gawel, L. Gross, H. L. Anderson, *Science* **2019**, *365*, 1299–1301.

[3] A. Nandi, E. Solel, S. Kozuch, *Chem. Eur. J.* **2020**, *26*, 625–628.

[4] G. V. Baryshnikov, R. R. Valiev, A. V. Kuklin, D. Sundholm, H. Ågren, *J. Phys. Chem. Lett.* **2019**, *10*, 6701–6705.

[5] Z. S. Pereira, E. Z. Da Silva, *J. Phys. Chem. A* **2020**, *124*, 1152–1157.

[6] A. J. Stasyuk, O. A. Stasyuk, M. Solà, A. A. Voityuk, *Chem. Commun.* **2020**, *56*, 352–355.

[7] S. Hussain, H. Chen, Z. Zhang, H. Zheng, *Chem. Commun.* **2020**, *56*, 2336–2339.

[8] T. Bally, *Angew. Chem. Int. Ed.* **2006**, *45*, 6616–6619.

[9] S. Kozuch, *RSC Adv.* **2014**, *4*, 21650–21656.

[10] K. Nakamura, Y. Osamura, S. Iwata, *Chem. Phys.* **1989**, *136*, 67–77.

[11] B. K. Carpenter, *J. Am. Chem. Soc.* **1983**, *105*, 1700–1701.

[12] D. W. Whitman, B. K. Carpenter, *J. Am. Chem. Soc.* **1982**, *104*, 6473–6474.

[13] D. W. Whitman, B. K. Carpenter, *J. Am. Chem. Soc.* **1980**, *102*, 4272–4274.

[14] C. Castro, W. L. Karney, *Angew. Chem. Int. Ed.* **2020**, *59*, 2–14.

[15] V. Parasuk, J. Almlöf, M. W. Feyereisen, *J. Am. Chem. Soc.* **1991**, *113*, 1049–1050.

[16] D. A. Plattner, K. N. Houk, *J. Am. Chem. Soc.* **1995**, *117*, 4405–4406.

[17] T. Torelli, L. Mitas, *Phys. Rev. Lett.* **2000**, *85*, 1702–1705.

[18] S. Arulmozhiraja, T. Ohno, *J. Chem. Phys.* **2008**, *128*, 114301.

[19] F. Diederich, Y. Rubin, C. B. Knobler, R. L. Whetten, K. E. Schriver, K. N. Houk, Y. Li, *Science* **1989**, *245*, 1088–1090.

[20] P. W. Fowler, N. Mizoguchi, D. E. Bean, R. W. A. Havenith, *Chem. Eur. J.* **2009**, *15*, 6964–6972.

[21] M. Feyereisen, M. Gutowski, J. Simons, J. Almlöf, *J. Chem. Phys.* **1992**, *96*, 2926–2932.

[22] J. Hutter, H. P. Lüthi, F. Diederich, *J. Am. Chem. Soc.* **1994**, *116*, 750–756.

[23] J. M. L. Martin, J. El-Yazal, J.-P. François, *Chem. Phys. Lett.* **1995**, *242*, 570–579.

[24] R. O. Jones, *J. Chem. Phys.* **1999**, *110*, 5189–5200.

[25] A. E. Boguslavskiy, H. Ding, J. P. Maier, *J. Chem. Phys.* **2005**, *123*, 034305.

[26] N. Pavliček, B. Schuler, S. Collazos, N. Moll, D. Pérez, E. Guitián, G. Meyer, D. Peña, L. Gross, *Nat. Chem.* **2015**, *7*, 623–628.

[27] B. Schuler, S. Fatayer, F. Mohn, N. Moll, N. Pavliček, G. Meyer, D. Peña, L. Gross, *Nat. Chem.* **2016**, *8*, 220–224.

[28] N. Pavliček, P. Gawel, D. R. Kohn, Z. Majzik, Y. Xiong, G. Meyer, H. L. Anderson, L. Gross, *Nat. Chem.* **2018**, *10*, 853–858.

[29] X. Cao, Y. Yang, X. Wang, *J. Chem. Soc. Perkin 1* **2002**, *2*, 2485–2489.

[30] P. A. Magriotis, M. E. Scott, K. D. Kim, *Tetrahedron Lett.* **1991**, *32*, 6085–6088.

[31] G. W. Kabalka, G. Dong, B. Venkataiah, *Tetrahedron Lett.* **2005**, *46*, 763–765.

[32] G. B. Jones, J. M. Wright, G. W. Plourde, G. Hynd, R. S. Huber, J. E. Mathews, *J. Am. Chem. Soc.* **2000**, *122*, 1937–1944.

[33] G. W. Plourde, P. M. Warner, D. A. Parrish, G. B. Jones, *J. Org. Chem.* **2002**, *67*, 5369–5374.

[34] P. J. Kropp, N. J. Pienta, *J. Org. Chem.* **1983**, *48*, 2084–2090.

[35] R. E. Maleczka, B. Ghosh, W. P. Gallagher, A. J. Baker, J. A. Muchnij, A. L. Szymanski, *Tetrahedron* **2013**, *69*, 4000–4008.

[36] S. Zhang, H. Dong, J. Gui, W. Tian, *Tetrahedron Lett.* **2012**, *53*, 1882–1884.

[37] Y. Zhao, J. Kang, C. M. Park, P. E. Bagdon, B. Peng, M. Xian, *Org. Lett.* **2014**, *16*, 4536–4539.

[38] S. Dorok, B. Ziemer, G. Szeimies, *Chem. Eur. J.* **2002**, *8*, 4506–4509.

[39] R. Tarhouni, B. Kirschleger, M. Rambaud, J. Villieras, *Tetrahedron Lett.* **1984**, *25*, 835–838.

[40] J. M. Wright, G. B. Jones, *Tetrahedron Lett.* **1999**, *40*, 7605–7609.

[41] A. B. Lemay, K. S. Vulic, W. W. Ogilvie, *J. Org. Chem.* **2006**, *71*, 3615–3618.

[42] M. L. Ho, A. B. Flynn, W. W. Ogilvie, *J. Org. Chem.* **2007**, *72*, 977–983.

[43] M. Ide, Y. Yauchi, R. Shiogai, T. Iwasawa, *Tetrahedron* **2014**, *70*, 8532–8538.

[44] M. Ide, Y. Yauchi, T. Iwasawa, *Eur. J. Org. Chem.* **2014**, 3262–3267.

[45] Y. Yauchi, M. Ide, R. Shiogai, T. Chikugo, T. Iwasawa, *Eur. J. Org. Chem.* **2015**, 938–943.

[46] D. R. Kohn, P. Gawel, Y. Xiong, K. E. Christensen, H. L. Anderson, *J. Org. Chem.* **2018**, *83*, 2077–2086.

[47] F. Ramirez, N. B. Desai, N. McKelvie, *J. Am. Chem. Soc.* **1962**, *84*, 1745–1747.

[48] P. Fritsch, *Justus Liebigs Ann. Chem.* **1894**, *279*, 319–323.

[49] W. Zhang, J. A. Stone, M. A. Brook, G. A. McGibbon, *J. Am. Chem. Soc.* **1996**, *118*, 5764–5771.

[50] C. Wang, C. Wu, S. Ge, *ACS Catal.* **2016**, *6*, 7585–7589.

[51] M.-L. Yao, G. W. Kabalka, D. W. Blevins, M. S. Reddy, L. Yong, *Tetrahedron* **2012**, *68*, 3738–3743.

[52] T. Ishiyama, N. Matsuda, N. Miyaura, A. Suzuki, *J. Am. Chem. Soc.* **1993**, *115*, 11018–11019.

[53] Y. Rubin, C. B. Knobler, F. Diederich, *J. Am. Chem. Soc.* **1990**, *112*, 4966–4968.

[54] G. E. Jones, D. A. Kendrick, A. B. Holmes, *Org. Synth.* **1987**, *65*, 52.

[55] Y. Tobe, T. Fujii, H. Matsumoto, T. Kunihiro, D. Noguchi, N. Nakagawa, M. Sonoda, K. Naemura, Y. Achiba, T. Wakabayashi, *J. Am. Chem. Soc.* **2000**, *122*, 1792–1755.

[56] M. Suzuki, A. Comito, S. I. Khan, Y. Rubin, *Org. Lett.* **2010**, *12*, 2346–2349.

[57] R. S. Rowland, R. Taylor, *J. Phys. Chem.* **1996**, *100*, 7384–7391.

[58] T. Lu, Q. Chen, Z. Liu, *Chem Rxiv* **2019**, preprint.

[59] D. Lungerich, A. V. Nizovtsev, F. W. Heinemann, F. Hampel, K. Meyer, G. Majetich, P. V. R. Schleyer, N. Jux, *Chem. Commun.* **2016**, *52*, 4710–4713.

[60] L. Gross, F. Mohn, N. Moll, P. Liljeroth, G. Meyer, *Science* **2009**, *325*, 1110–1114.

[61] P. Hapala, G. Kichin, C. Wagner, F. S. Tautz, R. Temirov, P. Jelínek, *Phys. Rev. B* **2014**, *90*, 085421.

[62] D. G. De Oteyza, P. Gorman, Y. C. Chen, S. Wickenburg, A. Riss, D. J. Mowbray, G. Etkin, Z. Pedramrazi, H. Z. Tsai, A. Rubio, et al., *Science* **2013**, *340*, 1434–1437.

[63] B. Schuler, W. Liu, A. Tkatchenko, N. Moll, G. Meyer, A. Mistry, D. Fox, L. Gross, *Phys. Rev. Lett.* **2013**, *111*, 106103.

[64] L. Gross, F. Mohn, N. Moll, B. Schuler, A. Criado, E. Guitián, D. Peña, A. Gourdon, G. Meyer, *Science* **2012**, *337*, 1326–1329.

[65] A. Riss, S. Wickenburg, P. Gorman, L. Z. Tan, H. Z. Tsai, D. G. De Oteyza, Y. C. Chen, A. J. Bradley, M. M. Ugeda, G. Etkin, et al., *Nano Lett.* **2014**, *14*, 2251–2255.

[66] J. Van Der Lit, F. Di Cicco, P. Hapala, P. Jelinek, I. Swart, *Phys. Rev. Lett.* **2016**, *116*, 096102.

[67] V. Blum, R. Gehrke, F. Hanke, P. Havu, V. Havu, X. Ren, K. Reuter, M. Scheffler, *Comput. Phys. Commun.* **2009**, *180*, 2175–2196.

[68] J. Heyd, G. E. Scuseria, M. Ernzerhof, *J. Chem. Phys.* **2003**, *118*, 8207–8215.

[69] A. Tkatchenko, M. Scheffler, *Phys. Rev. Lett.* **2009**, *102*, 073005.

[70] B. C. Stipe, M. A. Rezaei, W. Ho, S. Gao, M. Persson, B. I. Lundqvist, *Phys. Rev. Lett.* **1997**, *78*, 4410–4413.

[71] Y. Kim, T. Komeda, M. Kawai, *Phys. Rev. Lett.* **2002**, *89*, 126104.

[72] J. N. Ladenthin, L. Grill, S. Gawinkowski, S. Liu, J. Waluk, T. Kumagai, *ACS Nano* **2015**, *9*, 7287–7295.

[73] V. Schendel, B. Borca, I. Pentegov, T. Michnowicz, U. Kraft, H. Klauk, P. Wahl, U. Schlickum, K. Kern, *Nano Lett.* **2016**, *16*, 93–97.

[74] J. Repp, G. Meyer, K. H. Rieder, *Phys. Rev. Lett.* **2004**, *92*, 4.

[75] N. Pavliček, Z. Majzik, S. Collazos, G. Meyer, D. Pérez, E. Guitián, D. Peña, L. Gross, *ACS Nano* **2017**, *11*, 10768–10773.

[76] G. Rapenne, L. Grill, T. Zambelli, S. M. Stojkovic, F. Ample, F. Moresco, C. Joachim, *Chem. Phys. Lett.* **2006**, *431*, 219–222.

[77] Y. Zhang, B. Schuler, S. Fatayer, L. Gross, M. R. Harper, J. D. Kushnerick, *Ind. Eng. Chem. Res.* **2018**, *57*, 15935–15941.

[78] F. Mohn, B. Schuler, L. Gross, G. Meyer, *Appl. Phys. Lett.* **2013**, *102*, 073109.

[79] N. Pavliček, A. Mistry, Z. Majzik, N. Moll, G. Meyer, D. J. Fox, L. Gross, *Nat. Nanotechnol.* **2017**, *12*, 308–311.

[80] I. Swart, T. Sonnleitner, J. Repp, *Nano Lett.* **2011**, *11*, 1580–1584.

[81] S. Ding, L.-J. Song, L. W. Chung, X. Zhang, J. Sun, Y.-D. Wu, *J. Am. Chem. Soc.* **2013**, *135*, 13835–13842.

[82] Z. A. Krasnaya, S. S. Yufit, T. S. Levchenko, V. F. Kucherov, *Tetrahedron* **1967**, *23*, 3687–3697.

[83] B. C. Berris, K. Peter, C. Vollhardt, *Tetrahedron* **1982**, *38*, 2911–2917.

[84] M. Solas, S. Suárez-Pantiga, R. Sanz, *Green Chem.* **2019**, *21*, 213–218.

Chapter 4

Towards antiaromatic cyclo[*n*]carbons

This chapter details the synthesis and properties of a series of cyclocarbon oxides as precursors to antiaromatic cyclo[*n*]carbons. Cyclocarbon oxide precursors to cyclo[24]carbon ($C_{32}O_8$) and cyclo[20]carbon ($C_{28}O_8$) were synthesised *via* deprotection of their corresponding acetal precursors. Both cyclocarbon oxides were found to be highly unstable. The electronic absorption properties, NMR characteristics and crystal structures of the cyclocarbon oxides and their acetal precursors were studied and it was suggested that their instability might stem from their conformational flexibility and antiaromaticity. The on-surface sublimation of both precursors was attempted but unfortunately all attempts were unsuccessful and no intact molecules could be found on the surface. Initial investigations into the synthesis of a cyclo[16]carbon precursor $C_{22}O_6$ were carried out and remain to be further investigated. Finally, a number of possible future avenues for this project are described.

4 Towards antiaromatic cyclo[*n*]carbons

4.1 Acknowledgements

The author planned all synthetic routes detailed in this chapter and carried out the synthesis and characterisation of all compounds except from investigations into the cyclo[16]carbon precursor $C_{22}O_6$ which were carried out by Isaac Ettedgui (Part II student, synthetic procedures can be found in his thesis) under the supervision of the author. NICS and molecular orbital calculations were performed by Dr Michael Jirásek. All AFM investigations in this chapter were performed by Katharina Kaiser, Felix Hermann and Dr Leo Gross at IBM Research–Zurich.

Some of the discussion in the introduction of this chapter has been submitted for publication:

Harry L. Anderson, Connor W. Patrick, Lorel M. Scriven and Steffen L. Woltering "A short history of cyclocarbons", *manuscript submitted.*

The author wrote the first draft of the theoretical section of this publication, subsequently all authors contributed to writing the manuscript. Parts of the text in this chapter are similar to this publication.

Dr Steffen L. Woltering is gratefully acknowledged for proofreading this chapter.

4.2 Introduction

The previous chapters in this thesis have detailed the synthesis of cyclo[18]carbon from two different precursors, $C_{24}O_6$ and $C_{18}Br_6$. These studies achieved the first structural characterisation of a cyclo[*n*]carbon. However, these precursors only gave structural insights into one particular species, aromatic cyclo[18]carbon. This chapter focuses on the properties and attempted synthesis of different sizes of antiaromatic cyclo[*n*]carbons, cyclo[16]carbon, cyclo[20]carbon and cyclo[24]carbon, from their corresponding cyclocarbon oxide precursors.

Before discussing the structures of different sizes of cyclo[*n*]carbons the concept of aromaticity will be introduced as this is a key issue in the debate surrounding the predicted structures of aromatic and antiaromatic cyclo[*n*]carbons. Aromaticity was first discussed by Hofmann in 1857[1] and since then the most widely used definition of aromaticity has become the one introduced by Erich Hückel[2] with his, now well known, Hückel's rules. These rules state that for planar, cyclic conjugated systems with $(4n + 2)$ π electrons an aromatic structure with minimal bond length alternation (BLA) is expected. The concept of antiaromaticity was first introduced by Breslow[3] and it is now well known that for systems with $(4n)$ π electrons an antiaromatic structure with significant BLA is expected. These rules enable us to predict which compounds are aromatic however they do not describe what the concept of aromaticity means. This raises the question of how to describe the properties of an aromatic compound; the most commonly used definitions are that aromatic compounds tend to be a) lower energy than their linear chain equivalent[4], b) possess bond lengths between that of a single and double bond[5,6] with low BLA and c) exhibit a diatropic ring current[7].

The aromatic stabilisation energy of a compound describes the stability of an aromatic compound relative to its linear chain analogue[4]. Aromatic molecules with [$4n + 2$] π electrons are predicted to be stabilised and antiaromatic molecules with [$4n$] π electrons destabilised. A closely related way to assess the aromatic stabilisation of a compound is by considering hypothetical isodesmic reactions whereby the nature of the bonds broken in the reactant are the same as the bonds formed in the product[8,9]. For example, if benzene is considered in an isodesmic reaction (Figure 4.1) then 150 kJ/mol of energy is required to break the conjugation due to its aromatic stabilisation.

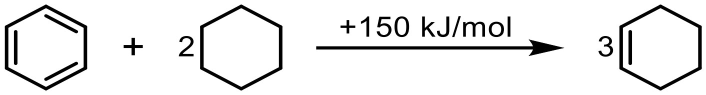

Figure 4.1 Isodesmic reaction representing the aromatic stability of benzene[9].

Another technique to quantify the extent of aromaticity in a system, which is particularly relevant to the cyclo[n]carbons, is the extent of BLA in the system[5,6,10,11]. Two examples of archetypal aromatic systems are benzene and graphene which have bond lengths of 1.398 and 1.422 Å respectively[11] which are between the length of typical single and double bonds. For comparison 1,3-butadiene has a single bond length of 1.467 Å and a double bond length of 1.349 Å[11]. Thus, deviation of bond lengths away from the ideal benzene bond lengths represents a decrease in aromaticity. This can also be quantified by the Harmonic Oscillator Model of Aromaticity[10] (HOMA), as shown below, which uses a reference optimum bond length for a system R_{opt} which is often equal to the bond length of benzene.

$$HOMA = 1 - \frac{\alpha}{n}\sum_{i=1}^{n}(R_{opt} - R_i)^2$$

Where n is the number of bonds taken into consideration in the summation and α is a normalisation factor for the system. α ensures that the *HOMA* is 0 for a structure with complete bond length alternation and 1 for a totally aromatic structure with equal bond lengths. This equation can then be used to assess the extent of bond length alternation and aromaticity in systems such as polyaromatic hydrocarbons.

An alternative approach to quantify aromaticity, which will be exploited in this chapter, is the observation that aromatic compounds exhibit a diatropic ring current in the presence of an external magnetic field[7]. This phenomenon is exemplified in [18]-annulene[12] which is an aromatic 18 π electron system in its neutral state (Figure 4.2). In the presence of an external magnetic field B_{ext} a diamagnetic ring current J_{ind} is induced in the annulene ring. This diamagnetic ring current J_{ind} induces a magnetic field B_{ind} which is in the opposite direction to the external magnetic field in the centre of the annulene ring (Figure 4.2). The induced magnetic field causes a reduction in the net magnetic field of the inner ring protons and therefore they are shielded and shifted upfield to –3.2 ppm. Whereas the outer protons of the annulene ring experience a net increase in the magnetic field and are deshielded and shifted downfield to 9.3 ppm.

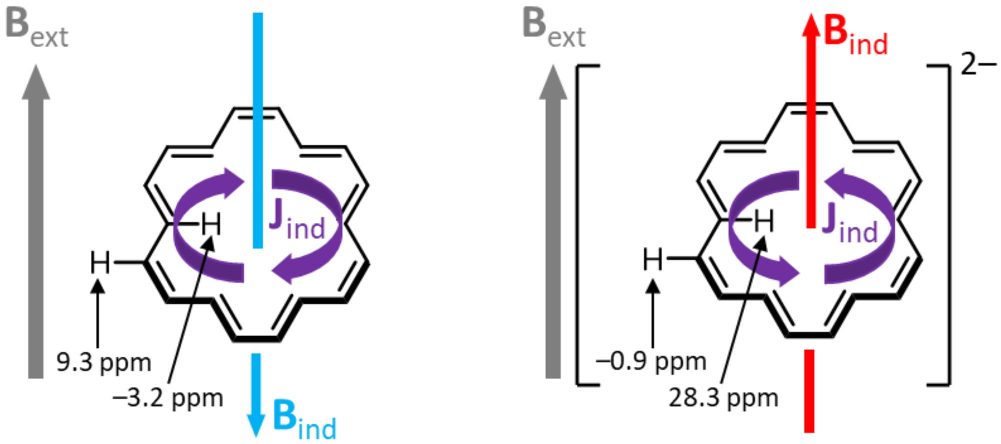

Figure 4.2 Representation of diatropic and paratropic ring currents in [18]-annulene and its dianion *via* their ^{1}H NMR shifts[13].

The dianion of [18]-annulene has 20 π electrons and therefore is an antiaromatic system and exhibits a paratropic ring current J_{ind} which induces a magnetic field B_{ind} which is in the same direction as the external magnetic field B_{ext} in the centre of the ring. This causes a net increase in the magnetic field in the centre of the ring and deshielding of the central ring protons causing them to be shifted downfield to 28.3 ppm whereas the external ring protons are shielded and shifted upfield to –0.9 ppm. This effect has been observed in many other systems[14,15] and will be exploited in this chapter.

Induced ring currents can be explored theoretically *via* Nucleus Independent Chemical Shift (NICS) calculations[16,17]. These calculations were introduced by Schleyer in 1996[16] and have become a standard means of investigating the properties of aromatic molecules. They are based on the use of a "ghost" atom, also known as a NICS probe, which is placed at points of interest around the molecule and the chemical shift is then calculated at each point. NICS calculations can be complicated by local diatropic currents generated by σ bonds, known as σ-effect distortions, however these effects are usually very short range and become negligible as the height above the molecule is increased. Both 1D and 2D NICS scans can be performed however 2D NICS scans are generally preferred as they are less susceptible to σ effect distortions. Generally 2D NICS scans are calculated at a height of 1 Å above the plane of the nuclei so that there are minimal local effects due to σ bonds and these are referred to as NICS(1) calculations whereas calculations performed in the plane of the nuclei are NICS(0) calculations. These calculations will be exploited in this chapter to explore the properties of the acetal precursors to the cyclocarbon oxides. NICS calculations can be plotted as either NICS(*iso*) or NICS(*ZZ*) values. NICS(*iso*) values are calculated by taking an average of the three possible orientations of the external magnetic field (all perpendicular to each other) whereas NICS(*ZZ*) values are calculated by considering the external and induced magnetic fields perpendicular to the plane of the molecule under consideration.

The structure of aromatic cyclo[18]carbon was resolved and studied in Chapter 2 and 3 of this thesis. We revealed a nine-fold symmetric structure. Cyclo[18]carbon should be a doubly aromatic molecule with two perpendicular π systems, each containing 18 π electrons, and therefore Hückel's rules would predict an aromatic structure with no BLA which is in contrast to the experimental result. This demonstrates that the link between cyclo[*n*]carbon structure and aromaticity is not straightforward and led us to investigate the theoretical background regarding the structures of different sizes of cyclo[*n*]carbons and C_n clusters.

The structure of carbon clusters is highly dependent on the number of carbon atoms in the cluster (Figure 4.3). Theoretical studies[18,19] indicate that the most stable structures for carbon clusters C_n evolve as n increases from linear chains (for small n) to rings (for intermediate n) to polycyclic cages (for large n) as shown in Figure 4.3. Up to C_{10} carbon clusters generally adopt a linear arrangement of carbon atoms due to the ring strain that would be imposed in a cyclic structure. This has been supported by various spectroscopic studies[20,21] as well as theoretical studies[18,19]. The exception to this rule is C_6 for which calculations give a cyclic structure as the energy minimum[22–27] due to the aromatic stabilisation in the cyclic structure relative to the linear chain (Table 4.1). From C_{10} onwards, cyclic structures, the cyclo[*n*]carbons, are calculated as the energy minima by a variety of different calculation types[22–25]. The transition from a monocyclic to bicyclic/polycyclic/cage structures appears to occur at around C_{20}[18,28].

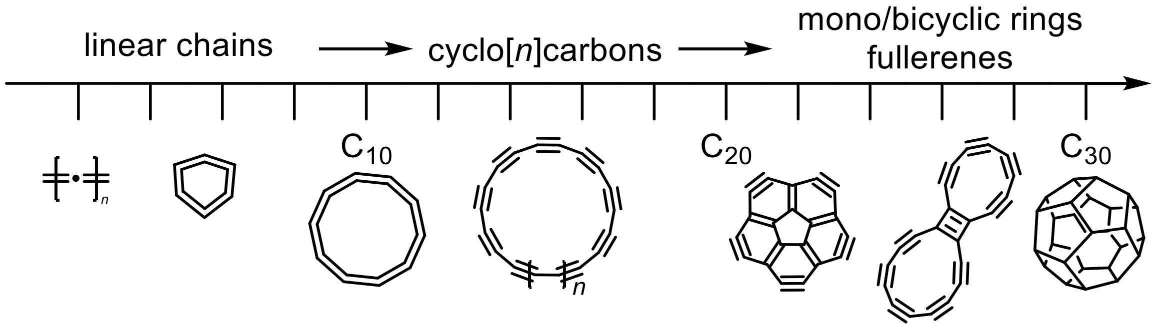

Figure 4.3 Change in C_n structure as n increases.

Cyclo[20]carbon and cyclo[24]carbon are particularly interesting cyclo[*n*]carbons to investigate as there has been intense theoretical debate surrounding the possible structures they may exhibit[29–34]. For C_{20} the most commonly proposed structures are a cyclo[20]carbon structure[30], a corannulene-like structure[28] or a fullerene structure[35]

(Figure 4.4). Fullerenes must possess twelve pentagons in their structure and therefore C_{20} is the smallest possible fullerene[18] and has been detected in its fullerene form from gas-phase debromination of a $C_{20}HBr_{13}$ fullerene precursor[32].

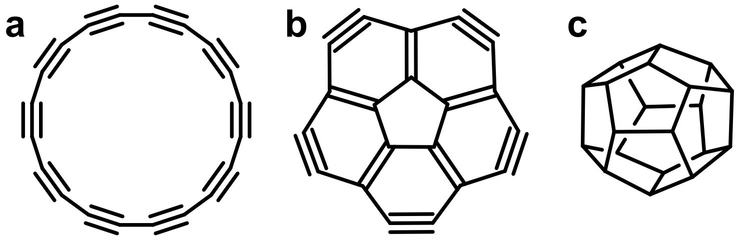

Figure 4.4 Possible structures of C_{20} proposed in the literature[28] **a**) cyclo[20]carbon, **b**) corannulene structure **c**) fullerene structure.

Over the last half century there has been intense theoretical debate surrounding the possible structures of the cyclo[*n*]carbons. Generally aromatic molecules are expected to exhibit structures with no BLA therefore doubly aromatic C_n molecules ($n = 4k + 2$) might be expected to adopt regular cumulenic $D_{n\mathrm{h}}$ geometries with *n* C=C bonds (BLA = 0). Whereas Jahn-Teller distortions in antiaromatic C_n molecules with $n = 4k$ would be expected to cause BLA resulting in alternating single C–C and triple C≡C bonds and a polyynic $D_{(n/2)h}$ geometry[22]. However the situation is complicated as second-order Jahn-Teller distortions in larger $n = 4k + 2$ rings[22] would also be expected to favour polyynic $D_{(n/2)\mathrm{h}}$ or $C_{(n/2)\mathrm{h}}$ geometries. These principles provide some guidance however the situation is more complicated and bond angle alternation (BAA) frequently arises, particularly for small cyclocarbons[36]. These effects result in four types of geometries for the cyclo[*n*]carbons as illustrated in Figure 4.5.

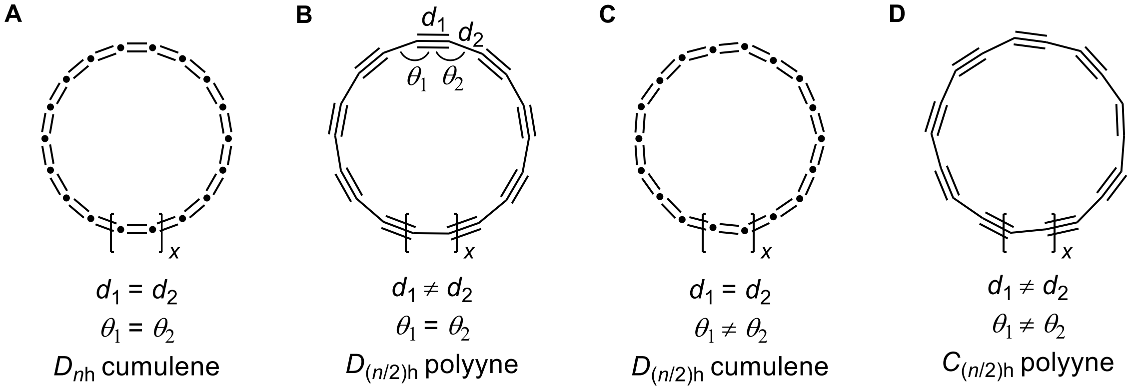

Figure 4.5 Four possible symmetries of a cyclo[*n*]carbon **A**) cumulenic D_{nh}, **B**) polyynic $D_{(n/2)h}$ **C**) cumulenic $D_{(n/2)h}$ ($\theta_1 \neq \theta_2$), **D**) polyynic $C_{(n/2)h}$ ($\theta_1 \neq \theta_2$).

The predictions of the lowest energy geometry **A**–**D** for C_n where n = 6–24 from many computational studies are summarised in Table 4.1. This theoretical review points to the following three generalisations.

- Small aromatic rings ($n = 4k + 2$) with $n \leq 10$ have structure **C** (BLA = 0; BAA ≠ 0).
- Small antiaromatic rings ($n = 4k$) with $n \leq 16$ have structure **D** (BLA ≠ 0; BAA ≠ 0).
- Large rings ($n \geq 24$) have polyyne structures **D** or **B** (BLA ≠ 0).

The structures of intermediate rings ($16 < n < 24$) are difficult to calculate and the results are highly dependent on the computational method. For example, most density functional theory (DFT) and second-order Møller-Plesset (MP2) calculations predict that the lowest-energy geometry of C_{18} is cumulenic (**A** or **C**), whereas Hartree-Fock (HF), quantum Monte Carlo (QMC) and coupled cluster methods predict that the polyyne form is the ground state (**B** or **D**). The cyclo[*n*]carbons are a challenging system for DFT calculations as they are highly susceptible to delocalisation error[37,38] which occurs when there is an incorrect correlation between the ground state energy and the number of electrons. Therefore, if exchange correlation is not correctly taken into account when calculating the structure of $n = 4k + 2$ cyclo[*n*]carbons then this can lead to overstabilisation of the totally aromatic structure **A**[25,39]. However if hybrid-DFT functionals which include enough exchange correlation (such as rCAM-B3LYP, RSE-PBE and ωB97XD) are used then these calculations can also correctly predict a polyyne structure for the larger rings[37,38,40].

Table 4.1 Theoretical review of the predicted ground state geometries of even cyclo[*n*]carbons.

year	C_6	C_8	C_{10}	C_{12}	C_{14}	C_{16}	C_{18}	C_{20}	C_{22}	C_{24}	level of theory
1986[41]	C										HF
1989[42]							**B**				HF
1990[43]			**C**								CISD/DZP
1991[44]							**B** **A**				MP2 SCF
1991[34]								**B**			SCF
1992[45]			**C**								SCF and CCSD/ cc-pVDZ
1992[46]							**B** **A**	**B** **B**	 **A**	**B** **B**	SCF MP2
1994[39]	**C**		**C**	**D**	**A**	**D**	**A**				DFT
1995[47]			**C** **C**		**C** **D**		**C** **D**				DFT/ 6-31G*/B-LYP RHF/ 6-31G*
1995[48]	**C**	**D**	**C**	**D**	**C**	**D**	**C**				DFT/cc-pVDZ/B3LYP
1998[49]							**A**				LDA
1999[22]	**C**		**C**		**C**		**C**		**D**		hybrid DFT ensures electron correlation
2000[50]	**C**		**C**		**B**		**B**				QMC
2000[51]	**C**	**D**	**C**	**D**	**C**	**D**	**C**	**B**	**C**		DFT/cc-pVDZ/B3LYP
2005[52]							**C**		**C**		DFT/6-31G(d)/B3LYP
2008[23]	**C**		**C**		**D**		**D**		**D**		CCSD cc-pVTZ
2009[24]	**C**	**D**	**C**	**D**	**C**	**D**	**C**	**D**	**C**	**D**	DFT/6-31G(d)/B3LYP
2010[37]			**C**		**B**		**B**		**B**		DFT/cc-pVDZ/rCAM-B3LYP
2016[26]	**C**	**D**	**C**	**D**	**C**	**D**	**C**	**D**	**C**	**D**	DFT/6-311++g(d,p)
2019[38]							**B**				DFT/def2-TZVP/RSX-PBE
2019[53]							**B**				CASSCF
2020[40]	**C**	**D**	**C**	**D**	**D**	**D**	**D**	**D**	**D**	**D**	DFT/6-311++G(d,p)

The crossover from BAA to BLA in the size range *n* = 6–26 is illustrated for aromatic rings ($n = 4k + 2$) in Figure 4.6 by comparing results from a range of theoretical methods[23,40,50,51]. Different levels of theory agree in predicting a decline in BAA from about 55° in C_6 to < 5°

in C_{22}, and many of them predict an increase in BLA from 0 in C_6 and C_{10} to about 0.1 Å in C_{22}, however predictions diverge in the intermediate size range (particularly for C_{14} and C_{18}). The cause of the crossover from BAA to BLA is worth considering, it is predicted to be caused by symmetry lowering second-order Jahn-Teller (SOJT) effects[23,50] which overcome the aromatic stabilisation that is the driving force for equal bond lengths in aromatic systems; this is analogous to the Peierls distortion in the solid state[54].

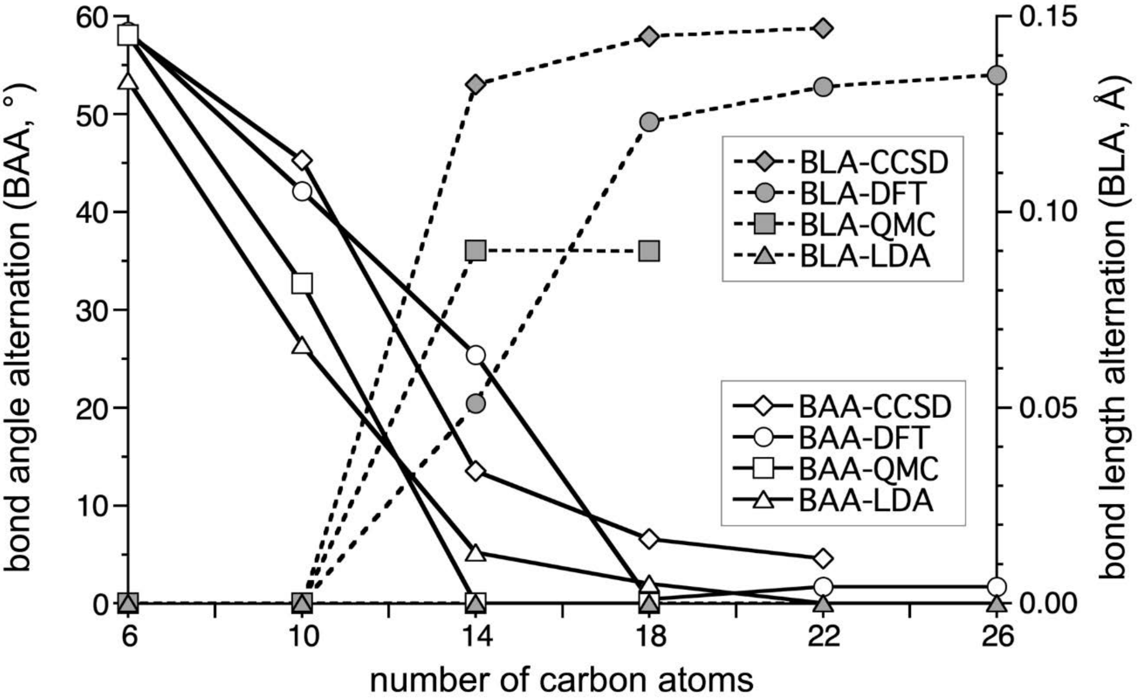

Figure 4.6 Evolution of BAA and BLA for even rings C_6–C_{26} predicted from different theoretical methods: CCSD cc-pVTZ[23]; DFT/6-311++G(d,p)/ωB97XD[40]; QMC[50] and LDA/84Ry[51].

The debate surrounding the structure of different sizes of cyclo[*n*]carbons led us to attempt the synthesis of different sizes of cyclocarbon oxides as cyclo[*n*]carbon precursors (Figure 4.7). Unmasking of compounds $C_{24}O_6$ and $C_{18}Br_6$ to C_{18} have been discussed in previous chapters (Chapter 2 and 3 respectively). This chapter focuses on efforts towards the synthesis of antiaromatic cyclo[*n*]carbons; C_{24}, C_{20} and C_{16} from their corresponding cyclocarbon oxide precursors.

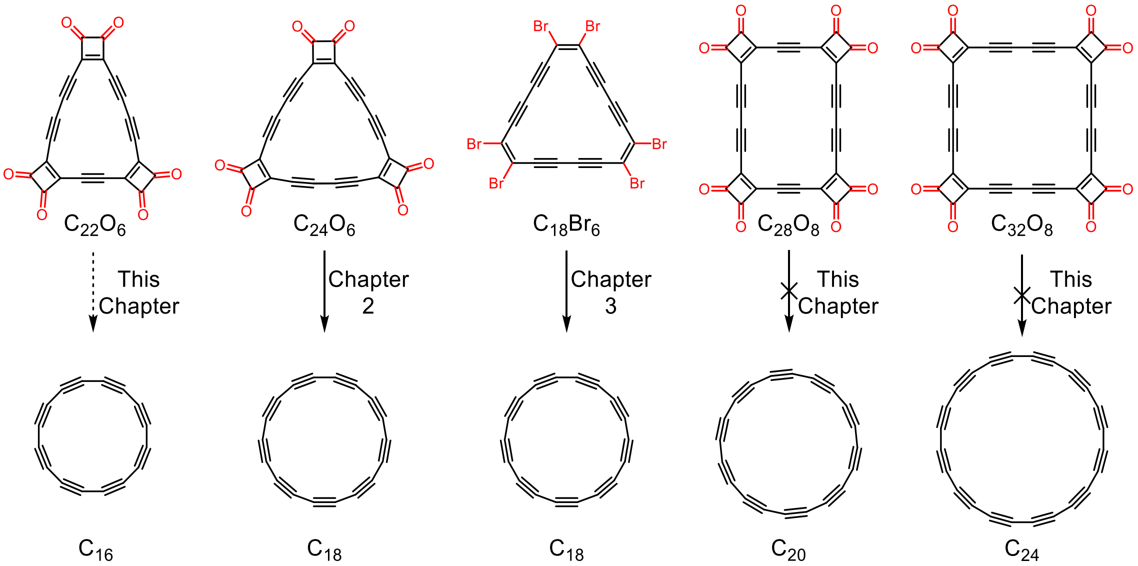

Figure 4.7 Precursors for the synthesis of different C*n*.

This chapter details the synthesis of $C_{32}O_8$ and $C_{28}O_8$ and initial attempts towards the synthesis of $C_{22}O_6$. $C_{32}O_8$ was synthesised successfully however multiple attempts at on-surface sublimation proved unsuccessful. Therefore smaller cyclocarbon oxides precursors were pursued to facilitate on-surface sublimation. Upon optimisation of the synthetic procedures $C_{28}O_8$ was successfully synthesised. The unsuccessful sublimation attempts of $C_{28}O_8$ will be detailed in which only molecular fragments were observed. The electronic absorption properties, NMR characteristics and crystal structures of the acetal protected precursors and their corresponding cyclocarbon oxides will then be discussed. Synthetic attempts towards the synthesis of $C_{22}O_6$ are discussed as well as other possible future directions for this project.

4.3 Results and Discussion

The general synthetic strategy towards the cyclocarbon oxides involves the synthesis of acetal protected precursors (**14**, **26–28**) as early attempts by Diederich[55] towards the synthesis of these compounds without acetal protection led to decomposition in all cases. Therefore, acetal protected precursors must be prepared and subsequently deprotected with sulfuric acid to reveal the cyclocarbon oxides as light and temperature sensitive solids (Figure 4.8).

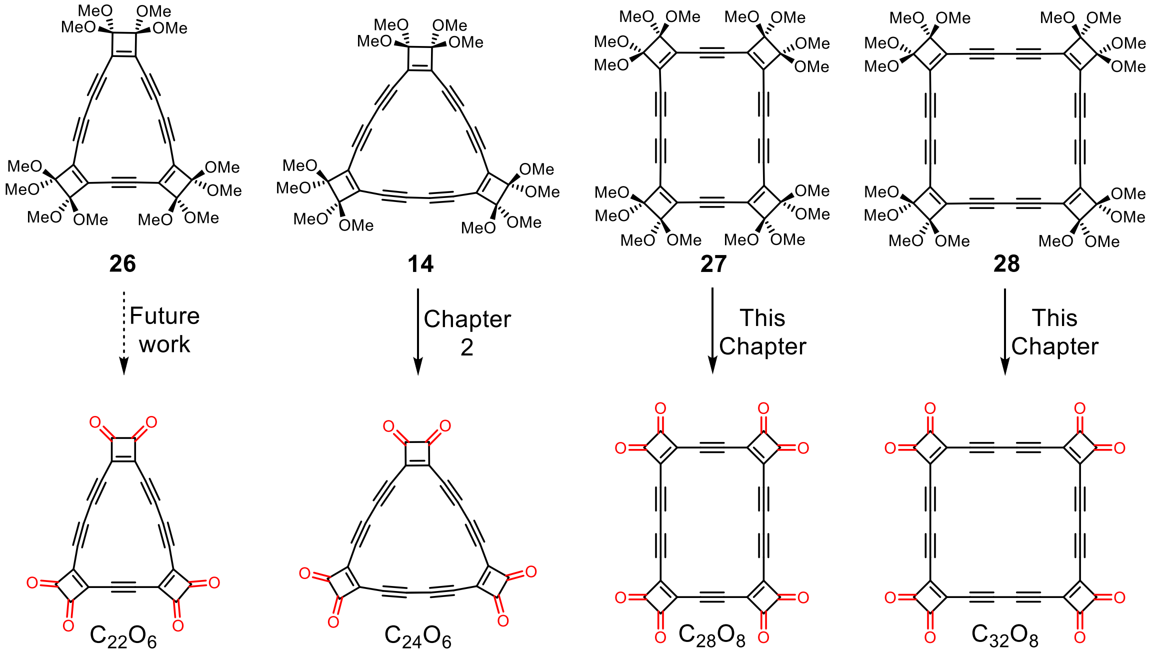

Figure 4.8 Acetal protected precursors and their corresponding cyclocarbon oxides.

The synthesis and on-surface properties of $C_{24}O_6$ are described in Chapter 2. This section will discuss the synthesis of acetal protected precursors to $C_{28}O_8$ (**27**) and $C_{32}O_8$ (**28**) and the unmasking to their corresponding cyclocarbon oxides. It will then detail initial attempts towards the synthesis of $C_{22}O_6$.

4.3.1 Synthesis of $C_{32}O_8$

Cyclo[24]carbon oxide $C_{32}O_8$ was prepared using modified procedures developed by Rubin and Diederich[56,57] in an analogous manner to the synthesis of $C_{24}O_6$ detailed in Chapter 2 (for the synthesis of **13** see Section 2.3.1). The monomer **13** was subjected to Hay coupling conditions[58] to give **28** in 8% yield as well as **14** in 7% yield, the cyclic pentamer was also detected but never fully isolated as it is unlikely that larger species will remain intact upon on-surface sublimation. The acetal protected precursor was deprotected in the absence of light using H_2SO_4 and extracted with 1,2-dichloroethane to yield $C_{32}O_8$ as a highly unstable red solid (Scheme 4.1). $C_{32}O_8$ was found to undergo significant decomposition in solution and in solid form over a period of a couple of days. Therefore, the deprotection to $C_{32}O_8$ was always carried out immediately prior to use. The deprotection of **28** occurred in much lower yield than that for compound **14** which is likely due to the much lower stability of $C_{32}O_8$ compared to $C_{24}O_6$.

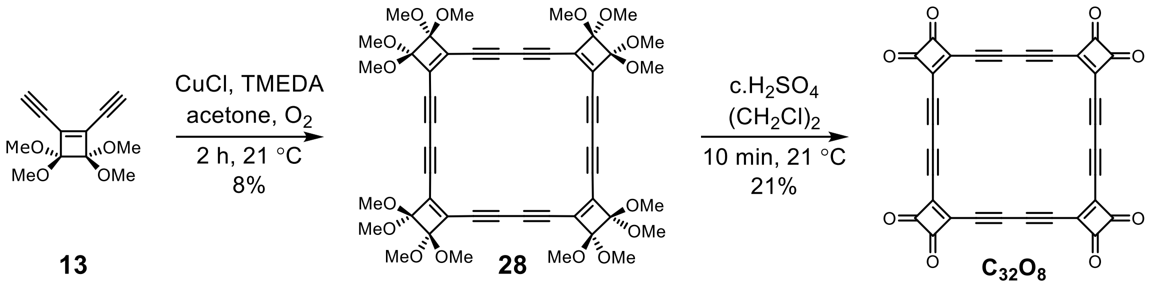

Scheme 4.1 Synthesis of $C_{32}O_8$.

The acetal protected ring **28**, similar to **14**, is stable and has been stored at –20 °C for up to a year without any noticeable decomposition. Single crystals of **28** were grown by layer diffusion of $CHCl_3$/ hexane (Figure 4.9). The crystals are triclinic (*P-1*) with one molecule and one chloroform molecule per unit cell and half a molecule in the asymmetric unit. The crystal structure shows a nearly planar geometry for the central ring structure with OMe groups above and below the plane of the ring. The acetylene bending shows very minor deviation from the ideal 180° geometry of an acetylene unit with angles of 175.9°, 178.4°, 178.6°, 178.0°, 178.4°, 178.2° and 175.2° for the acetylenic carbons in the unit cell implying there is minimal strain imposed on the acetylene units. The bond length alternation in this structure will be discussed in Section 4.3.5.

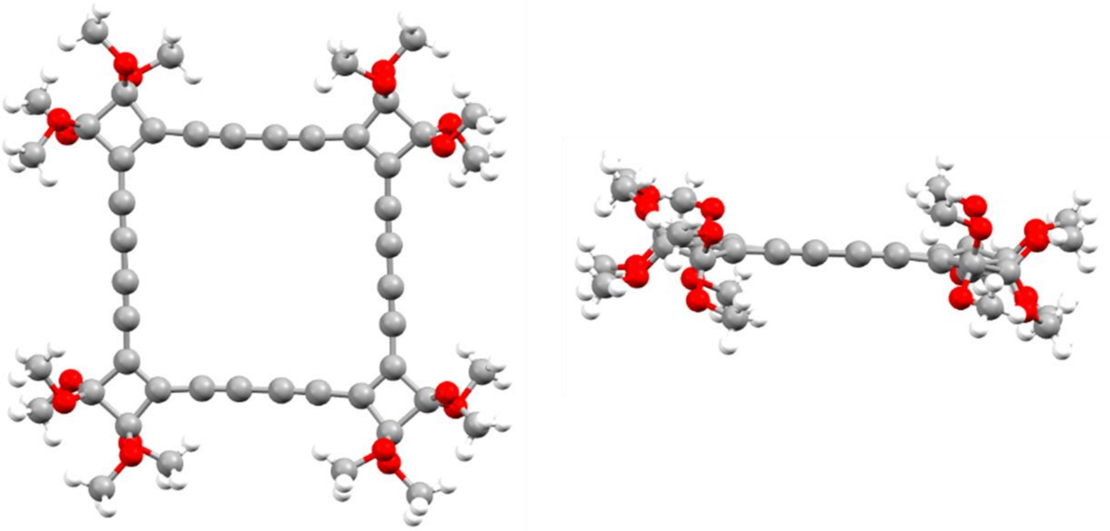

Figure 4.9 Single crystal X-ray structure of **28** showing front facing and side view. Solvent molecule ($CHCl_3$) omitted for clarity.

Acetal **28** was deprotected to $C_{32}O_8$ by dropping concentrated sulfuric acid onto **28** followed by extraction with 1,2-dichloroethane. $C_{32}O_8$ was found to be highly unstable; significant decomposition was observed even in samples that were kept at –20 °C in the absence of light for four days in contrast to $C_{24}O_6$ (see 2.3.1). Similar rates of decomposition were observed both in solution and in the solid state. Therefore, the deprotection of $C_{32}O_8$ was carried out the day before shipping to IBM Research–Zurich for on-surface analysis. $C_{32}O_8$ was immediately stored as a solid at –78 °C after deprotection and kept at this temperature during shipping and the samples were sublimed by the IBM team as soon as they arrived. Unfortunately, the $C_{32}O_8$ molecules did not appear to withstand the sublimation process as no intact molecules were found on the surface after the sublimation process. We repeated the deprotection and shipment to IBM for on-surface sublimation on two occasions however in no instance were intact molecules observed on the surface.

The sublimation process for on-surface unmasking involves the transfer of the compound onto a thin wafer that is then flash heated to 600 °C while the door to the UHV chamber is opened so that the molecules are sublimed onto the sample. The larger the molecule the less volatile it is and therefore it is less likely to remain intact upon sublimation. As the $C_{32}O_8$ precursor did not appear to remain intact upon sublimation our attention turned towards the synthesis of smaller cyclocarbon oxide precursors which will be detailed in the next section.

4.3.2 Synthesis of $C_{28}O_8$

The synthesis of $C_{28}O_8$ was embarked upon using modifications of Liebeskind's methodology[59,60] (Scheme 4.2).

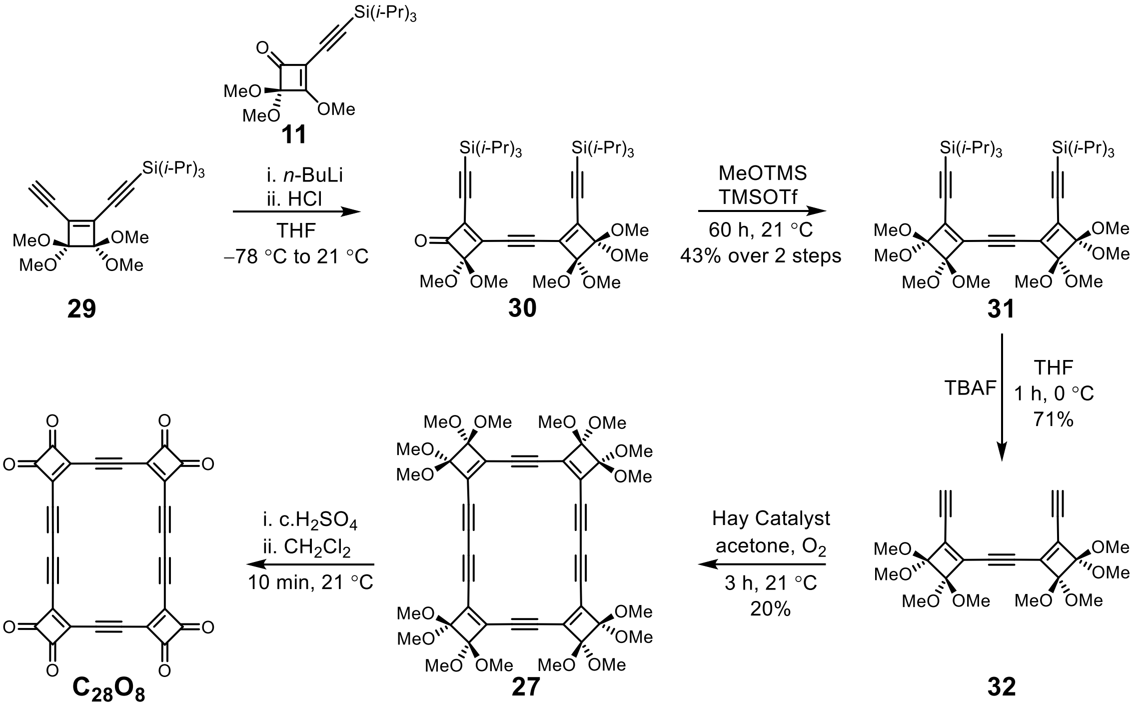

Scheme 4.2 Synthesis of $C_{28}O_8$.

29 and **11** were prepared by literature procedures (see ref [57] and Section 2.3.1). It was predicted that lithiation of **29** and addition to **11** would yield the desired product **30** *via* an acid mediated rearrangement (Scheme 4.3). Initial attempts to lithiate **29** at 0 °C led to immediate decomposition. Lithiation at –78 °C resulted in an opaque green suspension which, upon addition of ketone **11** and stirring at –78 °C led to a deep red solution which yielded the desired product **30** upon quenching with 3 M HCl however the isolated pure yield was low (24%). Optimisation of the reaction conditions was performed as shown in Table 4.2. The effect of increasing the reaction temperature and time was explored. Upon longer reaction times increased baseline decomposition was observed by TLC. The final optimised conditions used were to increase the reaction temperature from –78 °C to 0 °C and the reaction time reduced to 1 h (Table 4.2, **G**) before performing the acid quench. Using these conditions TLC analysis showed predominantly **30** with very small amounts of starting materials **29** and **11**.

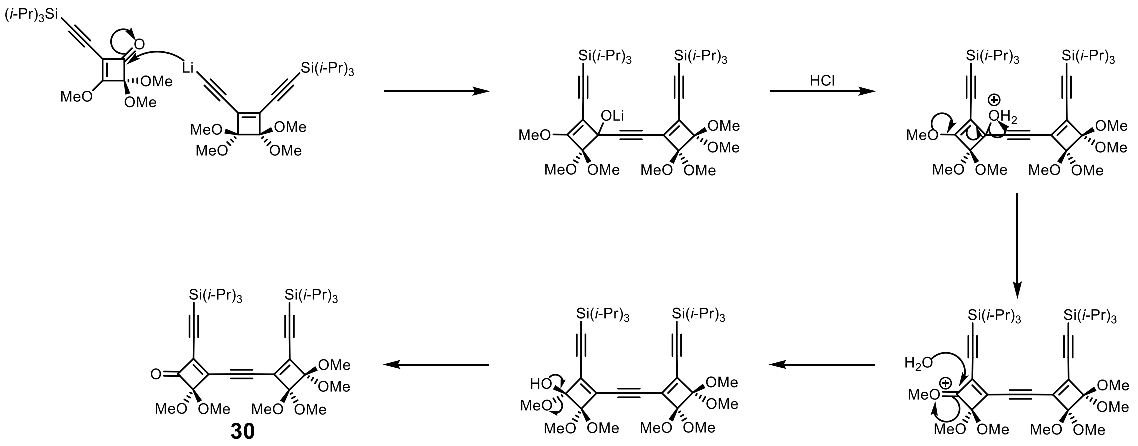

Scheme 4.3 Mechanism for formation of **30**.

Table 4.2 Reaction optimisation for formation of **30**.

	Lithiation	Reaction temp	Outcome
A	0 °C for 0.5 h	–78 °C	Complete decomposition of **29**
B	–78 °C for 1 h	–78 °C for 2 h	**30** observed by TLC but **29** and **11** still present
C	–78 °C for 1 h	–78 to –45 °C for 1 h	**30** observed by TLC but **29** and **11** still present
D	–78 °C for 1 h	–78 °C for 14 h	**30** observed by TLC but **29** and **11** still present
E	–78 °C for 1 h	–78 to –10 °C for 1 h	**30** observed by TLC but **29** and **11** still present but in smaller amounts
F	–78 °C for 1 h	–78 to –10 °C for 6 h	**30** observed but increased baseline decomposition
G	–78 °C for 1 h	–78 to 0 °C for 1 h	**30** observed by TLC with minimal **29** and **11** detected

Purification of **30** from residual **29** and **11** was highly challenging by column chromatography and thus the crude reaction mixture was subjected to acetal formation before purification was carried out. Acetal formation was performed by dissolving the crude in MeOTMS and catalytic TMSOTf and stirring for 3 days to yield **31** as an off-white solid. However this reaction proved challenging on occasion due to reproducibility issues. Upon optimisation of the reaction conditions of lithiation and acetal formation a maximum yield of formation of **31** from **29** of ~40% over two steps was reproducibly obtained for this reaction.

The deprotection of **31** was investigated and found to proceed cleanly at 0 °C using tetrabutylammonium fluoride to give **32** as the monomer for cyclisation as an off-white solid that appeared to be stable for a few days at –20 °C. However, deprotection was carried out on the same day as cyclisation to minimise decomposition. Cyclisation was carried out using preformed Hay catalyst[58] that was added to an oxygen-saturated solution of **32** in acetone. Cyclisation yielded the crude as a brown oil containing **27** and larger polymeric species which were purified by column chromatography to give **27** as a red oil that was then recrystallised to yield deep red crystals of **27** in a yield of 20%. No larger ring sizes were observed in the reaction mixture, only polymeric species, due to the preorganisation in the system.

The acetal protected ring **27** was stable and could be stored at room temperature for weeks without any noticeable decomposition. Single crystals of **27** were grown by vapour diffusion of a saturated solution of **27** in $CHCl_3$ and hexane (Figure 4.10). The crystals are monoclinic (*P* 21/*c*) with two molecules per unit cell and half a molecule in the asymmetric unit. The crystal structure shows a nearly planar geometry for the central ring structure with OMe groups above and below the plane of the molecule. Similar to **28** the acetylene bending shows very minor deviation from the ideal 180° geometry with angles of 177.9°, 178.3°, 176.4°, 178.0°, 177.9° and 178.3°. There is one angle with a greater deviation from planarity of 173.3° however this is along the monoacetylene bridge and appears to be due to a random deviation of the carbon position, likely due to relieving strain in the structure. The bond length alternation in this structure will be discussed in Section 4.3.5.

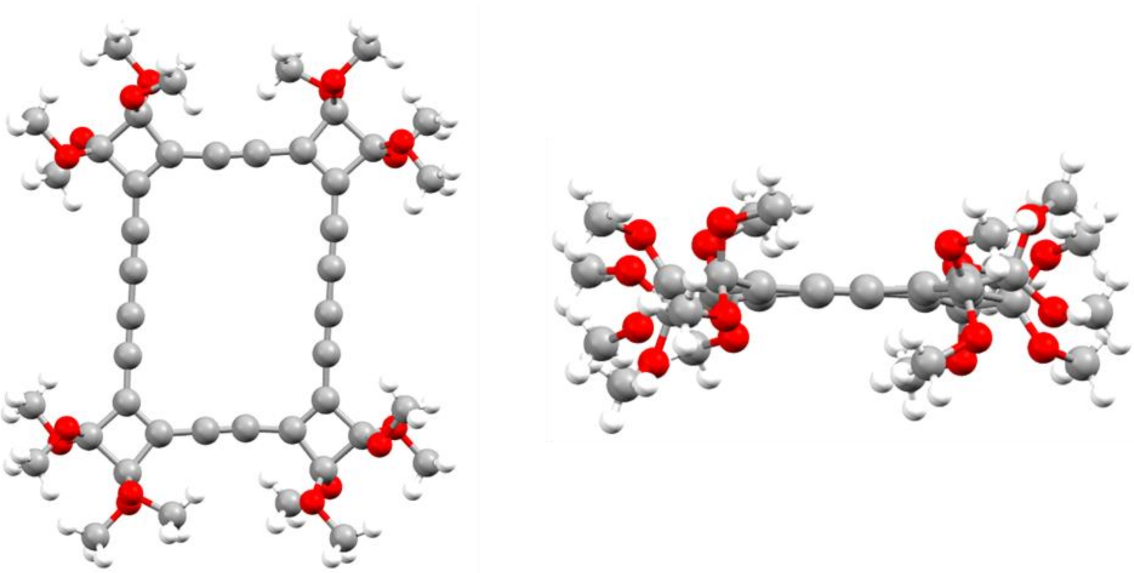

Figure 4.10 Single crystal X-ray structure of **27** showing front facing and side view. Solvent molecule ($CHCl_3$) omitted for clarity.

The acetal protected ring **27** was deprotected in the absence of light by dropping concentrated sulfuric acid onto **27**, the resultant dark red solution was extracted with CH_2Cl_2 to yield a clear orange solution of $C_{28}O_8$ in CH_2Cl_2. The resultant solution was stirred with $CaCO_3$ to remove any traces of acid which was then removed *via* syringe filtration to yield a deep orange solution of $C_{28}O_8$ in CH_2Cl_2. The reaction was monitored by IR with $C_{28}O_8$ exhibiting a strong characteristic carbonyl stretch at 1784 cm^{-1}. Monitoring of the reaction by TLC was not possible as the cyclocarbon oxides are not stable on silica. Investigations had previously been made (during the synthesis of $C_{24}O_6$) into detecting the cyclocarbon oxides by various mass spectrometry techniques including HR-ESI, APCI and MALDI however none of these led to detection of any relevant signals. Laser desorption mass spectrometry was attempted using MALDI-MS without a matrix however this did not lead to any signal detection and the same was found for $C_{28}O_8$. This is perhaps not surprising as the cyclocarbon oxides are known to fragment upon ionisation producing their corresponding cyclo[*n*]carbons and fullerene signals[56,57,61,62]. However, these signals have only been detected by laser desorption Fourier transform mass spectrometry which is not available in our department.

In all cases attempted removal of the solvent (CH_2Cl_2) from $C_{28}O_8$ was unsuccessful as it always resulted in a black solid that could not be redissolved to obtain the orange solution present prior to solvent removal. This was concluded to be due to decomposition by cross linking reactions between molecules. $C_{28}O_8$ was therefore always handled and stored as a dilute solution (< 1 mM) in dry CH_2Cl_2. Multiple attempts were made to obtain a ^{13}C NMR spectrum. Initially extraction of **27** in H_2SO_4 was performed with CD_2Cl_2 to give a clear red extract that was then stirred with calcium carbonate and the resultant suspension filtered and carefully concentrated to 0.5 mL to give a deep red solution. However upon recording the carbon spectrum the sample underwent significant decomposition and the solution turned black. This was predicted to be due to the instability of $C_{28}O_8$ as a concentrated solution (~10 mM) due to cross linking reactions between molecules. Therefore a second attempt was performed but the concentration of the sample was halved (~5 mM) and the spectrum was recorded at low temperature however no peaks were observed in the final spectrum due to decomposition.

When Diederich and Rubin first isolated the cyclocarbon oxides[55] they were initially unable to extract them from their sulfuric acid solutions and therefore they obtained their ^{13}C NMR spectra *via* an *in situ* deprotection of the acetal precursors in D_2SO_4. Therefore 20 mg of **27** was dissolved in D_2SO_4 to give a dark red solution and its 176 MHz ^{13}C NMR was immediately recorded. A D_2O capillary was used to lock the sample however no external reference capillary containing a carbon was added as there was a concern it would saturate the spectrum and cause a reduction in intensity of the product peaks. As a result the spectrum is unreferenced however the peak values are in relatively good agreement with the other cyclocarbon oxides[56] (Figure 4.11). The spectrum shows the seven expected peaks for

$C_{28}O_8$ with three acetylenic peaks and two peaks each in the expected region for the ketone and double bond as well as a large peak corresponding to extruded MeOH (Figure 4.11). There are impurity peaks in the spectrum likely due to side reactions between the product and the extruded MeOH however integration of the signals allows for the identification of separated spin systems. As there are no protons in this compound the carbon peaks should all have comparable integrations which is the case for all the peaks corresponding to $C_{28}O_8$ with the impurity peaks having either lower (0.16) or higher (~4) integrals relative to the $C_{28}O_8$ signals. The identity of these impurities is unfortunately not known as no further NMR experiments could be performed on the sample due to decomposition.

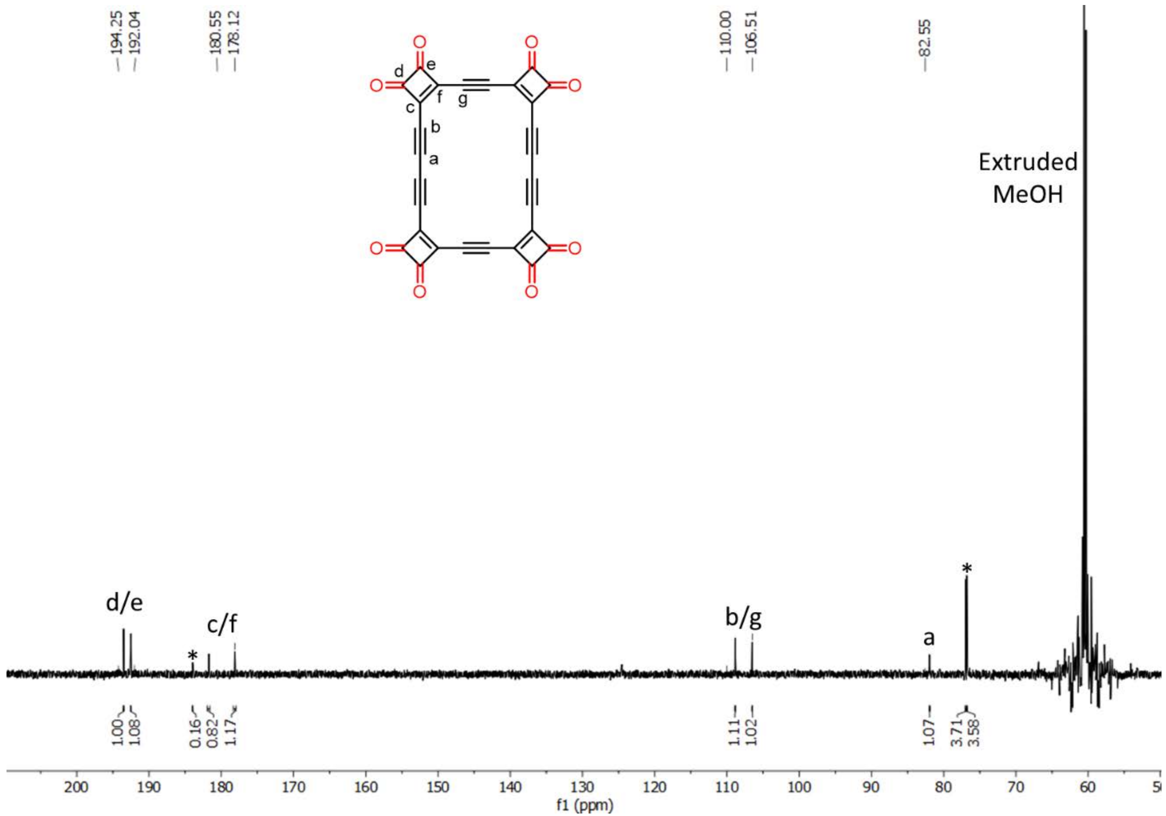

Figure 4.11 ^{13}C NMR spectrum of $C_{28}O_8$ in D_2SO_4 (176 MHz, D_2SO_4, 294 K) with a D_2O capillary. Spectrum is unreferenced as no carbon standard was included however values show good agreement with other cyclocarbon oxides[56]. *: impurity signals.

If $C_{28}O_8$ was kept as a dilute solution in dry CH_2Cl_2 and stored in the absence of light in the freezer (–20 °C) then the solution appeared to be relatively stable with only a small change in absorbance observed by UV analysis over three days (Figure 4.12). Note that this experiment cannot be taken as a precise measure of decomposition due to potential CH_2Cl_2 evaporation during the sample handling and storage. However it gives a good indication that if the sample is handled appropriately then the molecules should be intact after shipment to IBM Research–Zurich for on-surface sublimation.

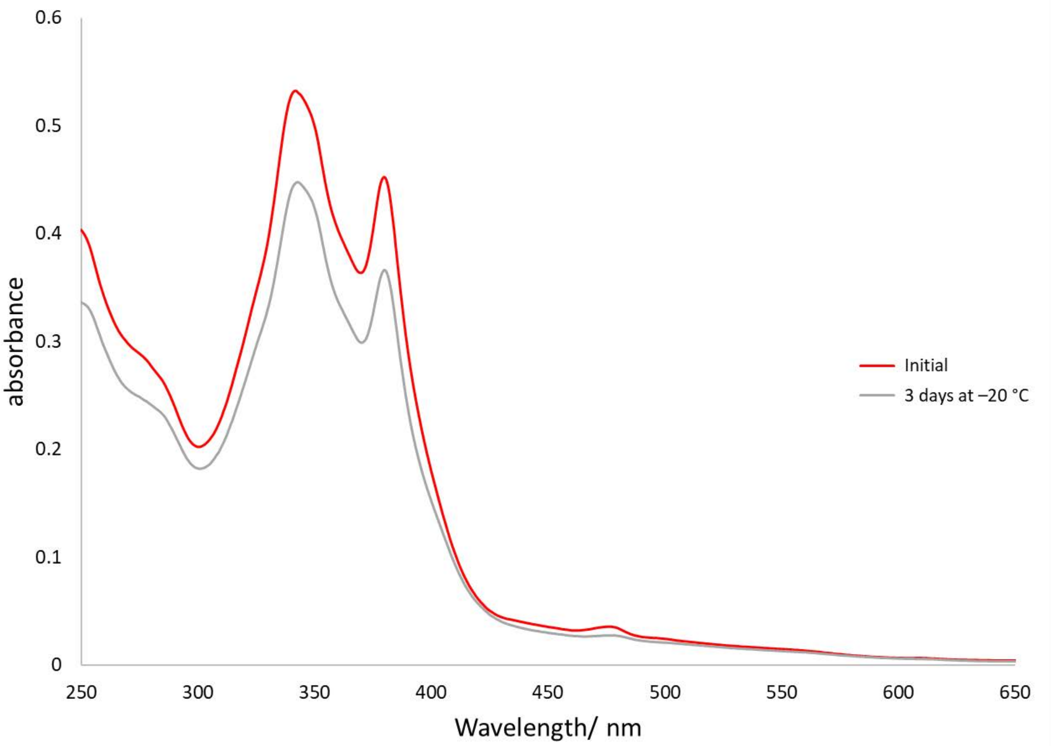

Figure 4.12 Stability studies by UV analysis of solution of $C_{28}O_8$. An initial UV of a sample of $C_{28}O_8$ in $CHCl_3$ was taken. The sample was then stored at –20 °C for 3 days and a UV of the same concentration was performed. (unknown concentration due to low compound stability on solvent removal, max possible initial concentration assuming 100% deprotection yield of 50 μM).

Due to the unstable nature of $C_{28}O_8$ deprotection of **27** was carried out on the day of shipment to IBM Research– Zurich and the samples were sent as solutions in CH_2Cl_2 at –78 °C. The sublimation process used by the IBM team involves the transfer of a very small amount (< 0.1 mg) of compound onto the sublimation wafer that is then placed into the vacuum chamber which is pumped down to ultrahigh vacuum (base pressure of $p \approx 10^{-10}$ mbar) and then flash heated to 600 °C as the door to the sample chamber is opened to transfer the molecules onto the sample. Therefore it was predicted that by dropping the solution of $C_{28}O_8$ onto the wafer to form a thin film of compound upon CH_2Cl_2 evaporation then minimal decomposition would occur when the wafer was dried in the vacuum chamber and subsequently some molecules could be transferred onto the surface. This approach was encouraged by a similar process being used for IR analysis. To obtain an IR spectrum a solution of $C_{28}O_8$ in CH_2Cl_2 was dropped onto the IR window and the CH_2Cl_2 was then left to evaporate for 1 min before the IR spectrum was recorded. Using this technique the characteristic IR stretching frequency at 1784 cm^{-1} was observed which implies some of the molecules were still intact after the drying process and it was predicted that this would be the same for the sublimation process.

Unfortunately upon sublimation of $C_{28}O_8$ no intact molecules could be found on the surface only molecular fragments and polyyne chains (Figure 4.13). The AFM images show partially broken molecules with multiple bright lobes in chain like structures which presumably correspond to polyyne chains formed by partial unmasking on sublimation. In some cases (Figure 4.13a,c) bent sections of the molecule with dark features characteristic of ketone groups can be observed which implies some of the cyclobutenedione groups survived sublimation. However no intact molecules could be found on the surface which is likely due to the highly reactive nature of $C_{28}O_8$, possibly either due to its conformational flexibility or its antiaromatic character. The sublimation was attempted three times by the IBM team however on all occasions they were unsuccessful in finding any intact molecules.

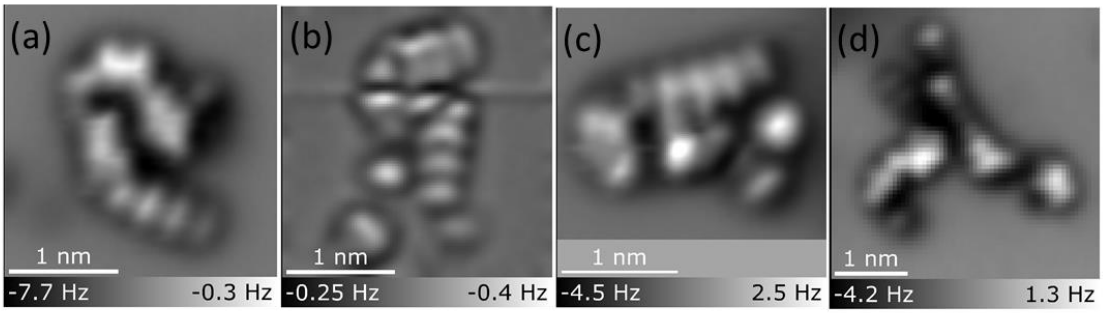

Figure 4.13 AFM images of different molecular fragments resulting from the sublimation of $C_{28}O_8$. **a**) $\Delta z = 1.3$ Å, $I = 1$ pA, $V = 0.4$ V, **b**) $\Delta z = -0.6$ Å, $I = 0.5$ pA, $V = 0.4$ V, **c**) $\Delta z = 0.7$ Å, $I = 0.5$ pA, $V = 0.4$ V, **d**) $\Delta z = 1.2$ Å, $I = 0.5$ pA, $V = 0.4$ V.

4.3.3 UV studies of the cyclocarbon oxides

The cyclocarbon oxides and their acetal precursors (**14**, **27**, **28**) are a convenient model set of [4*n* + 2] and [4*n*] annulene derivatives. The first [18]-annulene was synthesised by Sondheimer in 1962[63–65] and since then it has been accepted that as the rigidity of a [4*n* + 2] and [4*n*] annulene derivative skeleton is increased then the stability of the system is increased[66]. For the cyclocarbon oxides and their acetal precursors the rigidity of the annulene ring skeleton is increased by the introduction of cyclobutene units as well as acetylene bonds to the π-skeleton. This structural rigidity can be investigated through the electronic absorption properties of the cyclocarbon oxides and their acetal protected precursors[67]. The acetal protected precursors to the cyclocarbon oxides (**14**, **27**, **28**) show remarkable stability and this can be attributed to their rigid annulene skeleton which is demonstrated in their crystal structures (see Section 4.3.5) and their electronic absorption patterns (Figure 4.14).

The acetal protected precursors (**14**, **27**, **28**) all show a similar well-structured absorption pattern which indicates that the molecules adopt a well-defined geometry in solution (Figure 4.14). They all exhibit absorption maxima between 337-361 nm due to the similar size of their conjugated π-systems and exhibit comparable molar absorption coefficients. It might be expected that **14** would have the shortest wavelength of absorption maximum as it has the smallest conjugated system compared to **27** and **28**. However this is not the case and there does not appear to be a clear correlation between the wavelength of the absorption maxima and the size of the conjugated π-system apart from the fact that all acetal precursors absorb in approximately the same wavelength region. All absorption spectra show similar spectral profiles due to the structural similarity of these compounds.

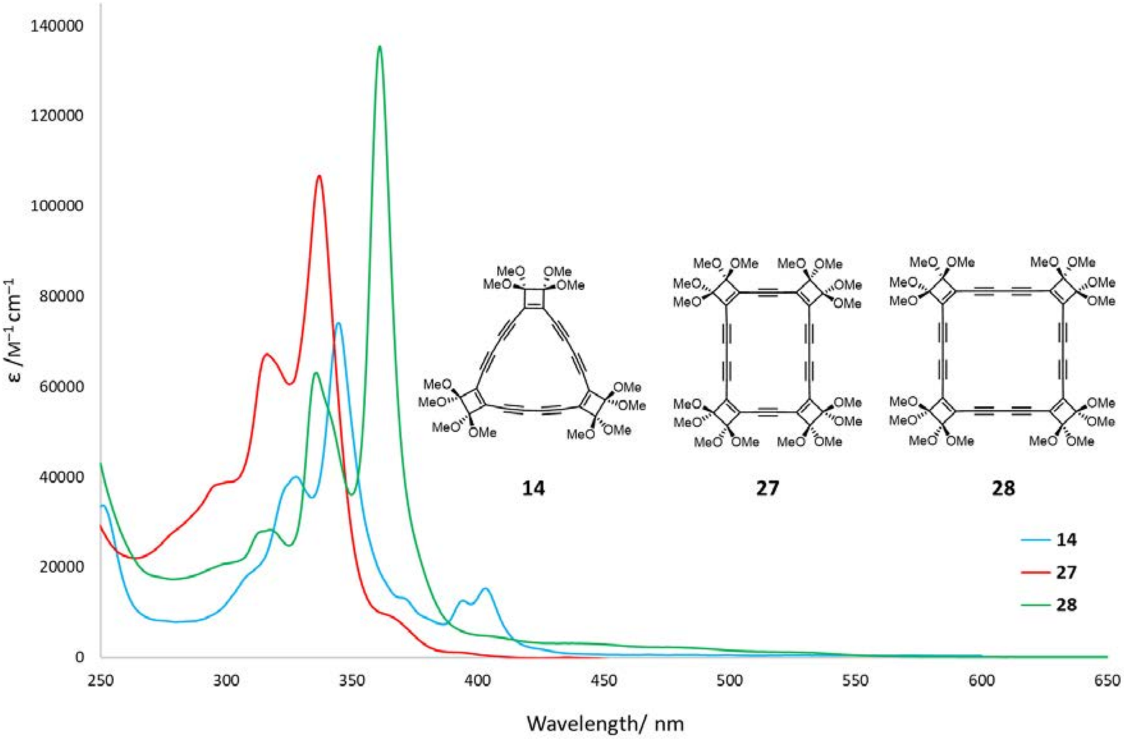

Figure 4.14 UV spectra of acetal precursors **14**, **27** and **28**. Spectra recorded at 9.1 µM (**14**), 11 µM (**27**) and 5.4 µM (**28**) in $CHCl_3$. Spectra are plotted as the molar extinction coefficient.

These absorption profiles can also be compared with absorption profiles of [18] and [24]-dehydroannulene (**33** and **34**, Figure 4.15) which were first synthesised by Sondheimer[63,64]. [18]-Dehydroannulene **33** has an absorption profile with strong absorptions between 300 and 350 nm which is similar to the absorption profile of **14**. One might initially expect the absorption spectra of **27** and **28** to be comparable to that of [24]-dehydroannulene **34**. However [24]-dehydroannulene **34** has a broad absorption profile and lacks the characteristic absorptions observed between 300 and 350 nm for [18]-dehydroannulene **33**. This has been attributed to its non-planar structure and its ability to adopt many different conformations in solution which contributes to its broad absorption profile. This is further confirmed by a non-planar conformation seen in its crystal structure (Figure 4.15**c**). As the absorption profiles of **27** and **28** are similar to that of **14** this suggests that they must all have a similar rigid planar structure which is in agreement with their crystal structures (4.3.5).

Their ability to adopt a rigid structure is likely due to the stability endowed by the external cyclobutene units and the acetylene bonds along the exterior of the annulene skeleton.

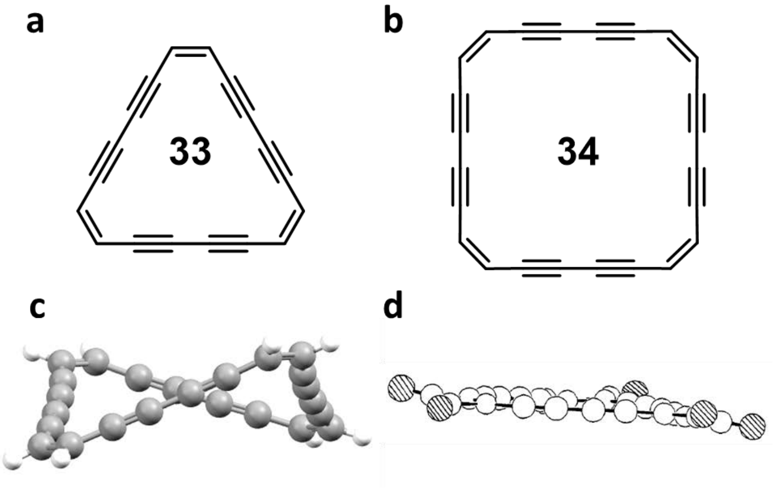

Figure 4.15 Structures of **a**) [18]-dehydroannulene **33**, **b**) [24]-dehydroannulene **34**, **c**) crystal structure of [24]-dehydroannulene **34**, crystal structure generated from reported structure in ref [68] and **d**) Side view crystal structure of $C_{24}O_6$, figure reprinted with permission from the American Chemical Society: Journal of the American Chemical Society[56].

Upon deprotection of **14**, **27** and **28** to their corresponding cyclocarbon oxides different behaviour is observed for the different cyclocarbon oxides. Comparison of the absorption profiles of **14** and $C_{24}O_6$ reveal comparable spectral profiles but with a bathochromic shift of 35 nm of $C_{24}O_6$ relative to **14** (Figure 4.16). The bathochromic shift in the system is a result of increased π-conjugation in $C_{24}O_6$ relative to **14** due to increased conjugation across the ketone groups. The similar spectral profiles suggest that the two molecules adopt similar conformations in solution. This is further supported by their crystal structures which both demonstrate a planar structure in the solid state (see Figure 4.15d and Section 4.3.5). This could be the origin of the stability of $C_{24}O_6$ relative to $C_{28}O_8$ and $C_{32}O_8$ as $C_{24}O_6$ is structurally similar in solution to **14** which is stable for prolonged periods.

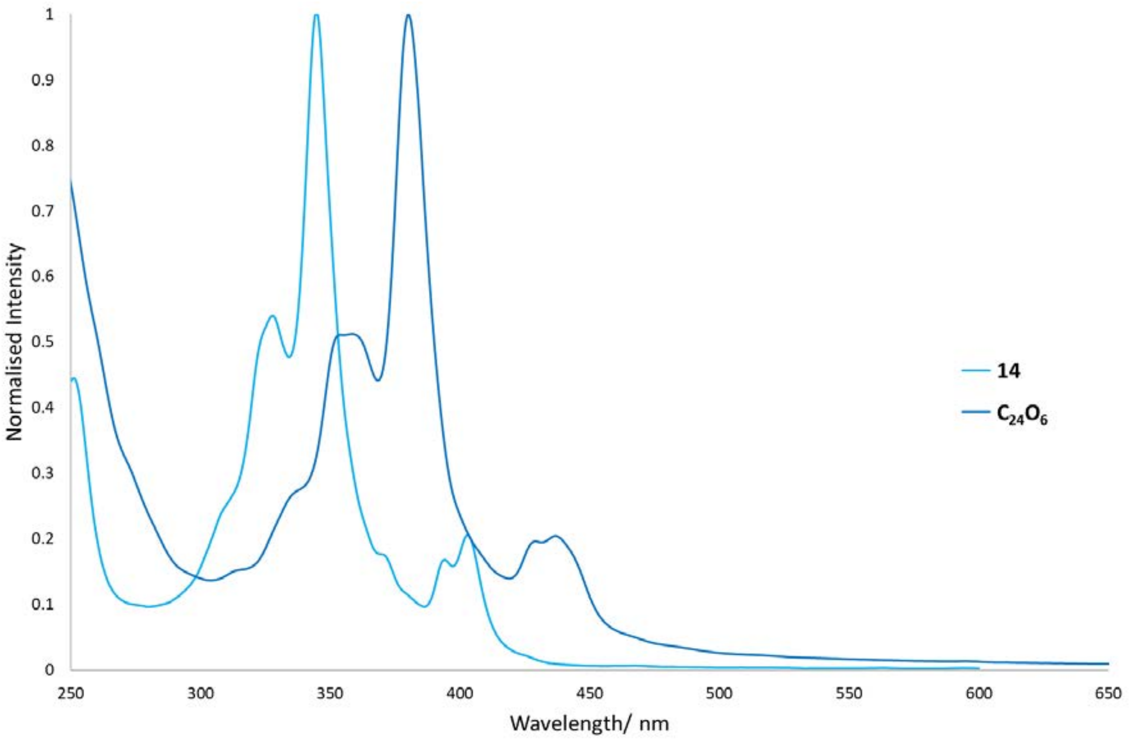

Figure 4.16 UV spectra of **14** (9.1 µM) and $C_{24}O_6$ (9.3 µM) in $CHCl_3$. Spectral intensities were normalised to the maximum absorption value for comparison.

The behaviour upon deprotection of **27** and **28** to their corresponding cyclocarbon oxides is different than for **14**. Upon deprotection of **27** a much broader absorption profile is observed for $C_{28}O_8$ relative to **27** (Figure 4.17) which is likely due to the fact that $C_{28}O_8$ can adopt many different conformations in solution. The same behaviour is observed upon deprotection of **28** (Figure 4.18) with $C_{32}O_8$ exhibiting a broad absorption profile similar to that of $C_{28}O_8$. For both $C_{28}O_8$ and $C_{32}O_8$ the spectral profiles are shifted towards the visible relative to **27** and **28** due to increased π-conjugation of the cyclocarbon oxides across their ketone groups relative to their acetal precursors. Both $C_{28}O_8$ and $C_{32}O_8$ are less stable than $C_{24}O_6$ which could be due to their ability to adopt different conformations in solution in contrast to $C_{24}O_6$ which is predicted to have a rigid structure which endows stability. In addition it is likely that $C_{28}O_8$ and $C_{32}O_8$ can access conformations required for the decomposition reaction profiles whereas $C_{24}O_6$ is unable to and therefore $C_{28}O_8$ and $C_{32}O_8$ are more prone to decomposition.

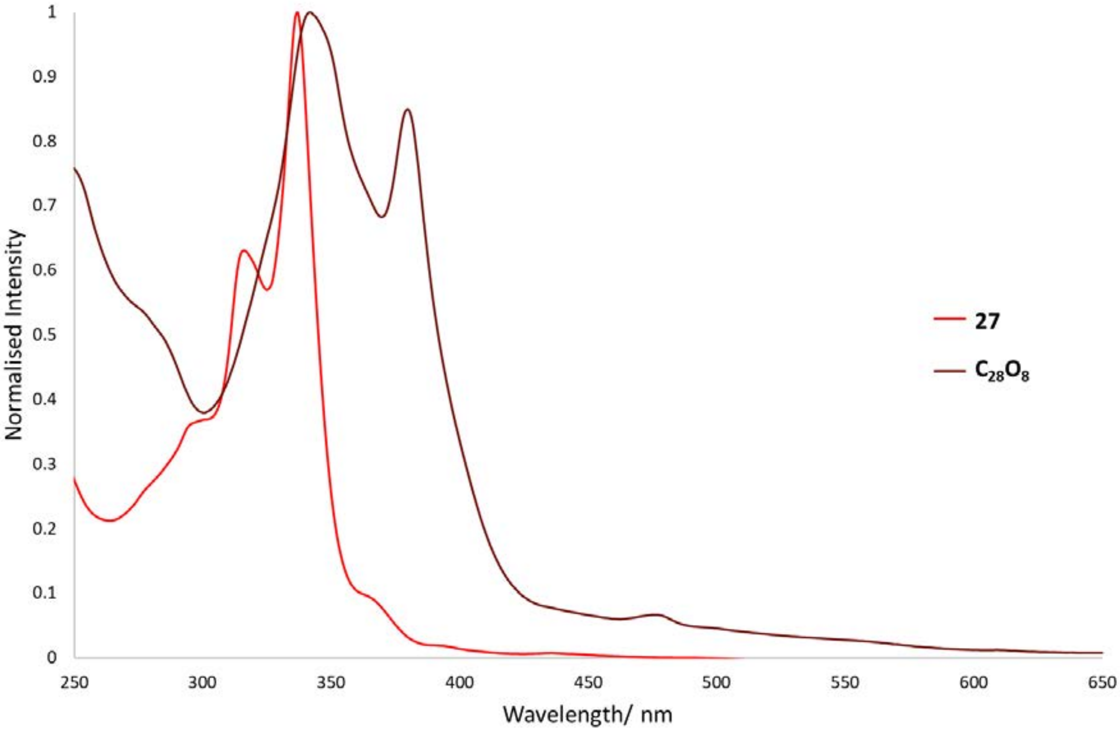

Figure 4.17 UV spectra of **27** (11 μM) and $C_{28}O_8$ (unknown concentration due to low stability on solvent removal, max possible concentration assuming 100% deprotection yield of 50 μM) in $CHCl_3$. Spectral intensities were normalised to the maximum absorption value for comparison.

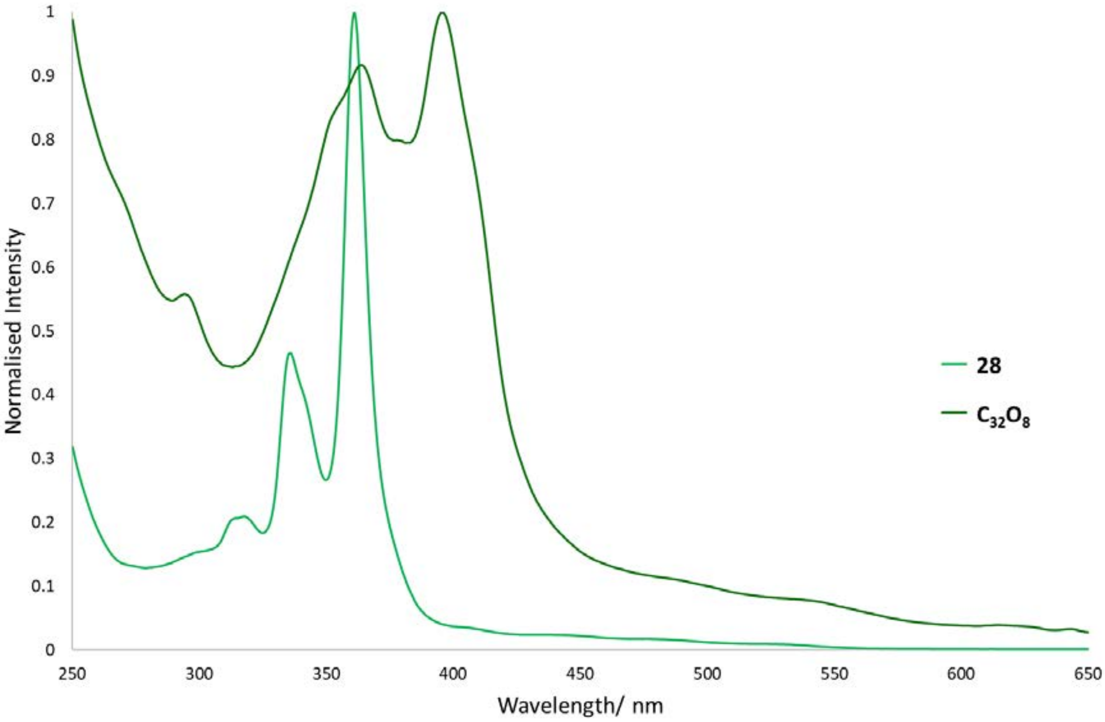

Figure 4.18 UV spectra of **28** (5.4 μM) and $C_{32}O_8$ (54 μM) in $CHCl_3$. Spectral intensities were normalised to the maximum absorption value for comparison.

The absorption spectra of $C_{28}O_8$ and $C_{32}O_8$ are in agreement with the absorption spectra of [24]-dehydroannulene[63,64] which also exhibits a broad absorption profile due to its conformational flexibility. This data suggests that $C_{32}O_8$ and $C_{28}O_8$ will exhibit many different conformations in solution in contrast to $C_{24}O_6$ and this is the origin of their low stability.

4.3.4 NMR studies of the cyclocarbon oxides

The acetal protected cyclocarbon oxide precursors provide a convenient set of model compounds to investigate the effects of aromaticity in [4*n* + 2] and [4*n*] annulene derivatives. The OMe groups can act as a probe for the ring currents in these systems as they lie above and below the plane of the ring pointing outwards (see crystal structures in 4.3.5) and therefore are affected by the ring current outside the ring. An aromatic ring system, such as **14**, exhibits a diamagnetic ring current in the presence of an external magnetic field. This diamagnetic ring current generates an induced magnetic field in the opposite direction to the external field in the centre of the ring and in the same direction as the external magnetic field on the outside of the ring.

For aromatic **14** the OMe protons should experience a net increase in the magnetic field, relative to the unconjugated monomer, and will be deshielded and shifted downfield. Whereas for antiaromatic **27** and **28** the external OMe probes should experience a net decrease in the magnetic field and will be shielded and shifted upfield. Analysis of the ^{1}H shifts of the OMe protons (Figure 4.19) in **14**, **27** and **28** shows the expected behaviour with antiaromatic **27** and **28** shifted upfield (3.37 for **28** and 3.32 and 3.35 ppm for **27**) relative to the unconjugated monomer **13** (3.50 ppm) and aromatic **14** shifted downfield (3.70 ppm).

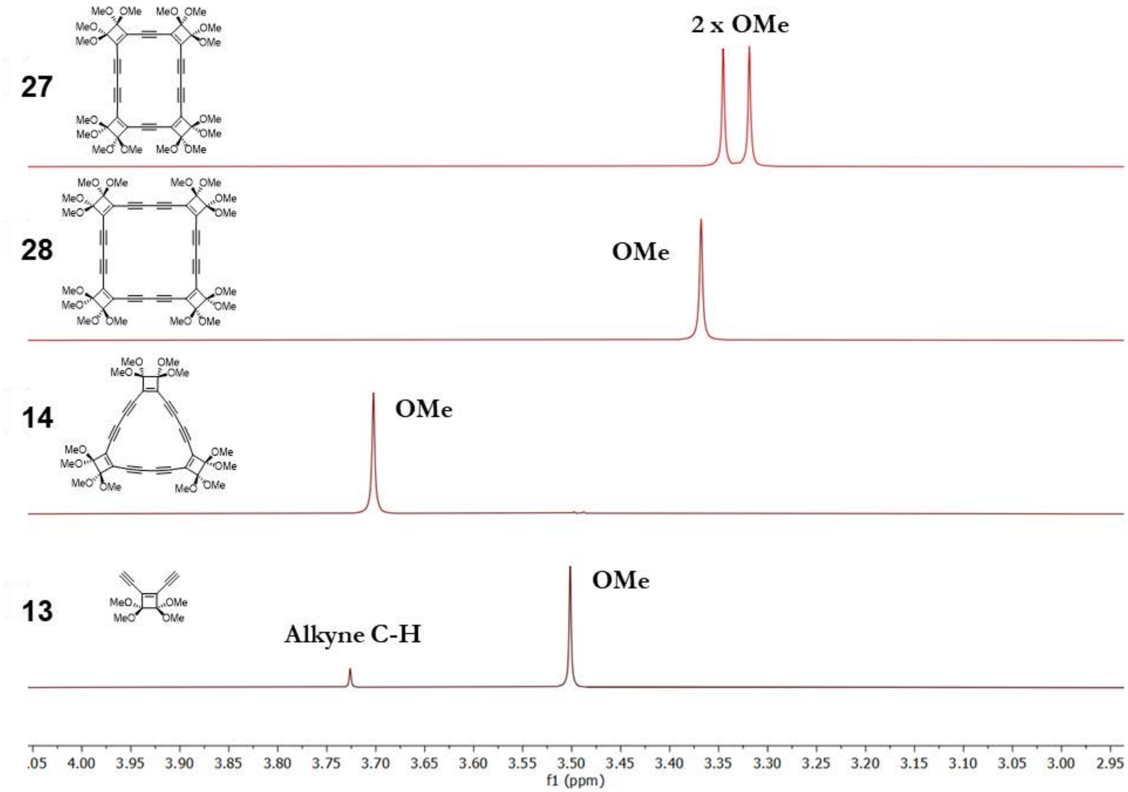

Figure 4.19 ^{1}H NMR spectra (101 MHz, $CDCl_3$, 294 K) of acetal protected cyclocarbon oxides (**14**, **27** and **28**) and the corresponding monomer (**13**).

These ^{1}H shifts are in general agreement with calculated NICS values for this set of compounds (Table 4.3) however the magnitude of the shift change relative to the monomer is larger for the calculated values than for the experimental ones; the experimental shift difference values are approximately a third of the size of the calculated ones.

Table 4.3 Calculated ^{1}H shifts of **14**, **27** and **28**. Δ = δ(monomer) – δ(compound)

	13 (monomer)	**14**	Δ	**27**	Δ	**28**	Δ
Calculated/ ppm	3.65	4.24	–0.59	3.26	0.39	3.28	0.37
Experimental/ ppm	3.50	3.70	–0.2	3.32, 3.35	0.18 0.15	3.37	0.13

The calculated NICS(*ZZ*) plots are shown in Figure 4.20. **14** is an 18 π electron aromatic system and therefore a large shielding is predicted in the centre of the ring due to the induced ring current and a predicted deshielding around the edge of the ring which would correspond to a downfield shift of the OMe protons, which is in accordance with the experimental result (Figure 4.19). For the antiaromatic acetal precursors **26,** **27** and **28** a large shielding is predicted around the edge of the ring which would correspond to an upfield shift of the OMe probes, which is in accordance with the experimental result for **27** and **28**. The proton shifts of **26** are predicted to be in the same range as for **27** and **28**.

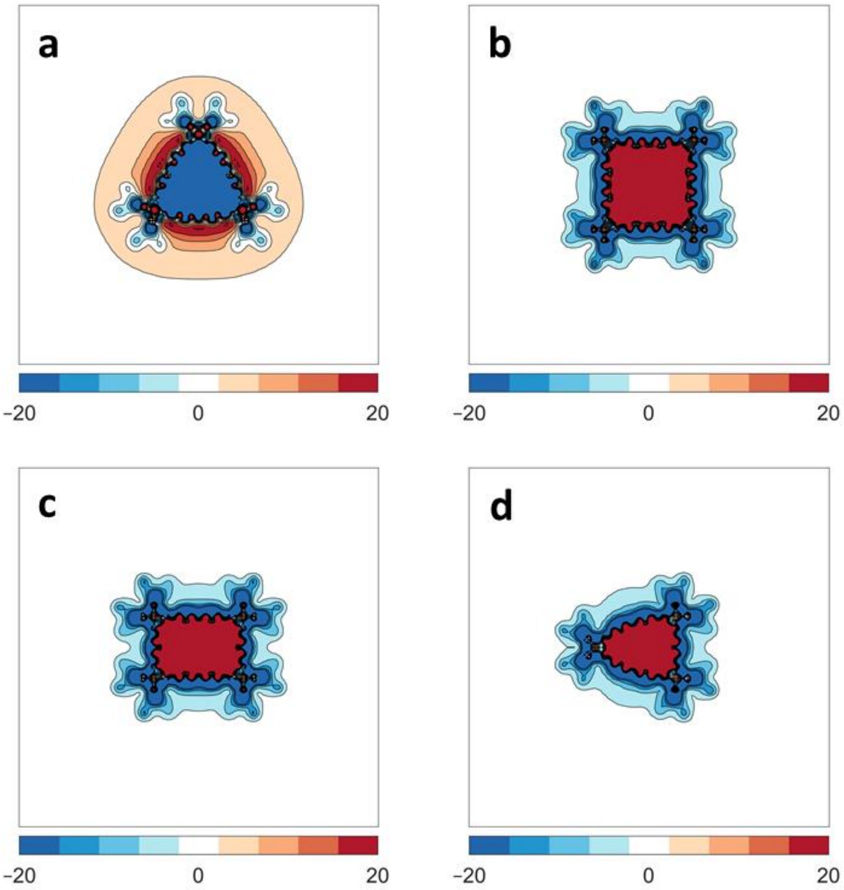

Figure 4.20 NICS(*ZZ*) calculations of **a**) Aromatic **14**, **b**) Antiaromatic **28**, **c**) Antiaromatic **27** and **d**) Antiaromatic **26**.

The magnitude of the shifts of the OMe protons is relatively small compared to that in [18]-annulene[12] but they are in accordance with similar ^{1}H spectra of related acetal protected compounds studied by Diederich *et al*[67]. The calculated HOMOs and LUMOs (Figure 4.21) demonstrate that the conjugated π-system is localised around the core of the molecule and not over the external cyclobutene rings. This therefore explains the small magnitude of the change in ^{1}H shift of the OMe probes due to their remote distance from the π-system.

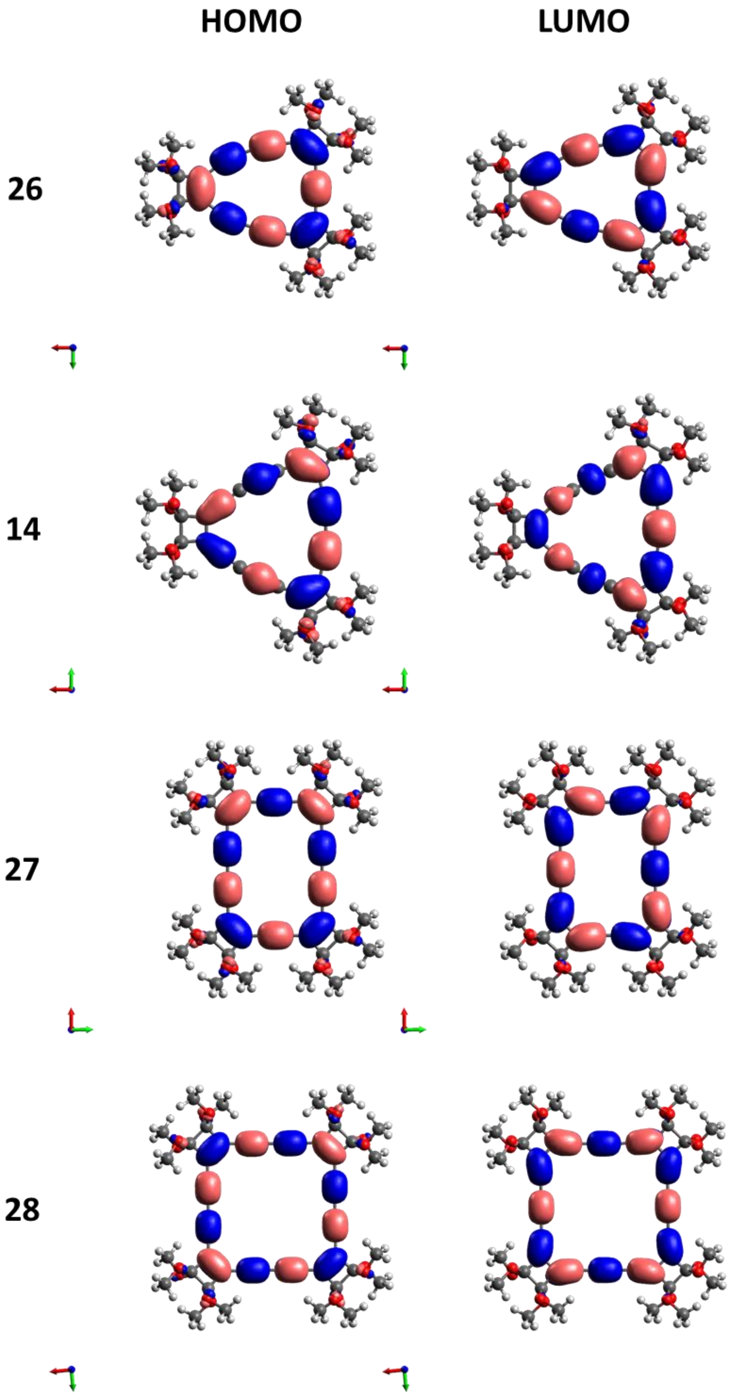

Figure 4.21 Calculated HOMOs and LUMOs of acetal protected precursors **14, 26–28**. Geometries were optimised using B3LYP functional and a 6-31G* basis set. The Natural Transition Orbitals were generated by Avogadro software using the isosurface value 0.02.

These results demonstrate that the acetal protected precursors provide a convenient model system for studying aromaticity in these systems as their ^{1}H shift differences are in accordance with calculated values.

4.3.5 Crystal structure studies of the cyclocarbon oxides

The crystal structures of **14**, **27** and **28** were obtained (see Section 2.3.1, 4.3.1, 4.3.2 and Figure 4.22). All crystal structures have a low R-factor (**14**, *R* = 3.8%, **27**, *R* = 5.0% and **28**, *R* = 5.6%) which allows for comparison of BLA and BAA in these systems.

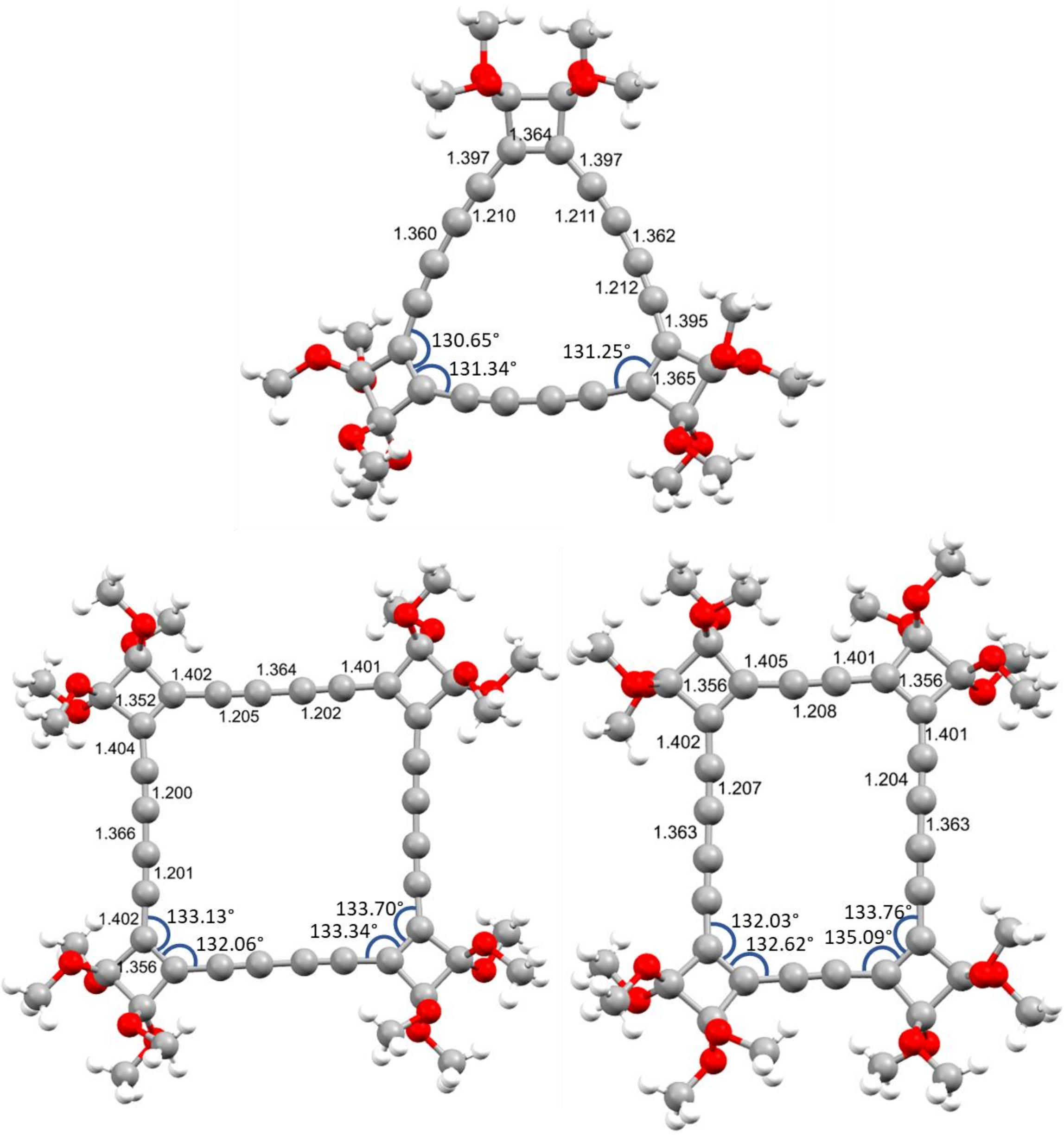

Figure 4.22 Crystal structures of acetal protected precursors (**14**, **27** and **28**). All bond lengths are given in Å. Data taken from the asymmetric unit and solvent molecules omitted for clarity.

These structures show clear bond length alternation in the acetylenic sides of the molecule which can be analysed using the equation BLA = $a - b$. a is the average length of the central single bond on the longest side of the molecules and b is the average triple bond length. The largest bond length alternation is calculated for **28** (0.163 Å) which is larger than the bond length alternation for **27** (0.157 Å) and larger again than for **14** (0.150 Å).

Table 4.4 Calculated bond length alternation in acetal protected precursors (**14**, **27** and **28**)

Molecule	*a*	*b*	BLA
14	1.361 Å	1.211 Å	0.150 Å
27	1.363 Å	1.206 Å	0.157 Å
28	1.365 Å	1.202 Å	0.163 Å

Antiaromatic compounds are expected to have a greater bond length alternation compared to aromatic ones (see Section 4.2). Therefore for the acetal precursor compounds you would expect to see a larger bond length alternation for antiaromatic $C_{32}O_8$ precursor **28** and $C_{28}O_8$ precursor **27** compared to aromatic $C_{24}O_6$ precursor **14**. The observed BLA values are in general larger for **27** and **28** than **14** however the trend is not clear cut as the bond length alternation calculated for **27** is smaller than expected and the difference in BLA values is not as large as might be expected (Table 4.4) therefore no clear conclusions about the BLA in these systems can be drawn from this data.

Another interesting observation that can be obtained from the crystal structures of **14**, **27** and **28** is found in the bond angles in these structures. The ideal angle for an [18]-dehydroannulene is 120° and for a [20 or 24]-dehydroannulene is 135°. The calculated angle[67] for a cyclobutene annulated monomer (**35,** Figure 4.23) is 136.3° and therefore the strain in **27** and **28** is expected to be lower than that of **14** as the ideal monomer geometry is closer to the preferred angle in the tetrameric species than the trimer. This can be observed in the crystal structure of the **14** (Figure 4.22) which shows considerable bending of the acetylene units to widen the angle surrounding the cyclobutenedione unit to minimise its strain. Therefore it is likely that the strain in this compound is distributed along the acetylene bonds. However, the strain in **14** does not seem to reduce its stability as the compound is stable at ambient conditions for prolonged periods.

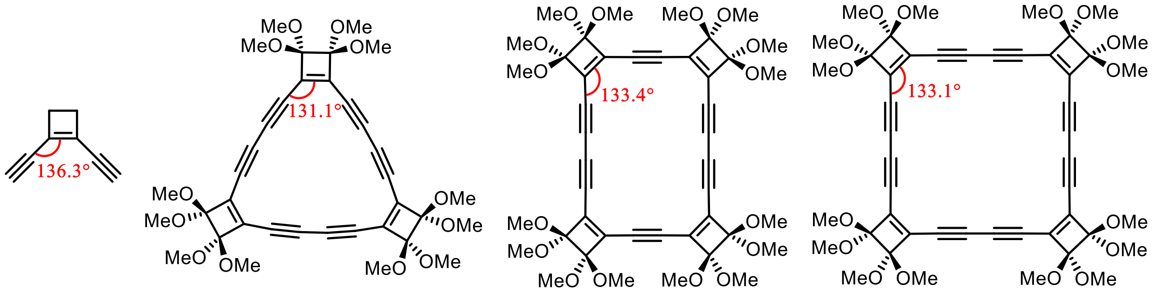

35 **14** **27** **28**

Figure 4.23 Average internal bond angles of the dehydroannulenes. Data for **35** taken from ref [68].

The synthesis of cyclo[18]carbon from $C_{24}O_6$ demonstrates that the cyclocarbon oxides have significant promise as cyclo[*n*]carbon precursors. This chapter has thus far demonstrated that the synthesis of alternate sizes of cyclocarbon oxides is possible and can be achieved by tailoring the structure of the acetal precursor. The properties of the cyclocarbon oxides and their acetal precursors have been well understood and I believe that with further synthetic attempts towards alternative cyclocarbon oxides then the on-surface synthesis of different sized cyclo[*n*]carbons will be realised.

4.4 Future Directions

My DPhil has just touched the surface of potential investigations into the cyclo[n]carbons and I hope that this work will be carried on and yield many more exciting results. My vision for the future of this project is to first further investigate different sizes of cyclo[n]carbons either with cyclocarbon oxide precursors or alternative precursors. I then envisage investigations into potential on-surface fusion reactions of the cyclo[n]carbons to form extended networks as well as investigating the different charge states of the cyclo[n]carbons.

4.4.1 Synthesis of $C_{22}O_6$

The low stability of $C_{28}O_8$ and $C_{32}O_8$ make them challenging compounds to handle and study, the origin of this low stability is predicted to be due to their flexible non-planar nature. $C_{24}O_6$ demonstrated much higher stability due to its rigid structure. $C_{22}O_6$ (Figure 4.8) was chosen as a synthetic target as it is predicted to have a similar rigid structure to $C_{24}O_6$, and therefore may have higher stability. In addition it has a lower molecular weight than all the cyclocarbon oxides discussed above which will facilitate its on-surface sublimation. The synthetic route towards this compound was devised by the author and the synthesis of this compound was first attempted by a talented master's student Isaac Ettedgui under the supervision of the author. Unfortunately his efforts towards this synthesis were halted due to lab closures related to Covid-19. However this project should be feasible for a new member of team cyclocarbon to attempt in the future. Herein the synthetic approach towards the target molecule, devised by the author, will be detailed.

The synthesis of $C_{22}O_6$ is more complex than that of $C_{28}O_8$ as it requires a stepwise approach in contrast to the syntheses detailed previously which all relied on an intermolecular Glaser-Hay coupling to yield the desired ring in a statistical manner. However, for $C_{22}O_6$ a more stepwise synthesis is needed due to the required monoacetylene bridge in the molecule as shown in Scheme 4.4. The synthesis is based on the need to prepare an asymmetrically protected unit, **39**. This was prepared in an analogous manner to the symmetrically protected unit **31** using modifications of Liebeskind's methodology[59,60] but instead using a trimethyl silyl (TMS) protecting group on the siloxy ketone, **36** to yield the desired compound **37**. This then undergoes acetal protection in an analogous manner to **30** to prepare the asymmetrically protected unit **38**. This synthesis was performed by Isaac and he prepared **38** in 12% yield over two steps from **29**. I believe upon scaling of this synthesis **38** could be prepared in higher yield. Selective deprotection of the asymmetrically protected **38** was then carried out with K_2CO_3 in 61% yield to give the monodeprotected unit, **39**.

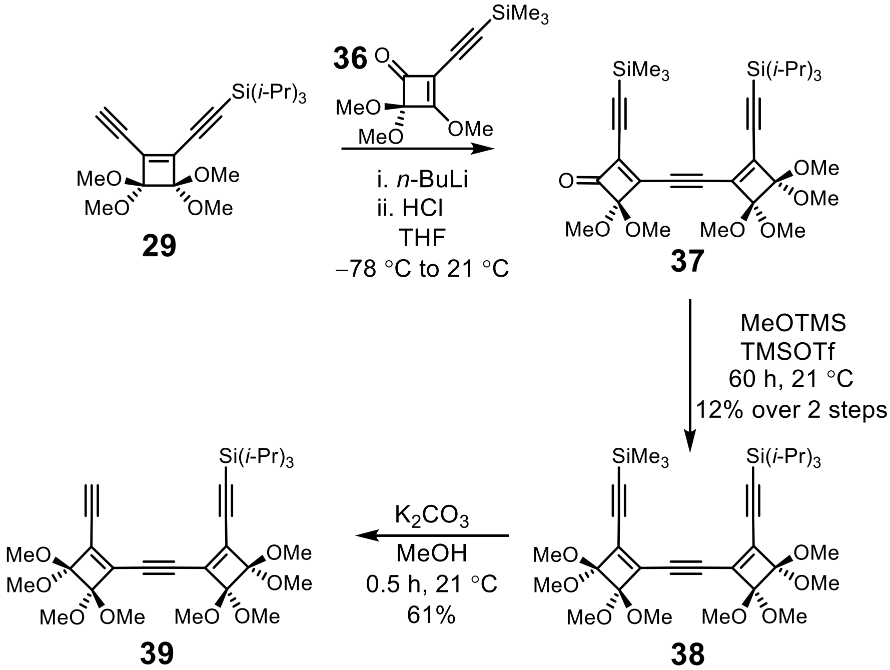

Scheme 4.4 Synthesis of the asymmetrically protected unit for cyclisation, **39**.

There are then two possible options for the synthetic strategy; Hay coupling[69] or a Cadiot Chodkiewicz coupling[70] (Scheme 4.5). A Cadiot Chodkiewicz strategy is advantageous as there is less potential for side product formation compared to the Hay coupling which would produce multiple different side products and require an excess of **29** however Cadiot Chodkiewicz couplings can be unreliable. An initial attempt towards a cross coupling was attempted using the brominated acetylene **40**, which was prepared from **29** using *N*-

bromosuccinimide and catalytic silver nitrate in 32% yield, and the asymmetrically protected unit **39**. A first attempt at this coupling by Isaac did not appear to yield the desired product however upon optimisation it is likely this strategy could be successful. If the Cadiot Chodkiewicz coupling proves unsuccessful then a statistical Hay coupling could be attempted with excess **29** to yield the desired product **41** as well as side products **42** and **43**. Due to the differing number of acetal protected cyclobutene groups in these compounds (**41**–**43**) they should have sufficiently different polarity to be separated on silica. However this synthetic route will require a large amount of **29** to be synthesised which is synthetically demanding.

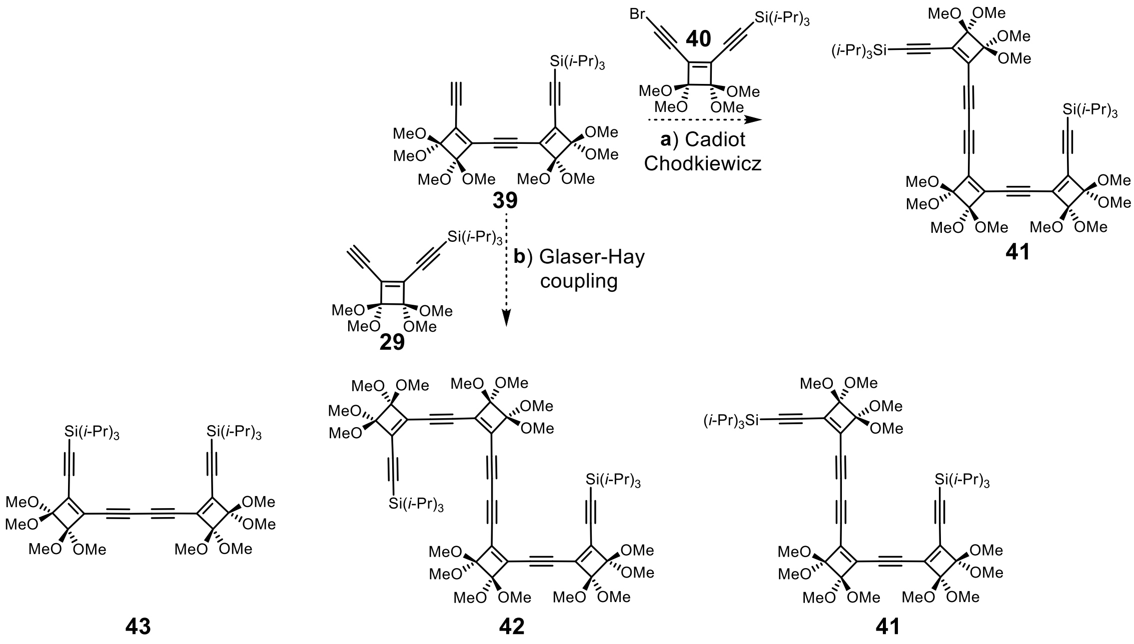

Scheme 4.5 Proposed synthesis of **41** *via* two possible methods **a**) Cadiot Chodkiewicz and **b**) Glaser-Hay coupling.

Once the desired unit **41** has been synthesised then a TBAF deprotection can be used to yield the desired precursor **44** which can be submitted to an intramolecular Hay cyclisation to yield the desired acetal precursor **26**. The acetal precursor **26** can then be deprotected in an analogous manner to the previous acetal precursors **14**, **27** and **28** with concentrated sulfuric acid. It is likely that $C_{22}O_6$ will exhibit comparable stability to $C_{24}O_6$ as they both should adopt a rigid structure and therefore it will hopefully be a successful precursor to C_{16} and remain intact upon sublimation for on-surface investigations.

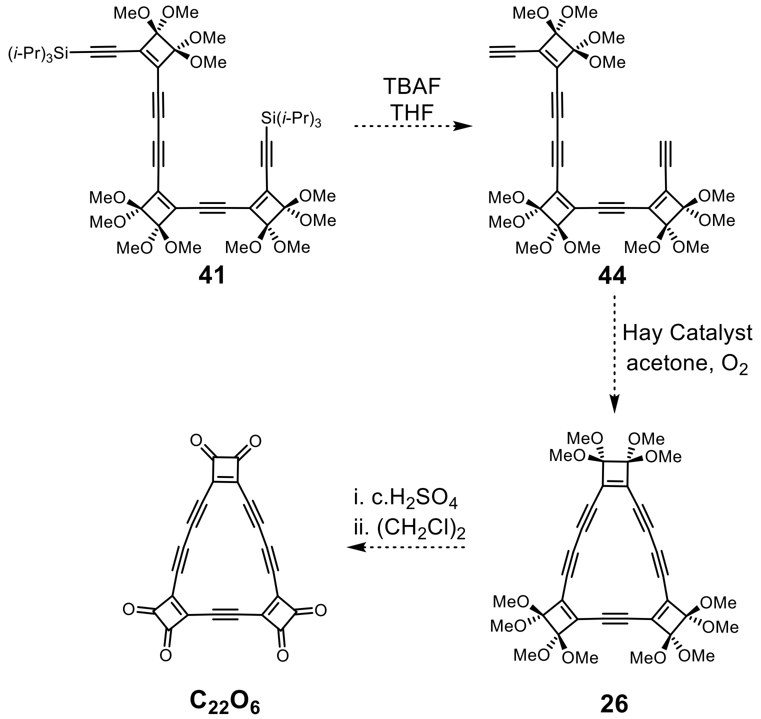

Scheme 4.6 Proposed synthesis of $C_{22}O_6$ via an intramolecular Glaser-Hay coupling.

4.4.2 Cyclo[*n*]carbon fusion reactions

An exciting future avenue will be investigations into on-surface cyclo[*n*]carbon fusion reactions. On-surface synthesis by atom manipulation is an exciting new field with still only a relatively small number of successful examples having been reported[71–76]. The cyclo[*n*]carbons are exciting candidates for on-surface molecular fusion reactions due to their high reactivity (see Section 2.4.5). It had been predicted that the bromocyclocarbons (see Chapter 3) would provide suitable candidates for the on-surface molecular fusion as $C_{18}Br_6$ unmasks in a mild fashion to cyclo[18]carbon and therefore we had hoped if two cyclo[18]carbon molecules could be formed in close proximity to each other a fusion reaction could occur (see Section 3.4.3). Unfortunately the sublimation of $C_{18}Br_6$ led to well dispersed molecules which meant that the precursor molecules were not in close enough proximity to attempt a fusion reaction. In order to facilitate fusion reactions a precursor would need to be developed that unmasks in a mild fashion to a cyclo[*n*]carbon and undergoes facile sublimation to generate a high density of molecules on the surface. The cyclocarbon oxides are unlikely to be suitable candidates as $C_{24}O_6$ unmasks in a relatively low yield to cyclo[18]carbon (see Section 2.4.4). A modification of the bromocyclocarbon precursors such as smaller analogues with lower molecular weight could be possible candidates as they should unmask in a mild fashion and undergo facile sublimation. An example is shown in Figure 4.24 whereby a precursor could be unmasked to cyclo[12]carbon which could then undergo ring fusion to cyclo[24]carbon or form a bicyclic system, both instances would be exciting examples of on-surface molecular fusion reactions.

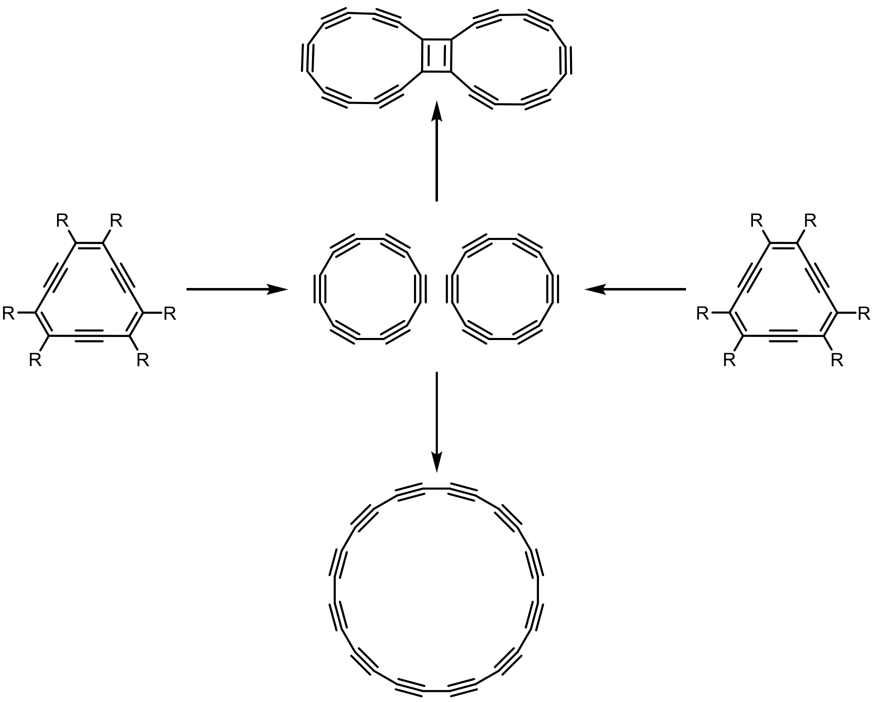

Figure 4.24 Potential on-surface molecular fusion reactions of cyclo[*n*]carbons. Example shown here for cyclo[12]carbon fusion but could be applied to any size of cyclo[*n*]carbon. R represents a suitable leaving group in the cyclo[*n*]carbon precursor. Arrows represent on-surface atom manipulation reactions.

This approach could be extended to the formation of infinite graphdiyne networks (Figure 4.25). This concept was first proposed by Diederich in 1992[77] however it was not realised due to the low stability of the cyclo[*n*]carbons. However if the on-surface formation of cyclo[*n*]carbons can be optimised so that multiple cyclo[*n*]carbons are formed in close proximity then it may be possible to trigger on-surface 2D polymerisation to form infinite graphdiyne and study its properties.

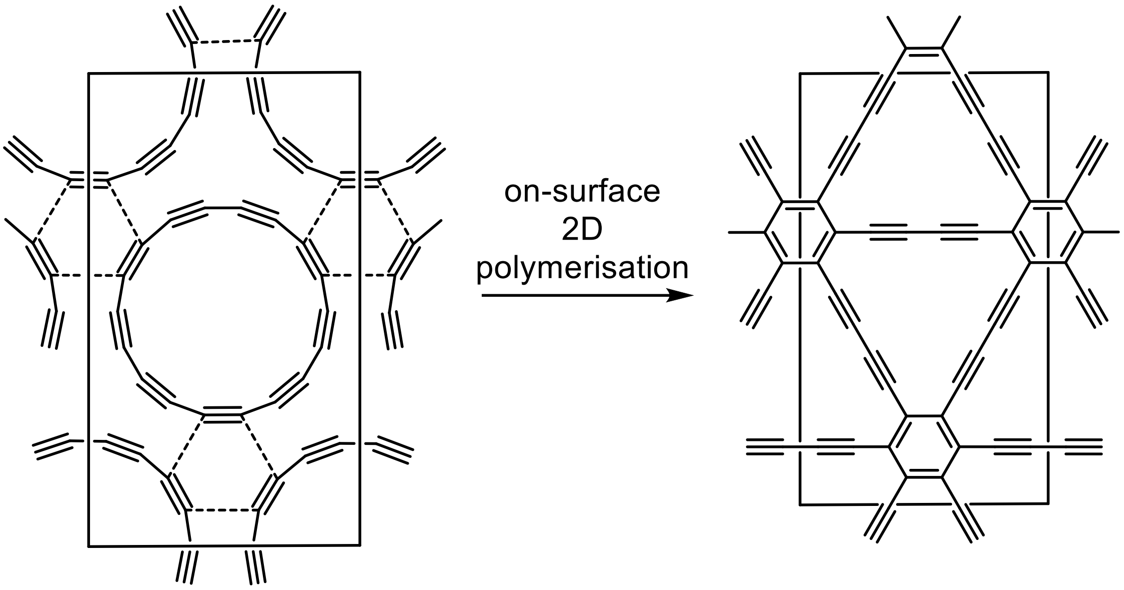

Figure 4.25 Synthetic approach to infinite network graphdiyne.

4.4.3 Different charge states of the cyclo[*n*]carbons

Another interesting avenue to investigate is the different charge states of the cyclo[*n*]carbons. Recent exciting advances in imaging of molecules in different charge states[74,78–82] has led to the possibility that if a cyclo[*n*]carbon precursor could be successfully unmasked by atom manipulation on multilayer sodium chloride then its charge state could be controlled and it could be imaged in different charge states. This concept has been demonstrated on multiple different molecules by Gross *et al.*[82] whereby they performed AFM on thick insulating films consisting of 20 or more monolayers of sodium chloride. Using this method they were able to control the charge states of various organic molecules and image their structures in different charge states. The negative charge state of cyclo[18]carbon has been imaged (see 2.4.3) and cyclo[18]carbon was found to distort to a less symmetric conformation and was more reactive in its negative charge state. Therefore investigations of alternative charge states of cyclo[18]carbon and different cyclo[*n*]carbons would be a very interesting area as it could give further insights into the aromaticity and bond length alternation in these systems. However for this to be achieved, as in Section 4.4.2 a cyclo[*n*]carbon precursor that unmasks in a mild fashion and undergoes facile sublimation to generate a high density of molecules on the multilayer sodium chloride needs to be achieved.

4.5 Conclusions

In conclusion, a series of cyclocarbon oxides, $C_{32}O_8$, $C_{28}O_8$ and $C_{24}O_6$, and their corresponding acetal precursors (**28**, **27** and **14**) were successfully synthesised and studied. The synthesis of the novel cyclocarbon oxide $C_{28}O_8$ was successfully carried out upon optimisation of the synthetic route. The electronic absorption properties of this set of cyclocarbon oxides and their acetal precursors revealed the origin of the low stability of $C_{32}O_8$ and $C_{28}O_8$ as likely being due to their flexible conformation in solution. NMR studies of the acetal precursors (**14**, **27** and **28**) revealed that these compounds are a convenient model system to study ring currents in these systems as their ^{1}H NMR shifts showed the expected behaviour due to the diatropic and paratropic ring currents in the different systems and were in agreement with calculated NICS values. The crystal structures of the acetal precursors (**14**, **27** and **28**) were studied and their relative bond length alternation discussed. Unfortunately the on-surface sublimation of both $C_{28}O_8$ and $C_{32}O_8$ was unsuccessful with only molecular fragments observed after sublimation and therefore the properties of antiaromatic cyclo[20]carbon and cyclo[24]carbon could not be studied. The future directions for this project have been detailed including the attempted synthesis of $C_{22}O_6$ and other future aims for this project.

4.6 Experimental Data

4.6.1 Synthetic General Methods

Reagents (Alfa Aesar, Aldrich, Acros, Fluorochem, Fisher Scientific) were used without further purification. Dry solvents (THF, $CHCl_3$, CH_2Cl_2) for reactions were purified by a MBraun MB-SPS-5-Bench Top under nitrogen (H_2O content < 20 ppm). All other solvents used were HPLC grade and dried over molecular sieves (acetone, $(CH_2Cl)_2$). Reactions, unless otherwise stated, were carried out in oven-dried glassware under a N_2 atmosphere. Flash column chromatography was carried out on a Biotage Isolera One with a 200–400 nm UV detector. Analytical thin layer chromatography (TLC) was performed on aluminium sheets coated with silica gel 60 F254 (Merck). UV light (254 nm) was used for visualisation. Evaporation *in vacuo* was performed at 15–40 °C and 5–1010 mbar. Reported yields refer to pure compounds dried under high vacuum (< 0.1 mbar). ^1H and ^{13}C nuclear magnetic resonance (NMR) were recorded on Bruker AVIII HD 400 spectrometer at 400 MHz (^1H) and 101 MHz (^{13}C) and a Bruker AVIII 700 at 176 MHz (^{13}C) at 294 K. Chemical shifts, δ, reported in ppm downfield from tetramethylsilane using residual deuterated solvent signals as internal reference except for $C_{28}O_8$ where the spectrum is unreferenced ($CDCl_3$: $\delta_H = 7.26$ ppm, $\delta_C = 77.16$ ppm). High-resolution mass spectrometry (HR-MS) measurements were performed by the mass spectrometry service at the University of Oxford on a Waters GTC classic.

4.6.2 Synthetic Protocols

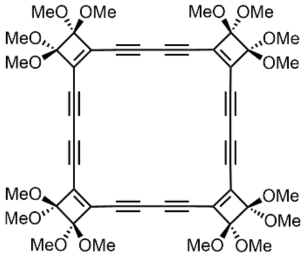

Synthesis of compound 28: Freshly prepared CuCl[83] (5.0 g, 51 mmol) was stirred in acetone (50 mL) under N_2. TMEDA (2.7 mL, 18 mmol) was added to this suspension and the resulting opaque, pale blue solution was stirred for 30 minutes. The solid was allowed to settle and the supernatant solution (15.0 mL, 5.29 mmol) withdrawn and immediately added to a vigorously stirred solution of **13** (1.15 g, 5.17 mmol) in acetone (300 mL) at 21 °C with a $CaCl_2$ drying tube and under an O_2 atmosphere for 2 h. Upon completion the reaction was diluted with $CHCl_3$ (300 mL) and the organic phase washed with water (2 × 600 mL). The organic extracts were combined and dried over $MgSO_4$ and the solvent removed *in vacuo* at 30 °C. The crude was purified by column chromatography, SiO_2 (petroleum ether/ethyl acetate 8:2) to yield **28** as a red solid (96 mg, 0.11 mmol, 8%) as well as **14** as a yellow solid (76 mg, 0.12 mmol, 7%). Single crystals of **28** were grown by layer diffusion of $CHCl_3$/ hexane to yield red cubic crystals. **^{1}H NMR** (400 MHz, $CDCl_3$): 3.37 (s, 48H) ppm. **^{13}C NMR** (101 MHz, $CDCl_3$): 138.5, 108.3, 88.7, 79.7, 52.3 ppm. **MALDI-TOF m/z:** 849.50, (mass corresponds to $C_{47}H_{45}O_{15}^+$: 849.28). **IR (ATR):** $\tilde{\nu}$ = 826, 875, 982, 1034, 1084, 1179, 1206, 1252, 1356, 1458, 2837, 2942 cm^{-1}. **M.p.:** decomposes at ≈ 200 °C. **UV/vis ($CHCl_3$): λ_{max} (ε)** = 408 (4244), 361 (134091), 342 (51705), 335 (61969), 319 (27529), 314 (27529), 298 nm (20205 M^{-1} cm^{-1}).

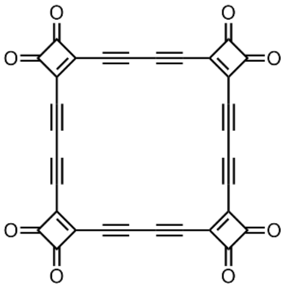

Synthesis of $C_{24}O_6$: All reaction vessels were kept under nitrogen and wrapped with aluminium foil to exclude light. Concentrated H_2SO_4 (0.2 mL) was dropped onto **28** (10 mg, 0.011 mmol) to form a dark red emulsion which was stirred for 5 minutes at 21 °C. Then, $(CH_2Cl)_2$ (10 mL) was added and the resulting solution stirred vigorously for 10 minutes. The clear orange organic phase containing traces of acid was transferred *via* syringe to a flask containing $CaCO_3$ (0.4 g). The extraction with $(CH_2Cl)_2$ was repeated until the organic extracts were colourless. The combined organic phases were filtered with 0.45 μm PTFE syringe filters to yield a clear orange solution. The solvent was removed *in vacuo* and crude material was dried under high vacuum in the dark to yield $C_{32}O_8$ as an unstable, light sensitive red solid which was stored in the dark at –20 °C and observed to decompose over a couple of days under these conditions (1.2 mg, 2 μmol, 21%). **^{13}C NMR** (101 MHz, $CDCl_3$): 190.4, 180.0, 107.4, 82.6 ppm. **IR (ATR): $\tilde{\nu}$** = 611, 621, 649, 800, 919, 1015, 1193, 1356, 1457, 1560, 1785 (strong), 2107, 2853, 2924 cm^{-1}. **UV/vis ($CHCl_3$): λ_{max} (ε)** = 380 (6205), 363 (7178), 352 (6524), 296 (4301), 269 nm (6205 M^{-1} cm^{-1}). ^{13}C NMR and IR spectra match that of the literature[56].

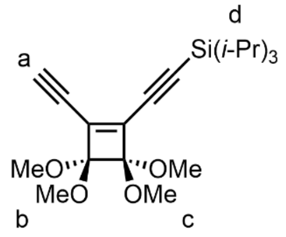

Synthesis of compound 29: K_2CO_3 (245 mg, 1.78 mmol) was added to a colourless solution of **12** (800 mg, 1.78 mmol) in MeOH (50 mL) and the reaction stirred for 15 minutes. The solvent was removed *in vacuo* and filtered through a silica plug (Et_2O/ petroleum ether 1:1) to yield **29** as a yellow oil (664 mg, 1.75 mmol, 99%). **^{1}H NMR** (400 MHz, $CDCl_3$): 3.67 (s, 1H; **a**), 3.52 (s, 6H; **b**/**c**), 3.51 (s, 6H; **b**/**c**), 1.08 (s, 21H; **d**) ppm. **^{13}C NMR** (101 MHz): 137.4, 134.7, 108.3, 108.1, 108.0, 97.6, 90.6, 75.3, 52.2, 52.1, 18.7, 11.3 ppm. **HR-ESI-MS m/z:** 401.2123 (mass corresponds to $C_{31}H_{34}O_4NaSi^+$: 401.2119) **IR (ATR): $\tilde{\nu}$** = 624, 661, 678, 715, 821, 883, 904, 984, 1038, 1080, 1179, 1203, 1257, 1367, 1384, 1463, 2094, 2137, 2361, 2837, 2866, 2894, 2943, 3249 (broad) cm^{-1}.

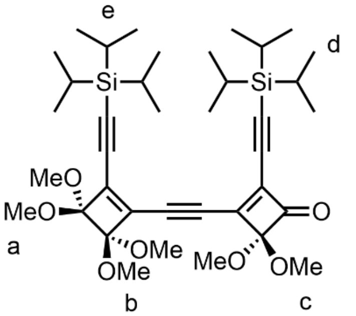

Synthesis of compound 30: (**NB 29** should be prepared on the day of use) Both **29** and **11** were passed through a $MgSO_4$ plug and dried under high vacuum for one hour prior to use. *n*-BuLi (1.57 mL, 1.6 M in hexanes, 2.51 mmol) was added to a solution of **29** (839 mg, 2.22 mmol) in Et_2O (5 mL) at –78 °C and a colour change from clear yellow to opaque green was observed. The solution was stirred at –78 °C for 1 h. A solution of **11** (708 mg, 2.09 mmol) in Et_2O (10 mL) was added and the resultant solution warmed to 0 °C and stirred for 1 h. 3 M HCl (10 mL) was then added and the two-phase mixture stirred vigorously for 1 h. The acidic layer was decanted and the organic layer washed with a sat. aqueous solution of $NaHCO_3$. The resultant organic layer was dried over $MgSO_4$ and the crude was subjected to the next step without further purification (assume 100% yield 1.43 g, 2.09 mmol). On one occasion a portion of the crude was purified by column chromatography, SiO_2 (petroleum ether/ ethyl acetate 9:1) to yield a small amount of pure **30** as a yellow oil for characterisation purposes. **^{1}H NMR** (400 MHz, $CDCl_3$): 3.53 (s, 6H; **a**/**b**), 3.52 (s, 6H; **a**/**b**), 3.49 (s, 6H; **c**), 1.08 (s, 21H; **e**/**d**), 1.07 (s, 21H; **e**/**d**) ppm. **^{13}C NMR** (101 MHz, $CDCl_3$): 189.6, 158.5, 141.2, 139.2, 132.8, 117.6, 111.9, 111.1, 108.6, 108.2, 107.3, 97.9, 93.1, 90.8, 53.2, 52.2, 52.2, 18.6 (broad), 11.3, 11.2 ppm. **HR-ESI-MS m/z:** 685.3945 (mass corresponds to $C_{38}H_{61}O_7Si_2^+$: 685.3950). **IR (ATR): $\tilde{\nu}$** = 609, 624, 662, 678, 717, 749, 803, 822, 900, 984, 1037, 1082, 1180, 1204, 1236, 1347, 1384, 1462, 1554, 1619, 1787, 1930, 2132, 2177, 2362, 2838, 2866, 2893, 2943 cm^{-1}.

Synthesis of compound 31: TMSOTf (0.25 mL, 1.37 mmol) was added to a solution of **30** (assume 100% 1.43 g, 2.09 mmol) in MeOTMS (6.33 mL, 45.9 mmol) under N_2. The resultant solution was stirred for 72 h and then quenched with a sat. aqueous solution of $NaHCO_3$ (20 mL) and extracted with Et_2O (2 × 20 mL) to yield the crude as a dark brown oil which was purified by column chromatography, SiO_2 (petroleum ether/ ethyl acetate 95:5) to yield **31** as an off white solid (656 mg, 0.90 mmol, 43% over two steps). **^{1}H NMR** (400 MHz, $CDCl_3$): 3.51 (s, 12H; **a**/**b**), 3.48 (s, 12H; **a**/**b**), 1.06 (s, 42H; **c**) ppm. **^{13}C NMR** (101 MHz, $CDCl_3$): 136.6, 134.0, 109.1, 108.4, 108.2, 98.1, 93.2, 52.2, 52.1, 18.7, 11.3 ppm. **HR-ESI-MS m/z:** 753.4185 (mass corresponds to

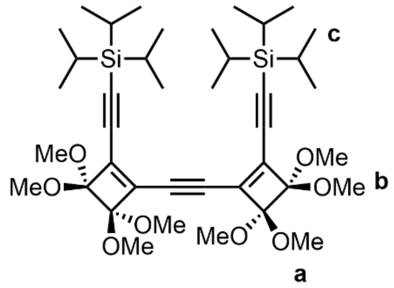

$C_{40}H_{66}O_8NaSi_2^+$: 753.4188). **IR (ATR):** $\tilde{\nu}$ = 621, 675, 719, 883, 941, 985, 1041, 1080, 1180, 1255, 1341, 1463, 2133, 2367, 2836, 2866, 2943 cm^{-1}. **M.p.:** 107–110 °C

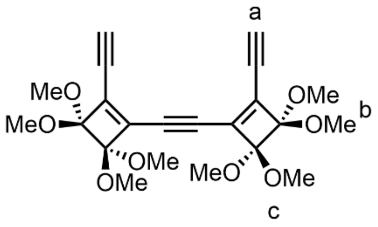

Synthesis of compound 32: Tetrabutylammonium fluoride (2.06 mL, 1.0 M in THF, 2.06 mmol) was added to a solution of **31** (685 mg, 0.94 mmol) in THF, 1% H_2O (30 mL) at 0 °C and the solution changed from pale yellow to pale red with a gradual colour change to brown over 20 minutes. The reaction was quenched after 20 minutes with H_2O (30 mL) and extracted with diethyl ether (40 mL). The organic phase was dried over $MgSO_4$ and purified by column chromatography, SiO_2 (petroleum ether/ ethyl acetate 1:1) to yield **32** as an off-white solid (301 mg, 0.72 mmol, 77%). **^{1}H NMR** (400 MHz, $CDCl_3$): 3.76 (s, 2H; **a**), 3.50 (s, 12H; **b**/**c**), 3.49 (s, 12H; **b**/**c**) ppm. **^{13}C NMR** (101 MHz, $CDCl_3$): 136.2, 135.6, 108.6, 108.1, 93.0, 92.3, 75.3, 52.2, 52.1 ppm. **HR-ESI-MS m/z:** 419.1692 (mass corresponds to $C_{22}H_{27}O_8^+$: 419.1700). **IR (ATR):** $\tilde{\nu}$ = 671, 872, 933, 983, 1040, 1079, 1180, 1195, 1253, 1333, 1457, 1457, 2093, 2360, 2360, 2838, 2943, 3238 (broad) cm^{-1}. **M.p.:** turns black around 135 °C, no further change up to 250 °C

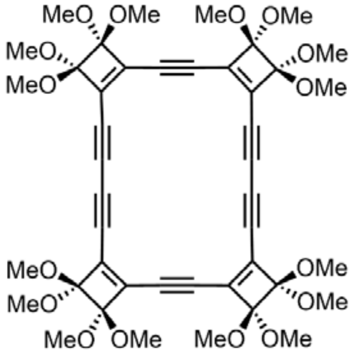

Synthesis of compound 27: TMEDA (0.27 mL, 1.81 mmol) was added to a suspension of CuCl (500 mg, 5.10 mmol) in acetone (5 mL). The resultant pale green suspension was stirred for 30 minutes under N_2 and the supernatant solution (2.1 mL, 0.72 mmol) was withdrawn and added to a vigorously stirred solution of **32** (301 mg, 0.72 mmol) in acetone (70 mL) under O_2. A colour change from clear orange to brown was observed upon addition of the catalyst and a gradual yellow tinge was observed over the course of the reaction. The reaction mixture was stirred for 3 h and then diluted with $CHCl_3$ (200 mL) and washed with water (2 × 200 mL) to yield the crude as a brown oil. This was purified by column chromatography, SiO_2 (petroleum ether:

ethyl acetate 1:1) to yield crude **27** as a red oil which was further purified by recrystallisation ($CHCl_3$, petroleum ether) to yield pure **27** as a red crystalline solid (59 mg, 0.07 mmol, 20%). **^{1}H NMR** (400 MHz, $CDCl_3$): 3.35 (s, 24H), 3.32 (s, 24H) ppm. **^{13}C NMR** (101 MHz, $CDCl_3$): 139.3, 137.8, 108.0, 107.9, 96.4, 88.9, 79.7, 52.3, 52.0 ppm. **HR-ESI-MS m/z:** 855.2834 (mass corresponds to $C_{44}H_{48}O_{16}Na^+$: 855.2835). **IR (ATR):** $\tilde{\nu}$ = 667, 688, 754, 843, 874, 982, 1033, 1080, 1161, 1177, 1194, 1254, 1438, 2032, 2161, 2835, 2942 cm^{-1}. **M.p.:** 187–190 °C **UV/vis ($CHCl_3$): λ_{max} (ε)** = 337 (116021), 317 (73180), 296 (74273), 277 nm (30595 M^{-1} cm^{-1}).

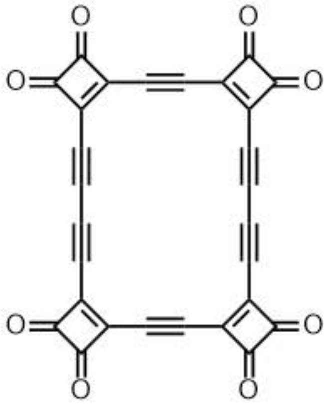

Synthesis of $C_{28}O_8$: All reaction vessels were kept under nitrogen and wrapped with aluminium foil to exclude light. Concentrated H_2SO_4 (0.2 mL) was dropped onto **27** (10 mg, 0.012 mmol) to form a deep-red emulsion which was stirred for 5 min at 21 °C. Then CH_2Cl_2 (10 mL) was added and the resulting solution stirred vigorously for 10 minutes. The clear orange organic phase was transferred *via* syringe to a flask containing $CaCO_3$ (0.4 g). The extraction with CH_2Cl_2 was repeated until the extracts were colourless. The combined organic phases over $CaCO_3$ were filtered through 0.45 μm PTFE syringe filters to yield a clear orange solution (~20 mL). This solution was concentrated *in vacuo* in the absence of light to a volume of approximately 7 mL. It was then transferred to a vial and concentrated further using a flow of nitrogen to ~3 mL, care had to be taken when removing solvent as any solution splashed up the sides of the vial would undergo decomposition. This concentrated solution was then used for characterisation purposes (IR and UV) however it was not possible to determine the concentration. Due to the instability of this compound to solvent removal the yield for this reaction could not be determined. To obtain a sample suitable for NMR 20 mg of **27** was dissolved in D_2SO_4 and the spectrum was immediately recorded. **^{13}C NMR** (176 MHz, D_2SO_4): 194.3, 192.0, 180.6, 178.1, 110.0, 106.5, 82.6 ppm. **IR (ATR): $\tilde{\nu}$ =** 763, 802, 1022, 1261, 1377, 1458, 1521, 1784 (strong), 2950 (residual solvent), 3122 (residual solvent) cm^{-1}. **UV/vis ($CHCl_3$): λ_{max} (ε, minimum values) =** 477 (707), 380 (9040), 350 (9980), 343 (10602), 285 (5258), 276 (5734) nm.

4.6.3 Selected Spectra

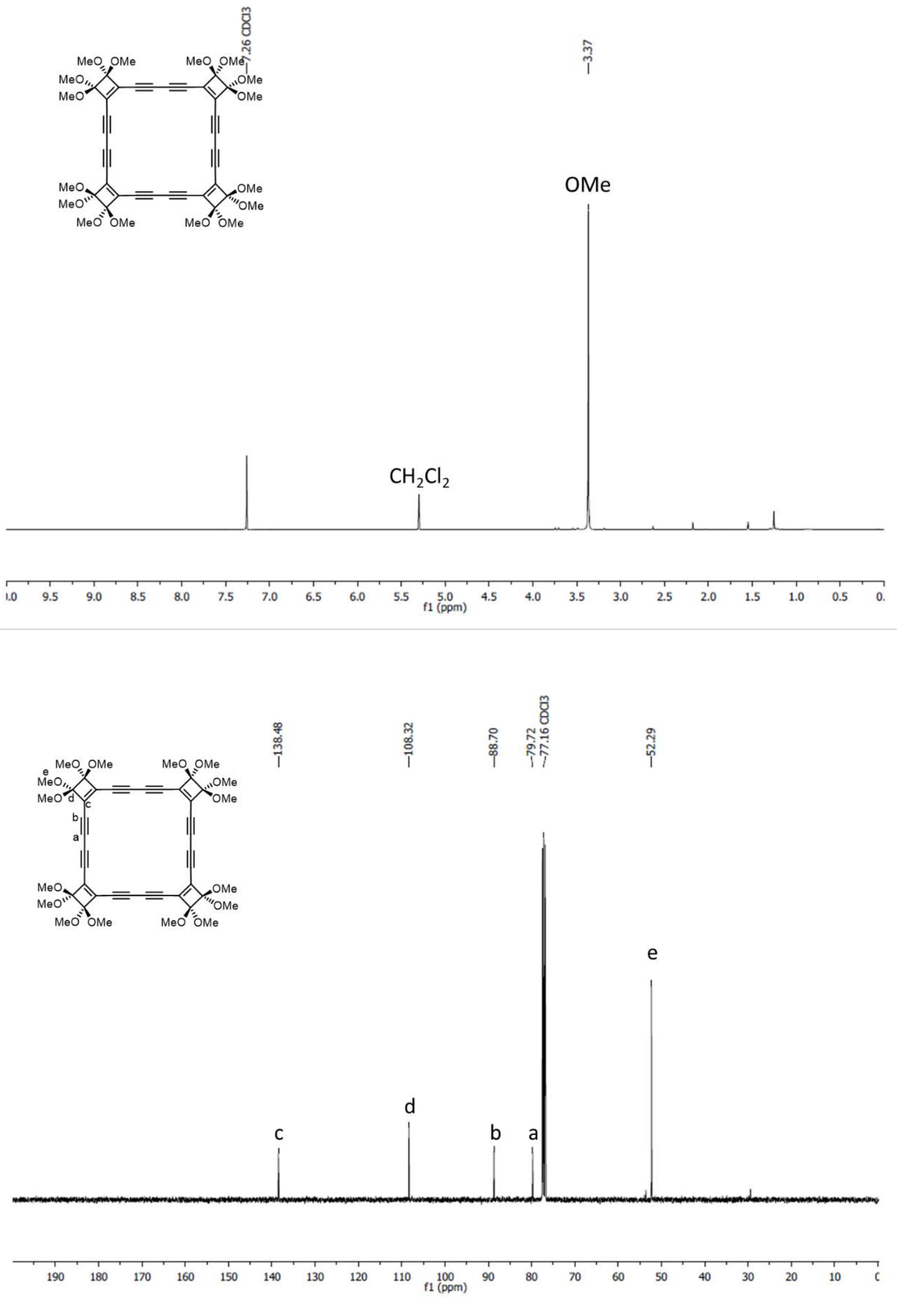

Figure 4.26 ^{1}H NMR (400 MHz, CDCl$_3$, 294 K) and ^{13}C NMR (101 MHz, CDCl$_3$, 294 K) spectra of **28**.

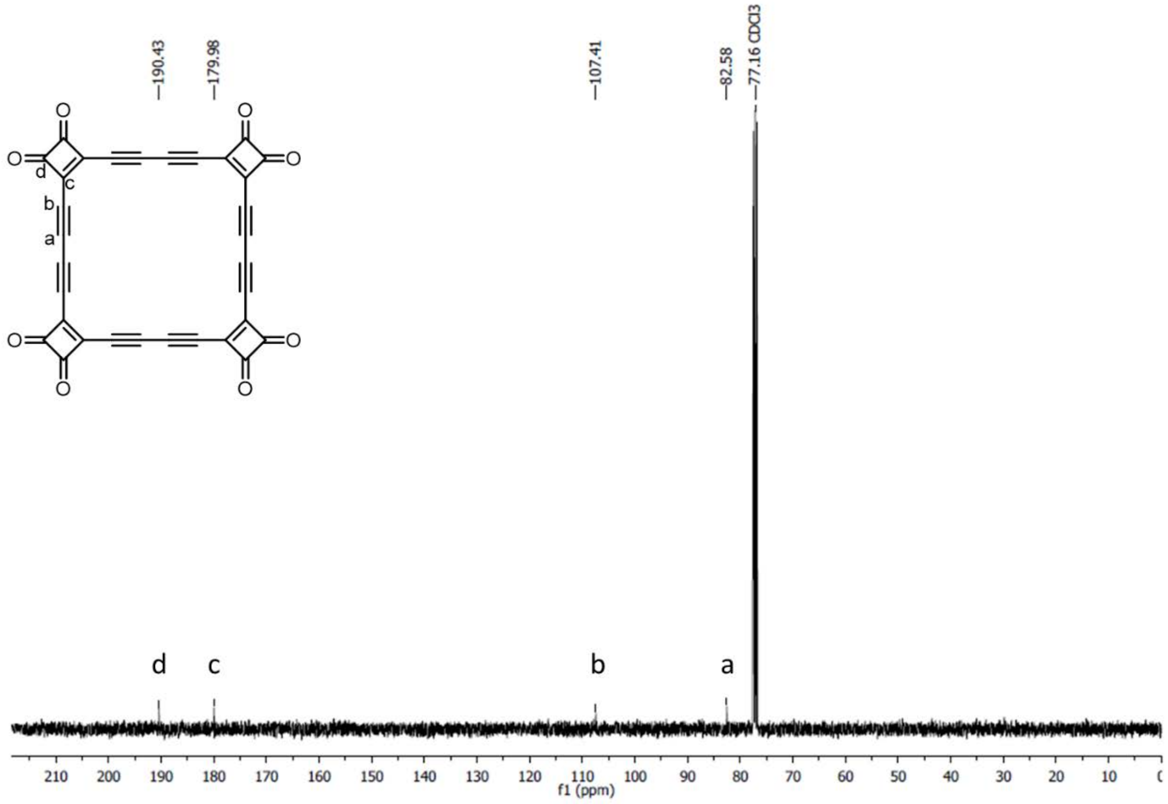

Figure 4.27 ^{13}C NMR (101 MHz, $CDCl_3$, 294 K) spectrum of $C_{32}O_8$.

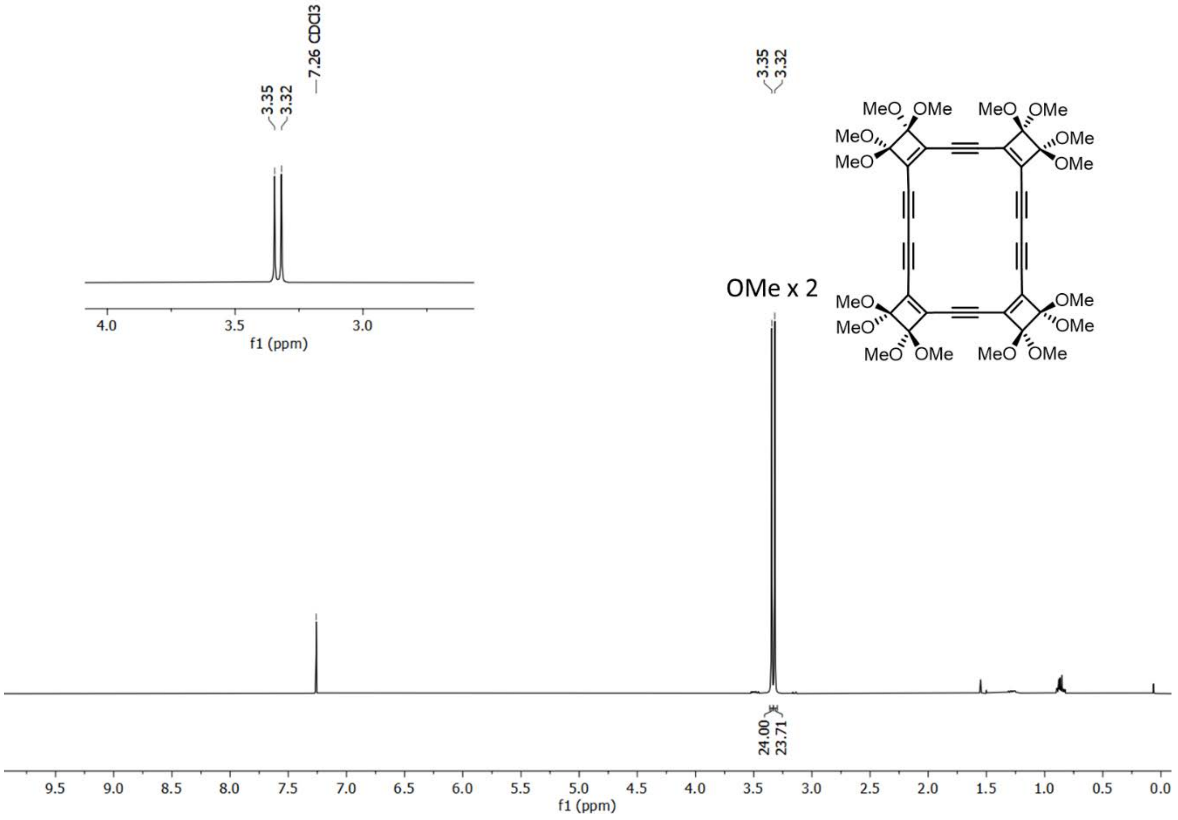

Figure 4.28 ^{1}H NMR (400 MHz, $CDCl_3$, 294 K) spectrum of **27**.

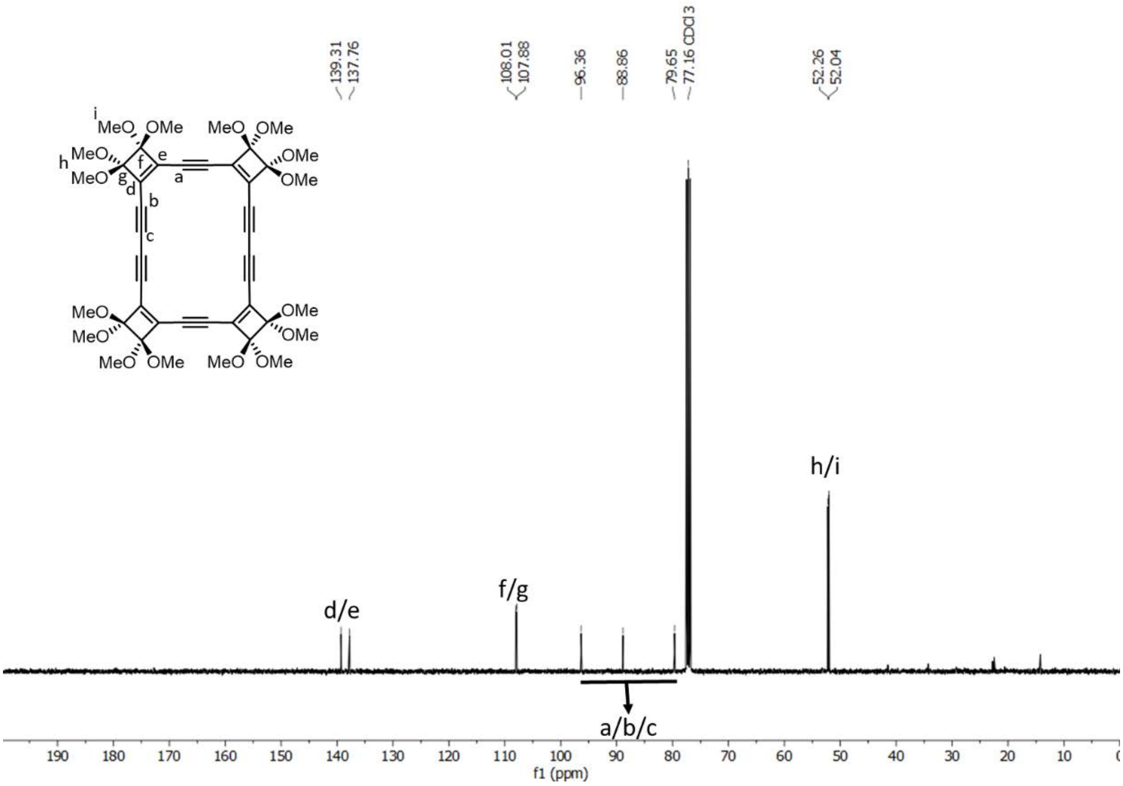

Figure 4.29 ^{13}C NMR (101 MHz, CDCl$_3$, 294 K) spectrum of **27**.

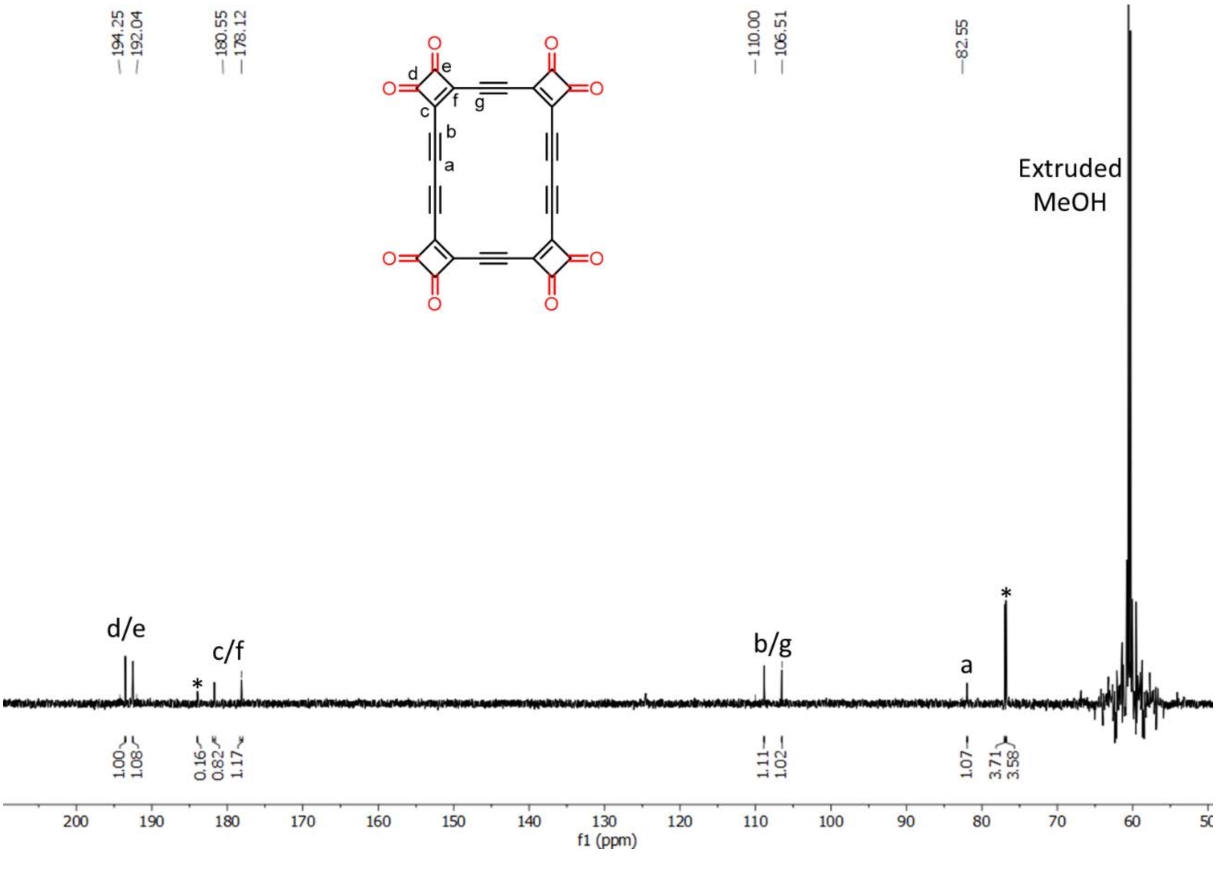

Figure 4.30 ^{13}C NMR (176 MHz, D$_2$SO$_4$, 294 K) spectrum of C$_{28}$O$_8$.

4.7 References

[1] A. W. Von Hofmann, *Proc. R. Soc.* **1857**, *8*, 1–3.

[2] E. Hückel, *Z. Phys. Chem.* **1932**, *76*, 628–648.

[3] R. Breslow, J. Brown, J. J. Gajewski, *J. Am. Chem. Soc.* **1967**, *89*, 4383–4390.

[4] J. D. Roberts, M. C. Caserio, *Basic Principles of Organic Chemistry*, Addison-Wesley, **1977**.

[5] T. M. Krygowski, M. Cyrański, *Tetrahedron* **1996**, *52*, 1713–1722.

[6] M. K. Cyrański, T. M. Krygowski, *Tetrahedron* **1999**, *55*, 6205–6210.

[7] V. I. Minkin, M. N. Glukhovstev, B. Y. Simkin, *Aromaticity and Antiaromaticity*, Wiley, **1994**.

[8] J. A. Pople, L. Radom, W. J. Hehre, *J. Am. Chem. Soc.* **1971**, *93*, 289–300.

[9] D. A. Ponomarev, V. V. Takhistov, *J. Chem. Educ.* **1997**, *74*, 201–203.

[10] J. Kruszewski, T. M. Krygowski, *Tetrahedron Lett.* **1972**, *13*, 3839–3842.

[11] T. M. Krygowski, M. K. Cyrański, *Chem. Rev.* **2001**, *101*, 1385–1420.

[12] L. M. Jackman, F. Sondheimer, Y. Amiel, D. A. Ben-Efraim, Y. Gaoni, R. Wolovsky, A. A. Bothner-By, *J. Am. Chem. Soc.* **1962**, *84*, 4307–4312.

[13] J. F. M. Oth, E. P. Woo, F. Sondheimer, *J. Am. Chem. Soc.* **1973**, *95*, 7337–7345.

[14] M. D. Peeks, T. D. W. Claridge, H. L. Anderson, *Nature* **2017**, *541*, 200–203.

[15] M. Rickhaus, M. Jirasek, L. Tejerina, H. Gotfredsen, M. D. Peeks, R. Haver, H. W. Jiang, T. D. W. Claridge, H. L. Anderson, *Nat. Chem.* **2020**, *12*, 236–241.

[16] P. von R. Schleyer, C. Maerker, A. Dransfeld, H. Jiao, N. J. R. van Eikema Hommes, *J. Am. Chem. Soc.* **1996**, *118*, 6317–6318.

[17] A. Stanger, *J. Org. Chem.* **2006**, *71*, 883–893.

[18] R. O. Jones, *J. Chem. Phys.* **1999**, *110*, 5189–5200.

[19] J. M. L. Martin, P. R. Taylor, *J. Phys. Chem.* **1996**, *100*, 6047–6056.

[20] S. Yang, K. J. Taylor, M. J. Craycraft, J. Conceicao, C. L. Pettiette, O. Cheshnovsky, R. E. Smalley, *Chem. Phys. Lett.* **1988**, *144*, 431–436.

[21] G. Von Helden, P. R. Kemper, N. G. Gotts, M. T. Bowers, *Science* **1993**, *259*, 1300–1302.

[22] M. Saito, Y. Okamoto, *Phys. Rev. B* **1999**, *60*, 8939–8942.

[23] S. Arulmozhiraja, T. Ohno, *J. Chem. Phys.* **2008**, *128*, 114301.

[24] P. W. Fowler, N. Mizoguchi, D. E. Bean, R. W. A. Havenith, *Chem. Eur. J.* **2009**, *15*, 6964–6972.

[25] C. Neiss, E. Trushin, A. Görling, *ChemPhysChem* **2014**, *15*, 2497–2502.

[26] K. Remya, C. H. Suresh, *RSC Adv.* **2016**, *6*, 44261–44271.

[27] S. Xu, F. Liu, J. Xu, Y. Cui, C. Wang, *J. Mol. Model.* **2020**, *26*, 111.

[28] D. Manna, J. M. L. Martin, *J. Phys. Chem. A* **2016**, *120*, 153–160.

[29] J. M. L. Martin, J. El-Yazal, J.-P. François, *Chem. Phys. Lett.* **1996**, *248*, 345–352.

[30] K. Raghavachari, D. L. Strout, G. K. Odom, G. E. Scuseria, J. A. Pople, B. G. Johnson, P. M. W. Gill, *Chem. Phys. Lett.* **1993**, *214*, 357–361.

[31] G. von Helden, M. T. Hsu, N. G. Gotts, P. R. Kemper, M. T. Bowers, *Chem. Phys. Lett.* **1993**, *204*, 15–22.

[32] H. Prinzbach, A. Weller, P. Landenberger, F. Wahl, J. Wörth, L. T. Scott, M. Gelmont, D. Olevano, B. V. Issendorff, *Nature* **2000**, *407*, 60–63.

[33] S. Sokolova, A. Lüchow, J. B. Anderson, *Chem. Phys. Lett.* **2000**, *323*, 229–233.

[34] V. Parasuk, J. Almlöf, *Chem. Phys. Lett.* **1991**, *184*, 187–190.

[35] H. W. Kroto, *Int. J. Mass Spectrom. Ion Process.* **1994**, *138*, 1–15.

[36] L. Belau, S. E. Wheeler, B. W. Ticknor, M. Ahmed, S. R. Leone, W. D. Allen, H. F. Schaefer, M. A. Duncan, *J. Am. Chem. Soc.* **2007**, *129*, 10229–10243.

[37] T. Heaton-Burgess, W. Yang, *J. Chem. Phys.* **2010**, *132*, 234113.

[38] É. Brémond, Á. J. Pérez-Jiménez, C. Adamo, J. C. Sancho-García, *J. Chem. Phys.* **2019**, *151*, 211104.

[39] J. Hutter, H. P. Lüthi, F. Diederich, *J. Am. Chem. Soc.* **1994**, *116*, 750–756.

[40] N. D. Charistos, A. Muñoz-Castro, *Phys. Chem. Chem. Phys.* **2020**, *22*, 9240–9249.

[41] K. Raghavachari, R. A. Whiteside, J. A. Pople, *J. Chem. Phys.* **1986**, *85*, 6623–6628.

[42] F. Diederich, Y. Rubin, C. B. Knobler, R. L. Whetten, K. E. Schriver, K. N. Houk, Y. Li, *Science* **1989**, *245*, 1088–1090.

[43] C. Liang, H. F. Schaefer, *J. Chem. Phys.* **1990**, *93*, 8844–8849.

[44] V. Parasuk, J. Almlöf, M. W. Feyereisen, *J. Am. Chem. Soc.* **1991**, *113*, 1049–1050.

[45] J. D. Watts, R. J. Bartlett, *Chem. Phys. Lett.* **1992**, *190*, 19–24.

[46] M. Feyereisen, M. Gutowski, J. Simons, J. Almlöf, *J. Chem. Phys.* **1992**, *96*, 2926–2932.

[47] D. A. Plattner, K. N. Houk, *J. Am. Chem. Soc.* **1995**, *117*, 4405–4406.

[48] J. M. L. Martin, J. El-Yazal, J.-P. François, *Chem. Phys. Lett.* **1995**, *242*, 570–579.

[49] E. J. Bylaska, J. H. Weare, R. Kawai, *Phys. Rev. B* **1998**, *58*, R7488–R7491.

[50] T. Torelli, L. Mitas, *Phys. Rev. Lett.* **2000**, *85*, 1702–1705.

[51] E. J. Bylaska, R. Kawai, J. H. Weare, *J. Chem. Phys.* **2000**, *113*, 6096–6106.

[52] G. A. Rechtsteiner, C. Felix, A. K. Ott, O. Hampe, R. P. Van Duyne, M. F. Jarrold, K. Raghavachari, *J. Phys. Chem. A* **2001**, *105*, 3029–3033.

[53] G. V. Baryshnikov, R. R. Valiev, A. V. Kuklin, D. Sundholm, H. Ågren, *J. Phys. Chem. Lett.* **2019**, *10*, 6701–6705.

[54] R. Hoffmann, *Angew. Chem. Int. Ed. Engl.* **1987**, *26*, 846–878.

[55] Y. Rubin, C. B. Knobler, F. Diederich, *J. Am. Chem. Soc.* **1990**, *112*, 1607–1617.

[56] Y. Rubin, M. Kahr, C. B. Knobler, F. Diederich, C. L. Wilkins, *J. Am. Chem. Soc.* **1991**, *113*, 495–500.

[57] Y. Rubin, T. C. Parker, S. J. Pastor, S. Jalisatgi, C. Boulle, C. L. Wilkins, *Angew. Chem. Int. Ed.* **1998**, *37*, 1226–1229.

[58] A. S. Hay, *J. Org. Chem.* **1962**, *27*, 3320–3321.

[59] L. S. Liebeskind, R. W. Fengl, K. R. Wirtz, T. T. Shawe, *J. Org. Chem.* **1988**, *53*, 2482–2488.

[60] L. S. Liebeskind, K. R. Wirtz, *J. Org. Chem.* **1990**, *55*, 5350–5358.

[61] S. W. McElvany, M. M. Ross, N. S. Goroff, F. Diederich, *Science* **1993**, *259*, 1594–1596.

[62] N. S. Goroff, *Acc. Chem. Res.* **1996**, *29*, 77–83.

[63] F. Sondheimer, Y. Amiel, *J. Am. Chem. Soc.* **1957**, *79*, 5817–5820.

[64] F. Sondheimer, R. Wolovsky, *J. Am. Chem. Soc.* **1959**, *81*, 1771.

[65] F. Sondheimer, R. Wolovsky, Y. Amiel, *J. Am. Chem. Soc.* **1962**, *84*, 274–284.

[66] E. Vogel, W. Haas, B. Knipp, J. Lex, H. Schmickler, *Angew. Chem. Int. Ed. Engl.* **1988**, *27*, 406–409.

[67] Y. Li, Y. Rubin, F. Diederich, K. N. Houk, *J. Am. Chem. Soc.* **1990**, *112*, 1618–1623.

[68] M. Suzuki, A. Comito, S. I. Khan, Y. Rubin, *Org. Lett.* **2010**, *12*, 2346–2349.

[69] A. Hay, *J. Org. Chem.* **1960**, *25*, 1275–1276.

[70] P. Cadiot, W. Chodkiewicz, *Comptes rendus l'Academie des Sci.* **1955**, *241*, 1055–1057.

[71] S. W. Hla, L. Bartels, G. Meyer, K. H. Rieder, *Phys. Rev. Lett.* **2000**, *85*, 2777–2780.

[72] Y. Jiang, Q. Huan, L. Fabris, G. C. Bazan, W. Ho, *Nat. Chem.* **2013**, *5*, 36–41.

[73] L. Gross, B. Schuler, N. Pavliček, S. Fatayer, Z. Majzik, N. Moll, D. Peña, G. Meyer, *Angew. Chem. Int. Ed.* **2018**, *57*, 3888–3908.

[74] F. Albrecht, D. Rey, S. Fatayer, F. Schulz, D. Pérez, D. Peña, L. Gross, *Angew. Chem. Int. Ed.* **2020**, *59*, 1–6.

[75] L. M. Scriven, K. Kaiser, F. Schulz, A. J. Sterling, S. L. Woltering, P. Gawel, K. E. Christensen, H. L. Anderson, L. Gross, *J. Am. Chem. Soc.* **2020**, *142*, 12921–12924.

[76] K. Kaiser, L. M. Scriven, F. Schulz, P. Gawel, L. Gross, H. L. Anderson, *Science* **2019**, *365*, 1299–1301.

[77] F. Diederich, Y. Rubin, *Angew. Chem. Int. Ed. Engl.* **1992**, *31*, 1101–1123.

[78] T. Leoni, O. Guillermet, H. Walch, V. Langlais, A. Scheuermann, J. Bonvoisin, S. Gauthier, *Phys. Rev. Lett.* **2011**, *106*, 216103.

[79] I. Swart, T. Sonnleitner, J. Repp, *Nano Lett.* **2011**, *11*, 1580–1584.

[80] F. Mohn, J. Repp, L. Gross, G. Meyer, M. S. Dyer, M. Persson, *Phys. Rev. Lett.* **2010**, *105*, 266102.

[81] R. Stomp, Y. Miyahara, S. Schaer, Q. Sun, H. Guo, P. Grutter, S. Studenikin, P. Poole, A. Sachrajda, *Phys. Rev. Lett.* **2005**, *94*, 056802.

[82] S. Fatayer, F. Albrecht, Y. Zhang, D. Urbonas, D. Peña, N. Moll, L. Gross, *Science* **2019**, *365*, 142–145.

[83] R. Keller, H. Wycoff, L. E. Marchi, *Inorg. Synth.* **1946**, *2*, 1–4.